Rotor Blades and Ground Effect

Richard Purvis

Department of Mathematics

University College London

University of London

A thesis submitted for the degree of

Doctor of Philosophy

Supervisor: Prof F. T. Smith FRS

October 2001

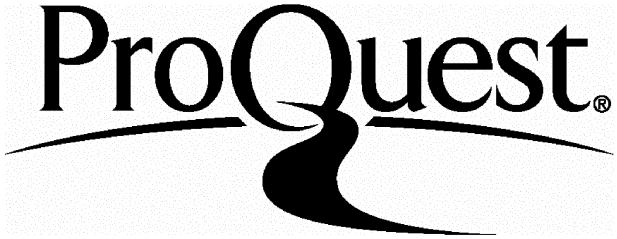

Abstract

This thesis uses numerical, asymptotic and flow structural techniques to examine various aspects of rotor blade flows and ground effect. It explores two- and three-dimensional flows, generally concentrating upon regimes that have a degree of relevance to typical rotor blade flows. Chapter 2 considers, as a first step towards understanding a general rotor blade system in ground effect, a finite rotating disc near horizontal ground. More specifically, it concentrates on determining the layer shape beyond the disc rim that, due to the presence of the ground, cannot remain flat without violating a pressure condition across it. Chapter 3 examines the flow past many blades in ground effect using both a numerical approach and considering various limits of interest to illuminate some of the important features such as enhanced lift and sheltering effects. Chapter 4 then extends this by exploring the many blade limit, whereby the flow develops a periodic structure once sufficiently many blades have been passed.

We then move on to three-dimensional configurations. Chapter 5 takes the previous work further by considering the interactive case that arises after a very large number of blades have been passed, generating a pressure-displacement interaction in the boundary layer. We examine the case of three-dimensional blades, considering the full triple deck problem and then the short blade limit, investigating the flow structure for this physically relevant case. Chapter 6 considers the flow past a three-dimensional hump on a blade of a rotor, examining the flow structure and solution and tentatively using this to propose a description of the flow past the trailing corner of a typical rotor blade. Finally Chapter 7 returns to ground effect, exploring the flow past a single, three-dimensional blade near the ground. It uses a compact difference technique to examine the flow solution for a particular blade shape and investigates the idea of change-over points, where the effective leading edge becomes a trailing edge switching the boundary conditions, these points being generally unknown in advance.

Acknowledgments

Firstly, and most importantly, I would like to thank my supervisor Professor Frank Smith for all his enthusiasm, advice and patience throughout this project. His guidance and support have been invaluable and have been foremost in making the past three years as enjoyable as they have been. Thanks are also due to Professor E R Johnson for his assistance and to the Engineering and Physical Sciences Research Council for their financial support.

I would also like to thank my family for their unwaiving interest and encouragement in whatever I have attempted and tried to achieve. I shall be eternally grateful for everything they have done for me. Finally, I shall be forever indebted to Lucy for her love, support, friendship and endurance throughout the last few years.

Contents

1 Introduction **16**

2 A Disc Rotating Near Horizontal Ground **27**

2.1 Introduction 27

2.2 The problem 30

2.2.1 Governing equations 30

2.2.2 The far field response 33

2.2.3 Flow induced by an infinite disc rotating above the ground . . 35

2.3 Determining the layer shape 36

2.3.1 An integral equation for the layer shape 36

2.3.2 The numerical solution of the integral equation 40

2.3.3 Small h 49

2.4 The full pressure condition 54

3 Planar Flow Past Many-Blades in Ground Effect 62

3.1 Introduction 62

3.2 Problem formulation 65

3.2.1 The boundary layer problem 65

3.2.2 The outer inviscid problem 68

3.3 Solving the outer problem 70

3.3.1 The solution 70

3.3.2 The solution of the integral equations 75

3.4 Numerical methods 77

3.4.1 The boundary layer calculation 77

3.4.2 Numerically determining ψ 79

3.4.3 The iteration procedure 82

3.5 Results 83

3.6 Inviscid limits 93

3.6.1 Large blade heights — $h \gg 1$ 93

3.6.2 Small ground clearances — $h \ll 1$ 98

4 Many Blades in Ground Effect - A Periodic Approach 101

4.1 Introduction 101

4.2 The flow structure 103

4.2.1 Region II 106

4.2.2 Region I 111

4.2.3 Region III 113

4.3 Solution method and comparisons 117

5 Three-Dimensional Interactive Multi-Blade Flow 124

5.1 Introduction 124

5.2 The full three dimensional problem 126

5.3 The short blade limit 131

5.3.1 Region I 132

5.3.2 Region II 134

5.3.3 Region III 135

5.3.4 Region IV 138

5.3.5 Region V 139

6 Three-Dimensional Boundary-Layer Flow Over a Hump and Past a trailing Corner 147

6.1 Introduction 147

6.2 Problem formulation 150

6.2.1 Main deck 152

6.2.2 Upper deck 153

6.2.3 Lower deck 154

6.3 The linearised problem and its solution 155

6.4 Results 160

6.5 Jet effect 167

6.6 The trailing corner problem 170

7 Three-Dimensional Car Undertrays and Blades Near the Ground 173

7.1 Introduction 173

7.2 The two-dimensional problem 175

7.3 The three-dimensional problem 181

7.4 Compact difference solution 185

7.5 Results 191

7.6 Local analysis 197

7.6.1 Inflow-inflow corner 199

7.6.2 Outflow-outflow corner 200

7.6.3 Inflow-outflow corner 202

7.6.4 Nearing an inflow-to-outflow (cross-over) point 204

8 Conclusions and Further Work 207

8.1 Summary 207

8.2 Further work 210

A Some Standard Results 212

A.1 The Blasius solution for the flow past a flat plate 212

A.2 The Von Karman solution for the flow induced by an infinite rotating disc 213

A.3 The triple-deck structure 214

A.4 The double-deck structure 216

B Mean Blasius Flow in the Interactive Regime **218**

C Truncation Errors and Difference Operators **221**

C.1 Difference operators 221

C.2 The δ-operators 222

List of Figures

2.1 The flow geometry: a finite horizontal disc rotating at a constant distance h above horizontal ground, together with an arbitrary fixed body shape H. 29

2.2 The far-field problem 33

2.3 An example of the panel method discretisation of the disc and body shape, showing the line segments and control points. Shown here there are only fourteen panels. In practice many more were taken in order to ensure a closer and more accurate representation of the body shape. 42

2.4 The expected exponential decay of the Tchebyshev coefficients for the case $h = 5$. 46

2.5 Layer shapes beyond a rotating disc at various distances h from the ground. h ranges from 5, for the smallest deflection, to 0.1 for the largest. 47

2.6 Comparison of the layer shapes for a disc with and without a spherical body shape at two different heights, $h = 5$ and $h = 2$. The body shape is shown and has a radius of 0.4. The solid line is the layer shape with the body present. 48

2.7 Comparison of the layer shapes for a disc at a height $h = 1$ with and without a spherical body shape. The body shape is shown and has a radius of 0.4. The solid line is the layer shape with the body present. 49

2.8 Comparison of the layer shapes for a disc at a height $h = 1$ with and without a large cylindrical body shape. The solid line is the layer shape with the body present while the lowest line is the disc without any body shape and the top line is a disc with no body shape but at a height $h = 0.1$ (the length of the stem joining the disc and cylinder) 50

2.9 The next order small-h problem showing the v_0^- and p_{-1}^- boundary conditions. Both v_0^- and p_{-1}^- satisfy Laplace's equation. 52

2.10 Comparison between the small h analytical result near the disc rim (solid line) and the layer shape for $h = 0.1$ from the numerical calculations. 54

2.11 Comparison between the layer shapes for the pressure jump case (solid line) and the no pressure jump case (dotted line) for $h = 2$ with $\alpha = 1$. 58

2.12 Comparison between the layer shapes for the pressure jump case (solid line) and the no pressure jump case (dotted line) for $h = 0.3$ with $\alpha = 1$. 59

2.13 Comparison between the layer shapes for the pressure jump case (solid line) and the no pressure jump case (dotted line) for $h = 0.1$ with $\alpha = 1$. Note the similarity in the linear layer shape for the pressure jump case here and for $h = 0.3$ case in figure 2.12. 60

2.14 Comparison between the layer shapes for $h = 5$ and varying the value of A from $\alpha = 0$, the uppermost solid line, through $\alpha = 0.1$ and $\alpha = 1$ to $\alpha = 10$ the lowest line. 61

3.1 The flow configuration of $n(= 4$ here) blades at a distance h above horizontal ground. 65

3.2 A typical aerofoil showing the definitions of $f^+(x)$ and $f^-(x)$. 66

3.3 Contours Γ_+, $\Gamma_=$ and Γ_- for a point away from $y = 0$. 72

3.4 Contours Γ_+, $\Gamma_=$ and Γ_- for a point on $y = 0$, circumnavigating the point z. 73

3.5 Displacement thicknesses $\delta^{\pm}(x)$ and wake shapes $s(x)$ for five flat blades at heights from $h = 4$ to $h = 1/2$. 84

3.6 As figure 3.5 except that h ranges from $1/4$ to $1/64$. 85

3.7 Plots of the above, below and ground pressures $p^+(x), p^-(x)$ and $p^=(x)$, for the case of five flat blades, with h values ranging from $h = 4$ to $h = 1/2$. 86

3.8 As figure 3.7 except that h ranges from $1/4$ to $1/32$. 87

3.9 Displacement thicknesses and wake center line shapes for five blades at positive angle of attack for various heights. 89

3.10 Displacement thicknesses and wake center line shapes for five blades at negative angle of attack for various heights. 90

3.11 Displacement thicknesses $\delta^{\pm}(x)$ and wake shapes $s(x)$ for two flat blades. 91

3.12 Pressures $p^{=}$ (solid line), p^{+} (dotted line) and p^{-} (dashed line) for two flat blades. 92

3.13 Displacement thicknesses $\delta^{\pm}(x)$ and wake shapes $s(x)$ for two blades at positive angle of attack for heights $h = 2$ to $h = 0.0625$ as in figure 3.11. 93

3.14 Displacement thicknesses $\delta^{\pm}(x)$ and wake shapes $s(x)$ for two blades at negative angle of attack for heights $h = 2$ to $h = 0.0625$ as in figure 3.11. 94

3.15 Non-dimensional lift on each of the five flat blades for the various heights presented earlier 95

3.16 The wake centre line shapes and viscous displacements for nine blades at angle of attack. Note the near periodicity in $s(x)$. 96

4.1 A single blade-wake period 104

4.2 The scaled u velocity profiles mid-blade in the boundary layer for a ten blade case. Note the near periodicity for small y and the gradual growth for large y. The scales used are those determined below for the innermost layer. 105

4.3 The scaled u velocity profiles mid-wake in the boundary layer for a ten blade case. Note the near periodicity for small y and the gradual growth for large y. The scales used are those determined below for the innermost layer. 106

4.4 A Comparison of the wake-center line shapes for a ten blade case. The uppermost line is wake one, the lowermost wake nine. Notice the near periodicity as increasingly more blades are passed. 107

4.5 Schematic of the proposed flow structure, with regions I and II being viscous, and region III being inviscid and containing the ground. . . . 108

4.6 Comparison between the wake shapes $s(x)$ for the current periodic method and blade 4 of the five blade case from chapter 3 for $h = 0.25$. The shape from this chapter is the lower of the two. 120

4.7 Comparison between the wake shapes $s(x)$ for the current periodic method and blade 4 of the five blade case from chapter 3 for $h = 0.0625$. The shape from this chapter is the lower of the two. 121

4.8 Comparison between the underneath pressures p^- for the current periodic method and for blade 4 of the five blade case from chapter 3 for $h = 0.25$. The shape from this chapter is the lower of the two. . . 122

4.9 Comparison between the underneath pressures p^- for the current periodic method and for blade 4 of the five blade case from chapter 3 for $h = 0.0625$. The shape from this chapter is the lower of the two. . 123

5.1 The proposed five region structure with the as yet undetermined y scales. 132

5.2 A sample pressure solution, varying in x for various z values, with $L_1 = 1$, $L = 1$ with $J = \sin(\frac{2\pi z}{L_1})$, $K = \cos(\frac{2\pi z}{L_1})$, $\delta = \sin(\frac{2\pi z}{L_1})$ 145

5.3 A sample pressure solution, varying in x for various z values, with $L_1 = 20$, $L = 1$ with J, K, δ as in figure 5.2. Note the pressure solution is nearly linear as suggested in the analysis in the text. . . . 146

6.1 Sketch in planform of the trailing corner problem, illustrating the double- and triple- deck regions away from the corner and the unknown matching as the trailing corner is approached. 149

6.2 Sketches of the assumed oncoming velocity profiles u_0 and w_0, which are of Blasius and Von Karman types, respectively. 151

6.3 Sketch of the hump showing the length scales discussed in the text. . 152

6.4 Contour Plot of the Pressure solution. The dashed line corresponds to$P = 0$. Between the lines $P < 0$ and P is positive elsewhere. The contour intervals are 0.02 161

6.5 Contour Plot of the displacement A. The contour interval is 0.04. . . 162

6.6 Plot of the farfield A(x) solution for varying θ, where $\tan\theta = x/z$. Note the corridor effects at $\theta = 0^o, 45^o$ where the solution is singular. 168

7.1 The flow structure and setup of the two-dimensional problem. 176

7.2 Rectangular planform and direction of the oncoming flow. 184

7.3 Velocity profiles and pressure for $\alpha = 15^o$, showing the values as x varies for different z values. 192

7.4 As figure 7.3 but for $\alpha = 25^o$. 193

7.5 As figure 7.3 but for $\alpha = 35^o$. 194

7.6 As figure 7.3 but for $\alpha = 45^o$. 195

7.7 As figure 7.3 but for $\alpha = 7.5^o$. 196

7.8 Streamlines for $\alpha = 25^o$. 197

7.9 Streamlines for $\alpha = 7.5^o$. 198

7.10 Flow geometry and co-ordinates for the inflow-inflow corner. 199

7.11 Flow geometry and co-ordinates for the outflow-outflow corner. 201

7.12 Flow geometry and co-ordinates for the inflow-outflow corner. 202

7.13 Flow geometry and co-ordinates for the inflow edge near x_0 where the normal velocity approaches zero as a potential cross-over point is reached 205

Chapter 1

Introduction

Fluid flows induced by a rotor blade have much practical importance, not least with respect to helicopter aerodynamics. For many years the helicopter has played an important role in both military and civilian air transportation, from troop deployment to offshore air taxis, traffic reporting to medical emergencies. The usefulness of a helicopter over other aircraft is its ability to perform tasks that fixed wing vehicles cannot, such as vertical take off and landing and the capacity to hover. In fact, this maneuverability is one of the driving forces behind helicopter use and one of the major design considerations is the ability to operate efficiently for long periods in hover. There are many other practical applications of rotor blade studies, for example in fans, propeller blades, food mixers, hover mowers, and so on, but we shall mostly have the helicopter applications in mind.

However, the aerodynamics of a helicopter are very challenging as the flow it generates is extremely complicated and difficult to measure. Aside from the increased complexity generated by interaction with the tail rotor, effects of the helicopter

body, of vibration, of other aircraft, of buildings and of ground effect (to name a few), the flow induced by the rotor alone (even with only a single blade present) is not easy to understand. An isolated system of rotor blades has many difficulties of its own to be considered. Among these are the development of the rotor wake and the shedding of tip vortices, as well as the importance of blade-vortex interactions where the tip vortices shed from a blade collide with the subsequent one.

There is a vast array of literature considering helicopter blade flows, see for example the books by Gessow and Myers (1952), Bramwell (1976), Johnson (1980), Stepniewski and Keys (1984), Seddon (1990) and Newman (1994) which examine basic helicopter dynamics in various flight regimes. There are also many reviews of more specific topics such as those by Gessow (1986) who compares predictive capabilities in the 1940's and 1950's with those of the 1980's and Johnson (1986) who reviews advances in the aerodynamics of rotary wings. Also of great interest are McCroskey (1995) and Caradonna (1992) who detail the computational techniques used in the calculation of rotor blade and wake flows. Reviews of helicopter design and a history of helicopter development are given by Reichert (1985) and Phillipe *et al* (1985). More recently Conlisk (1997) presents a review of current trends in computational and experimental investigations into rotor blade flows.

Experimental measurements are the foundation of helicopter design, see for example Caradonna and Tung (1981), Parthasarathy *et al* (1985), Hoad *et al* (1988), Hoad (1990), Lorber (1991) and McAlister *et al* (1995) among many, many others. However, experiments are both expensive to perform and difficult to conduct. Moreover, the analysis of the very complicated flow field is tricky and the many interactions present can mask the underlying physical mechanisms at work. It is therefore de-

sirable to carry out analytical and computational investigations, both to attempt to limit (or focus) the use of experiments and to obtain a better grasp of the underlying fluid dynamics governing and driving the flow.

The classical momentum representation of a rotor, or the actuator disc, was first introduced by Glauert (1937) based on earlier work for marine propellers. Up until the 1960s it provided the basis for helicopter design and is still consulted in assessing the basic trends of rotor performance today. As a rotor blade produces upwards thrust it drives a column of air through the rotor plane. The idea of the momentum theory is that the rotor is conceived as an 'actuator disc' across which there is a uniform jump in pressure. It is then possible, considering energy conservation in the form of Bernoulli's theorem, to derive an expression for the thrust imparted by the disc on the fluid and the flow velocity through the disc in terms of the velocity far downstream in the rotor wake. See for example Seddon (1990) or Bramwell (1976) for the full details. However, while this gives a useful rule-of-thumb with regard to measuring rotor performance, with a simple measure of wake velocity giving an approximation of the thrust imparted by a particular rotor, it is quite simplistic. If detail of the rotor wake itself is required, or any consideration of tip vortices or blade wake interactions is necessary (all of which are important aspects of helicopter design in reality), then the actuator disc concept has to be largely abandoned and the presence of genuine individual blades needs to be recognised.

The other main thrust of research into rotor blade flows comes from computational approaches, see for example Bliss and Miller (1990), Egolf and Sparks (1986), Ramachandran *et al* (1993) again amongst many. Also of interest is Srinivasan and Sankar (1995) who review various computational approaches to capturing the flow

and Conlisk (1997) who gives a more detailed discussion and a more exhaustive list of references. For the most part computations are based either upon inviscid potential methods or on direct numerical simulations of the Navier-Stokes equations. The inviscid models generally require a coupling with a model of viscous effects near the blades. This tends to limit their usefulness as the empirical formulae used are either too simplistic, ignoring blade-vortex interactions for example, or are invalid for certain parts of the flow, particularly near blade tips. Likewise, the accuracy of direct numerical simulations is generally accepted to be limited due to the complexity of the flow structure, especially at higher Reynolds numbers. Difficulties arise in resolving the crucial blade-vortex interactions, in examining the impact of tip vortices and in tracking wake positions. Two studies which focus on this aspect of blade-vortex interaction are Hassan *et al* (1992) who approach the problem numerically and Gorton *et al* (1995) who present some experimental results. A major problem is that the numerical approaches can capture only a little of the blade-vortex events that are observed in experiments.

There are generally three approaches to considering the rotor wake: rigid wake and prescribed wake methods (see Landgrebe (1972)), and free wake methods. Each has its own limitations. The rigid wake model, although simple to implement, ignores varying wake shape (or contraction) and as such is now rarely used. The prescribed wake method uses experimental data to fix the wake shape before carrying out any computations. It is computationally efficient and has reasonable agreement with experiment but it requires experimental data for the wake and so in that sense is not predictive. Finally the free-wake method calculates the wake shape as part of the overall solution. This is very expensive computationally but with the advent of

increasingly powerful computers the free wake method is becoming the standard.

It seems clear that addressing the blade-wake and the tip vortex interactions present a considerable challenge. This is, as discussed before, without beginning to consider other effects such as the impact of the other helicopter components on the rotor blade and the influence of external bodies. In particular, hovering in ground effect is an area of interest due to the change in aerodynamics as the rotor nears the ground, with the lift generated being found in practice to be enhanced when the vehicle is within about a rotor diameter from the ground. This has implications both for safety and control of the aircraft near the ground as well as providing the opportunity to exploit the phenomenon. In fact, the earliest helicopters could only achieve hover near the ground as they were not powerful enough to hover without the enhanced lift acquired near the ground. There has been much investigation into ground effect on an aerofoil, see for example Newman (1982), Widnall and Barrows (1970), Tuck and Bentwich (1983) and references therein, and in particular Jones (2000) who includes viscous effects as well as the inviscid mechanisms considered in the earlier articles. There has been less investigation of the mechanisms important for the rotor near the ground. See for example Lighthill (1979), who adapts the actuator disc concept to a ground effect context, and Zbrozek (1950). However, there seems to be little investigation with regard to viscous effects.

Despite the Reynolds number typically being large in many practical helicopter configurations, until recently relatively little effort had been made with regard to boundary layer studies, see for example Crabtree *et al* (1963) and Loitsianskii (1962). Smith and Timoshin (1996a) began to address this by examining the boundary layer flow induced by a system of rotating blades. Considering symmetric cases primarily,

they developed a robust numerical scheme to investigate a variety of rotor configurations, varying the number of blades, the sizes of the blades and the gaps between them among other aspects. Several interesting limits were considered such as the axisymmetric terminal form at large radial distances which was shown to be common to all blade configurations. It was also shown that, for many blades, a double viscous structure appears in the boundary layer. Several new interactions were found in this multiple blade setting such as blade-wake interactions and viscous-inviscid interactions, especially near corners and blade tips. Possibly the most significant of these is the concept of inner-outer interaction, whereby the inner boundary layer solution and the inviscid outer solution become coupled. This is caused by introducing non-symmetry into the rotor and requires the two parts to be solved hand-in-hand rather than sequentially as is usually the case. In order to examine these new interactions in more detail Smith and Timoshin (1996b) examined multiple blade-wake interactions in a two-dimensional setting, which is comparable with a rotor blade under certain circumstances, specifically at large radial distances and in the many blade limit. This article investigated the importance of inner outer interaction, solving both the many blade boundary-layer problem and the outer inviscid problem. Non-symmetry introduces a pressure difference across each blade. However, the wake cannot support a pressure jump and so this pressure difference has to be reduced to zero at the trailing edge (due to the Kutta condition requiring the flow to be smooth) and throughout the wake. The wake shape therefore has to adjust to enable this pressure continuity condition to be satisfied. Moreover, the wake position must be determined in order for the initial conditions for flow over the next blade to be known. Once again the many blade limit is found to be of interest, with a pe-

riodic inner tier to the boundary layer and a relatively simple slowly growing outer tier. Several viscous-inviscid effects peculiar to multi-blade flows were identified, including sheltering effects.

Bowles and Smith (2000a) then considered interactive flow past symmetric multiple blades, where the leading order pressure in the boundary layer is no longer prescribed. This regime arises once the flow has passed over many blades and wakes, and has settled down to a streamwise periodic state, each period consisting of a single blade and wake. The authors found that a pressure-displacement interaction law covers the entire blade wake period (unlike most interactive flows which are generally local in nature). Numerical results were presented and the short blade limit, where the length of the blade is small compared to the length of the period, was examined. The flow structural representation of the flow field with short blades present is driven by the need to balance a sharp drop in pressure along the blade with a slow growth in pressure through the wake in order to satisfy the necessary periodicity conditions. Bowles and Smith (2000b) then extended this to examine the interactive pressure-displacement problem for a periodic array of two-dimensional non-symmetric blades. The interaction is complicated this time as, in addition to the interaction law mentioned just above, the flow must also adjust to enable the pressure continuity condition at the trailing edge and throughout the wake to be satisfied. This happens by way of a pressure jump at the leading edge.

The aim of the present thesis is to continue the basic boundary layer-cum-inviscid zone investigations into rotor blades discussed above. We will attempt to examine ground effect and the influence of three-dimensionality on a rotor blade flow. The Navier-Stokes equations are our starting point for the investigations that follow and

are given in detail in Chapter 2, for the axisymmetric case, in Chapter 3, for the two-dimensional case, and Chapter 5, for the three-dimensional case, along with the relevant non-dimensionalisations and definitions of the Reynolds number.

In Chapter 2, as a first step towards considering a genuine rotor blade in ground effect, we examine the flow induced by a finite disc rotating at a fixed height above the ground. Smith and Timoshin (1996a) determined that the far-field response of any slender bounded rotor blade system is the same regardless of the number of blades it has, or if it is a complete disc. Similarly they also discovered an interesting limit when many blades are present, whereby from outside the boundary layer the mean flow is seen to be Von Karman flow (Von Karman (1921)), i.e. the axisymmetric flow due to a complete rotating disc. Both of these limits suggest that investigation of the ground effect on a rotating disc flow may have some relevance, albeit asymptotically, to the influence of the ground on a genuine rotor system with blades and wakes present.

The need for the layer shape to be distorted from the horizontal position it occupies in the absence of the ground is discussed in Chapter 2 before the far-field response is determined. The problem of evaluating the entire layer shape is then considered, initially via an approximate pressure continuity condition across the layer. A numerical scheme is developed based upon using a ring sink representation of the layer and a panel method (Hess (1990)) description of the disc. Various results are then presented for differing heights of the disc above the ground and also an investigation of the impact of including a body shape beneath the disc. Finally, we reinstate the full pressure condition of a pressure jump across the layer proportional to its curvature (Papageorgiou and Smith (1988) and references therein) and adapt the

solution method by introducing ring vortices along the layer (De Bernardinis and Moore (1986)).

Chapter 3 investigates the ground effect on a sequence of several blades in two dimensions. Jones (2000) examined a single wing in ground effect, and this chapter aims to extend the examination to several blades, considering blade-vortex interactions and resolving the viscous-inviscid coupling discussed above. The solution requires the viscous boundary layer and the inviscid outer problem to be solved simultaneously. The outer problem is solved to yield a singular integral equation for the lift which is then evaluated hand-in-hand with a many-blade boundary layer calculation. Results are presented for varying numbers of blades, various heights and different angles of attack for blade shapes which are flat plates. We also examine two limits: that of large ground clearances which reduces, at leading order, to the case of no ground effect examined by Smith and Timoshin (1996a), and the case of small ground clearances where we show the flow takes on a simple form beneath each blade and that the lift generated is proportional to the inverse of the ground clearance.

In an extension of Chapter 3, Chapter 4 examines the case of many two-dimensional blades in ground effect where the flow solution becomes two tiered in effect with a periodic inner tier and a slowly growing outer tier as in Smith and Timoshin (1996b). The outer solution from Chapter 3 is modified to incorporate the now periodic viscous displacement from the boundary layer. Comparison with the results from Chapter 3 indicates that 'many' equates in practice to only three or four blades, thus making this a useful limiting case.

In Bowles and Smith (2000a) and Bowles and Smith (2000b), the authors considered

the interactive flow past many two-dimensional blades, a regime which develops once sufficiently many blades have been passed, firstly for symmetric cases and then for non-symmetric lifting cases. In Chapter 5 we attempt to extend these studies to examine interactive flow past three-dimensional blades. We limit ourselves here to symmetric blades, initially formulating the full three-dimensional problem before examining the physically relevant case of short blades. The regime of short blades is of interest as in a typical rotor blade there is far more 'gap' than blade. The flow structure in this regime is considered, consisting of five regions, and we present some predicted solutions for the pressure.

We seek in Chapter 6 to develop a representation of the three-dimensional flow past a trailing corner. The importance of tip vortices and blade wake interactions (Conlisk (1997)) make an understanding of how they are shed from the trailing edges of a rotating blade significant. However, there is something of a dilemma at the trailing corner (blade tip). Away from the corner the basic flow structure is known; in one direction it is the jet dominated double-deck structure of Smith and Duck (1977) while along the other edge it is the two-dimensional triple deck structure of Stewartson (1969) (among others) that is key. These two structures are observed at different length scales and how they combine consistently at the corner is not clear at the onset. As a first step to resolving this we examine the flow past a three-dimensional hump embedded within a three-dimensional boundary layer (this is an issue with its own significance as rotor blades are not in general smooth). There has of course been many studies of three-dimensional triple-deck type problems, see for example Sykes (1980), Duck and Burggraf (1986), Davis (1991), Rhyzov and Terent'ev (1997), Ovenden (2001) and references therein. Here we obtain the

solution of this hump problem by considering the linearised case and exploiting the Fourier transform in a similar manner to Smith *et al* (1977), is presented and the interaction between the double- and triple- deck structures is then considered. This leads to a proposed structure for the trailing corner problem.

Chapter 7 returns to ground effect, investigating the flow past a three-dimensional blade very close to the ground. This has particular relevance to racing car under-tray design as well as being a useful starting point for considering many blades in hover. The two dimensional case was investigated by Jones (2000) and Jones and Smith (2000), the latter of which introduced the three-dimensional problem. After a discussion of the extra complications induced by a three-dimensional blade, such as determining the appropriate boundary conditions on the planform edge, we develop a fourth order accurate compact difference scheme (Spotz (1995)) to examine a particular three-dimensional problem, that of a rectangular planform at incidence.

The final chapter, Chapter 8, contributes a summary of the work in this thesis and contains some suggestions on follow-up research.

Chapter 2

A Disc Rotating Near Horizontal Ground

2.1 Introduction

As a first step towards understanding the ground effect on a general rotating blade system, we consider here a finite horizontal circular disc rotating with a uniform angular velocity at a constant distance above horizontal ground. This is of interest, not just because it has some similarity to a general rotor system, but also as it has some more direct parallels. Specifically, the far field response of any slender bounded rotor system is the same (Smith and Timoshin (1996a)) with any azimuthal dependence eroding away with increasing distance from the rotor axis and so the responses here are relevant to a system with genuine blades and wakes present. Another limit of particular relevance is that of a rotor with many blades. In this case (again see Smith and Timoshin (1996a)) the flow is seen to have a two tiered

structure: a fast varying inner tier incorporating the blade-wake interactions and a slowly varying outer tier containing mean Von Karman flow, where the viscous Von Karman flow is the solution for an infinite rotating disc in free space (see appendix A). Therefore from outside the boundary layer we effectively see the same solution in both the many-blade and the present configurations.

For a finite disc rotating with uniform velocity in free space the solution is well known. The disc acts as a centrifugal pump, pulling fluid vertically into the disc boundary layer and throwing it out radially in a thin entraining layer. For a disc near the ground the boundary layer part of the calculation is the same; the disc still pulls in the same amount of fluid and creates a thin layer beyond its rim. However, consideration of the outer inviscid flow shows that, due to the influence of the ground, the free layer shape can no longer remain flat without violating the required pressure condition across the wake.

Our aim is to investigate what influence, if any, the presence of the ground has on the shape of the layer beyond a finite rotating disc. We take as our starting point the steady, axisymmetric, incompressible, non-dimensionalised Navier-Stokes equations with no swirl velocity (and hence are valid only in the outer inviscid flow),

$$\frac{\partial U}{\partial r} + \frac{U}{r} + \frac{\partial V}{\partial z} = 0, \tag{2.1}$$

$$U\frac{\partial U}{\partial r} + V\frac{\partial U}{\partial z} = -\frac{\partial P}{\partial r} + \frac{1}{Re}\Big(\frac{\partial^2 U}{\partial r^2} + \frac{1}{r}\frac{\partial U}{\partial r} - \frac{U}{r^2} + \frac{\partial^2 U}{\partial z^2}\Big), \tag{2.2}$$

$$U\frac{\partial V}{\partial r} + V\frac{\partial V}{\partial z} = -\frac{\partial P}{\partial z} + \frac{1}{Re}\Big(\frac{\partial^2 V}{\partial r^2} + \frac{1}{r}\frac{\partial V}{\partial r} + \frac{\partial^2 V}{\partial z^2}\Big). \tag{2.3}$$

The radial and vertical velocities are given by $U(r,z)$ and $V(r,z)$ respectively, and Re is the non-dimensional Reynolds number based on Ω, the angular velocity, R, the disc radius, and ν the kinematic viscosity of the fluid. We assume $Re = \frac{\Omega R}{\nu} \gg 1$.

The flow geometry (see figure 2.1) is that of an impermeable disc of radius unity rotating at an $O(1)$ height h above the ground. This generates a thin entraining layer on the disc and continuing beyond the disc rim. The unknown shape of this curve is described as C. The entrainment velocity into the lower side of the layer is $Re^{-\frac{1}{2}}v_e^-(s)$ and into the upper side is $Re^{-\frac{1}{2}}v_e^+(s)$ where s is the distance along C from the axis of the disc. The unit normal $\hat{\mathbf{n}}$ to the curve and disc is chosen so that $\hat{\mathbf{n}} \cdot \hat{\mathbf{z}} > 0$ where $\hat{\mathbf{z}}$ is a unit vector along the z-axis. The disc can also be attached to an arbitrary stationary axisymmetric body, a case which is taken up later; the boundary of the body and the disc is then denoted by H and $\hat{n}$ describes the normal to the layer, disc and body.

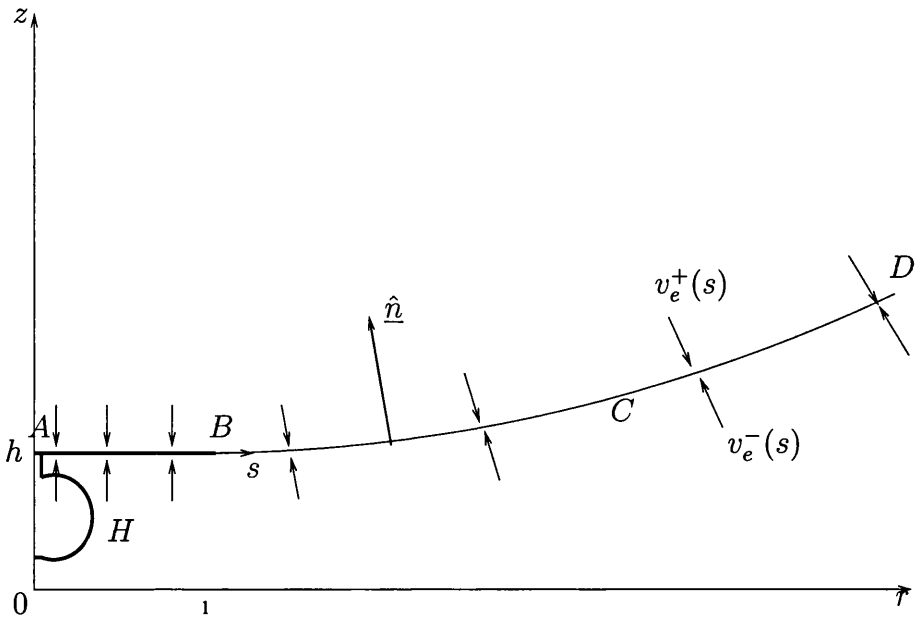

Figure 2.1: The flow geometry: a finite horizontal disc rotating at a constant distance h above horizontal ground, together with an arbitrary fixed body shape H.

In section 2.2 below we set out the problem, subject initially to an approximate

pressure condition, and examine two limits of interest: namely that of the large r response of the layer shape and the flow induced by an infinite disc near the ground. Given this starting point we then turn, in section 2.3, to the full problem of determining the complete layer shape from the disc rim to the far field. We derive an integral equation which allows us to pose a minimization problem to calculate the required shape. We then present some results for various h values for the disc with no body shape present and also consider the case with a body shape to investigate what influence this has on the shape of the viscous shear layer. The case of small h is considered in 2.3.3 and the layer shape is shown to have infinite curvature at the disc rim which compares well with the results from the integral equation calculations. Finally, in section 2.4, we consider the full pressure condition across the layer, revising the integral equation readily to accommodate the new requirements, and compare these new results with the model from 2.3.

2.2 The problem

2.2.1 Governing equations

As the inviscid flow of interest here is driven solely by matching with the entrainment velocities into boundary layer we expand the velocities and pressure as

$$U(r,z) = 0 + \epsilon u(r,z) + \dots \tag{2.4}$$

$$V(r,z) = 0 + \epsilon v(r,z) + \dots \tag{2.5}$$

$$P(r,z) = p_\infty + \epsilon^2 p(r,z) + \dots \tag{2.6}$$

where $\epsilon = Re^{-1/2}$. Substituting these into (2.1) - (2.3) along with the assumption that $Re \gg 1$ leaves us with the axisymmetric Euler equations for u, v and p:

$$\frac{\partial u}{\partial r} + \frac{u}{r} + \frac{\partial v}{\partial z} = 0, \tag{2.7}$$

$$u\frac{\partial u}{\partial r} + v\frac{\partial u}{\partial z} = -\frac{\partial p}{\partial r}, \tag{2.8}$$

$$u\frac{\partial v}{\partial r} + v\frac{\partial v}{\partial z} = -\frac{\partial p}{\partial z}. \tag{2.9}$$

It is reasonable to assume initially that the flow is irrotational and by the principle of conservation of vorticity it will then remain so for all time. It is therefore possible to pose the full problem in terms of the velocity potential Φ where $u = \partial\Phi/\partial r$ and $v = \partial\Phi/\partial z$. The velocity potential, continuous through all space outside of the body H, satisfies

$$\nabla^2\Phi = \frac{\partial^2\Phi}{\partial r^2} + \frac{1}{r}\frac{\partial\Phi}{\partial r} + \frac{\partial^2\Phi}{\partial z^2} = 0 \quad \text{in} \quad r \geq 0, \quad z \geq 0, \tag{2.10}$$

with

$$\frac{\partial\Phi}{\partial z} = 0 \quad \text{on} \quad z = 0, \quad r \geq 0, \tag{2.11}$$

$$\frac{\partial\Phi}{\partial n} = 0 \quad \text{on} \quad \text{H}, \tag{2.12}$$

$$\frac{\partial\Phi}{\partial n} = -v_e^+(s) \quad \text{on} \quad \text{ABD}^+, \tag{2.13}$$

$$\frac{\partial\Phi}{\partial n} = v_e^-(s) \quad \text{on} \quad \text{ABD}^-. \tag{2.14}$$

These conditions are the inviscid tangential flow condition on the ground, on the body, and the entrainment into the boundary layer along either side of the disc and the layer. In the full problem there may be some inner-outer interaction, causing the entrainment velocities $v_e^\pm$ to depend upon the layer shape $Z(r)$ but we are going to model the entrainment velocities as known and the boundary layer flow to be

independent of the shape of the viscous shear layer. We also have a relation on the pressures at the wake. We first make the approximation that the pressure is continuous across the layer and later turn to the more accurate case where the pressure jump across the layer is proportional to its curvature. So, for the time being, we also require

$$p^+(s) - p^-(s) = 0 \quad \text{across the wake BD,} \tag{2.15}$$

as a model. The model is found to yield a significant result for the far-field response and to generate an accurate computational approach for more general cases considered in section 2.4. For a rotating disc in the absence of ground effect the entrainment velocities are given by

$$v_e^+ = v_e^- = \begin{cases} \gamma & \text{on} \quad AB \\ \gamma/r & \text{on} \quad C \end{cases} \tag{2.16}$$

where γ is a constant. The first relation in (2.16) comes from the Von Karman solution and the second is from Smith and Timoshin (1996a) which shows the decay in entrainment of fluid into the boundary layer going as $1/r$. This is not the complete story however as, in reality, the entrainment velocities vary smoothly, with a small region over the disc rim smoothly connecting the entrainment from the constant velocities along the disc to the $1/r$ decay into the layer beyond the rim. As this is very local it is thought not to have an impact on the overall solution. As the problem is linear, the choice of the constant γ is unimportant and is, for convenience, set as $\gamma = 1/2$.

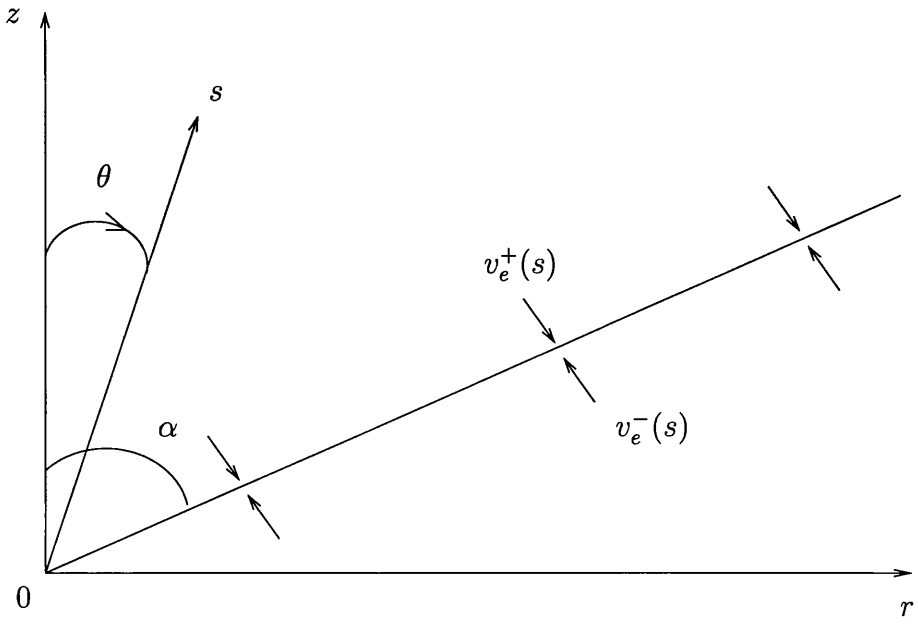

Figure 2.2: The far-field problem

2.2.2 The far field response

From the far field the disc and the ground can be viewed as effectively coincident, leaving two distinct regions: one above and one below the entrainment layer which is assumed to asymptote to a straight line through the origin of an unknown slope (given by an angle α). The problem to be solved, in terms of the velocity potential Φ, but in spherical coordinates (s, θ), is given by (2.10) subject to

$$\frac{\partial \Phi}{\partial \theta} = 0 \quad \text{when} \quad \theta = 0, \tag{2.17}$$

$$\frac{\partial \Phi}{\partial \theta} = 0 \quad \text{when} \quad \theta = \frac{\pi}{2}, \tag{2.18}$$

$$\frac{\partial \Phi}{\partial \theta} = \pm\gamma \quad \text{when} \quad \theta = \alpha^{\mp}, \tag{2.19}$$

which are a symmetry condition, the no penetration ground condition and the requirement of entrainment velocities into the layer, respectively (see figure 2.2). The

angle α is the inclination of the layer to the vertical and is to be determined. We also require the pressure to be continuous across the layer. Solving these equations yields the velocity potential Φ as

$$\Phi = \begin{cases} -A_1[\ln(s\sin\theta) - \frac{1}{2}\ln(\frac{1-\cos\theta}{1+\cos\theta})] & \text{if} \quad \theta < \alpha \\ -A_2\ln(s\sin\theta) & \text{if} \quad \theta > \alpha \end{cases} \tag{2.20}$$

and Stokes's streamfunction Ψ as

$$\Psi = \begin{cases} A_1 s[\cos\theta - 1] & \text{if} \quad \theta < \alpha \\ A_2 s\cos\theta & \text{if} \quad \theta > \alpha \end{cases} \tag{2.21}$$

respectively, where A_1, A_2 are constants adjusted to satisfy the entrainment condition (2.19). The deflection angle α is now determined from applying Bernoulli's theorem along the layer. This gives us the requirement that $(\frac{\partial\Phi}{\partial s})^2 + (\frac{1}{s}\frac{\partial\Phi}{\partial\theta})^2$ needs, in order to give pressure continuity across the layer, to be the same on either side, i.e. at $\theta = \alpha^{\pm}$. Applying this it becomes apparent that this can only be satisfied for

$$\alpha = \frac{\pi}{3} \tag{2.22}$$

These solutions form the far field solution for *any* bounded rotating blade system in the proximity of the ground. It holds for the rotating disc considered here but, to repeat, it also holds when there are genuine blades and wakes present as in a rotor blade, because the azimuthal dependence erodes away as r increases leaving the same far-field form regardless of the initial rotor set up.

2.2.3 Flow induced by an infinite disc rotating above the ground

We temporarily consider an unbounded rotating disc near the ground. This is of interest as it is gives an idea of what is happening beneath a finite disc near to the ground and is useful in the small h analysis near the disc rim considered in subsection 2.3.3. Above the disc we have the Von Karman solution with fluid constantly flowing in axially. However, beneath the disc the no penetration condition at the ground prevents this from happening; so what form does the flow take there?

We have to solve the Euler equations in the region between the disc and the ground subject to no penetration on the ground and constant entrainment into the layer on the disc. We consider $r \gg 1$ and, assuming v is independent of r at large distances, we write

$$v(r,z) = \bar{v}(z), \tag{2.23}$$

which, along with the Euler equations, imply the forms

$$\begin{aligned} u(r,z) &= r\bar{u}(z), \\ p(r,z) &= r^2\bar{p} + p_0(z), \end{aligned} \tag{2.24}$$

where $\bar{p}$ is a constant. Substituting these into the Euler equations reduces them to

$$2\bar{u} + \bar{v}' = 0, \tag{2.25}$$

$$\bar{u}^2 + v\bar{u}' = -2\bar{p}, \tag{2.26}$$

$$\bar{v}\bar{v}' = -p_0', \tag{2.27}$$

subject to

$$\bar{v}(h) = \gamma, \tag{2.28}$$

$$\bar{v}(0) = 0, \tag{2.29}$$

where γ is the constant entrainment into the discs boundary layer and $'$ denotes differentiation with respect to z. Integrating (2.27) immediately yields

$$p_0 = -\frac{1}{2}\bar{v}^2. \tag{2.30}$$

Differentiating (2.26) and substituting for $\bar{v}'$ from (2.25) gives

$$\bar{v}\bar{u}'' = 0. \tag{2.31}$$

Solving this, and applying a zero vorticity condition so that $\bar{u}' = 0$, yields the simple form for the velocities and pressure as

$$u = -\frac{\gamma r}{2h}, \tag{2.32}$$

$$v = \frac{\gamma z}{h}, \tag{2.33}$$

$$p = -\frac{r^2\gamma^2}{8h^2} - \frac{\gamma^2 z^2}{2h^2}. \tag{2.34}$$

So this determines the flow between an infinite disc and the ground, or the flow beneath a disc close to the ground but away from the disc rim. See also Debuchy *et al* (1998) who consider a similar limit for two infinite co-rotating discs at small h.

2.3 Determining the layer shape

2.3.1 An integral equation for the layer shape

We now seek to derive an integral formulation of the global problem in order to find the layer shape between the disc rim and the far-field form determined above. Let

$G(r, r_0, z, z_0)$ be the Green's function satisfying

$$\nabla^2 G = \delta(z - z_0)\delta(r - r_0)/r_0, \tag{2.35}$$

so that G is the velocity potential at (r, z) due to a ring source of total strength 2π at (r_0, z_0). Two forms for G are

$$\begin{aligned} G(r, r_0, z, z_0) &= \frac{1}{4}\int_0^\infty J_0(kr_0)J_0(kr)e^{(-k|z-z_0|)}\mathrm{d}k \\ &= \frac{2}{\pi R_1}K(\frac{2\sqrt{rr_0}}{R_1}) \end{aligned} \tag{2.36}$$

where K is the complete elliptic integral of the first kind and $R_1^2 = (r + r_0)^2 + (z - z_0)^2$. The first of these is from Morse and Feshbach (1953) who derive it from the streamfunction for a ring source and the second is from an integral relation given in Gradstein and Ryzhik (1965). The Green's function thus has a single logarithmic singularity when simultaneously $r = r_0 \neq 0$ and $z = z_0$. The second form listed in (2.36) is the most useful for our purposes. Let C be described as $z = Z(r)$.

Now consider the source velocity potential

$$\begin{aligned} \Phi_S(r, z) &= -\int_C r_0[v_e^-(s_0) + v_e^+(s_0)]G(r, r_0, z, Z(r_0))\mathrm{d}s_0 \\ &\quad -\int_C r_0[v_e^-(s_0) + v_e^+(s_0)]G(r, r_0, z, -Z(r_0))\mathrm{d}s_0. \end{aligned} \tag{2.37}$$

The first integral gives a distribution of ring sources of total strength $-2\pi r_0(v_e^- + v_e^+)$ per unit distance along C and the second the image of these ring sources in the plane $z = 0$. This form for Φ_S satisfies the governing equation, the ground condition and gives pressure continuity across the layer. The jump in $\partial\Phi_S/\partial n$ in crossing from $z > Z(r)$ to $z < Z(r)$ is now

$$[\frac{\partial \Phi_S}{\partial n}(s)]_C = -[v_e^-(s) + v_e^+(s)], \tag{2.38}$$

with Φ_S and its derivatives continuous away from C.

This holds for the layer but as yet we have taken no account of the disc (and possible body underneath). Let the normal velocity induced on H by the presence of Φ_S be

$$u_n^S(\mu) = \frac{\partial \Phi_S}{\partial n}|_H, \tag{2.39}$$

where μ is some convenient coordinate describing the surface H. Now define the body velocity potential Φ_H as the half-space potential that, when added to the source-induced flow on H, gives the required entrainment velocities there, i.e. satisfying

$$\begin{aligned} \nabla^2 \Phi_H &= 0, && (2.40) \\ \frac{\partial \Phi}{\partial z} &= 0 \quad \text{on} \quad z = 0, \quad r \geq 0, && (2.41) \\ \frac{\partial \Phi}{\partial n} &= -u_n^S(\mu) - v_e^{\pm}(\mu) \quad \text{on} \quad H, && (2.42) \end{aligned}$$

where $v_e^{\pm}(\nu)$ is non-zero only on the disc AB. This linear external Neumann problem can be solved straightforwardly by any convenient method.

The total potential

$$\Phi = \Phi_H + \Phi_S, \tag{2.43}$$

then satisfies the governing equation (2.10), the no penetration conditions (2.11) , (2.12) and the pressure condition (2.15). To satisfy the remaining entrainment conditions on the normal velocities at C it is sufficient to add to the jump condition (2.38) the requirement that the difference of the entrainment velocities on each side of C is $v_e^- - v_e^+$, and so fixing the correct entrainment on either side of the layer. Thus we introduce

$$\Delta(r) = \quad \frac{1}{2}\left(\frac{\partial \Phi}{\partial n}|_{C^-} + \frac{\partial \Phi}{\partial n}|_{C^+}\right)$$

$$= \frac{\partial \Phi_H}{\partial n}|_C - \int_C r_0[v_e^-(s_0) + v_e^+(s_0)]\frac{\partial G}{\partial n}(r, r_0, z, Z(r_0))\mathrm{d}s_0$$
$$- \int_C r_0[v_e^-(s_0) + v_e^+(s_0)]\frac{\partial G}{\partial n}(r, r_0, z, -Z(r_0))\mathrm{d}s_0, \qquad (2.44)$$

where the first integral is a Cauchy principal value. The necessary conditions are satisfied provided

$$\Delta(r) = \frac{1}{2}(v_e^- - v_e^+)(r) \quad \text{for all } r \geq 1. \qquad (2.45)$$

Together (2.44) and (2.45) give a singular integral equation determining $Z(r)$ and thus the shape of the layer cross-section C.

Since the unit normal to C has been chosen so that $\hat{\mathbf{n}} \cdot \hat{\mathbf{z}} > 0$,

$$\hat{\mathbf{n}} = (-Z'(r)\hat{\mathbf{r}} + \hat{\mathbf{z}})/\{1 + [Z'(r)]^2\}^{\frac{1}{2}}. \qquad (2.46)$$

The length $\mathrm{d}s$ is

$$\mathrm{d}s = \mathrm{d}r/|\hat{\mathbf{n}} \cdot \hat{\mathbf{z}}| = \{1 + [Z'(r)]^2\}^{\frac{1}{2}}\mathrm{d}r. \qquad (2.47)$$

Thus (2.44) becomes

$$\Delta(r) = \frac{\partial \Phi_H}{\partial n}|_C$$
$$- \int_1^\infty r_0[v_e^-(r_0) + v_e^+(r_0)](\frac{\partial G}{\partial z} - Z'(r)\frac{\partial G}{\partial r})(r, r_0, z, Z(r_0))H(r, r_0)\mathrm{d}r_0$$
$$- \int_1^\infty r_0[v_e^-(r_0) + v_e^+(r_0)](\frac{\partial G}{\partial z} - Z'(r)\frac{\partial G}{\partial r})(r, r_0, z, -Z(r_0))H(r, r_0)\mathrm{d}r_0 \qquad (2.48)$$

where

$$H(r, r_0) = \frac{(1 + [Z'(r_0)]^2)^{\frac{1}{2}}}{(1 + [Z'(r)]^2)^{\frac{1}{2}}}. \qquad (2.49)$$

2.3.2 The numerical solution of the integral equation

The solution of the integral equation (2.48), coupled with (2.45), for $\Delta(r)$ is now a numerical task. Before being able to determine $\Delta(r)$ we need to describe $Z(r)$ through some form of parameterization and we also need an efficient method of obtaining Φ_H. There are many possible ways of doing both but the methods presented here are thought to be sensible and appear to work well.

As C is expected to be very smooth it seems most efficient to use a Tchebyshev expansion to describe $Z(r)$ since the coefficients of the higher terms will decay exponentially fast, leading to an efficient representation of the layer shape. Further, it is convenient to map the region $1 \leq r < \infty$ onto a finite region. To increase the resolution at the edge B (see figure 2.1) where $Z'(r)$ changes most rapidly it is convenient to map this point to -1. Also to avoid unnecessarily high resolution at infinity where $Z'(r)$ changes most slowly it is convenient to map this to 0. The mapping used depends on the value of h. For most h values the mapping

$$\xi = -1/r \quad (-1 \leq \xi \leq 0) \tag{2.50}$$

is used. However, as will be seen, for $h << 1$ it is more useful to use the mapping

$$\xi = -1/r^2 \quad (-1 \leq \xi \leq 0). \tag{2.51}$$

Whichever is used, we then describe $Z'(r)$, the fundamental quantity in (2.48), as

$$Z'(r) = f(\xi) = \sum_{n=0}^{\infty} a_n T_n(\xi), \tag{2.52}$$

where T_n is the nth Tchebyshev polynomial

$$T_n(\xi) = \cos(n \cos^{-1} \xi). \tag{2.53}$$

Since $f(\xi)$ is a polynomial, $Z(r)$ can be obtained readily from $Z'(r)$ by the analytic integration

$$Z(r) = h + \int_1^r f(-1/r')\mathrm{d}r' \tag{2.54}$$

for (2.50) and similarly for (2.51). In order to immediately satisfy the far field and disc rim conditions $Z'(\infty) = 1/\sqrt{3}$ and $Z'(0) = 0$, we impose the requirements that $f(-1) = 0$ and $f(0) = 1/\sqrt{3}$ and so (2.52) gives

$$a_0 = 1/\sqrt{3} - \sum_{n=2}^{\infty} a_n T_n(0), \tag{2.55}$$

$$a_1 = a_0 + \sum_{n=2}^{\infty} a_n T_n(-1). \tag{2.56}$$

The undetermined coefficients are thus $a_2, a_3, a_4, \ldots$, as a_0 and a_1 are determined from the linear relations above, equations (2.55) and (2.56).

The chosen method for determining the body potential Φ_H is an axisymmetric panel method. See Hess and Smith (1967) for a detailed discussion of the method and Hess (1990) for a more recent review; we will give a brief overview here. The disc, and if present the body, is described as a series of source panels. The profile curve (i.e. at $\theta = 0$ say) is approximated by a series of J line segments. These segments, when rotated through 2π radians, describe the entire body. Each of these line segments then describes a line of ring sources with constant, but as yet undetermined, strength σ_i, where i is a typical panel. The centre point of each line segment is called the control point. See also figure 2.3.

The potential ϕ_1 and velocities u_1,v_1 at a point (r, z) due to a ring source of unit strength and radius a lying in the plane $z = b$ are given by

$$\phi_1 = \frac{4aK(k_1)}{[(r+a)^2 + (z-b)^2]^{\frac{1}{2}}}, \tag{2.57}$$

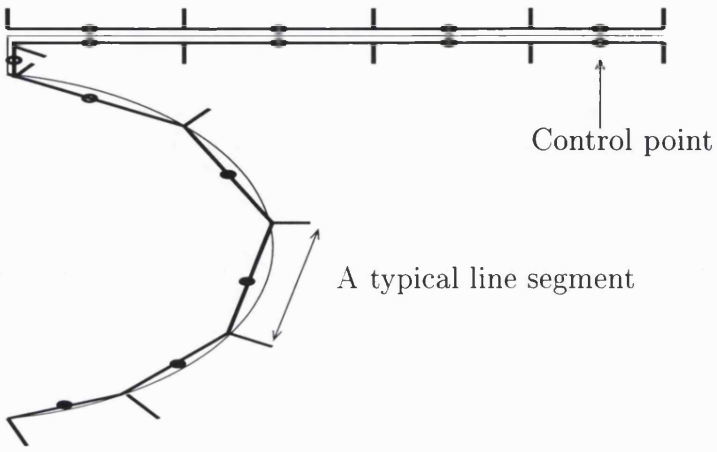

Figure 2.3: An example of the panel method discretisation of the disc and body shape, showing the line segments and control points. Shown here there are only fourteen panels. In practice many more were taken in order to ensure a closer and more accurate representation of the body shape.

$$u_1 = \frac{4a(z-b)E(k_1)}{[(r-a)^2+(z-b)^2][(r+a)^2+(z-b)^2]^{\frac{1}{2}}}, \tag{2.58}$$

$$v_1 = \frac{2a}{y[(r+a)^2+(z-b)^2]^{\frac{1}{2}}}[K(k_1)+\frac{r^2-a^2-(z-b)^2}{(r-a)^2+(z-b)^2}E(k_1)], \tag{2.59}$$

where

$$k_1^2 = \frac{4ar}{(r+a)^2+(z-b)^2}, \tag{2.60}$$

and K, E are complete elliptic functions. The potential, ϕ^{ik}, and velocities, u^{ik} and v^{ik}, induced at a given control point i due to a different line segment k can then be calculated by simply integrating the relevant equation from (2.57) - (2.59) along the line segment k. The segment i also induces a potential and velocities at its own control point. This is somewhat less straight forward as the integrals are singular

and must be considered as principal values. The problem is addressed in Hess and Smith (1967) where the authors develop a series expansion near to the singular point, which effectively carries out the integrals as principal values, and integrates as before away from the singular point. Using this technique to calculate ϕ^{ii}, u^{ii} and v^{ii}, we are in a position to determine the potential and velocities induced at each control point due to the presence of the entire representation of the body. The relevant quantities are given by

$$\phi^i = \sum_{k=1}^{J} \sigma_k \phi^{ik}, \tag{2.61}$$

$$u^i = \sum_{k=1}^{J} \sigma_k u_H^{ik}, \tag{2.62}$$

$$v^i = \sum_{k=1}^{J} \sigma_k v_H^{ik}. \tag{2.63}$$

We can now apply this to our problem (2.40) - (2.42). Firstly, in order to satisfy (2.41) we introduce an image of the body in the plane $z = 0$ where the original line segment and its image both have the same strength σ_i. Finally, we need to determine values of σ_i such that (2.42) is satisfied at each control point. This is relatively simple as the required velocities (2.42), evaluated at each control point, combined with (2.62) and (2.63) give a set of J linear, algebraic equations for the undetermined σ_i. When solved the σ_i and source panels give a representation of ϕ_H. Calculation of $\frac{\partial \Phi_H}{\partial n}$ on the layer C in (2.48) can be carried out using these calculated panel strengths and (2.57) - (2.59).

Now for any given $Z(r)$, $\Delta(r)$ can be calculated and so we are in a position to set up an iteration to determine the required layer shape. The iteration is posed as a

minimization of the integral

$$I = \int_1^\infty [\Delta(r) - \frac{1}{2}(v_e^- - v_e^+)(r)]^2 w(r) \mathrm{d}r, \tag{2.64}$$

where $w(r)$ is a weighting function, chosen here to be a sum of delta functions $\delta(r_i)$, corresponding to a least squares minimization over the collocation points $\{r_i\}$. These are distributed in a similar manner to the mapping (2.50) or (2.51), with more points near to the disc rim than in the far field.

For a given set of coefficients, $a_2, \ldots, a_N$, the value of I can be determined straightforwardly:

1. First calculate a_0 and a_1 from (2.55) and (2.56) to satisfy the far field and disc rim conditions on the layer shape.

2. Using the current $Z(r)$ guess, determine the induced velocities at the control points of the panel representation of the body from (2.42).

3. With the required control point velocities known, we can solve the necessary linear system to calculate each of the panel strengths σ_i fixing the body potential Φ_H.

4. It is now possible to calculate $\Delta(r)$ from (2.48), and hence the value of I can be determined for (2.64).

5. Check convergence, then either have a new guess at $a_2, \ldots, a_N$ and return to item (1) or finish.

The new guess at $a_2, \ldots, a_N$ required in item (5) is made using the NAG library routine E04FYF which uses a combined Gauss-Newton and modified Newton algorithm. One advantage of the panel method discussed earlier is that the solution of

the algebraic equations for σ_i (item (3) above) is in effect only done once throughout the entire minimization. The only change at each iteration is the required velocities at the control points so inverting the whole system of equations (2.62) - (2.63) is only carried out once for each body shape and height. As far as carrying out the integrals in (2.48) is concerned we truncate them at some point $r_\infty \gg 1$ and then, assuming the far-field form from 2.2.2, carry out the integrals beyond this point analytically while numerically determining them for $1 < r < r_\infty$. The value of r_∞ used was $r_\infty = 100$ and this was varied to ensure that there was no sensitivity in the solutions to our choice.

The typical number N of Tchebyshev polynomials required varies with h but is generally between 20 and 24 to give $a_N \approx \sqrt{E}$, where E is the least squares error. The expected exponential decay of the coefficients a_i can be seen clearly as in figure 2.4. The method was also applied without setting a_0, a_1 (i.e. minimising over all $N+1$ Tchebyshev coefficients) to check the far-field and near disc conditions were satisfied even when they were not initially forced. Although the minimization took longer to converge, the results were identical.

The results are shown in figure 2.5 for a disc with no body shape beneath it. It can be seen clearly that as h decreases the deflection of the layer is increased. The far field response can also be seen to emerge as r increases. As h is reduced further the layer shape, rather than monotonically tending towards the 30^o far field angle, overshoots it and tends to the far field form from above. This arises from the layer shape having infinite curvature at the disc rim as is shown in the next section.

Also shown, in figures 2.6 - 2.8, are some examples of the disc with a body shape beneath it. The body shape used was that of a sphere joined to the disc by a short

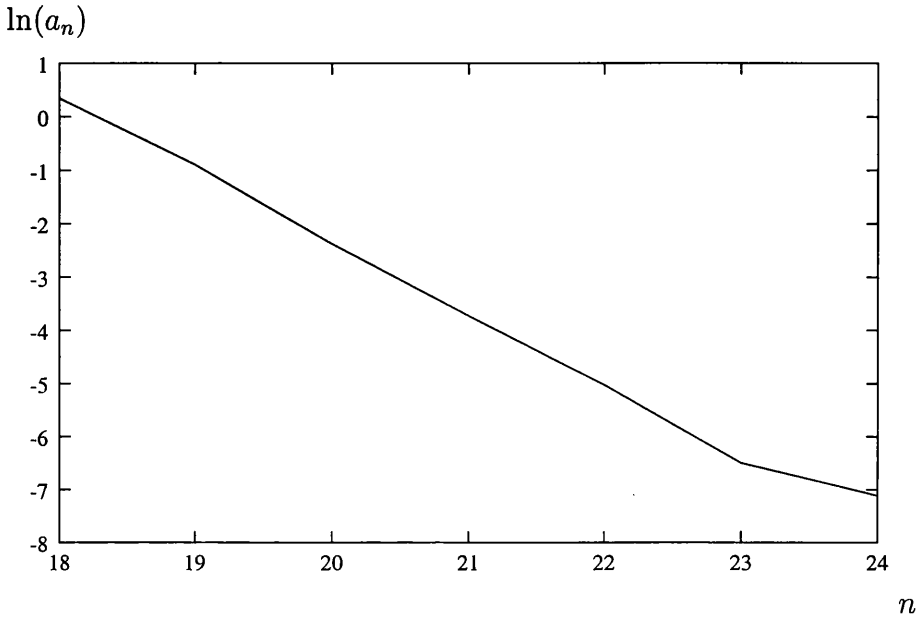

Figure 2.4: The expected exponential decay of the Tchebyshev coefficients for the case $h = 5$.

stem. The results show that for relatively large h a sphere of small radius has very little impact on the layer shape as a whole, as might be expected. For a large sphere, the layer shape is deflected up further than usual. This suggests that the body shape effectively brings the ground nearer. This can be seen easily by visualising, instead of a sphere, a cylinder of radius much greater than 1 as in figure 2.8. Here the disc will only see the body shape near the disc rim and so it will be this, rather than the ground effect, that forces the distortion of the layer shape and thus effectively the body replaces the ground near the disc. The same is true for the sphere except that the impact is slightly less severe. As h decreases it is observed that even a small sphere can have a considerable impact on the layer shape.

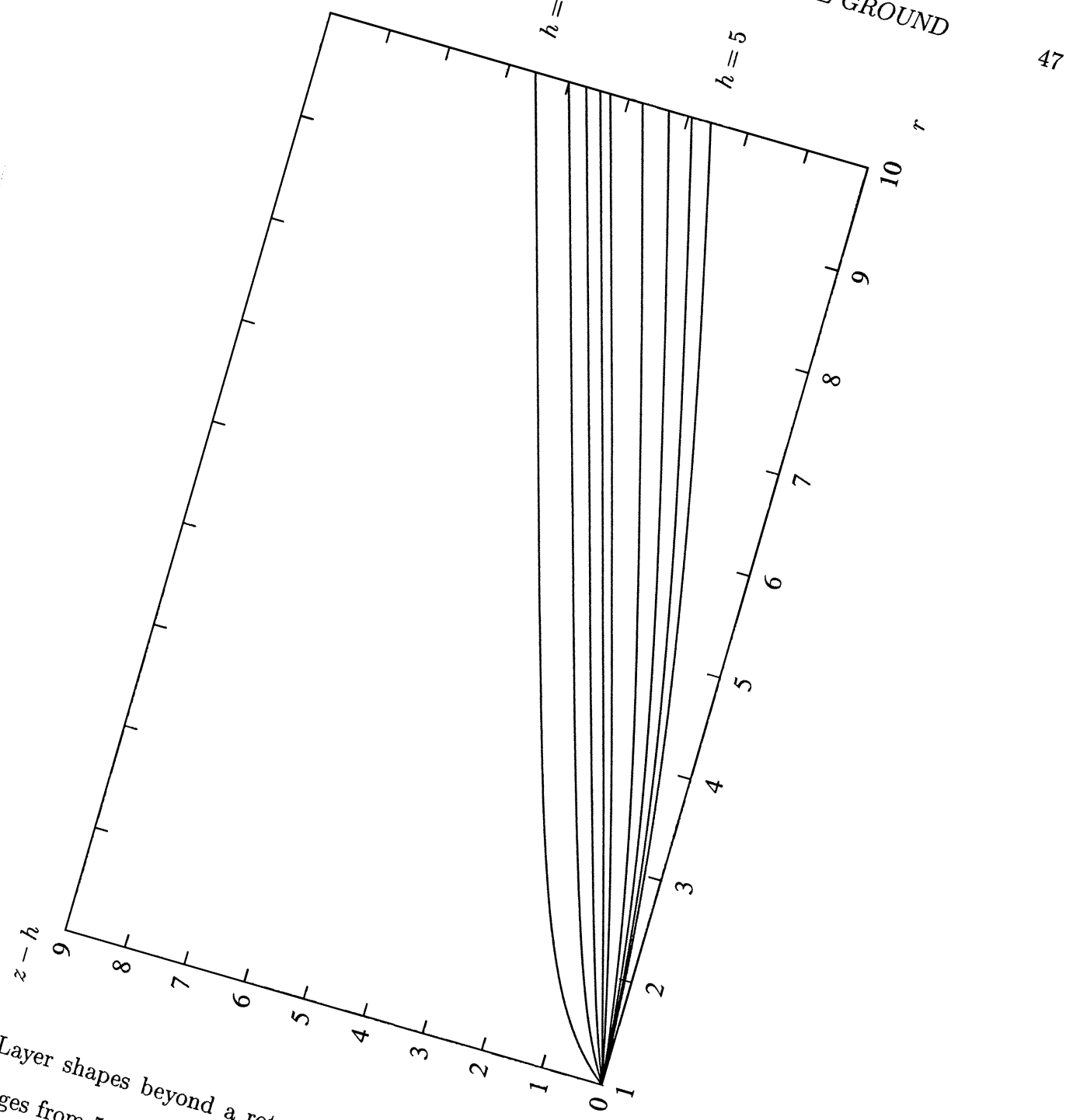

Figure 2.5: Layer shapes beyond a rotating disc at various distances h from the ground. h ranges from 5, for the smallest deflection, to 0.1 for the largest.

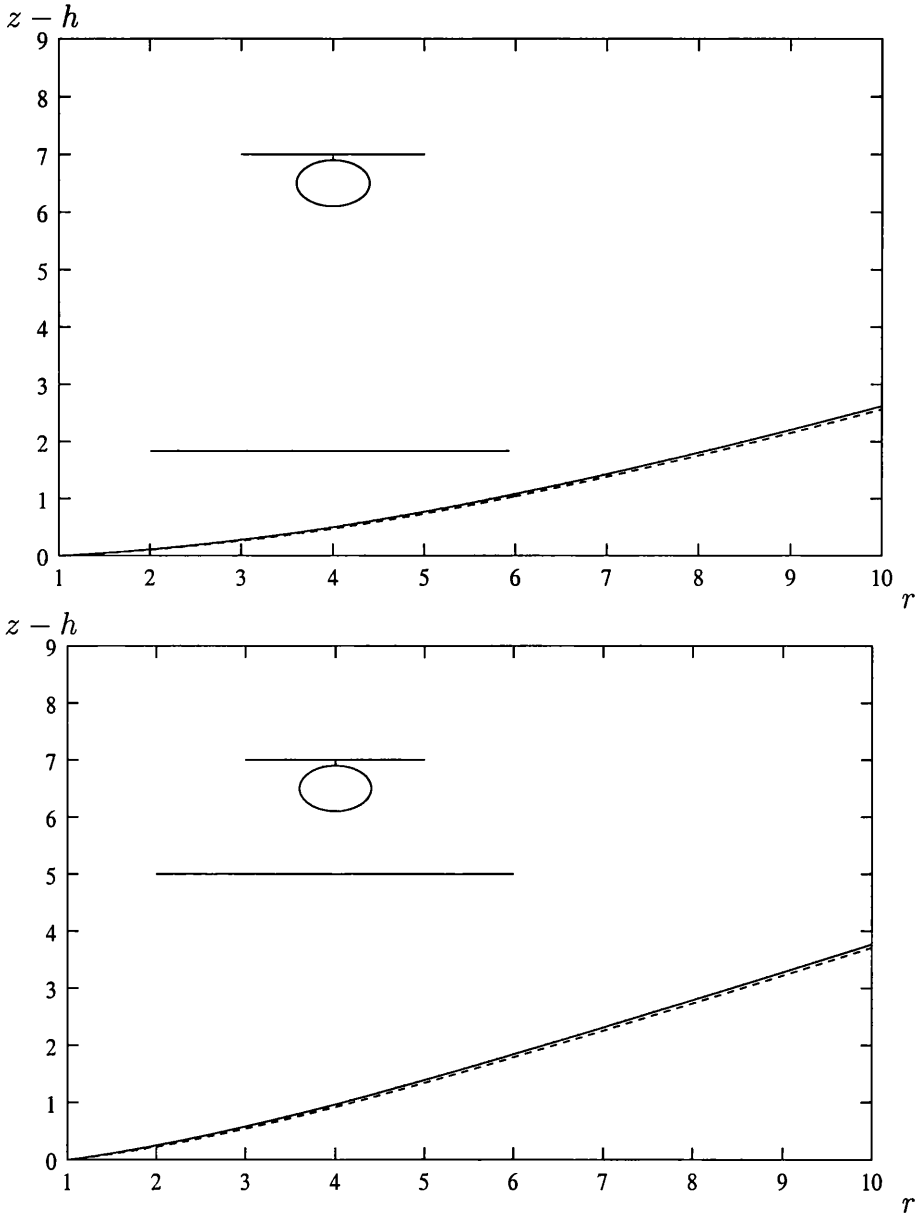

Figure 2.6: Comparison of the layer shapes for a disc with and without a spherical body shape at two different heights, $h = 5$ and $h = 2$. The body shape is shown and has a radius of 0.4. The solid line is the layer shape with the body present.

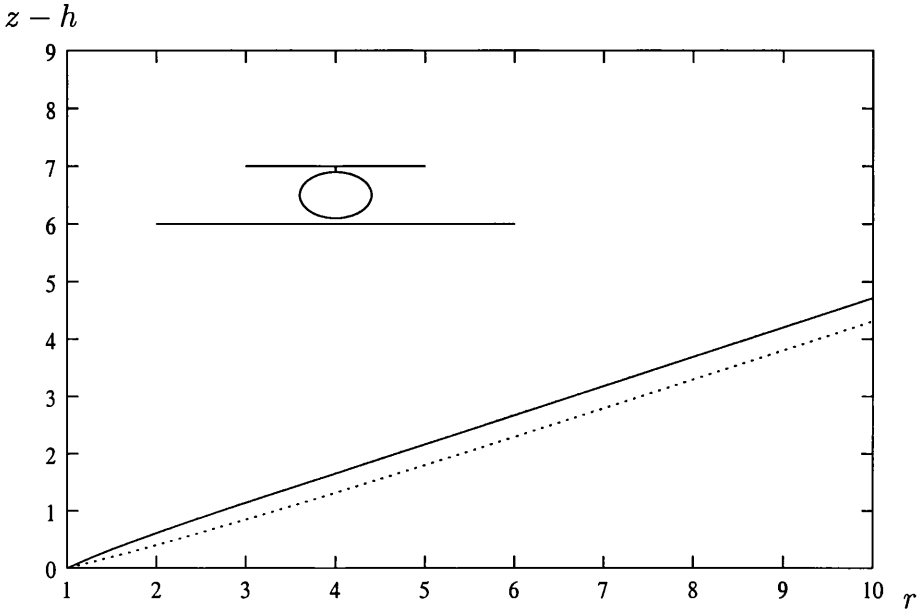

Figure 2.7: Comparison of the layer shapes for a disc at a height $h = 1$ with and without a spherical body shape. The body shape is shown and has a radius of 0.4. The solid line is the layer shape with the body present.

2.3.3 Small h

As can be seen from the numerical results the deflection of the layer shape becomes quite severe near the disc rim for $h \ll 1$. To examine why the flow solution behaves in this manner we now turn to the limit of small h. We consider an $O(h)$ by $O(h)$ region around the disc rim by writing $z = h + h\hat{z}$, $r = 1 + h\hat{r}$, $Z(r) = hZ_0(\hat{r}) + h^2 Z_1(\hat{r}) + \ldots$ and, in view of the infinite disc results from 2.2.3, expand the velocities and pressure as

$$(u^+, v^+, p^+) = (u_0^+ + \ldots, v_0^+ + \ldots, p_0^+ + \ldots), \tag{2.65}$$

$$(u^-, v^-, p^-) = (\frac{u_{-1}^-}{h} + u_0^- + \ldots, v_0^- + \ldots, \frac{p_{-2}^-}{h^2} + \frac{p_{-1}^-}{h} + \ldots) \tag{2.66}$$

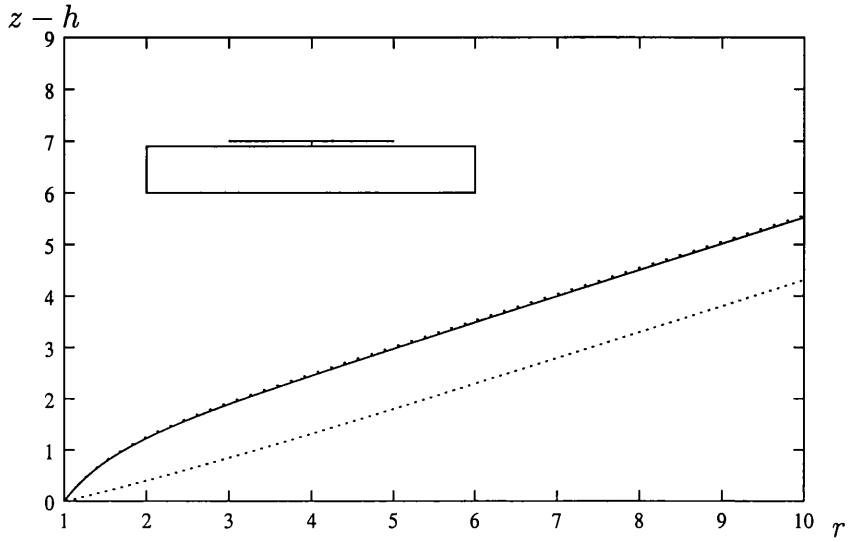

Figure 2.8: Comparison of the layer shapes for a disc at a height $h = 1$ with and without a large cylindrical body shape. The solid line is the layer shape with the body present while the lowest line is the disc without any body shape and the top line is a disc with no body shape but at a height $h = 0.1$ (the length of the stem joining the disc and cylinder)

above and beneath the disc and layer respectively. We then need to solve the Euler equations subject to

$$v^- = 0 \quad \text{when} \quad \hat{z} = -1, \tag{2.67}$$

$$v^- = c \quad \text{when} \quad \hat{z} = 0, \quad \hat{r} < 0, \tag{2.68}$$

$$v^- - Z_1'(\hat{r})u^- = c \quad \text{when} \quad \hat{z} = 0, \quad \hat{r} > 0, \tag{2.69}$$

$$p^+ = p^- \quad \text{on} \quad \hat{z} = Z(r), \tag{2.70}$$

$$(u_-, v_-, p_-) \to \text{infinite disc solution} \quad \text{as} \quad \hat{r} \to -\infty, \tag{2.71}$$

which are the no penetration condition on the ground, constant entrainment into the disc boundary layer, the known normal entrainment into the layer, pressure continuity across the layer. The final condition (2.71) actually emerges as part of the solution. Substituting the velocity expansions into the Euler equations and applying the relevant conditions yields the leading order terms beneath the system immediately as,

$$u_{-1}^{-} = -\frac{c}{2}, \tag{2.72}$$

$$p_{-2}^{-} = -\frac{c^2}{8}, \tag{2.73}$$

$$Z_0(\hat{r}) = 0, \tag{2.74}$$

In order to maintain pressure continuity it is necessary to add an $O(1/h^2)$ constant to p^+ to match with this region. The next order equations yield Laplace's equation for v_0^- and p_{-1}^- subject to

$$v_0^- = 0 \quad \text{on} \quad \hat{z} = -1, \tag{2.75}$$

$$v_0^- = c \quad \text{on} \quad \hat{z} = 0, \quad \hat{r} < 0, \tag{2.76}$$

$$v_0^- = c(1 - \frac{Z_1'}{2}) \quad \text{on} \quad \hat{z} = 0, \quad \hat{r} > 0, \tag{2.77}$$

$$p_{-1}^- = 0 \quad \text{on} \quad \hat{z} = 0, \quad \hat{r} > 0, \tag{2.78}$$

where the fourth of these conditions is necessary as p_{-1}^- is not a constant and is too large to be matched by the flow solution above the layer (also see figure 2.9).

To solve this problem we map the region into the complex $\bar{z}$-plane using the mapping $\bar{z} = e^{\pi\tilde{z}+i\pi}$, where $\tilde{z} = \hat{r} + i\hat{z}$. This leaves us with a half-plane problem subject to mixed boundary conditions along the $\bar{x}$-axis. So we need to find v_0^- and p_{-1}^-, both

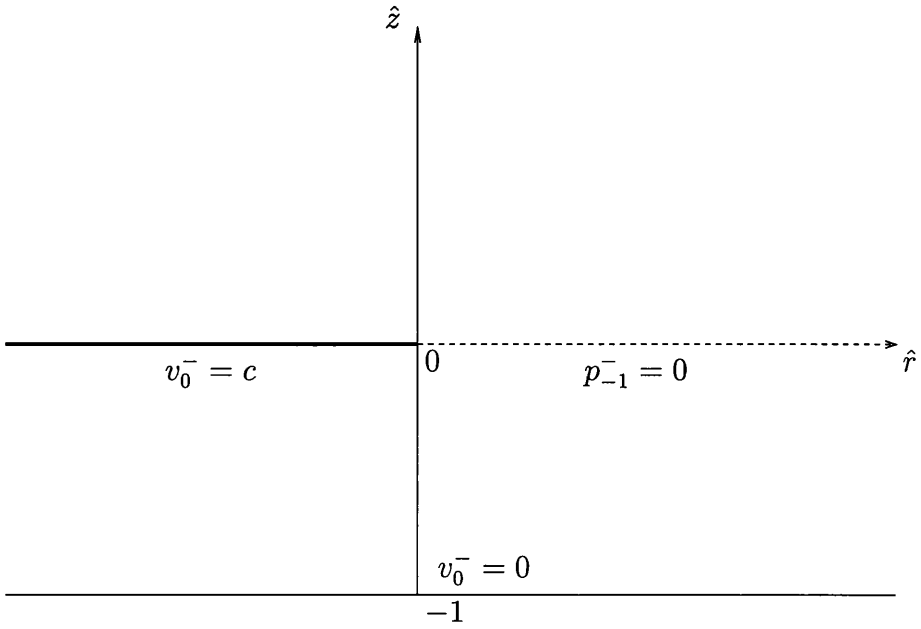

Figure 2.9: The next order small-h problem showing the v_0^- and p_{-1}^- boundary conditions. Both v_0^- and p_{-1}^- satisfy Laplace's equation.

satisfying the Cauchy-Riemann equations, and subject to

$$v_0^- = 0 \quad \text{on} \quad \bar{y} = 0, \quad \bar{x} > 0, \tag{2.79}$$

$$v_0^- = c \quad \text{on} \quad \bar{y} = 0, \quad -1 < \bar{x} < 0, \tag{2.80}$$

$$p_{-1}^- = 0 \quad \text{on} \quad \bar{y} = 0, \quad \bar{x} < -1. \tag{2.81}$$

Now consider the complex function

$$g(\bar{z}) = (\bar{z} + 1)^{-\frac{1}{2}}(P + iV), \tag{2.82}$$

analytic in the upper-half plane $\bar{y} > 0$. We can write

$$g(\bar{z}) = \begin{cases} |\bar{x} + 1|^{-\frac{1}{2}}(V - iP) & \text{for} \quad \bar{x} < -1, \quad \bar{y} = 0 \\ |\bar{x} + 1|^{-\frac{1}{2}}(P + iV) & \text{for} \quad \bar{x} > -1, \quad \bar{y} = 0 \end{cases} \tag{2.83}$$

and use Cauchy's integral formula to relate the real and imaginary parts of $g(\bar{z})$, giving

$$Re(g(\bar{x})) = \frac{1}{\pi}\int_{-\infty}^{\infty} \frac{Im(g(\bar{x}))}{\xi - \bar{x}} \mathrm{d}\xi. \tag{2.84}$$

This gives us, writing $p_{-1}^{-} \equiv P$, $v_0^{-} \equiv V$ and applying conditions (2.79) - (2.81),

$$\left.\begin{array}{ll} |\bar{x}+1|^{-1/2} & v_0^{-}(\bar{x} < -1) \\ |\bar{x}+1|^{-1/2} & p_{-1}^{-}(\bar{x} > -1) \end{array}\right\} = \frac{c}{\pi}\int_{-1}^{0} \frac{\mathrm{d}\xi}{(\xi+1)^{1/2}(\xi - \bar{x})}. \tag{2.85}$$

Carrying out this integral, using the substitution $\xi = \theta^2 - 1$, and mapping back to the original plane gives the velocity on $\hat{z} = 0$, $\hat{r} > 0$ as

$$v_0^{-}(\hat{r} > 0, 0) = \frac{2c}{\pi}\arctan\left(\frac{1}{\sqrt{e^{\pi\hat{r}} - 1}}\right). \tag{2.86}$$

and the layer shape, from (2.77), as

$$Z_1(\hat{r}) = 2\hat{r} - \frac{4}{\pi}\int_0^{\hat{r}} \arctan\left(\frac{1}{\sqrt{e^{\pi\xi} - 1}}\right)\mathrm{d}\xi. \tag{2.87}$$

So right at the disc rim, i.e. for $\hat{r} \ll 1$,

$$v_0^{-} = c - 2c\left(\frac{\hat{r}}{\pi}\right)^{1/2} + \ldots, \tag{2.88}$$

which gives the layer shape as

$$Z_1(\hat{r}) = \frac{8}{3\pi^{1/2}}\hat{r}^{3/2} + \ldots. \tag{2.89}$$

This has infinite curvature at the rim and explains the rapid change in the layer shape in the numerical results near the disc. The result also indicates why the mapping $x = -1/r^2$ in the parameterisation of the layer shape works better for small h than the $-1/r$ one. The other limit of interest is as $\hat{r} \to \infty$. There $v_0^{-} \to 0$ and the layer shape is given by

$$Z_1(\hat{r}) = 2\hat{r} + \ldots, \tag{2.90}$$

So we have just outside the disc rim region, i.e. for $\hat{r} \gg 1$,

$$Z(r) = h + h^2(\frac{2(r-1)}{h}) + \ldots = h(1 + 2(r-1)) + O(h^2), \qquad (2.91)$$

which, when compared to the far field result $Z(r) \sim \frac{r}{\sqrt{3}}$, explains the overshooting of the far field angle seen in the numerical results. A comparison of this small h analysis and the numerical calculation is shown in figure 2.10 where good agreement can be seen.

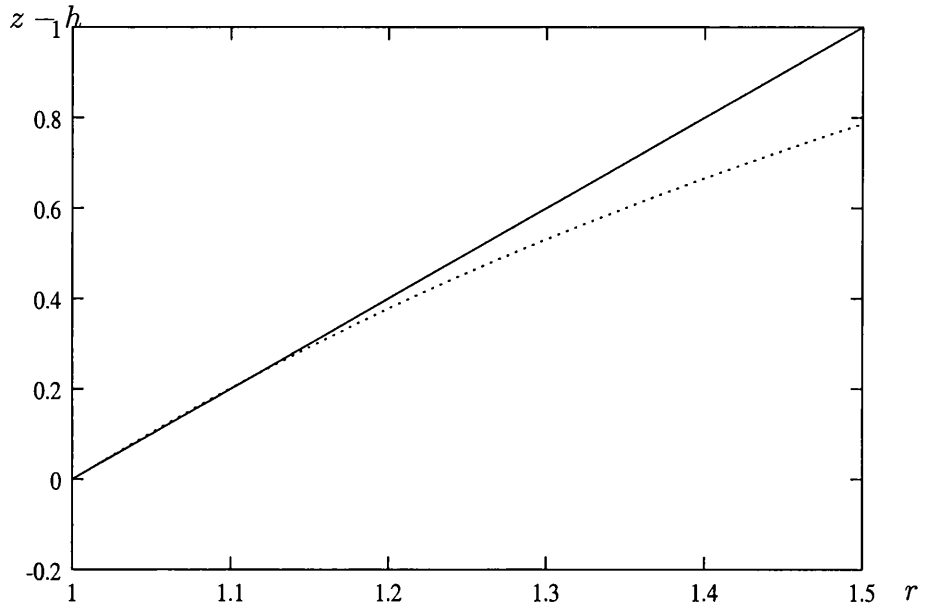

Figure 2.10: Comparison between the small h analytical result near the disc rim (solid line) and the layer shape for $h = 0.1$ from the numerical calculations.

2.4 The full pressure condition

As mentioned earlier the pressure condition used so far is a model one, adopted for starting purposes and to highlight the influences of entrainment and body shape. In

reality the layer can also support a pressure jump across it and so we now aim to include this effect here. Thus the previous pressure condition (2.15) across the layer is now replaced by the model

$$p^+ - p^- = [p] = -A(r)\frac{Z''(r)}{(1+(Z'(r))^2)^{\frac{3}{2}}} \tag{2.92}$$

where the function $A(r)$ is determined from the viscous shear layer. This model is based upon Papageorgiou and Smith (1988) and is an attempt to introduce a pressure jump into the problem. Roughly $A(r) \approx \bar{u}^2\delta$ where $\bar{u}$ is the radial velocity in the boundary layer and δ is the boundary layer thickness. Typically $\bar{u}$ decays as $1/r$ while δ grows as r. Hence we model $A(r)$ as

$$A(r) = \frac{\alpha}{r}, \tag{2.93}$$

where α is a constant, assumed known from the boundary layer flow. We will consider solutions for a variety of magnitudes of α.

An important point, which adds strength to the discussion in the previous sections, is that the far field analysis considered earlier (section 2.2.2) is still applicable as the straight line predicted there has $Z''(r)$ being zero and so (2.92) reduces to (2.15), leaving the problem as before. The question now is, can we adapt the existing method of section 2.3 to encompass this new pressure jump condition? The answer is yes. We effectively add to the existing series of ring sources a sheet of ring vortices along the layer. This, given the correct strength of vortices, keeps the normal velocity into the layer unchanged while introducing a jump in the tangential velocity (and therefore in p) allowing (2.92) to be satisfied.

In the original formulation we now introduce ϕ_v, the potential due to this series of ring vortices with unknown strength to give the necessary jump in u across the

layer. This generates two important changes to the original set up. Firstly ϕ_v causes a different velocity to be induced on the body so that (2.39) becomes

$$u_n^s(\nu) = \frac{\partial \phi_s}{\partial n} + \frac{\partial \phi_v}{\partial n} \tag{2.94}$$

but otherwise the ϕ_H determination is the same still requiring the solution of (2.40)-(2.42). The total potential is now defined as

$$\phi = \phi_H + \phi_s + \phi_v \tag{2.95}$$

and satisfies the governing equation (2.10), the no penetration conditions and the new pressure condition (2.92). Again, as before, the remaining entrainment conditions are satisfied provided that the difference in normal entrainment velocities on each side of C is $v_e^- - v_e^+$. So we introduce

$$\begin{aligned} \Delta_1(r) = & \quad \frac{1}{2}\left(\frac{\partial \phi}{\partial n}|_{C-} + \frac{\partial \phi}{\partial n}|_{C+}\right) \\ = & \quad \Delta(r) + \frac{1}{2}\left(\frac{\partial \phi_v}{\partial n}|_{C-} + \frac{\partial \phi_v}{\partial n}|_{C+}\right) \end{aligned} \tag{2.96}$$

with $\Delta(r)$ as in (2.44). Then once again the necessary conditions are satisfied by (2.45) (with Δ replaced by Δ_1). All that remains to be done now is to determine ϕ_v, or more accurately $\frac{\partial \phi_v}{\partial n}$. We introduce

$$\underline{r}_+(n) = (r, z) + \hat{\underline{n}}\eta, \tag{2.97}$$

$$\underline{r}_-(n) = (r, z) - \hat{\underline{n}}\eta, \tag{2.98}$$

so that $\underline{r}_+$,$\underline{r}_-$ are displaced normally off the sheet by a small distance η, where (r, z) is the point at which we are trying to find $\frac{\partial \phi_v}{\partial n}$. We then have

$$\begin{aligned} \left(\frac{\partial \phi_v}{\partial r}, \frac{\partial \phi_v}{\partial z}\right) = & \quad \frac{1}{2}\lim_{\eta \to 0_+} \int_1^\infty V^R(r_0)(\underline{G}_1(\underline{r}_+, r_0, Z(r_0)) + \underline{G}_1(\underline{r}_-, r_0, Z(r_0)))\mathrm{d}r_0 \\ + & \quad \frac{1}{2}\lim_{\eta \to 0_+} \int_1^\infty V^R(r_0)(\underline{G}_1(\underline{r}_+, r_0, Z(-r_0)) + \underline{G}_1(\underline{r}_-, r_0, Z(-r_0)))\mathrm{d}r_0, \end{aligned} \tag{2.99}$$

where $V^R(r)$ is the strength of the vortex rings required in order to satisfy (2.92), the second integral gives the effect of the image system and $\underline{G}_1$ is discussed below. The streamfunction for a single vortex ring is given by Lamb (1932) as

$$\psi(r,z,r_0,z_0) = (rr_0)^{\frac{1}{2}}\{(\frac{2}{k}-k)K(k) - \frac{2}{k}E(k)\} \tag{2.100}$$

where

$$k = \frac{(r-r_0)^2+(z-z_0)^2}{(r+r_0)^2+(z-z_0)^2} \tag{2.101}$$

and $K(k)$ and $E(k)$ are the complete elliptic functions of the first and second kind respectively. Using this, $\underline{G}_1$ can be constructed as

$$\underline{G}_1(r,z,r_0,z_0) = (\frac{\partial\psi}{\partial z}, -\frac{\partial\psi}{\partial r})(r,z,r_0,z_0). \tag{2.102}$$

We now have everything we need to calculate $\frac{\partial\phi_v}{\partial n}$, where

$$\frac{\partial\phi_v}{\partial n} = \frac{\partial\phi_v}{\partial z} - Z'(r)\frac{\partial\phi_v}{\partial r}, \tag{2.103}$$

if we can calculate the integrals on the right hand side of (2.99). To calculate these we make use of the integral formula derived in De Bernardinis and Moore (1986). They, in a method akin to that of Hess and Smith (1967) for the singularity in the panel method, derive a series expansion for $\underline{G}_1$ near the singularity before attempting integration. The integration of this local expansion effectively becomes a straight forward principal value integral which can be calculated analytically and then usual numerical integration elsewhere enables the integrals to be approximated. This method is shown by De Bernardinis and Moore (1986) to be accurate away from the symmetry line $r = 0$ but for r close to zero there is a great loss of accuracy. However, this loss should not be a problem in the current regime as we only need

to apply the integral formula for $r \geq 1$. The procedure is then as before; we define

$$I_1 = \int_1^\infty [\Delta_1(r) - \frac{1}{2}(v_e^- - v_e^+)(r)]^2 w(r) \mathrm{d}r, \tag{2.104}$$

the equivalent of (2.64), and perform a least squares minimisation as before to determine the layer shape.

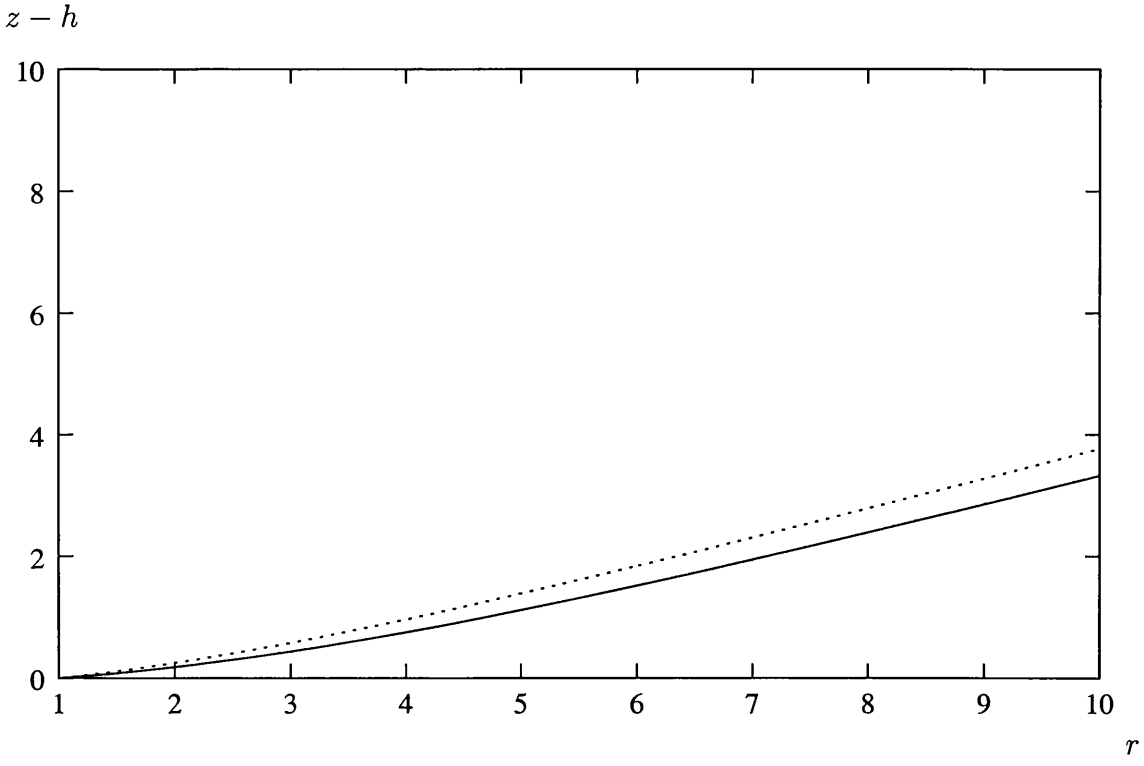

Figure 2.11: Comparison between the layer shapes for the pressure jump case (solid line) and the no pressure jump case (dotted line) for $h = 2$ with $\alpha = 1$.

Results are presented in figures 2.11 - 2.14 for a variety of heights and values of α. Several aspects, when compared to the original results of section 2.3, are apparent. The far field result is seen to be still holding for large r, giving the slope $\pi/6$ of section 2.2.2. The same trends again appear with the deflection of the layer shape

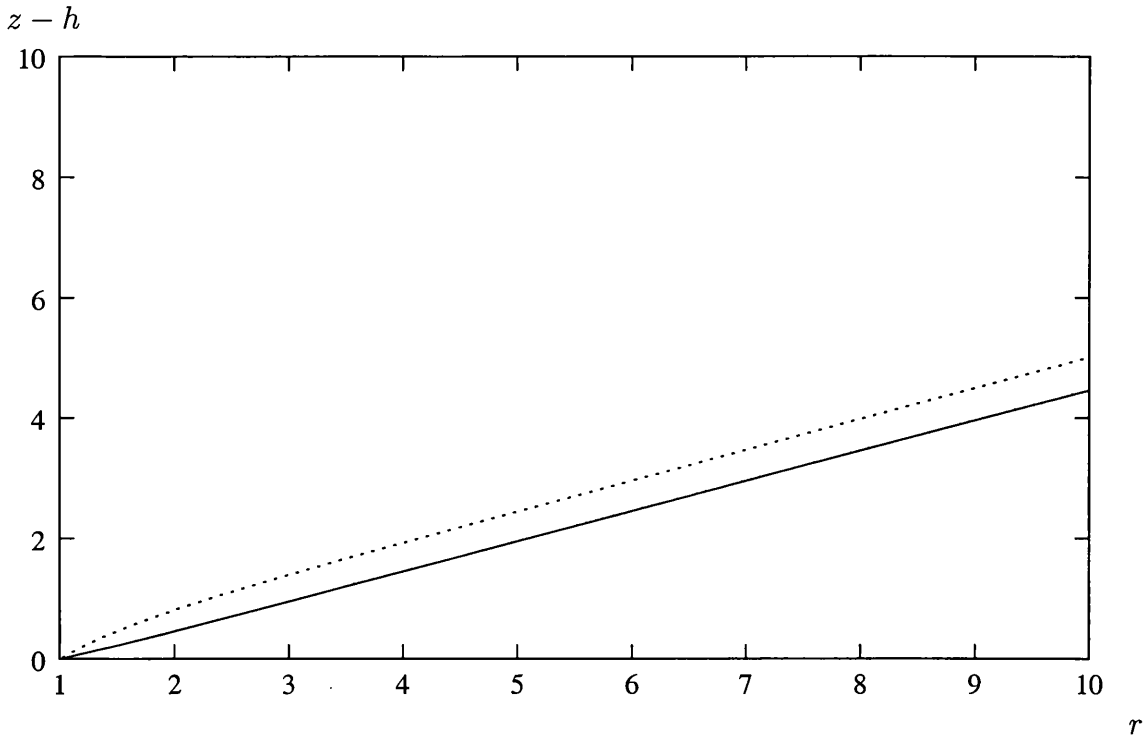

Figure 2.12: Comparison between the layer shapes for the pressure jump case (solid line) and the no pressure jump case (dotted line) for $h = 0.3$ with $\alpha = 1$.

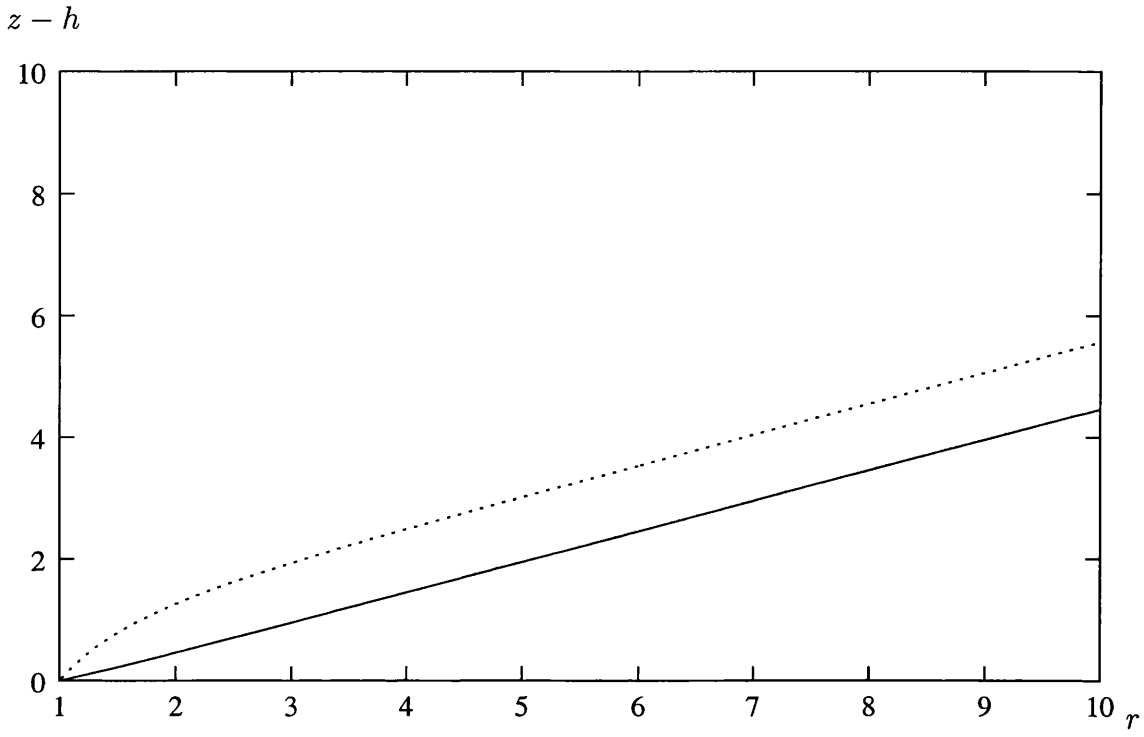

Figure 2.13: Comparison between the layer shapes for the pressure jump case (solid line) and the no pressure jump case (dotted line) for $h = 0.1$ with $\alpha = 1$. Note the similarity in the linear layer shape for the pressure jump case here and for $h = 0.3$ case in figure 2.12.

increasing as h decreases. The new results generally lie beneath the original ones, and the larger the designated value of α the less the overall deflection. For small h values we no longer have the abrupt change in the layer shape at the disc rim and we also no longer see the overshooting of the far field solution. It seems clear that for large A the right-hand side of (2.92) dominates, requiring $Z''(r)$ to be zero to leading order and hence $Z(r)$ to be linear in r. The tying together of the two main slopes, zero at the disc and $\pi/6$ in the far-field, should thus be of future interest, given the near-linear results for the wake shape in the computations.

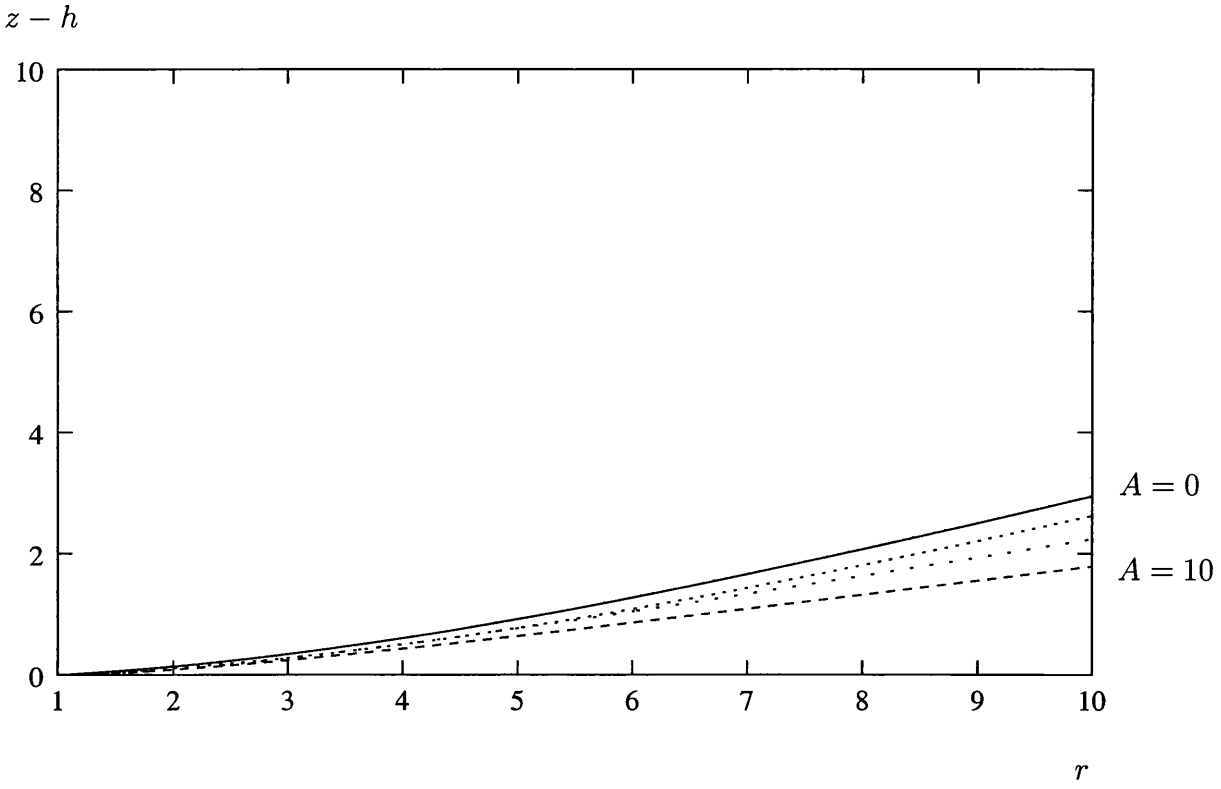

Figure 2.14: Comparison between the layer shapes for $h = 5$ and varying the value of A from $\alpha = 0$, the uppermost solid line, through $\alpha = 0.1$ and $\alpha = 1$ to $\alpha = 10$ the lowest line.

Chapter 3

Planar Flow Past Many Blades in Ground Effect

3.1 Introduction

Continuing our investigation of the ground effect on a hovering rotor blade system, in this chapter we turn to the case of the flow past multiple blades near horizontal ground. Although we limit ourselves to two dimensional flow here it still has some direct relevance to the full three dimensional case in the regimes of large r and that of the many-blade limit, as discussed in Smith and Timoshin (1996b) and the previous chapter.

This chapter effectively combines two previous studies in similar regimes. Firstly, Smith and Timoshin (1996b) considered the planar flow past many blades but with no ground effect. An important new interaction is encountered in their article due to non-symmetry, namely inner-outer interaction, whereby the entire boundary layer

and inviscid flows are coupled and must be solved simultaneously. This is discussed below and is of vital importance in the current regime also. Secondly, Jones (2000) considers the flow past a single aerofoil near the ground. There the author derives a solution for the outer flow given the presence of the ground but has no inner-outer coupling as there is only one blade present. Here we combine these two problems, examining the flow past many blades in ground effect, and we need to include both the inner-outer interaction aspect and the solving of the inviscid problem for many blades with the ground present. We extend the analysis of Jones (2000) for the outer flow past a single blade, to find the equivalent relation in this flow past many blades context, and develop a method to solve it in tandem with the inner boundary layer flow.

We take as our starting point the steady, two dimensional, incompressible, non-dimensionalised, Navier-Stokes equations

$$\frac{\partial U}{\partial x} + \frac{\partial V}{\partial y} = 0, \tag{3.1}$$

$$U\frac{\partial U}{\partial x} + V\frac{\partial U}{\partial y} = -\frac{\partial P}{\partial x} + \frac{1}{Re}\left(\frac{\partial^2 U}{\partial x^2} + \frac{\partial^2 U}{\partial y^2}\right), \tag{3.2}$$

$$U\frac{\partial V}{\partial x} + V\frac{\partial V}{\partial y} = -\frac{\partial P}{\partial y} + \frac{1}{Re}\left(\frac{\partial^2 V}{\partial x^2} + \frac{\partial^2 V}{\partial y^2}\right), \tag{3.3}$$

where Re is the Reynolds number defined to be $Re = U_\infty \hat{L}/\nu$, where ν is the kinematic viscosity of the fluid, U_∞ is the velocity of the free stream and $\hat{L}$ is a typical length scale, taken here as the length of a representative blade.

The configuration of the problem is that of n thin aerofoils, the ith one running from its leading edge $x = a_i$ to its trailing edge $x = b_i$. The blade shapes are given by $y = Re^{-\frac{1}{2}} f^{\pm}(x)$ where $f^+(x)$, $f^-(x)$ give the upper and lower blade shapes respectively and are assumed to be smooth and typically $O(1)$. We also require that

$f^+(x) = f^-(x)$ at leading and trailing edges. These blades are positioned in a slip-streaming arrangement at an $O(1)$ distance h above the ground and in an otherwise uniform stream with non-dimensional velocity $U_\infty = 1$. The ground is taken to be moving at the same speed as the free stream velocity. We take the first leading edge a_1 to be the origin. See also figures 3.1 and 3.2.

In section 3.2 we set out the two parts of the problem, both the boundary layer's multi-blade flow and the outer inviscid flow, driven by displacement effects from the boundary layer. We also discuss in more detail the all-important inner-outer interactions introduced above. Having set up the outer problem in terms of needing to find an analytic function in the complex plane, we turn in section 3.3 to solving the inviscid problem, determining integral equations for the velocity and pressure, and then solve these to enable us to calculate the outer flow. We move in section 3.4 to consider the numerical solution of the boundary layer problem from 3.2 and the outer flow from 3.3. Results are presented in 3.5 for several configurations, varying the number, the ground clearance and angle of attack of the blades. Finally in 3.6 we consider two limits of interest, those of large and small heights h. For large heights, we derive an expression for the leading order ground effect, recovering the no ground effect case of Smith and Timoshin (1996b). In the case of small h we find a relatively simple form for the pressure and velocities with good qualitative agreement with the relevant results from 3.5.

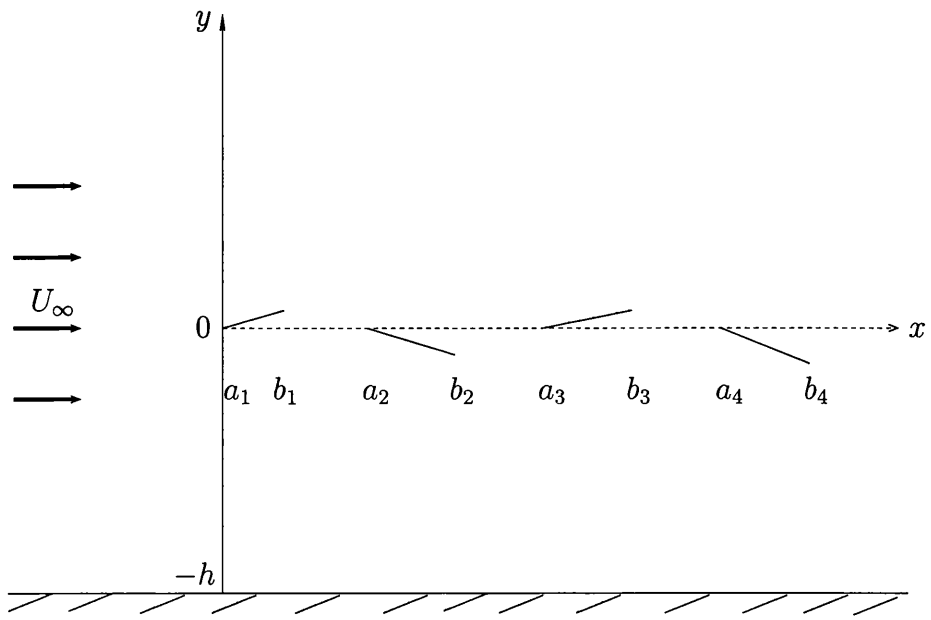

Figure 3.1: The flow configuration of $n(= 4$ here) blades at a distance h above horizontal ground.

3.2 Problem formulation

3.2.1 The boundary layer problem

The aim here is to resolve the viscous boundary-layer and wake motions for the flow past all the blades near the ground. Although the ground is outside the boundary layer, the effect of the ground does enter through coupling the solution of the boundary layer with considerations from the outer inviscid flow by means of unknown y-shifts in the wake shapes at each leading edge, as discussed briefly in the previous section and developed in more detail below.

We introduce the scaled boundary-layer coordinate Y in the normal direction given by $y = Re^{-\frac{1}{2}}[f(x) + Y]$ where $f(x)$ is the shape of the blade/ wake centre line. The

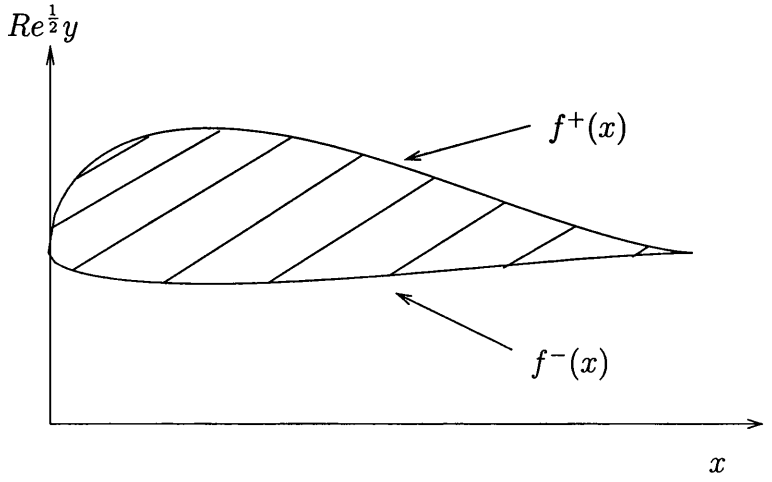

Figure 3.2: A typical aerofoil showing the definitions of $f^+(x)$ and $f^-(x)$.

governing equations (3.1) - (3.3) then become, for the scaled velocity components $\bar{u}[= U], \bar{v}[\equiv Re^{\frac{1}{2}}V - \bar{u}f'(x)]$,

$$\frac{\partial \bar{u}}{\partial x} + \frac{\partial \bar{v}}{\partial Y} = 0, \tag{3.4}$$

$$\bar{u}\frac{\partial \bar{u}}{\partial x} + \bar{v}\frac{\partial \bar{u}}{\partial Y} = 0 + \frac{\partial^2 \bar{u}}{\partial Y^2}, \tag{3.5}$$

subject to the no-slip and free stream conditions

$$\bar{u} = \bar{v} = 0 \quad \text{at} \quad Y = 0 \quad \text{on each blade,} \tag{3.6}$$

$$\bar{u} \to 1 \quad \text{as} \quad Y \to \pm\infty, \tag{3.7}$$

in turn, with the velocities being continuous in the wakes. There is also a starting condition at the first leading edge requiring

$$\bar{u} = 1 \quad \text{at} \quad x = 0, \quad \text{for} \quad Y \neq 0. \tag{3.8}$$

The pressure on the other hand takes the form

$$p = Re^{-\frac{1}{2}}p_B^{\pm}(x) + Re^{-1}P_B(x, Y), \tag{3.9}$$

with the leading order pressure being independent of the scaled normal co-ordinate Y.

The Prandtl shift used above is known on the blades, with $f(x) = f^{\pm}(x)$, but is unknown in the wakes as the wake centre line shape is unknown in advance. With a single aerofoil this does not affect the boundary layer calculation; you have the Blasius flow for an aligned finite flat plate over the aerofoil and a Goldstein-type flat plate wake beyond the trailing edge regardless of the wake shape which can then be obtained independently by examining the outer flow. However in the present multi-blade case the wake shape is crucial. Without knowing the position of the wake centre line as the wake hits the following blade the position of the leading edge in relation to the oncoming flow is unknown and must be determined before we can accurately obtain the flow solution in the boundary layer. The y-shifts in each wake flow, the distance by which the wake centre lines are deflected at the onset of each leading edge, are determined by considering the outer flow introduced in the next section. Likewise the inviscid flow, driven by the presence of the boundary layer, cannot be calculated until the boundary layer, and hence the displacement effects driving the problem, have been resolved. It is this that causes the inner-outer interaction mentioned in 3.1, with each aspect of the problem requiring the solution to the other.

We take this opportunity to define the scaled viscous displacement thicknesses $\delta_{\pm}$ as

$$\delta_{\pm}(x) = \pm \int_0^{\pm\infty} (1 - \bar{u}(x, Y))\mathrm{d}Y, \tag{3.10}$$

which implies the normal velocity takes the form

$$\bar{v} \to \pm\delta'_{\pm}(x) \quad \text{as} \quad Y \to \pm\infty, \tag{3.11}$$

in the outer reaches of the boundary layer.

3.2.2 The outer inviscid problem

Outside the boundary layer discussed in the previous section the free stream $U = 1$ is only slightly disturbed by the presence of the sequence of thin aerofoils and related boundary layers and as such we expand the velocities and pressure as

$$U = 1 + \epsilon u(x, y) + \ldots, \tag{3.12}$$

$$V = 0 + \epsilon v(x, y) + \ldots, \tag{3.13}$$

$$P = P_\infty + \epsilon p(x, y) + \ldots, \tag{3.14}$$

where $\epsilon = Re^{-1/2}$. Substituting these into (3.1) - (3.3) leaves us with the linearized Euler equations,

$$\frac{\partial u}{\partial x} + \frac{\partial v}{\partial y} = 0, \tag{3.15}$$

$$\frac{\partial u}{\partial x} = -\frac{\partial p}{\partial x}, \tag{3.16}$$

$$\frac{\partial v}{\partial x} = -\frac{\partial p}{\partial y}. \tag{3.17}$$

Combining (3.15) and (3.16) to eliminate u from these equations we are left with the Cauchy-Riemann equations for v and p, namely

$$\frac{\partial p}{\partial x} = \frac{\partial v}{\partial y}, \tag{3.18}$$

$$\frac{\partial p}{\partial y} = -\frac{\partial v}{\partial x}. \tag{3.19}$$

In order to solve this problem we consider it in the complex z-plane. We express the problem in terms of the complex function $w(x+iy) = p(x,y) + iv(x,y)$ which is analytic and required to be bounded in the far field and we define

$$w(x+0i) = p_+(x) + iv_+(x), \tag{3.20}$$

$$w(x-0i) = p_-(x) + iv_-(x), \tag{3.21}$$

$$w(x-hi) = p_=(x) + i0, \tag{3.22}$$

as the pressures and velocities just above and below the boundary layer, and the pressure on the ground (with $v_= = 0$ being the ground boundary condition), respectively. We also impose pressure continuity across the wake which requires

$$p_+(x) = p_-(x) \quad \text{in the wakes.} \tag{3.23}$$

This condition is required since the largest pressure jump that each wake can support is typically $O(Re^{-1})$ at most.

The outer flow is driven by displacement effects from the boundary layer. These enter this outer problem via velocity boundary conditions from the boundary layer at $y = 0\pm$. Matching these two regions requires that $v_\pm(x)$ are given by

$$v_\pm = \begin{cases} s'(x) & x < 0 \\ c'(x) \pm \frac{1}{2}t'(x) \pm \delta'_\pm(x) & x \quad \text{on blades} \\ s'(x) \pm \delta'_\pm(x) & x \quad \text{in wakes} \end{cases} \tag{3.24}$$

where $\epsilon c(x) = \epsilon(f^+(x) + f^-(x))/2$ is the camber of the blade, $\epsilon t(x) = \epsilon(f^+(x) - f^-(x))$ is the thickness of the blade, $\epsilon s(x) (= f^+(x) = f^-(x)$ in the wakes) is the wake centre line shape and $\delta_\pm(x)$ are the viscous displacement thicknesses given by (3.10). For given blade shapes, $c(x)$ and $t(x)$ are known while $s(x)$ is unknown

and must be determined as part of the whole inviscid solution. Also, $\delta_{\pm}(x)$ can be determined from the boundary layer through equation (3.10) only once $s(x)$, and hence the y-shifts, are computed.

3.3 Solving the outer problem

3.3.1 The solution

We now turn to solving the inviscid problem of finding the bounded analytic function $w(x+iy)$ subject to (3.20) - (3.23) and the boundary conditions (3.24). This will enable us to couple the inner and outer parts of the solution and hence lead us to a method of solving the problem. Firstly, in order to satisfy the ground condition (3.22), we introduce the image of the system of blades at $y = -2h$. This changes the problem to being the requirement to find the complex function $w(x+iy) = p(x,y) + iv(x,y)$, analytic in the complex plane and bounded in the far field but now satisfying

$$w(x+0i) = p_+(x) + iv_+(x), \tag{3.25}$$

$$w(x-0i) = p_-(x) + iv_-(x), \tag{3.26}$$

$$w(x-2hi+0i) = p_-(x) - iv_-(x), \tag{3.27}$$

$$w(x-2hi-0i) = p_+(x) - iv_+(x), \tag{3.28}$$

$$p_+(x) = p_-(x) \quad \text{in the wakes.} \tag{3.29}$$

We solve this problem, following the method employed by Jones (2000) for a single

blade, by applying Cauchy's Integral Formula for $w(x+iy)$, namely

$$w(z) = \frac{1}{2\pi i}\int_{\Gamma}\frac{w(\zeta)}{\zeta - z}\mathrm{d}\zeta \tag{3.30}$$

using the contour $\Gamma = \Gamma_+ + \Gamma_= + \Gamma_-$ in the complex ζ-plane as in figure 3.3 at a point away from $y = 0$. Carrying this out and considering the $\lim_{R\to\infty}$, where R is the radius of the semi-circles in $\Gamma_\pm$, summing the resulting terms and imposing the boundary conditions (3.25)-(3.28) gives

$$w(z) = \frac{1}{2\pi i}\int_{-\infty}^{\infty}\frac{[p](\xi)+i[v](\xi)}{\xi - z}\mathrm{d}\xi - \frac{1}{2\pi i}\int_{-\infty}^{\infty}\frac{[p](\xi)-i[v](\xi)}{\xi - i2h - z}\mathrm{d}\xi, \tag{3.31}$$

where we now using the notation

$$[v](x) = v_+(x) - v_-(x), \tag{3.32}$$

$$< v > (x) = v_+(x) + v_-(x), \tag{3.33}$$

$$[p](x) = p_+(x) - p_-(x), \tag{3.34}$$

$$< p > (x) = p_+(x) + p_-(x), \tag{3.35}$$

for the differences and sums of the velocities and pressures on each side of the boundary layer. Taking real and imaginary parts of (3.31) we obtain the pressure and normal velocity as

$$\begin{aligned} p(x,y) = \quad & \frac{1}{2\pi}\int_{-\infty}^{\infty}\Big(\frac{(\xi - x)}{(\xi - x)^2 + y^2} + \frac{(\xi - x)}{(\xi - x)^2 + (y+2h)^2}\Big)[v](\xi)\mathrm{d}\xi \\ & + \frac{1}{2\pi}\int_{-\infty}^{\infty}\Big(\frac{y}{(\xi - x)^2 + y^2} - \frac{(y+2h)}{(\xi - x)^2 + (y+2h)^2}\Big)[p](\xi)\mathrm{d}\xi, \end{aligned} \tag{3.36}$$

$$\begin{aligned} v(x,y) = \quad & \frac{1}{2\pi}\int_{-\infty}^{\infty}\Big(\frac{y}{(\xi - x)^2 + y^2} + \frac{(y+2h)}{(\xi - x)^2 + (y+2h)^2}\Big)[v](\xi)\mathrm{d}\xi \\ & - \frac{1}{2\pi}\int_{-\infty}^{\infty}\Big(\frac{(\xi - x)}{(\xi - x)^2 + y^2} - \frac{(\xi - x)}{(\xi - x)^2 + (y+2h)^2}\Big)[p](\xi)\mathrm{d}\xi, \end{aligned} \tag{3.37}$$

and to determine u we can simply apply equation (3.16) giving

$$u(x,y) = -p(x,y). \tag{3.38}$$

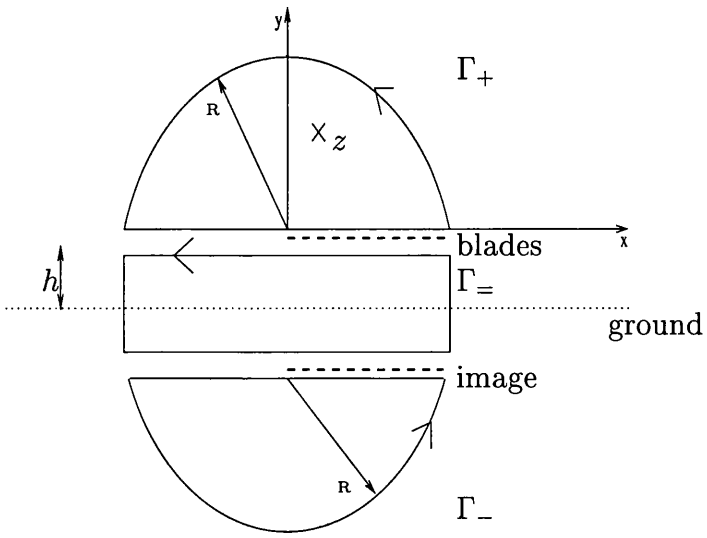

Figure 3.3: Contours Γ_+, $\Gamma_=$ and Γ_- for a point away from $y = 0$.

However, while $[p](x)$ is known to be zero in the wakes (from equation (3.29)), the pressure difference is unknown on the blades. To determine the outer solution we must determine $[p](x)$ for all x. In order to achieve this we again employ Cauchy's Integral Formula but this time at a point on $y = 0$ and use the new contours Γ_+, $\Gamma_=$, Γ_- where Γ_+, $\Gamma_=$ now circumnavigate the point x with a small semi-circle of radius ϵ as in figure 3.4. We consider the double limit $\lim_{R\to\infty} \lim_{\epsilon\to 0}$ and sum the resulting terms to obtain

$$\begin{aligned} w(x+0i) + w(x-0i) = \quad & \frac{1}{\pi i}\int_{-\infty}^{\infty} \frac{w(\xi+0i) - w(\xi-0i)}{\xi - x} \mathrm{d}\xi \\ - \quad & \frac{1}{\pi i}\int_{-\infty}^{\infty} \frac{w(\xi-2hi+0i) - w(\xi-2hi-0i)}{\xi - x - 2hi} \mathrm{d}\xi. \end{aligned} \tag{3.39}$$

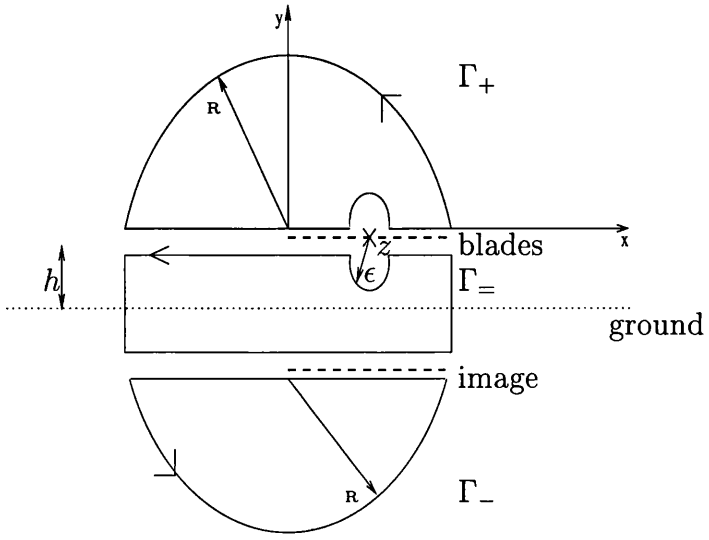

Figure 3.4: Contours Γ_+, $\Gamma_=$ and Γ_- for a point on $y = 0$, circumnavigating the point z.

Applying the boundary conditions (3.25) - (3.28) gives us, in terms of our new notation (3.32) - (3.35),

$$< p > (x) + i < v > (x) = \frac{1}{\pi i}\int_{-\infty}^{\infty} \frac{[p](\xi) + i[v](\xi)}{\xi - x} \mathrm{d}\xi - \frac{1}{\pi i}\int_{-\infty}^{\infty} \frac{([p](\xi) - i[v](\xi))(\xi - x + 2hi)}{(\xi - x)^2 + 4h^2} \mathrm{d}\xi. \tag{3.40}$$

Taking real and imaginary parts of (3.40) yields the integral relations

$$< v > = \frac{1}{\pi}\int_{-\infty}^{\infty} l(\xi - x)[v](\xi)\mathrm{d}\xi - \frac{1}{\pi}\int_{-\infty}^{\infty} (\frac{1}{\xi - x} - m(\xi - x))[p](\xi)\mathrm{d}\xi, \tag{3.41}$$

$$< p > = \frac{1}{\pi}\int_{-\infty}^{\infty} (\frac{1}{\xi - x} + m(\xi - x))[v](\xi)\mathrm{d}\xi - \frac{1}{\pi}\int_{-\infty}^{\infty} l(\xi - x)[p](\xi)\mathrm{d}\xi, \tag{3.42}$$

where we define $l(x)$ and $m(x)$ as

$$l(x) = \frac{2h}{x^2+4h^2}, \tag{3.43}$$

$$m(x) = \frac{x}{x^2+4h^2}. \tag{3.44}$$

These integral equations (3.41) and (3.42) for the velocity and pressure sums must be solved subject to the boundary conditions

$$[v](x) = \begin{cases} 0 & \text{for} \quad x < 0 \\ t'(x) + (\delta'_+ + \delta'_-)(x) & \text{on blades} \\ (\delta'_+ + \delta'_-)(x) & \text{in the wakes} \end{cases} \tag{3.45}$$

$$< v > (x) = \begin{cases} 2c'(x) + (\delta'_+ - \delta'_-)(x) & \text{on blades} \\ ? & \text{in the wakes} \end{cases} \tag{3.46}$$

$$[p](x) = \begin{cases} ? & \text{on blades} \\ 0 & \text{in the wakes} \end{cases} \tag{3.47}$$

$$< p > (x) = \begin{cases} ? & \text{on blades} \\ ? & \text{in the wakes} \end{cases} \tag{3.48}$$

from (3.23) and(3.24), where ? denotes that the quantity is unknown in that interval and is to be determined.

Equations (3.41) and (3.42) are important; it is these that are to be used to determine the unknowns in (3.45) - (3.48). Possibly the most significant quantity is $< v > (x)$ in the wakes as it is this, via (3.24), that will allow us to calculate the y-shifts required in the boundary layer calculation. Determining these y-shifts is considered towards the end of section 3.4 below. However, $< v > (x)$ cannot be determined from (3.41) until we have discovered $[p](x)$ on the blades (as $[v](x)$ is known for all

x through (3.45) and so once we know $[p](x)$ the integrals on the right-hand side of (3.41) can be evaluated). Once we have $[p](x)$ everything else follows from (3.41), (3.42), (3.45) - (3.48) along with the simple relations

$$v_{\pm}(x) = \frac{1}{2}(< v > (x) \pm [v](x)), \tag{3.49}$$

$$p_{\pm}(x) = \frac{1}{2}(< p > (x) \pm [p](x)). \tag{3.50}$$

3.3.2 The solution of the integral equations

The basic task is now to use our knowledge of $< v > (x)$ on the blades to determine the unknown pressure difference $[p](x)$ on the blades. In order to do this we consider the integral equation (3.41) and apply the pressure continuity condition (3.23) that $[p](x) = 0$ in the wakes. After a slight rearrangement, equation (3.41) becomes

$$\frac{1}{\pi}\int_{\text{blades}}\Big(\frac{1}{\xi - x} - m(\xi - x)\Big)[p](\xi)\mathrm{d}\xi = \frac{1}{\pi}\int_{-\infty}^{\infty} l(\xi - x)[v](\xi)\mathrm{d}\xi - < v > (x), \tag{3.51}$$

where

$$\int_{\text{blades}} \equiv \sum_{i=1}^{n}\int_{a_i}^{b_i}. \tag{3.52}$$

This is a singular Fredholm equation of the first kind for $[p](x)$ where the right-hand side can be calculated from the boundary layer calculation and the boundary conditions (3.45), (3.46). This type of integral equation is notoriously difficult to solve and we must reduce it to an integral equation of the second kind in order to resolve it. It has a Cauchy type kernel and we find its solution with the help of Muskhelishvili (1946).

We first re-write (3.51) as

$$\frac{1}{\pi}\int_{\text{blades}}\frac{[p](\xi)}{\xi - x}\mathrm{d}\xi = f(x) + \frac{1}{\pi}\int_{\text{blades}} m(\xi - x)[p](\xi)\mathrm{d}\xi, \tag{3.53}$$

where

$$f(x) = \frac{1}{\pi}\int_{-\infty}^{\infty} l(\xi - x)[v](\xi)\mathrm{d}\xi - < v > (x). \tag{3.54}$$

We then use a result from Muskhelishvili (1946) that gives the solution of

$$\frac{1}{\pi}\int_L \frac{\Phi(\xi)}{\xi - x}\mathrm{d}\xi = g(x), \tag{3.55}$$

where L is a set of n line segments along the x-axis running from a_i to b_i with i being a typical segment, subject to the constraint that $\Phi(b_i) = 0$ for all i, as

$$\Phi(x) = -\frac{S^{-\frac{1}{2}}(x)}{\pi}\int_L \frac{S^{\frac{1}{2}}(\xi)g(\xi)}{\xi - x}\mathrm{d}\xi, \tag{3.56}$$

where

$$S(x) = \left|\frac{(x - a_1)(x - a_2)\ldots(x - a_n)}{(x - b_1)(x - b_2)\ldots(x - b_n)}\right|. \tag{3.57}$$

However (3.55) is exactly our equation (3.53) with

$$g(x) = f(x) + \int_{\text{blades}} m(\xi - x)[p](\xi)\mathrm{d}\xi, \tag{3.58}$$

$\Phi \equiv [p]$; and $[p](b_i) = 0$ is the Kutta condition requiring the solution to be smooth at the trailing edges. Applying this, which is effectively an inverse integral operator, to our problem (3.53) we obtain

$$[p](x) = S^{-\frac{1}{2}}(x)\Big[h(x) + \frac{1}{\pi}\int_{\text{blades}} M(x,\xi)[p](\xi)\mathrm{d}\xi\Big], \tag{3.59}$$

where for convenience we have introduced

$$h(x) = -\frac{1}{\pi}\int_{\text{blades}} \frac{S^{\frac{1}{2}}(\xi)f(\xi)}{\xi - x}\mathrm{d}\xi, \tag{3.60}$$

and

$$M(x,\xi) = -\frac{1}{\pi}\int_{\text{blades}} \frac{S^{\frac{1}{2}}(\xi_1)m(\xi_1 - \xi)}{\xi_1 - x}\mathrm{d}\xi_1. \tag{3.61}$$

So we have now reduced our Fredholm equation of the first kind (3.51) to one of the second kind (3.59) which is far easier to solve. To simplify matters somewhat further, pre-empting problems in calculating (3.59), we introduce

$$\psi(x) = S^{\frac{1}{2}}(x)[p](x) \tag{3.62}$$

to give us

$$\psi(x) = h(x) + \frac{1}{\pi}\int_{\text{blades}} S^{-\frac{1}{2}}(\xi)M(x,\xi)\psi(\xi)\mathrm{d}\xi. \tag{3.63}$$

Equation (3.63) now determines, via (3.62), the required pressure differences on the blades and hence the entire outer solution as discussed earlier. There are a variety of ways to tackle the solution (3.63). For simplicity we solve it iteratively as presented in the next section.

3.4 Numerical methods

3.4.1 The boundary layer calculation

To execute the boundary layer calculations we adopt a semi-explicit finite-difference approach of second order accuracy as in Smith and Timoshin (1996a) and Smith and Timoshin (1996b). The main reason for this is that it is, as in those papers, both robust and accurate, and does not appear to have too much difficulty in dealing with the leading and trailing edge irregularities present in such multi-blade flows. We discretize the momentum equation (3.5) as

$$\bar{u}_{i-1j}\frac{(\bar{u}_{ij} - \bar{u}_{i-1j})}{\Delta_x} + \bar{v}_{i-1j}\frac{\bar{u}_{ij+1} - \bar{u}_{ij-1}}{2\Delta_Y} = \frac{\bar{u}_{ij+1} - 2\bar{u}_{ij} + \bar{u}_{ij-1}}{\Delta_Y^2} \tag{3.64}$$

where $\bar{u}_{ij}$ $(j = -J \quad \text{to} \quad J)$ are the unknown $\bar{u}$ quantities at the x-station, $i\Delta_x$, for Y values $j\Delta_Y$ with step sizes Δ_x, Δ_Y in the x and y directions respectively. Along with the relevant boundary conditions from (3.6) - (3.7), this determines all of the required $\bar{u}_j$ values at the current station. We discretize the continuity equation (3.4) similarly as

$$\frac{\bar{u}_{ij} - \bar{u}_{i-1j}}{\Delta_x} = -\frac{\bar{v}_{ij+1} - \bar{v}_{ij-1}}{2\Delta_Y}, \tag{3.65}$$

allowing us to determine the $\bar{v}_{ij}$ values at any given x-station once the $\bar{u}_{ij}$ have been calculated from (3.64).

These discretisations are second order accurate in Y but as yet only first-order accurate in x. Second order x-accuracy is obtained by employing a double-stepping procedure. We make two approximations to $\bar{u}_{i,j}$ for each j, firstly with a single step length of Δ_x, giving $\bar{u}^s_{ij}$, and then with two steps of length $\Delta_x/2$ giving another approximation $\bar{u}^d_{ij}$. Extrapolation from these two values give an $O(\Delta_x^2)$ approximation to $\bar{u}_{ij}$ as

$$\bar{u}_{ij} = 2\bar{u}^d_{ij} - \bar{u}^s_{ij}, \tag{3.66}$$

and similarly for $\bar{v}_{ij}$. Typically $\Delta_x = 0.005$, $\Delta_Y = 0.05$ and $J = 20$ were sufficient to obtain accuracy to with $O(10^{-6})$ except perhaps far downstream with many blades present.

There is one remaining issue of significance. As mentioned earlier the position of each leading edge with respect to the oncoming velocity profile is unknown in advance. The outer problem serves to give an approximation of the y-shifts at each leading edge and these need to be incorporated here. So at each of the x-stations $a_i - \Delta_x$ a careful interpolation of the approaching flow is necessary in order to have the correct profile to integrate over the ith blade. Rather than just sweeping as before at these

points we know the leading edge to be at the point $Y = f^+(a_i)$ and we re-align the oncoming profiles of $\bar{u}_{i-1j}$ and $\bar{v}_{i-1,j}$ by interpolating them using cubic spline approximations and then shift them up or down by the relevant distance calculated through the Y-shift from the inviscid region. This is how the ground effect, via the inviscid problem, permeates the boundary layer calculation.

3.4.2 Numerically determining ψ

Our task now is to enable ψ to be determined numerically from (3.63), giving $[p](x)$ and hence the entire outer solution through equations (3.36) - (3.37) and (3.41) - (3.42). There are several parts to determining ψ. We need to calculate $h(x)$ and $M(x,\xi)$ in (3.63), taking care of the square root singularities and the Cauchy-type kernels. We then need to solve (3.63) for ψ for a given distribution of displacement thicknesses $\delta_\pm(x)$ from the boundary layer calculation. This enables us to resolve the outer problem and then allows us to calculate new guesses for the y-shift values needed for the boundary layer calculation in 3.4.1.

Throughout the rest of this chapter we will limit our discussion to blades of unit length, i.e. we take $b_i - a_i = 1$, and also to gaps of unit length, i.e. $a_i - b_{i-1} = 1$. We do this in order to be able to illustrate the method of solution, and the solutions themselves, without excessive complication. This should not be too great a limitation as the main features of the flow are still present although it does prevent us from investigating the effect of varying blade lengths and gap sizes. Similar substitutions and methods to those presented below exist for non-uniform blade lengths although the final equations are more complicated.

Firstly we consider the calculation of

$$h(x) = -\frac{1}{\pi}\int_{\text{blades}} \frac{S^{\frac{1}{2}}(\xi)f(\xi)}{\xi - x}\mathrm{d}\xi. \tag{3.67}$$

We introduce $\hat{S}_j(x)$ where

$$\hat{S}_j(x) = \left|\frac{x - b_j}{x - a_j}\right| S(x), \tag{3.68}$$

which gives, on substituting into (3.67),

$$h(x) = -\frac{1}{\pi}\int_{\text{blades}} \left|\frac{\xi - a_j}{\xi - b_j}\right|^{\frac{1}{2}} \frac{\hat{S}_j^{\frac{1}{2}}(\xi)f(\xi)}{\xi - x}\mathrm{d}\xi. \tag{3.69}$$

There are two problems to be addressed: on each blade the integral has a square root singularity (at $\xi = b_i$) and, if x is on the blade, also has a Cauchy-type kernel. To deal with the square root singularity we make the substitution

$$\xi = b_j - \cos^2\theta = \sin^2\theta + a_j, \tag{3.70}$$

for each integral, where j is the relevant blade. (Note for the more general case of irregular length blades and varying gap sizes the substitution is given by

$$\xi = b_j - (b_j - a_j)\cos^2\theta = a_j + (b_j - a_j)\sin^2\theta, \tag{3.71}$$

and similarly for the following substitutions. Again, for clarity we are limiting ourselves to the case given by (3.70).) We also, for convenience, write

$$x = \sin^2\phi + a_i. \tag{3.72}$$

Substituting (3.70), (3.72) into (3.69) and rearranging gives us

$$\begin{aligned} h(\sin^2\phi + a_i) = \quad & -\frac{2}{\pi}\sum_{j=1, j\neq i}^{j=n}\int_0^{\frac{\pi}{2}} \frac{\hat{S}_j^{\frac{1}{2}}(\sin^2\theta + a_j)f(\sin^2\theta + a_j)}{\sin(\theta+\phi)\sin(\theta-\phi) + (a_j - a_i)}\sin^2\theta\mathrm{d}\theta \\ & -\frac{2}{\pi}\int_0^{\frac{\pi}{2}} \frac{\hat{S}_j^{\frac{1}{2}}(\sin^2\theta + a_j)(\theta-\phi)}{\sin(\theta+\phi)\sin(\theta-\phi)}\frac{f(\sin^2\theta + a_j)}{(\theta-\phi)}\sin^2\theta\mathrm{d}\theta \end{aligned} \tag{3.73}$$

where the first of these integrals is no longer singular and the second is now a Cauchy Principal Value integral. The first is straightforward to evaluate numerically. To calculate the second we make use of a NAG library routine D01AQF. This is now possible as the non-Cauchy part of (3.73) is no longer singular since

$$\lim_{\theta\to\phi}\Big(\frac{\sin^2\theta(\theta-\phi)}{\sin(\theta+\phi)\sin(\theta-\phi)}\Big)=\frac{1}{2}\tan\phi. \tag{3.74}$$

Making similar substitutions for the calculation of M gives us

$$\begin{aligned} M(\sin^2\phi+a_i,\xi)= \quad & -\frac{2}{\pi}\sum_{k=1,k\neq i}^{k=n}\int_0^{\frac{\pi}{2}}\frac{\hat{S}^{\frac{1}{2}}(\sin^2\theta_1+a_k)m(\sin^2\theta_1+a_k-\xi)}{\sin(\theta_1+\phi)\sin(\theta_1-\phi)+(a_k-a_i)}\sin^2\theta_1\mathrm{d}\theta_1 \\ & -\frac{2}{\pi}\int_0^{\frac{\pi}{2}}\frac{\hat{S}^{\frac{1}{2}}(\sin^2\theta_1+a_j)(\theta_1-\phi)m(\sin^2\theta_1-\xi)}{\sin(\theta_1+\phi)\sin(\theta_1-\phi)(\theta_1-\phi)}\sin^2\theta_1\mathrm{d}\theta_1, \end{aligned} \tag{3.75}$$

These can be evaluated in a similar manner to the $h(x)$ integrals.

We are now in a position to determine ψ from (3.63). To solve this Fredholm equation of the second kind we adopt a very simple iteration procedure. We make an initial guess ψ_0 and then set up an iteration using equation (3.63), i.e. we use

$$\begin{aligned} &\psi_{k+1}(\sin^2\phi+a_i)=h(\sin^2\phi+a_i)+ \\ &\frac{2}{\pi}\int_{\text{blades}}S^{-\frac{1}{2}}(\sin^2\theta+a_i)M(sin^2\phi+a_i,\sin^2\theta+a_j)\sin\theta\cos\theta\psi_k(\theta)\mathrm{d}\theta. \end{aligned} \tag{3.76}$$

Typically to obtain convergence such that $|\psi_{k+1}-\psi_k|\sim O(10^{-6})$ we required around one-hundred iterations of (3.76).

Finally we need the outer problem to yield values of the y-shifts at each leading edge for the sake of the boundary layer calculation. We find these through (3.24).

In the wake we have that

$$v_{\pm} = s'(x) \pm \delta'_{\pm}(x). \tag{3.77}$$

Considering the velocity sum $< v > (x)$ we obtain

$$< v > (x) = 2s'(x) + (\delta'_{+} - \delta'_{-})(x). \tag{3.78}$$

Rearranging and integrating with respect to x gives us

$$s(x) = s(x_0) + \frac{1}{2}\int_{x_0}^{x} \{< v > (\xi) - (\delta'_{+}(\xi) - \delta'_{-}(\xi))\} \mathrm{d}\xi. \tag{3.79}$$

So in the wake between blades i and $i+1$, this gives the wake shape as

$$s(x) = s(b_i) + \frac{1}{2}\int_{b_i}^{x} \{< v > (\xi) - (\delta'_{+}(\xi) - \delta'_{-}(\xi))\} \mathrm{d}\xi, \tag{3.80}$$

and the y-shift $Y_s(a_{i+1})$ at the leading edge of blade $i+1$ as

$$Y_s(a_{i+1}) = s(b_i) + \frac{1}{2}\int_{b_i}^{a_{i+1}} \{< v > (\xi) - (\delta'_{+}(\xi) - \delta'_{-}(\xi))\} \mathrm{d}\xi, \tag{3.81}$$

where $s(b_i)$ is known from the position of the previous trailing edge, $< v > (x)$ is calculated from (3.41) and $\delta_{\pm}(x)$ from the boundary layer calculations. We can use this relation (3.81) to give an updated guess of the y-shift values for the next boundary layer sweep.

3.4.3 The iteration procedure

We now summarize the iteration procedure used to determine the complete boundary layer and inviscid flows.

1. Make an initial guess at the y-shift at each leading edge; typically $Y_s(a_j) = 0$ $\forall\ j$ is a sufficiently good first estimate.

2. Sweep through the boundary layer solution, interpolating where necessary to satisfy the current y-shift guesses.

3. Compute $\delta_{\pm}(x)$, and hence $[v](x)$, using (3.10) and the boundary layer solution.

4. Calculate $[p](x)$ by iterating (3.63), calculating $f(x)$ from the new $[v](x)$.

5. Using the $[p](x)$ values, calculate $< v > (x)$ through (3.41) and hence recalculate new y-shift approximations from (3.81).

6. Check on convergence; return to 2 and re-sweep, or finish.

Once the procedure has converged we can then calculate all the necessary p, u, v values in the outer problem. Depending on the configuration this iteration typically takes between 4 and 8 complete cycles to give accuracy to the order of 10^{-6} in successive y-shift approximations.

3.5 Results

In figures 3.5 - 3.16 we present results for various flow geometries, varying the number of blades, the blade height h and the angle of attack through $c(x)$. These figures show the viscous displacement thicknesses $\delta_{\pm}(x)$, wake shapes $s(x)$ and the pressures $p_{\pm}$, $p_{=}$. Although there is an infinity of different configurations possible we consider mainly two in detail, presenting results for two and five blades, varying h and considering three sample cases: that of flat blades and two examples of non-symmetry where the blades have positive and then negative angle of attack.

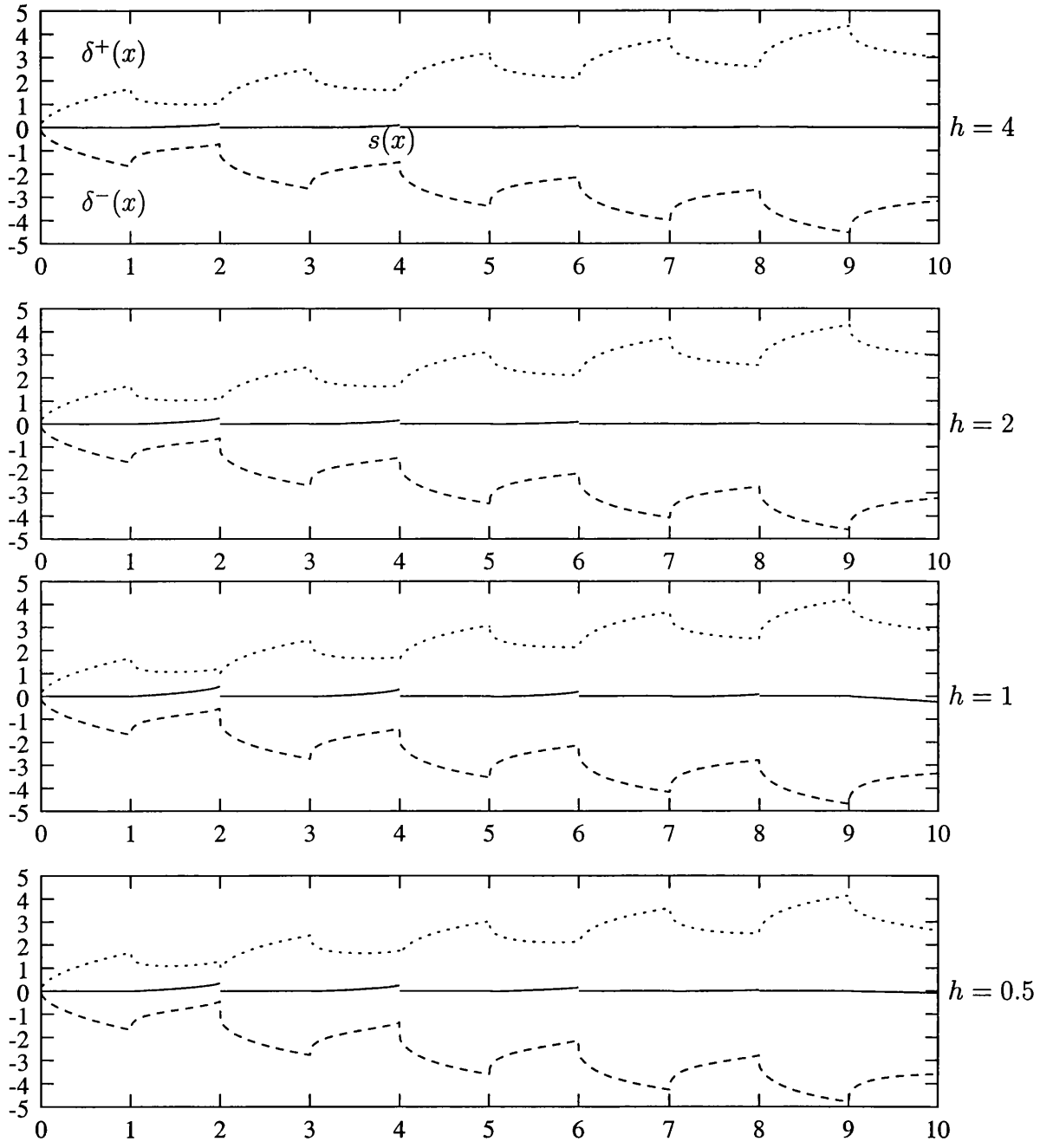

Figure 3.5: Displacement thicknesses $\delta^{\pm}(x)$ and wake shapes $s(x)$ for five flat blades at heights from $h = 4$ to $h = 1/2$.

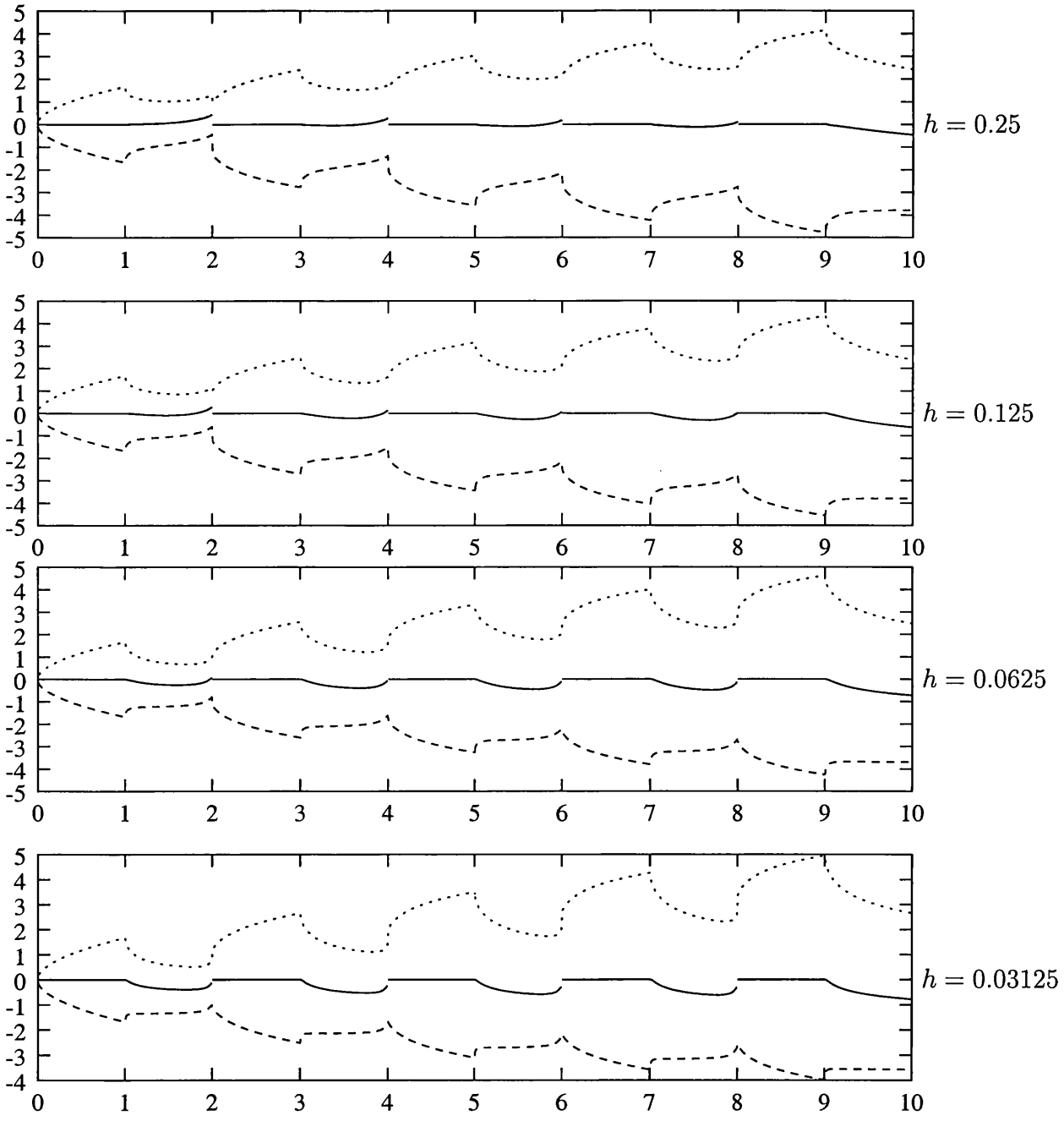

Figure 3.6: As figure 3.5 except that h ranges from 1/4 to 1/64.

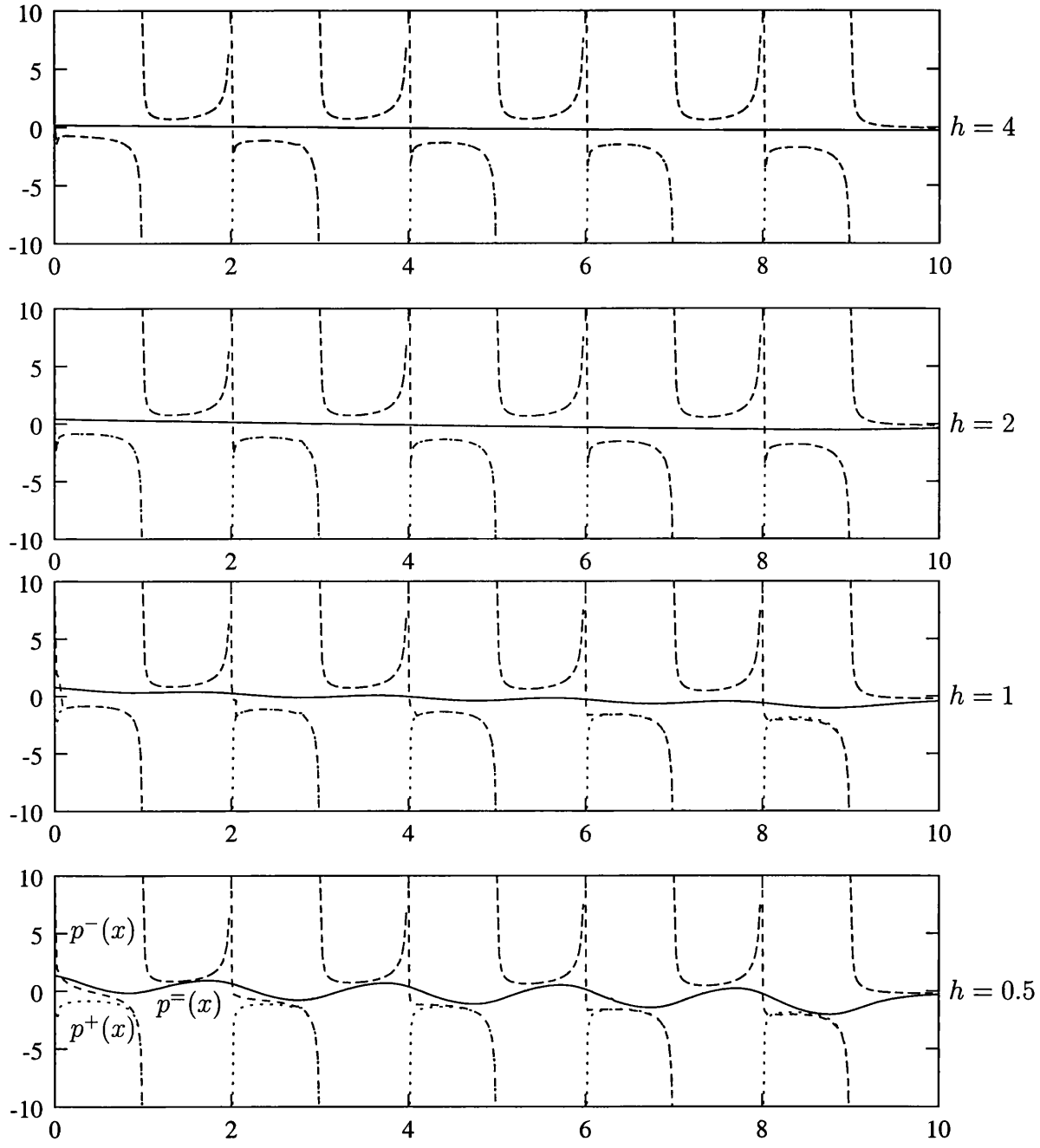

Figure 3.7: Plots of the above, below and ground pressures $p^+(x), p^-(x)$ and $p^=(x)$, for the case of five flat blades, with h values ranging from $h = 4$ to $h = 1/2$.

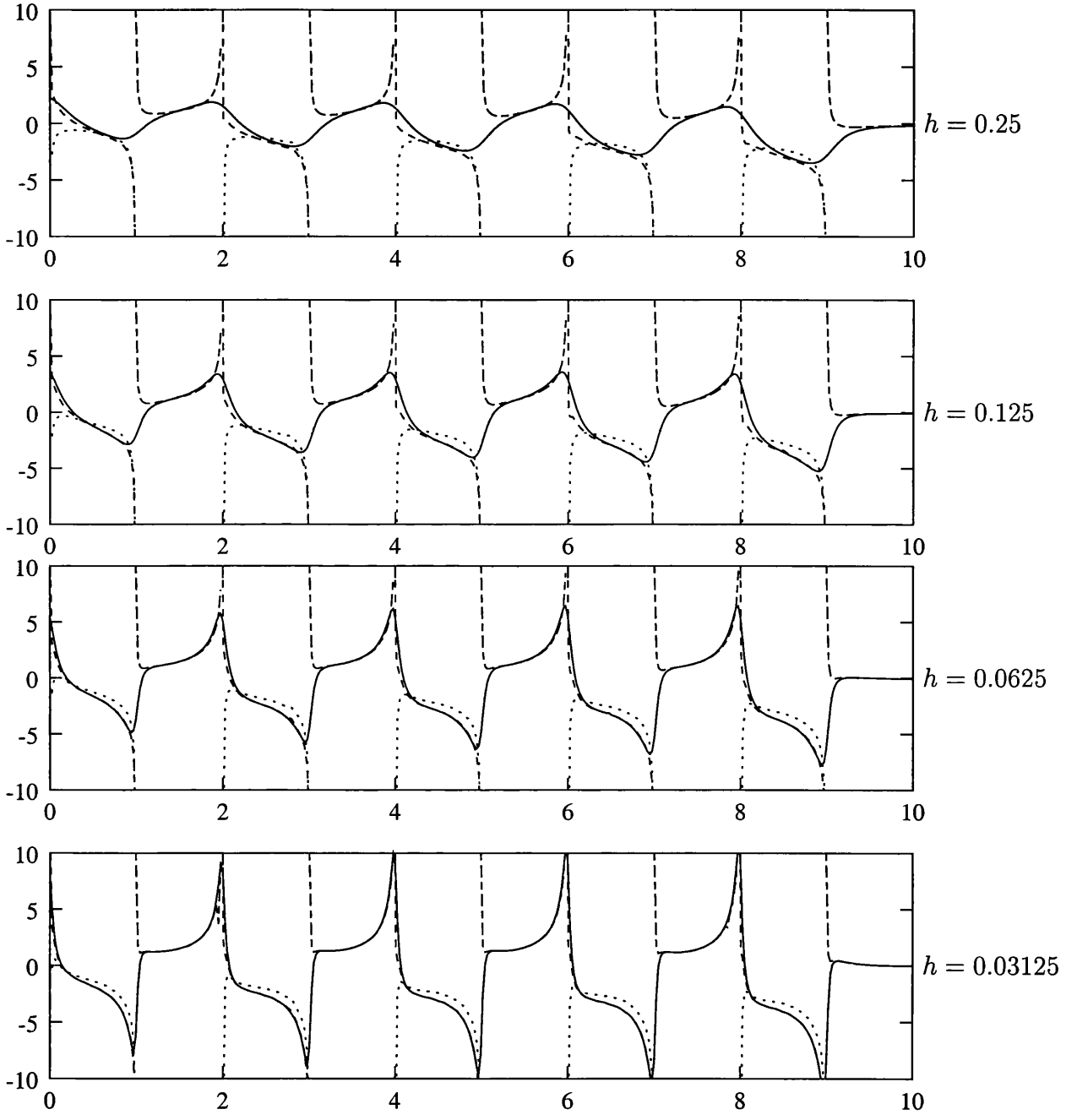

Figure 3.8: As figure 3.7 except that h ranges from 1/4 to 1/32.

Firstly we consider the case of five flat plates, each with zero camber and thickness. Figures 3.5 and 3.6 show the displacement thicknesses and figures 3.7 and 3.8 show the pressures for a variety of heights ranging from $h = 4$ to $h = 1/32$. There are several points to note. There is very little variation in the pressures with varying h for values of $h > \frac{1}{2}$. As h is decreased p_- increases rapidly while p_+ is relatively unchanged. Closer inspection of the small h cases suggests p_- increasing like $\frac{1}{h}$, a case which is explored further in the next section. Another striking feature of the small h cases is the very flat shapes in the lower displacement thicknesses in the wake. Physically this is due to the pressure requirement causing relatively little fluid to be entrained from beneath the wake compared to above and forcing the downward deflection of $s(x)$. The flow appears to have a relatively simple form here and we examine it in more detail in section 3.6 below. There also appears to be distinct leading and trailing edge regions, similar to those considered by Jones (2000), where $s(x)$ and the pressure adjust rapidly. We also present, in figures 3.9 and 3.10, a few examples of the displacement thicknesses for five blades at positive and negative angle of attack. Features similar to those discussed above can be seen.

In figure 3.11 we present similar results for two flat blades, seeing similar features to the five blade case. We also present, in figures 3.13 and 3.14 the case of two blades at an angle of attack with $c(x)$ no longer zero, considering in turn both positive and negative angles. Similar features are again observed here, with the flattening wake shape and increasing $[p]$ with reduced h still clearly visible. Other configurations of possible interest include having each blade with a different camber and also experimenting with varying the thickness of the blades also but these are not featured here.

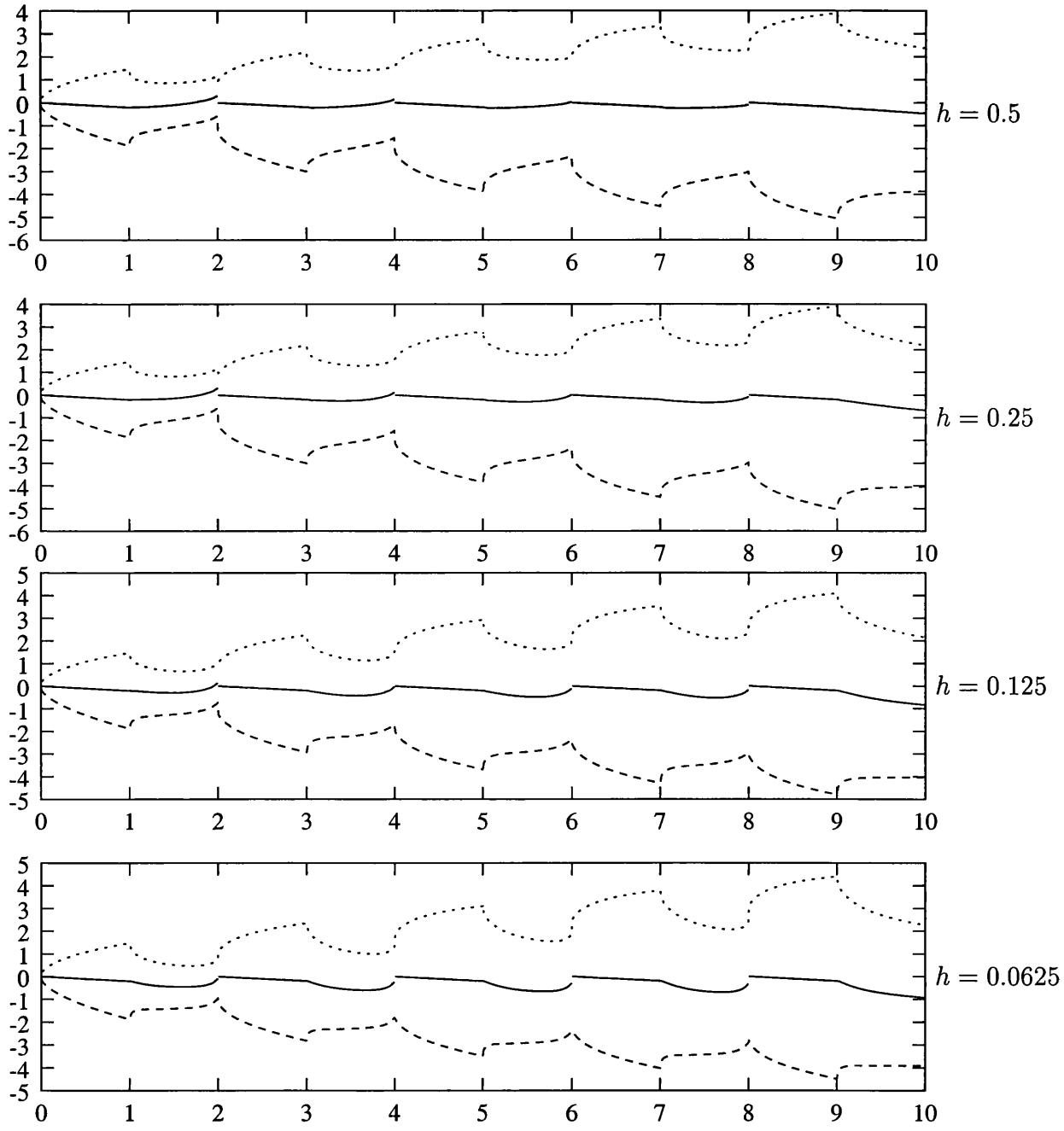

Figure 3.9: Displacement thicknesses and wake center line shapes for five blades at positive angle of attack for various heights.

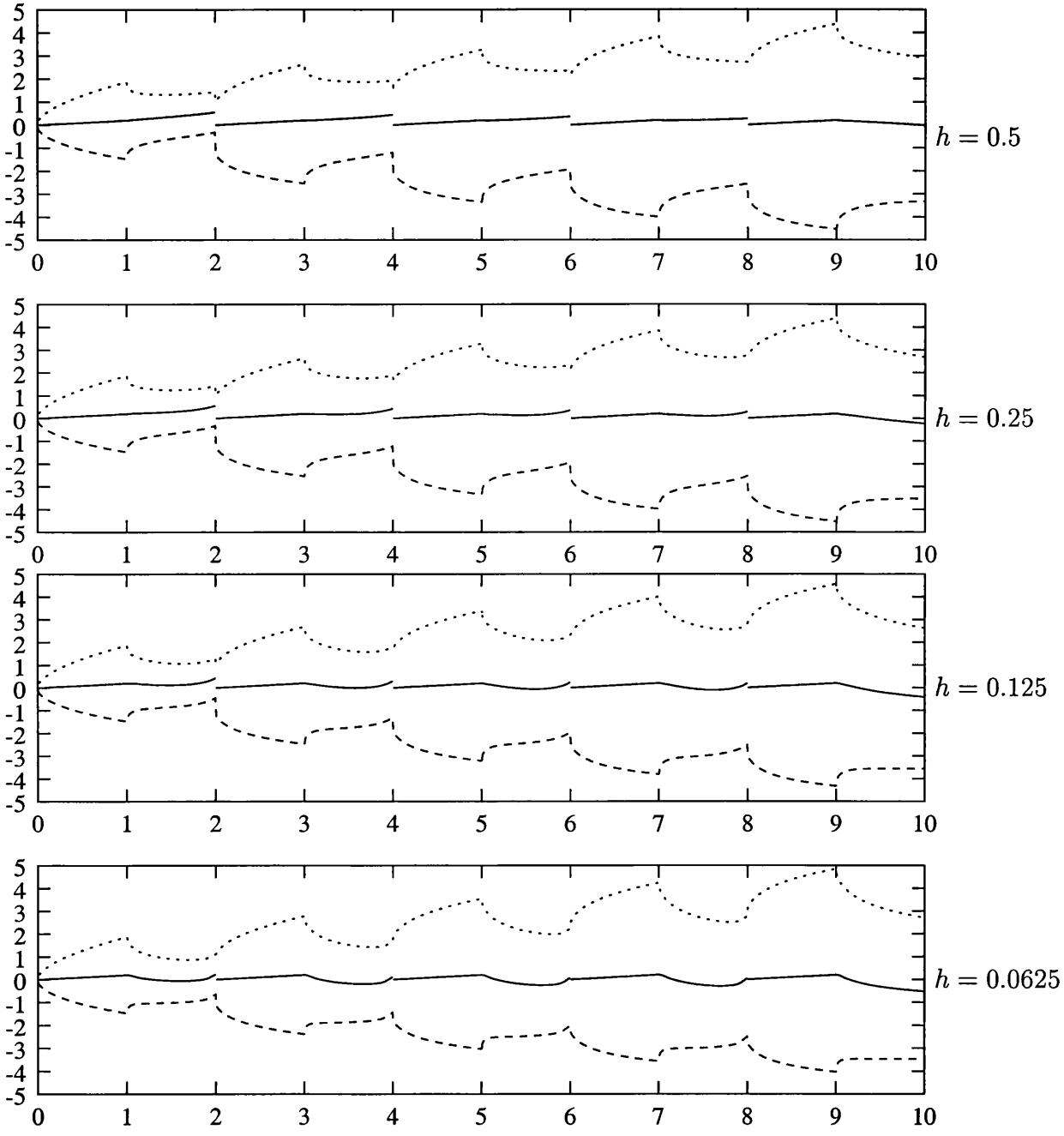

Figure 3.10: Displacement thicknesses and wake center line shapes for five blades at negative angle of attack for various heights.

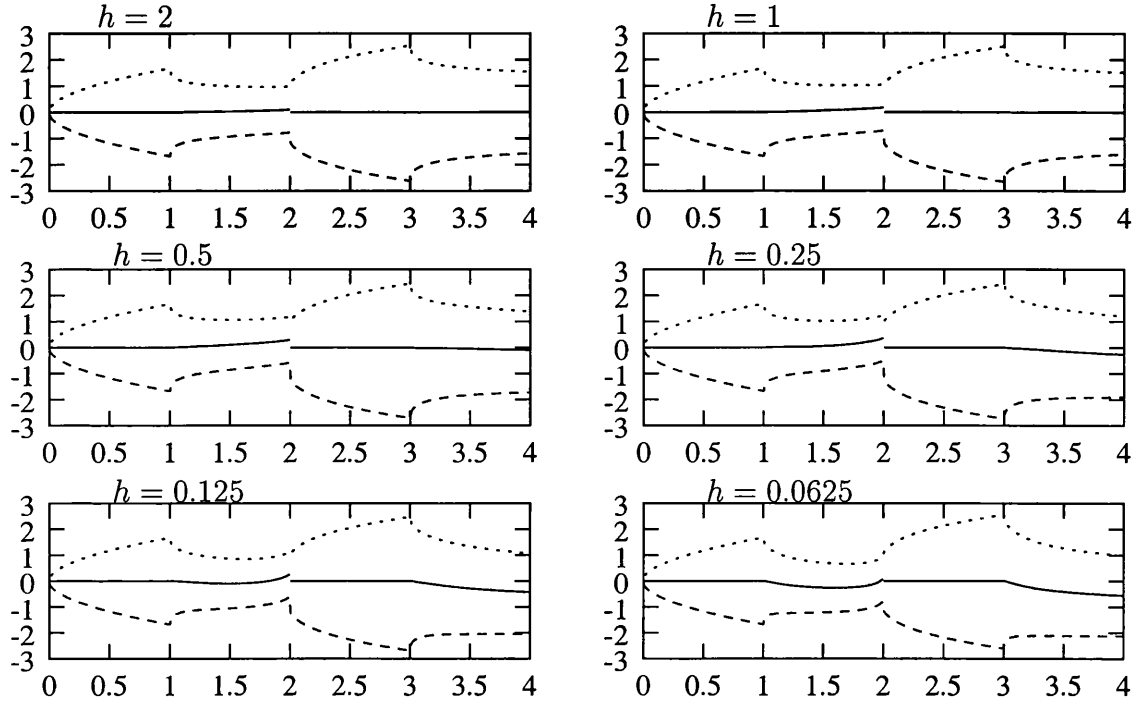

Figure 3.11: Displacement thicknesses $\delta^{\pm}(x)$ and wake shapes $s(x)$ for two flat blades.

In figure 3.15 we present the lift profiles, the integral of the pressure differences $[p](x)$ along each blade, for the five, flat blade case at each of the values of h considered. Away from the ground this configuration will not normally generate any lift; so any lift here is solely as a direct result of the influence of the ground. There are a few things to note. Firstly for the larger h values (greater than one half) there is effectively no lift generated. As h is reduced and there is a non-zero lift produced sheltering effects are clearly visible with more lift created on the first blade compared with the following ones. Finally, the lift can be seen to increase as $1/h$ as h is reduced even further.

Finally, we also present a single case of nine blades, at a height $h = 1/32$, in figure

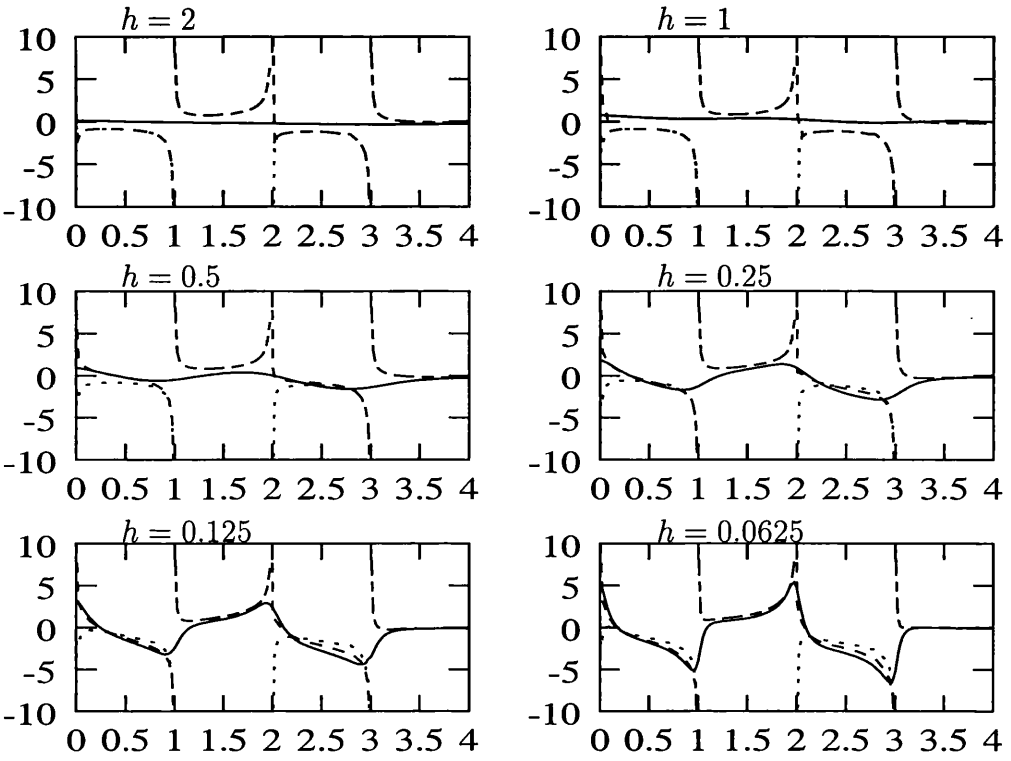

Figure 3.12: Pressures $p^{=}$ (solid line), p^{+} (dotted line) and p^{-} (dashed line) for two flat blades.

3.16. Note the very periodic nature of the wake shape beyond the third or fourth blade and the similar $\delta_{\pm}(x)$ shapes, ignoring the gradual growth for now. This suggests there are two important length scales present here: one shorter scale from leading edge to successive leading edge with a fast varying and periodic nature, and a longer slowly varying scale containing the steady growth in size of the boundary layer. This is considered in more detail in Chapter 4 where we consider periodic cases.

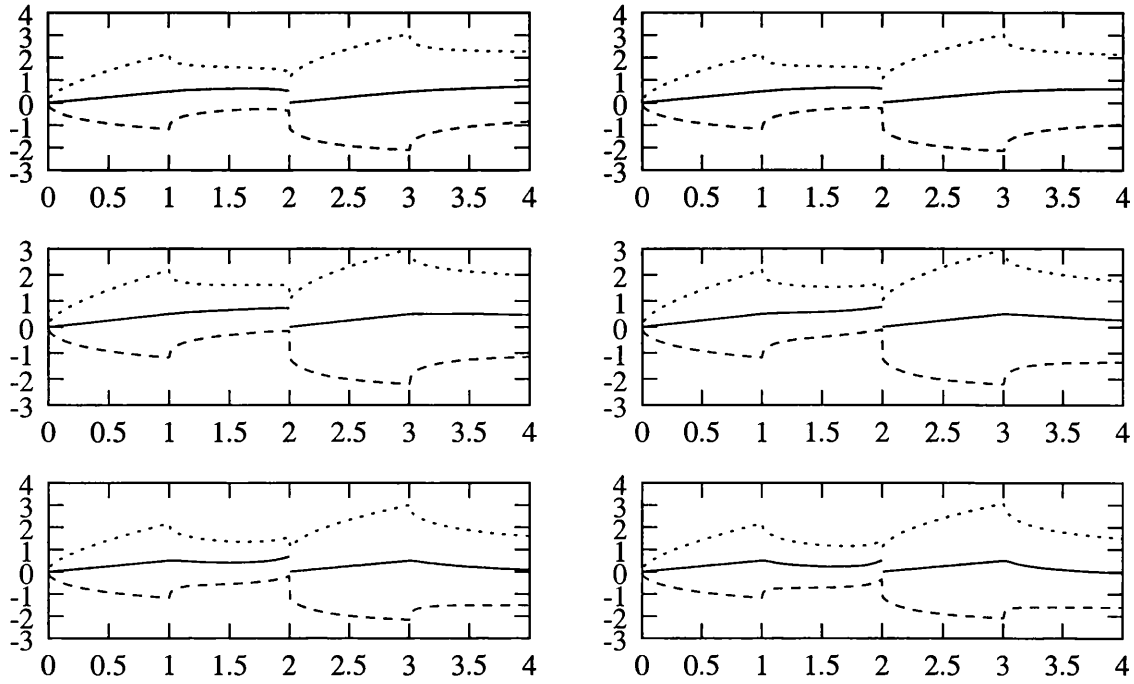

Figure 3.13: Displacement thicknesses $\delta^{\pm}(x)$ and wake shapes $s(x)$ for two blades at positive angle of attack for heights $h = 2$ to $h = 0.0625$ as in figure 3.11.

3.6 Inviscid limits

3.6.1 Large blade heights —— $h \gg 1$

We consider here large ground clearances, where the distance between the blades and the ground is large. We take as our starting point the integral equations (3.41) and (3.42) which we repeat here for clarity:

$$< v > (x) = \frac{1}{\pi}\int_{-\infty}^{\infty} l(\xi - x)[v](\xi)\mathrm{d}\xi - \frac{1}{\pi}\int_{-\infty}^{\infty}(\frac{1}{\xi - x} - m(\xi - x))[p](\xi)\mathrm{d}\xi, \tag{3.82}$$

$$< p > (x) = \frac{1}{\pi}\int_{-\infty}^{\infty}(\frac{1}{\xi - x} + m(\xi - x))[v](\xi)\mathrm{d}\xi - \frac{1}{\pi}\int_{-\infty}^{\infty} l(\xi - x)[p](\xi)\mathrm{d}\xi.$$

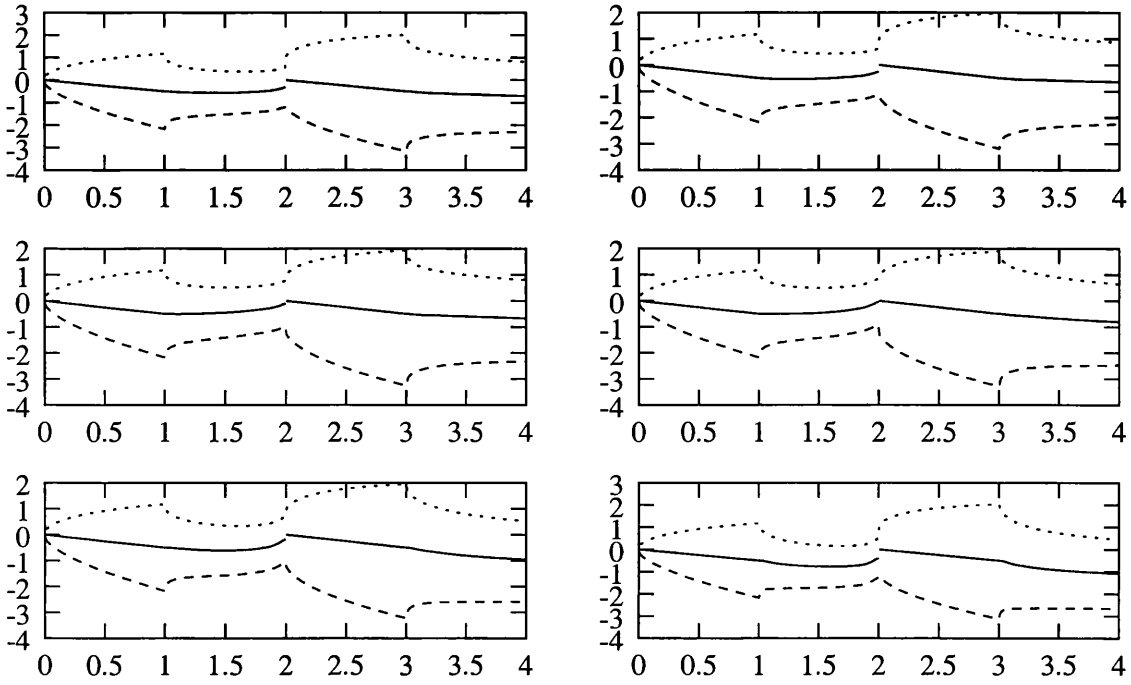

Figure 3.14: Displacement thicknesses $\delta^{\pm}(x)$ and wake shapes $s(x)$ for two blades at negative angle of attack for heights $h = 2$ to $h = 0.0625$ as in figure 3.11.

(3.83)

We expand the velocity and pressure sums and differences as

$$< v > (x) = < v >_0 (x) + \frac{1}{2h} < v >_1 (x) + \ldots, \tag{3.84}$$

$$[v](x) = [v]_0(x) + \frac{1}{2h}[v]_1(x) + \ldots, \tag{3.85}$$

$$< p > (x) = < p >_0 (x) + \frac{1}{2h} < p >_1 (x) + \ldots, \tag{3.86}$$

$$[p](x) = [p]_0(x) + \frac{1}{2h}[p]_1(x) + \ldots, \tag{3.87}$$

respectively and write

$$l(x) = \frac{2h}{x^2 + 4h^2} = \frac{1}{2h}(1 + \frac{x^2}{(2h)^2})^{-1} = \frac{1}{2h} - \frac{x^2}{(2h)^3} + \ldots, \tag{3.88}$$

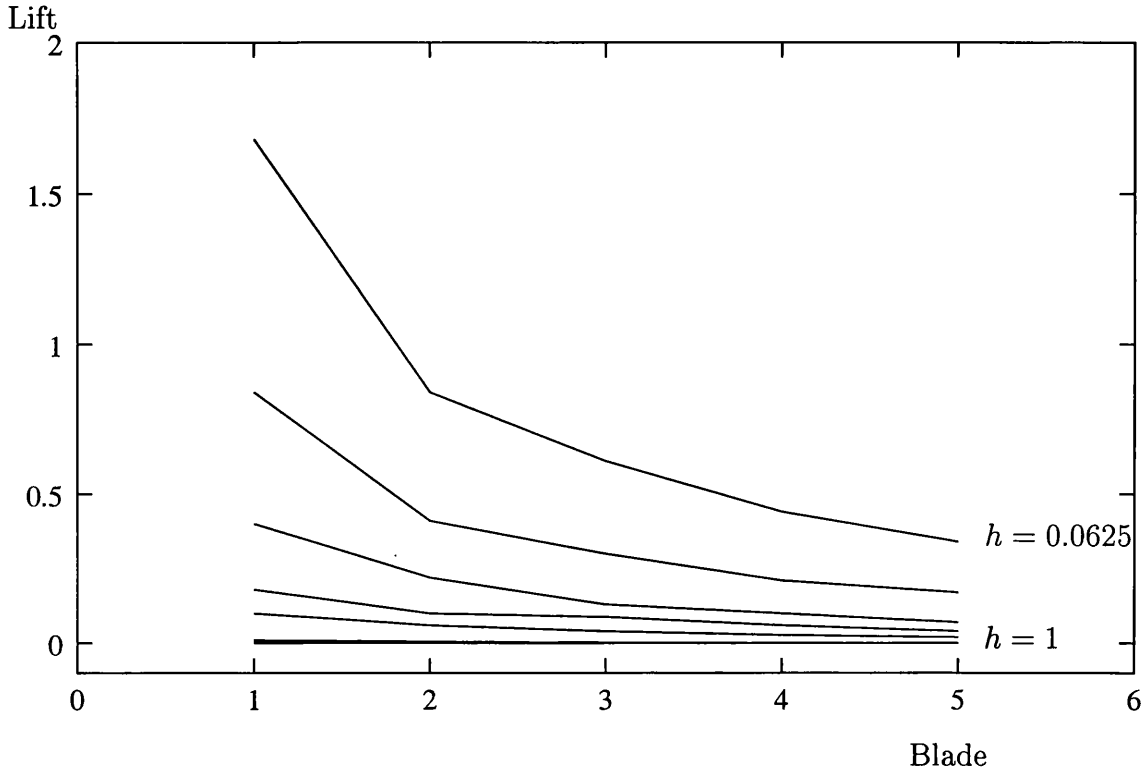

Figure 3.15: Non-dimensional lift on each of the five flat blades for the various heights presented earlier

$$m(x) = \frac{x}{x^2+4h^2} = \frac{x}{(2h)^2}(1+\frac{x^2}{(2h)^2})^{-1} = \frac{x}{(2h)^2} - \frac{x^3}{(2h)^4} + \ldots, \quad (3.89)$$

where these expansions hold for large h when $x \ll h$. Care must be taken for cases where $x \sim h \gg 1$ so as to ensure all the necessary terms are retained at each order. Substituting these expansions into (3.82), (3.83) yields, to leading order,

$$< v >_0 (x) = -\frac{1}{\pi}\int_{-\infty}^{\infty} \frac{[p]_0(\xi)}{\xi - x} d\xi, \quad (3.90)$$

$$< p >_0 (x) = \frac{1}{\pi}\int_{-\infty}^{\infty} \frac{[v]_0(\xi)}{\xi - x} d\xi. \quad (3.91)$$

We can invert (3.90) in a similar manner to the Fredholm equation of the first kind

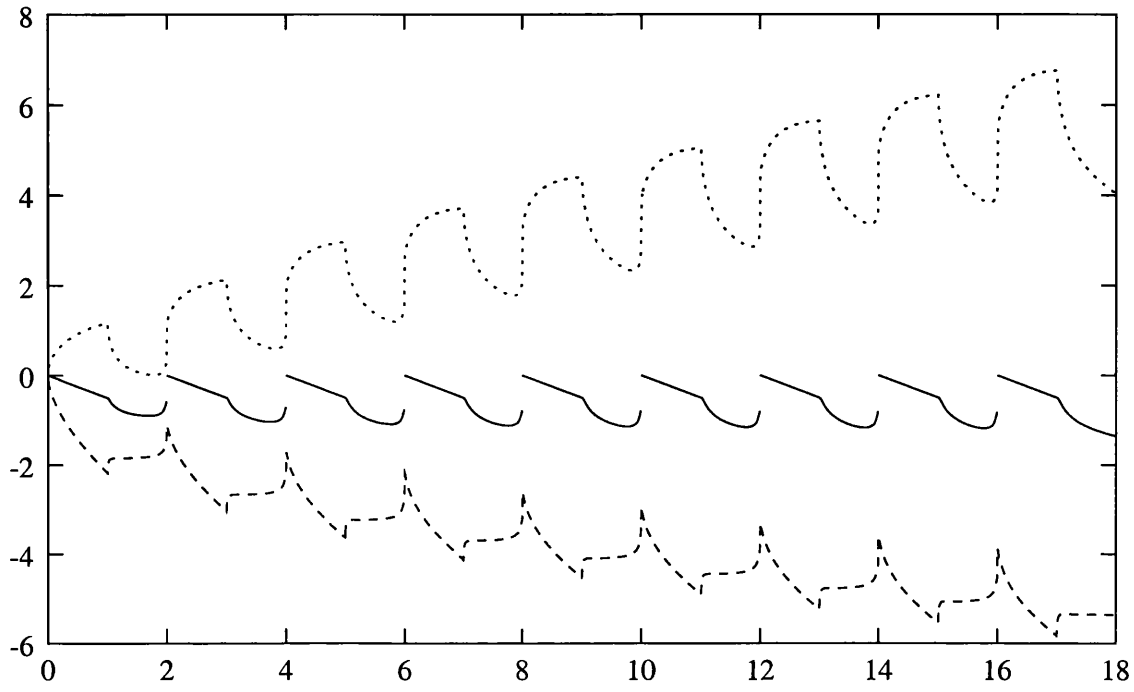

Figure 3.16: The wake centre line shapes and viscous displacements for nine blades at angle of attack. Note the near periodicity in $s(x)$.

in (3.53) to give

$$[p]_0(x) = \frac{S^{-\frac{1}{2}}(x)}{\pi} \int_{\text{blades}} \frac{S^{\frac{1}{2}}(\xi)}{\xi - x} < v >_0 (\xi) \mathrm{d}\xi. \tag{3.92}$$

This is, reassuringly, identically the equation in Smith and Timoshin (1996b) for the flow past multiple blades with no ground present. The entire leading order solution can now be calculated as before, with $[v]_0$ known everywhere and $< v >_0$ known on the blades from the boundary conditions, (3.92) giving the unknown pressure difference on the blades (with $[p]_0$ known to be zero in the wakes), (3.90) giving the unknown velocity sum and wake shape, and (3.91) giving the unknown pressure sums.

To next order, using the expansions from (3.88) and (3.89), we obtain the equations

$$< v >_1 (x) = \frac{1}{\pi}\int_{-\infty}^{\infty}[v]_0(\xi)\mathrm{d}\xi - \frac{1}{\pi}\int_{-\infty}^{\infty}\frac{[p]_1(\xi)}{\xi - x}\mathrm{d}\xi, \tag{3.93}$$

$$< p >_1 (x) = \frac{1}{\pi}\int_{-\infty}^{\infty}\frac{[v]_1(\xi)}{\xi - x}\mathrm{d}\xi - \frac{1}{\pi}\int_{-\infty}^{\infty}[p]_0(\xi)\mathrm{d}\xi. \tag{3.94}$$

This is not the complete story however as it ignores the region alluded to earlier of $\xi \sim h$. If we consider part of the second integral in (3.82) in this case we have that

$$\frac{1}{\pi}\int_{-\infty}^{\infty}\frac{\xi - x}{(\xi - x)^2 + (2h)^2}[p]_0(\xi)\mathrm{d}\xi = \frac{1}{\pi}\int_{-\infty}^{\infty}\frac{\hat{\xi}}{\hat{\xi}^2 + 1}[p]_0(2h\hat{\xi} + x)\mathrm{d}\hat{\xi} \tag{3.95}$$

where $\xi - x = (2h)\hat{\xi}$. We also know that

$$[p]_0(2h\hat{\xi} + x) \approx \frac{1}{\pi}\int_{-\infty}^{\infty}\frac{< v >_0 (\xi)}{(2h)\hat{\xi}}\mathrm{d}\xi \tag{3.96}$$

to leading order. Combining (3.95) and (3.96) yields an $O(1/2h)$ term rather than just the $O(1/(2h)^2)$ one that is present in the $x = O(1)$, $\xi = O(h)$ case and so this must be included in (3.93). Including this term in (3.93) (and the equivalent term in (3.94)) we obtain the complete expressions as

$$< v >_1 (x) = \frac{1}{\pi}\int_{-\infty}^{\infty}([v]_0 - < v >_0)(\xi)\mathrm{d}\xi - \frac{1}{\pi}\int_{-\infty}^{\infty}\frac{[p]_1(\xi)}{\xi - x}\mathrm{d}\xi, \tag{3.97}$$

$$< p >_1 (x) = -\frac{1}{\pi}\int_{-\infty}^{\infty}([p]_0 - < p >_0)(\xi)\mathrm{d}\xi + \frac{1}{\pi}\int_{-\infty}^{\infty}\frac{[v]_1(\xi)}{\xi - x}\mathrm{d}\xi, \tag{3.98}$$

Equations (3.97), (3.98) can be inverted as before to yield an expression for $[p]_1(x)$ on the blades and hence give the complete solution. This is the first sign of the effect of the ground; the $O(1/2h)$ correction is the leading order ground effect for large h. Notice that as $([v]_0 - < v >_0)(x) = 2v_-(x)$ (and likewise for the p terms), the first integrals in (3.97) and (3.98), which drive the solution at this order, are dependent only upon the leading order behaviour beneath the blade system. The solution of the complete problem is still a numerical one however with the boundary layer solution giving $[v]_0$.

3.6.2 Small ground clearances —— $h \ll 1$

We now turn to the other extreme of small ground clearances, although still sufficiently large that the ground is entirely outside the boundary layer. To do this we return to the original Cauchy-Riemann equations for v and p,

$$\frac{\partial p}{\partial x} = \frac{\partial v}{\partial y}, \tag{3.99}$$

$$\frac{\partial p}{\partial y} = -\frac{\partial v}{\partial x}. \tag{3.100}$$

Turning to small h we write $y + h = h\hat{y}$ and expand the velocities and pressures below the system of blades as

$$v_-(x,y) = v_0^- + \ldots, \tag{3.101}$$

$$p_-(x,y) = \frac{1}{h}p_{-1}^- + p_0^- \ldots. \tag{3.102}$$

Above the blades the leading order terms are $O(1)$ in both the pressure and normal velocity but we do not consider these here. Substituting into (3.99), (3.100) yields the leading order governing equations as

$$\frac{\partial p_{-1}^-}{\partial x} = -\frac{\partial v_0^-}{\partial \hat{y}}, \tag{3.103}$$

$$\frac{\partial p_{-1}^-}{\partial \hat{y}} = 0. \tag{3.104}$$

These must be solved subject to the boundary conditions at the underside of the blade, $\hat{y} = 1$, namely

$$v_0^-(x,0) = 0, \tag{3.105}$$

$$v_0^-(x,1) = c'(x) - \frac{1}{2}t'(x) - \delta_-'(x) \quad \text{on the blades,} \tag{3.106}$$

$$v_0^-(x,1) = s'(x) - \delta_-'(x) \quad \text{in the wakes,} \tag{3.107}$$

$$p_{-1}^- = 0 \quad \text{in the wakes,} \tag{3.108}$$

where the velocity conditions are from the inviscid tangential velocity condition on the ground and (3.24) and we require (3.108) as the leading order pressure above the blades is $O(1)$ and so for continuity across the wakes the pressure beneath must be zero at this order.

Differentiating (3.103) with respect to y, and substituting from (3.104) leaves $v^-_{0\hat{y}\hat{y}} = 0$ which we integrate to give

$$v^-_0 = A(x)\hat{y} + B(x). \tag{3.109}$$

The ground condition $v^-_0 = 0$ at $\hat{y} = 0$ implies $B(x) = 0$ and applying (3.106) gives

$$v^-_0 = (c'(x) - \frac{1}{2}t'(x) - \delta'_-(x))\hat{y}. \tag{3.110}$$

This, via equation (3.103), gives the leading order pressure underneath blade i as

$$p^-_{-1}(x) = p^-_{-1}(a_i) - \int_{a_i}^{x} \frac{\partial v^-_0(\xi)}{\partial \hat{y}} \mathrm{d}\xi, \tag{3.111}$$

$$= p^-_{-1}(a_i) - \left[c(x) + \frac{1}{2}t(\xi) + \delta_-(\xi)\right]_{a_i}^{x}, \tag{3.112}$$

where the constant of integration $p^-_{-1}(0)$ is unknown.

This analysis shows that, to leading order, the pressure is independent of y beneath the blades, i.e. $p_- = p_=$, which can be clearly seen emerging in the results for small h presented in section 3.5. Also for the flat plate case presented in figure 3.6, $c(x)$ and $t(x)$ are zero and so (3.112) gives the pressure responding as $\delta_-(x)$. Again this can be seen in the pressure plots for the relevant cases in 3.5. Perhaps more importantly it shows the pressure beneath the system increasing as $1/h$ while that above the system remains $O(1)$, giving an increasingly large pressure difference across the blade and so greatly enhancing any lift or downforce produced. A further feature of interest in

the numerical results is the flat shape of the lower displacement function $\delta_-(x)$ in the wakes. This can also be explained here, as in the wakes $p_{-1}^- = 0$ implies $v_0^- = 0$ with no fluid being entrained to leading order. The boundary condition (3.107) then implies

$$s(x) = \delta_-(x) + D, \tag{3.113}$$

where D is a constant of integration and so the graphs, showing $s(x) - \delta_-(x)$, would indeed be expected to be flat to leading order. We do not consider the leading and trailing edge regions discussed above in the present investigation although it is thought that the analysis of a single blade in Jones (2000) could be extended to the current many blade situation, fixing the unknown constants $p_{-1}^-(0)$ and D.

Chapter 4

Many Blades in Ground Effect - a Periodic Approach

4.1 Introduction

The results of the previous chapter show that, for the case of the flow past many blades near the ground, a seeming near-periodicity appears in the wake centre line shapes $s(x)$ of successive blades, downstream of the first three or four blades. In this chapter we explore the possibility of there being a periodic solution when many blades are present and consider the relevant flow structure. The method of the previous chapter works for this many blade case but computation time becomes very prohibitive as the number of blades increases and so from that perspective this limiting case is also useful to explore.

Below we present an analysis of the flow structure based on three distinct regions. The typical single boundary layer of Chapter 3 effectively splits into two: an outer

region varying relatively slowly in x and shown to be mean Blasius flow, and an inner viscous subregion. This inner region shelters the rest of the flow from the leading and trailing edges to some extent and varies over a far shorter length scale. We assume, guided by numerical results from the previous chapter and the analysis of the flow structure, that this inner tier is periodic. Finally the third region is the outer, inviscid one which is much the same as before, subject to a slight change in the displacement conditions driving the flow at the match between the outer and viscous regions. Implications of the periodicity assumption simplify the integral equations derived in the previous chapter somewhat but the basic premise remains largely the same; the outer, inviscid region determining an otherwise unknown y-shift in the innermost of the viscous layers which then in turn generates the displacement effects forcing the inviscid flow. In other words, the inner-outer interaction that is of prime importance in the previous work is still vital here.

The current structure appears once a large number of blades, $n \gg 1$, have been passed, up until $n \sim O(Re^{3/5})$, with Re also still large. Beyond this number of blades a new regime occurs with a new interaction in the boundary layer itself, causing a displacement driven pressure gradient to appear within the innermost region I, as discussed in Bowles and Smith (2000a), Bowles and Smith (2000b) and also in chapter 5. The issue of periodicity is an important one, particularly with regard to rotor blade flows as discussed in Chapter 1. Further, the periodic structure presented here is also valid in the case of a rotor blade with many blades, at large radial distances where rotational effects are not significant at leading order. The major difference is that region II contains mean Von Karman, rather than mean Blasius, flow.

Section 4.2 sets out the proposed structure, based on the symmetric cases of Smith and Timoshin (1996a), Smith and Timoshin (1996b), and discusses each of the three regions in turn: region II covering the majority of the boundary layer flow, region I, the viscous sublayer, and the inviscid region III, an extension of the outer solution from the previous chapter. Section 4.3 examines the solution method used, solving the periodic viscous flow in region I and exploring the solution of the outer region III problem. Again as before these are required to be solved hand-in-hand to determine the y-shift and displacement simultaneously. This section goes on to present some comparisons between the current proposed structure and the results of Chapter 3

4.2 The flow structure

The periodic problem we are examining here is that of a single blade with leading edge at $x = 0$, trailing edge at $x = t$ and the next leading edge at $x = L$, all at a distance h from horizontal ground. As in the previous chapter y is the outer normal scale and $Y = Re^{-\frac{1}{2}}y$ is the inner viscous normal scale. It is assumed that the flow has already come over a large number of identical L-periods upstream of the blade-wake pair of interest and likewise has a large number still to pass subsequently, see figure 4.1

The results for many blades using the method of the previous chapter suggest, along with similar analysis in Smith and Timoshin (1996a) and Smith and Timoshin (1996b) , a two tiered structure to the flow in the boundary layer. In figures 4.2 and 4.3 we present the u velocity profiles mid-blade and mid-wake in each relevant period for a representative ten blade case, obtained using the method of chapter 3.

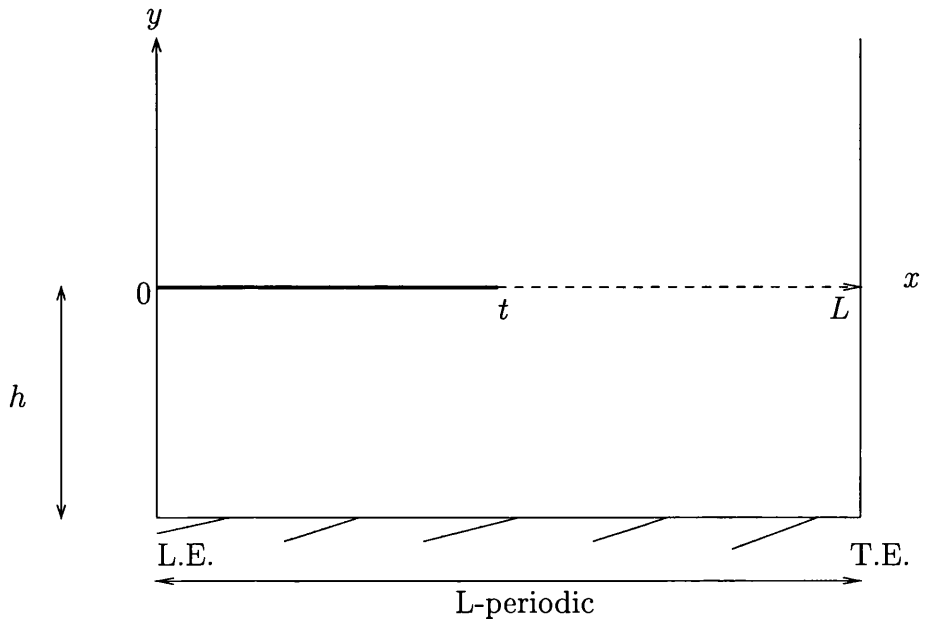

Figure 4.1: A single blade-wake period

The seemingly periodic nature of the inner tier can be seen in the relatively constant flow for small Y after about three or four blades in each figure but with a changing profile through the period. There is also a slowly growing outer viscous tier, with little change going from one blade into the following wake but gradual growth as many blades are passed. These results suggest a two tiered structure in Y in the boundary layer. The periodicity can be seen even more clearly in figure 4.4 which compares successive wake centre-line shapes.

After passing over a large number of blades, n say, there are two streamwise length scales of significance: one a longer, slowly varying scale over all the blades passed so far with $x = nx_l$ and the other having a fast varying dependence on the local shifted $x = x_s$ near the current blade. As such we express the x dependence in the

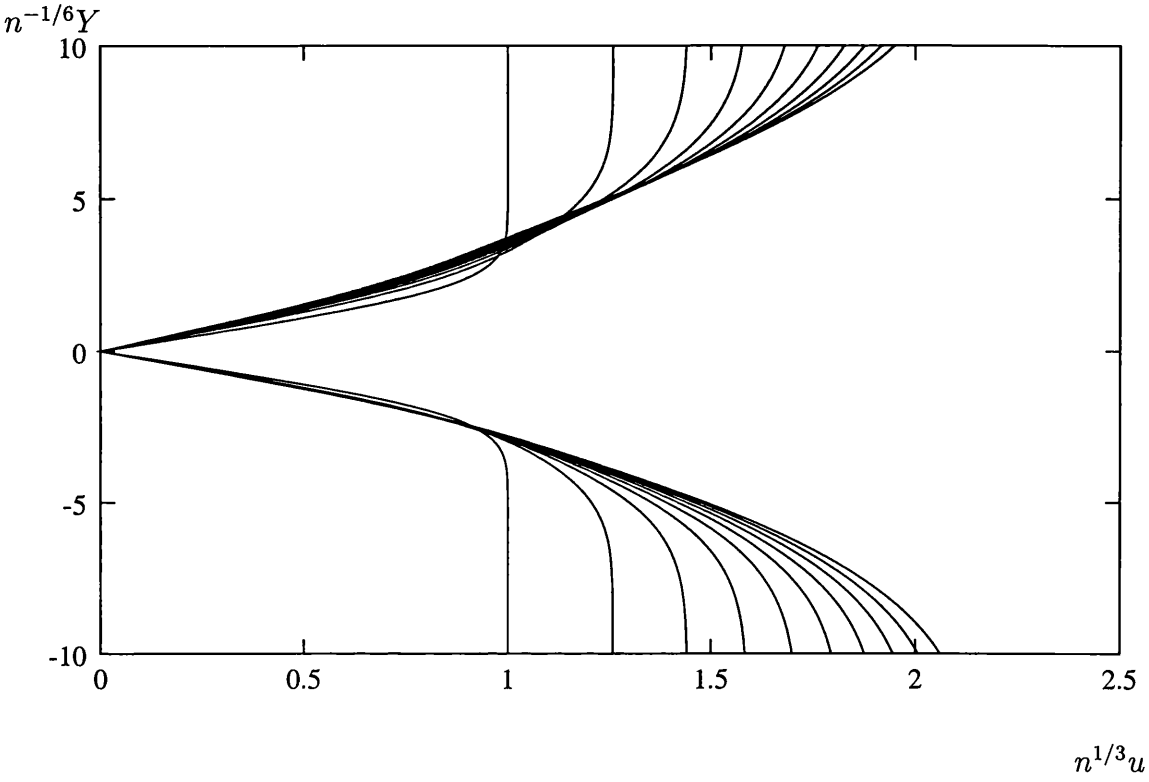

Figure 4.2: The scaled u velocity profiles mid-blade in the boundary layer for a ten blade case. Note the near periodicity for small y and the gradual growth for large y. The scales used are those determined below for the innermost layer.

boundary layer as

$$x = x_s + nx_l, \tag{4.1}$$

At a streamwise distance of order n downstream the normal viscous scale is of order $n^{1/2}$ as expected. The normal scaling of the inner tier is implied by the viscous-inviscid balance in the governing boundary layer equations between $u\frac{\partial}{\partial x} \sim \frac{\partial^2}{\partial Y^2}$ along with the known scalings $x_s \sim O(1)$ and $u \sim O(Yn^{-1/2})$. These imply $Yn^{-1/2} \sim Y^{-2}$, and give the normal scaling as $Y \sim n^{1/6}$ in the inner tier.

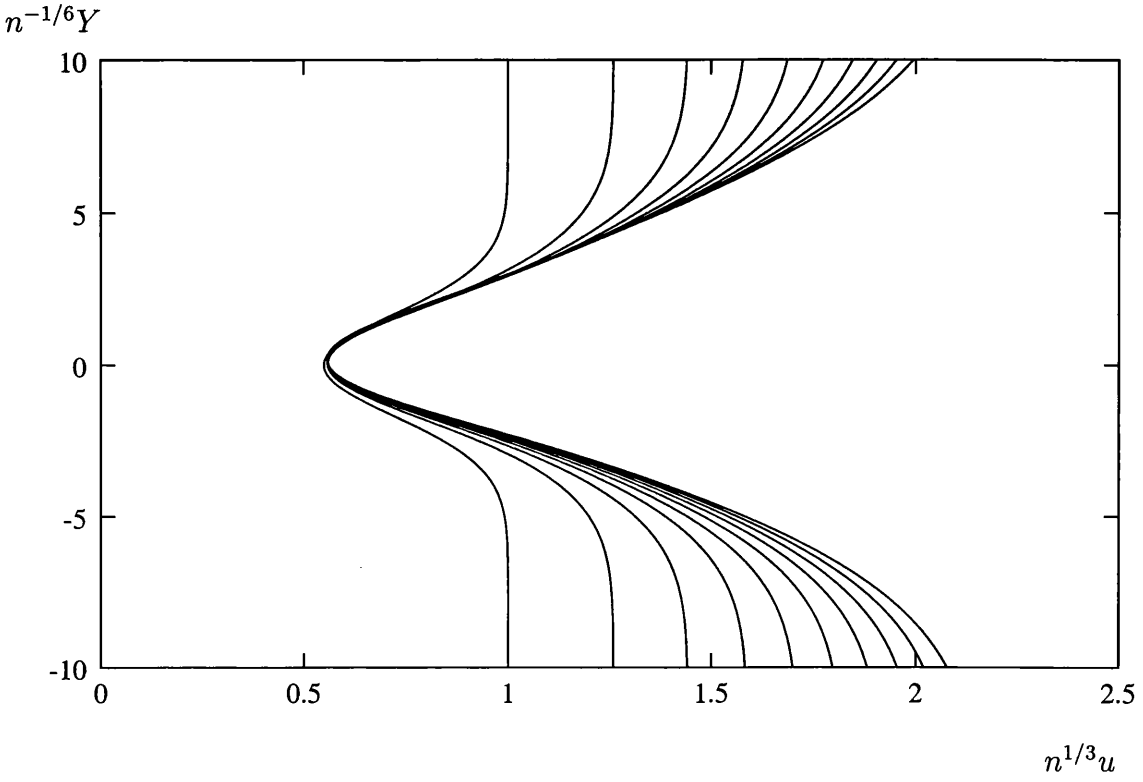

Figure 4.3: The scaled u velocity profiles mid-wake in the boundary layer for a ten blade case. Note the near periodicity for small y and the gradual growth for large y. The scales used are those determined below for the innermost layer.

We now discuss each region in more detail.

4.2.1 Region II

Firstly we consider region II covering the bulk of the boundary layer flow, see figure 4.5 for the proposed structure. Our starting point in this rotational region, and in the following sublayer region I, is the boundary layer equations (3.4), (3.5). As discussed just above we introduce the scaled normal co-ordinate $\tilde{Y}$, where $Y = n^{1/2}\tilde{Y}$

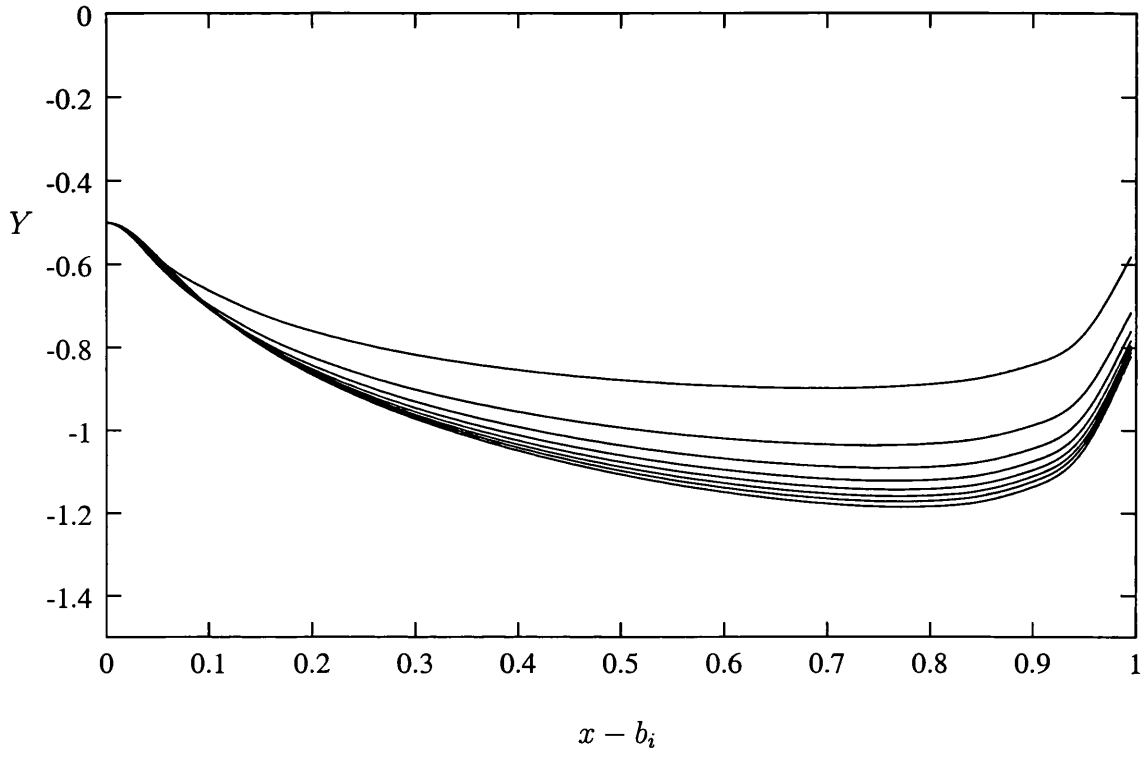

Figure 4.4: A Comparison of the wake-center line shapes for a ten blade case. The uppermost line is wake one, the lowermost wake nine. Notice the near periodicity as increasingly more blades are passed.

(Y being the scaled normal boundary coordinate) and expand the scaled velocities in this region as

$$\bar{u} = u_0(x_l, \tilde{Y}) + n^{-1/3}u_b(x_s, \tilde{Y}) + n^{-2/3}u_c(x_s, \tilde{Y}) + n^{-1}u_1(x_s, \tilde{Y}) + \ldots, \tag{4.2}$$

$$\bar{v} = n^{1/6}v_b(x_s, \tilde{Y}) + n^{-1/6}v_c(x_s, \tilde{Y}) + n^{-1/2}v_1(x_s, \tilde{Y}) + \ldots, \tag{4.3}$$

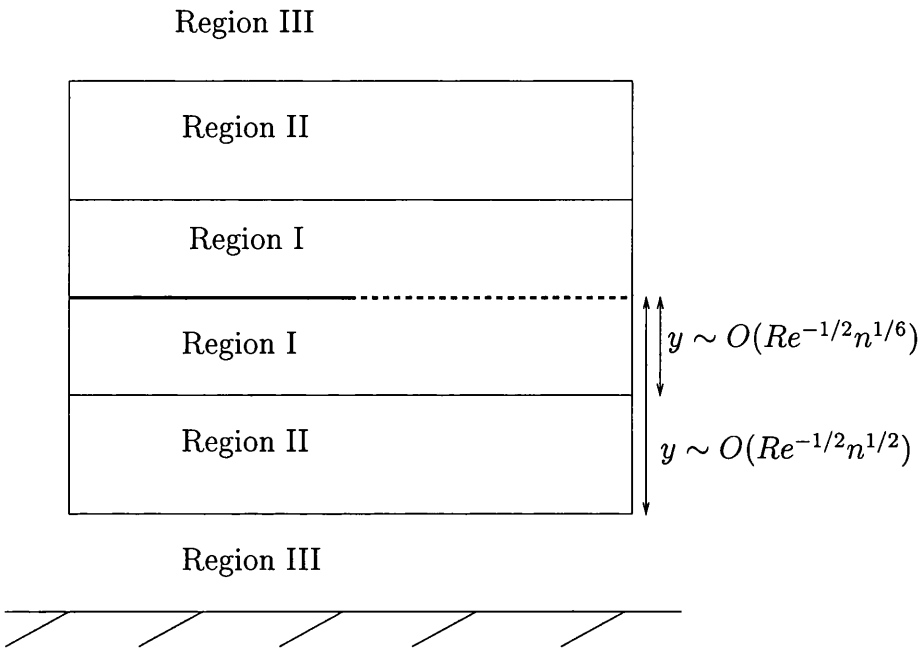

Figure 4.5: Schematic of the proposed flow structure, with regions I and II being viscous, and region III being inviscid and containing the ground.

where all the components are unknown and u_0 is independent of the fast varying scale x_s. The terms with fractional powers of n come from the requirement to match the velocities here with those in the innermost region I considered in the next section. Substituting into the governing boundary layer equations (3.4), (3.5) these expansions yield, to leading order,

$$\frac{\partial u_b}{\partial x_s} + \frac{\partial v_b}{\partial \tilde{Y}} = 0, \tag{4.4}$$

$$u_0 \frac{\partial u_b}{\partial x_s} + v_b \frac{\partial u_0}{\partial \tilde{Y}} = 0. \tag{4.5}$$

Substituting from (4.4) into (4.5) and rearranging gives us

$$u_0 \frac{\partial v_b}{\partial \tilde{Y}} - v_b \frac{\partial u_0}{\partial \tilde{Y}} = 0 \tag{4.6}$$

which, when solved using an integrating factor, leads to

$$v_b = -\frac{\partial b_\pm}{\partial x_s} u_0, \tag{4.7}$$

where $b_\pm(x_s)$ are unknown functions of integration with $\pm$ referring to the solution above and beneath the inner tier I respectively. Then (4.7) and (4.4) imply

$$u_b = b_\pm(x_s) \frac{\partial u_0}{\partial \tilde{Y}}. \tag{4.8}$$

These functions $b_\pm(x)$ correspond to a small displacement effect from region I either side of the blade-wake, with u_0 effectively evaluated at $\pm(\tilde{Y} + n^{-1/3} b_\pm(x) + \ldots)$ rather than $\pm\tilde{Y}$ both above and below.

At next order the governing equations become

$$\frac{\partial u_c}{\partial x_s} + \frac{\partial v_c}{\partial \tilde{Y}} = 0, \tag{4.9}$$

$$u_0 \frac{\partial u_c}{\partial x_s} + u_b \frac{\partial u_b}{\partial x_s} + v_c \frac{\partial u_0}{\partial \tilde{Y}} + v_b \frac{\partial u_b}{\partial \tilde{Y}} = 0. \tag{4.10}$$

Substituting for u_b,v_b from (4.7),(4.8) and using (4.9) to eliminate $\frac{\partial u_c}{\partial x_s}$ from (4.10) we obtain

$$u_0\frac{\partial v_c}{\partial \tilde{Y}} - v_c\frac{\partial u_0}{\partial \tilde{Y}} = -b_\pm\frac{db_\pm}{dx_s}(u_0\frac{\partial^2 u_0}{\partial \tilde{Y}^2} - (\frac{\partial u_0}{\partial \tilde{Y}})^2). \tag{4.11}$$

Again using an integrating factor this becomes

$$v_c = -b_\pm\frac{\partial b_\pm}{\partial x_s}\frac{\partial u_0}{\partial \tilde{Y}} - u_0\frac{\partial c_\pm}{\partial x_s}, \tag{4.12}$$

where $c_\pm(x_s)$ are unknown functions of integration. Then (4.9) implies

$$u_c = \frac{(b_\pm(x_s))^2}{2}\frac{\partial^2 u_0}{\partial \tilde{Y}^2} + c_\pm(x_s)\frac{\partial u_0}{\partial \tilde{Y}}. \tag{4.13}$$

Once again this corresponds to a displacement effect from region I, now equivalent to evaluating u_0 at $\pm(\tilde{Y} + n^{-1/3}b_\pm(x) + n^{-2/3}c_\pm(x))$ as

$$u_0(\tilde{Y} + \epsilon b + \epsilon^2 c) = u_0(\tilde{Y}) + (\epsilon b + \epsilon^2 c)\frac{\partial u_0}{\partial \tilde{Y}} + \frac{(\epsilon b + \epsilon^2 c)^2}{2}\frac{\partial^2 u_0}{\partial \tilde{Y}^2} + \ldots, \tag{4.14}$$

$$= u_0(\tilde{Y}) + \epsilon b\frac{\partial u_0}{\partial \tilde{Y}} + \epsilon^2(\frac{b^2}{2}\frac{\partial^2 u_0}{\partial \tilde{Y}^2} + c\frac{\partial u_0}{\partial \tilde{Y}}), \tag{4.15}$$

by using the Taylor series, where $\epsilon = n^{-1/3}$ is small.

The next order governing equations obtained are given by,

$$\frac{\partial u_1}{\partial x_s} + \frac{\partial u_0}{\partial x_l} + \frac{\partial v_1}{\partial \tilde{Y}} = 0, \tag{4.16}$$

$$u_0\frac{\partial u_1}{\partial x_s} + u_0\frac{\partial u_0}{\partial x_l} + u_b\frac{\partial u_c}{\partial x_s} + u_c\frac{\partial u_b}{\partial x_s} + v_1\frac{\partial u_0}{\partial \tilde{Y}} + v_b\frac{\partial u_c}{\partial x_s} + v_c\frac{\partial u_b}{\partial x_s} = \frac{\partial^2 u_0}{\partial \tilde{Y}^2}. \tag{4.17}$$

The problem here is that equations (4.16), (4.17) contain both the longer x_l scale and the shorter x_s scale. However at this point we are able to make use of our

assumption of periodicity over the shorter x_s scale. If we integrate (4.16) and (4.17) with respect to x_s over the entire period L, applying L-periodicity in u_1 and using our expressions for u_b, u_c, v_b, v_c, we obtain

$$\frac{\partial u_0}{\partial x_l} + \frac{\partial v_M}{\partial \tilde{Y}} = 0, \tag{4.18}$$

$$u_0 \frac{\partial u_0}{\partial x_l} + v_M \frac{\partial u_0}{\partial \tilde{Y}} = \frac{\partial^2 u_0}{\partial \tilde{Y}^2}, \tag{4.19}$$

where $v_M = \frac{1}{L}\int_0^L v_1 \mathrm{d}x_s$ is the mean value of v_1 over the period. The relevant boundary conditions at the wall are

$$u_0 = v_M = 0 \quad \text{at} \quad \tilde{Y} = 0\pm, \tag{4.20}$$

$$u_0 \to 1 \quad \text{as} \quad \tilde{Y} \to \pm\infty, \tag{4.21}$$

as discussed in Smith and Timoshin (1996a). Equations (4.18), (4.19) along with the requirements (4.20), (4.21) are exactly the equations of the Blasius semi-infinite flat plate boundary layer, with a well known solution as shown in appendix A. So this region has primarily mean Blasius flow, somewhat sheltered from the successive leading and trailing edges by the inner sublayer region I. It also serves however to communicate displacement effects from region I through to the inviscid flow in region III.

4.2.2 Region I

We turn now to the viscous sublayer region I. Here, covering a single blade and wake, we have a y-scale given by $Y = n^{1/6}\hat{Y}$ from the viscous-inviscid balance discussed above, which implies the forms

$$\bar{u} = n^{-1/3}\hat{u}_1 + n^{-2/3}\hat{u}_2 + \ldots, \tag{4.22}$$

$$\bar{v} = n^{-1/6}\hat{v}_1 + n^{-1/2}\hat{v}_2 + \ldots, \tag{4.23}$$

for the transverse and normal velocities respectively where the $\bar{u}$ scaling follows from $\hat{Y}$ and region II and the $\bar{v}$ scalings from continuity. Substitution into the governing boundary-layer equations (3.4),(3.5) gives the leading order problem in this region as

$$\frac{\partial \hat{u}_1}{\partial x_s} + \frac{\partial \hat{v}_1}{\partial \hat{Y}} = 0, \tag{4.24}$$

$$\hat{u}_1\frac{\partial \hat{u}_1}{\partial x_s} + \hat{v}_1\frac{\partial \hat{v}_1}{\partial \hat{Y}} = \frac{\partial^2 \hat{u}_1}{\partial \hat{Y}^2}, \tag{4.25}$$

subject to the conditions

$$\hat{u}_1 = \hat{v}_1 = 0 \quad \text{at} \quad \hat{Y} = 0 \quad \text{on the blade}, \tag{4.26}$$

$$\frac{\partial \hat{u}_1}{\partial \hat{Y}} \to \pm\lambda \quad \text{as} \quad \hat{Y} \to \pm\infty, \tag{4.27}$$

$$L - \text{periodicity in} \quad x_s, \tag{4.28}$$

$$\hat{Y} - \text{shift at leading edge}, \tag{4.29}$$

where (4.26) is the usual no-slip condition on the blade, (4.27) is a shear flow requirement needed to match with the flow in region II, i.e. with u_0 as $\tilde{Y} \to 0\pm$ implying $\lambda = \frac{\partial u_0}{\partial \tilde{Y}}(0)$, while (4.28) is the short scale periodicity assumption discussed earlier and (4.29) is the manifestation of the adjustment of this sublayer to enable pressure continuity across the wake in region III in a similar manner to chapter 3. Further, as part of the solution of this region the displacement effects $b^{\pm}(x)$ are determined, namely

$$\hat{u}_1 \sim \pm\lambda(|\hat{Y}| + b_{\pm}(x_s)) \quad \text{as} \quad \hat{Y} \to \pm\infty, \tag{4.30}$$

$$\hat{v}_1 \sim \mp\lambda\frac{db_{\pm}}{dx_s}\hat{Y} \quad \text{as} \quad \hat{Y} \to \pm\infty, \tag{4.31}$$

in accordance with the behavior of region II as $\tilde{Y} \to 0\pm$. The $O(1)$ factor λ is given by

$$\lambda = \frac{\partial u_0}{\partial \tilde{Y}}|_{\tilde{Y}=0\pm} = F''(0)x_L^{-1/2}, \tag{4.32}$$

where the function $F(x)$ is the Blasius function and where the constant $F''(0) = 0.3321$ is known. So λ is effectively constant over this shorter x_s length scale.

For completeness we also consider the next order to demonstrate how $c_\pm(x)$ can be determined. The governing equations become

$$\frac{\partial \hat{u}_2}{\partial x_s} + \frac{\partial \hat{v}_2}{\partial \hat{Y}} = 0, \tag{4.33}$$

$$\hat{u}_2\frac{\partial \hat{u}_1}{\partial x_s} + \hat{u}_1\frac{\partial \hat{u}_1}{\partial x_s} + \hat{v}_1\frac{\partial \hat{u}_1}{\partial \hat{Y}} + \hat{v}_2\frac{\partial \hat{u}_2}{\partial \hat{Y}} = \frac{\partial^2 \hat{u}_2}{\partial \hat{Y}^2}. \tag{4.34}$$

The boundary conditions here are given by

$$\hat{u}_2 = \hat{v}_2 = 0 \quad \text{at} \quad \hat{Y} = 0 \quad \text{on the blade}, \tag{4.35}$$

$$\frac{\partial \hat{u}_2}{\partial \hat{Y}} \to 0 \quad \text{as} \quad \hat{Y} \to \pm\infty, \tag{4.36}$$

$$L - \text{periodicity in} \quad x_s, \tag{4.37}$$

which are the no-slip, the match with region II and periodicity conditions, respectively. Then $c_\pm(x)$ can be determined as

$$\hat{u}_2 \sim \pm\lambda c_\pm(x_s) \quad \text{as} \quad \hat{Y} \to \infty, \tag{4.38}$$

as, due to the lack of streamwise pressure gradient, there is no $O(Y^2)$ term in U_0 in the main deck.

4.2.3 Region III

Finally we move to the inviscid region III. This region is effectively that discussed in the previous chapter. However the major change is that now, rather than be-

ing driven by the complete viscous displacement thicknesses $\delta^{\pm}(x)$, instead the important driving factor is the current local viscous displacement quantities $b_{\pm}(x_s)$ determined by the innermost region I.

In order to match with region II the velocities and pressures in this outer region are expanded as

$$u = n^{1/6}U_1 + \ldots, \tag{4.39}$$

$$v = n^{1/6}V_1 + \ldots, \tag{4.40}$$

$$p = n^{1/6}P_1 + \ldots, \tag{4.41}$$

where u, v, p are the $O(Re^{-1/2})$ perturbations of the free-stream discussed in section 3.2.2. We now limit ourselves to considering only the leading order displacement effects, neglecting the influence of $c_{\pm}$ on this outer region. The next order terms satisfy the same governing equations and similar boundary conditions and the solution at next order can be determined in a way similar to that presented below. Substituting into the governing linearised Euler equations leaves them unchanged to leading order, once again becoming the Cauchy-Riemann equations for the normal velocity and pressure, here given by

$$\frac{\partial V_1}{\partial y} = \frac{\partial P_1}{\partial x_s}, \tag{4.42}$$

$$\frac{\partial V_1}{\partial x_s} = -\frac{\partial P_1}{\partial y}. \tag{4.43}$$

The boundary conditions once again require pressure continuity across the wake and that the normal velocities match with the boundary layer as $y \to 0\pm$. The required

velocity conditions for this flat blade case are given by

$$V_{1\pm} = \begin{cases} \pm b'_{\pm}(x_s) & x_s \quad \text{on blades} \\ n^{\frac{1}{6}} s'(x_s) \pm b'_{\pm}(x_s) & x_s \quad \text{in wakes} \end{cases} \tag{4.44}$$

where $s'(x)$ is the shape of the wake centre line, to leading order, in the innermost region, and $b_{\pm}(x)$ are the displacements determined in region I and communicated through region II as discussed above. We could incorporate blade shapes and thicknesses (assuming the blades lie entirely within region I) which would add camber and thickness effects to the boundary conditions but we only consider flat blades here. Now we have to solve exactly the same problem as before, finding an analytic function $w(z) = P_1 + iV_1$ in the complex plane satisfying mixed boundary conditions. Following through the same analysis as in Chapter 3 we obtain the same integral equations with the velocity and pressure sums and differences given by

$$[V_1](x) = \begin{cases} (b'_+ + b'_-)(x_s) & \text{on blades} \\ (b'_+ + b'_-)(x_s) & \text{in the wakes} \end{cases} \tag{4.45}$$

$$< V_1 > (x) = \begin{cases} (b'_+ - b'_-)(x_s) & \text{on blades} \\ ? & \text{in the wakes} \end{cases} \tag{4.46}$$

$$[P_1](x) = \begin{cases} ? & \text{on blades} \\ 0 & \text{in the wakes} \end{cases} \tag{4.47}$$

$$< P_1 > (x) = \begin{cases} ? & \text{on blades} \\ ? & \text{in the wakes,} \end{cases} \tag{4.48}$$

in this case.

The solution of this problem can be carried out as before; however periodicity allows some rearrangement/simplification. Firstly we consider (3.58) which we repeat for

clarity

$$h(x) = -\frac{1}{\pi}\sum_{i=1}^{n}\int_{a_i}^{b_i}\frac{S^{1/2}(\tilde{\xi})f(\tilde{\xi})}{\tilde{\xi}-x}\mathrm{d}\tilde{\xi}. \tag{4.49}$$

In the current situation we assume what is in effect an infinite array of blades in both directions rather than a finite number of blades n. Therefore (4.49) becomes for the present regime

$$h(x) = -\frac{1}{\pi}\sum_{i=-\infty}^{\infty}\int_{a_i}^{b_i}\frac{S^{1/2}(\tilde{\xi})f(\tilde{\xi})}{\tilde{\xi}-x}\mathrm{d}\tilde{\xi}. \tag{4.50}$$

Exchanging the order of the sum and the integral and substituting for $\tilde{\xi}$ such that we are integrating over a single period, i.e. $\tilde{\xi} = \xi + iL$, with $L = a_{i+1} - a_i = b_{i+1} - b_i$, $a_j = jL$, $b_j = jL + t$, gives

$$h(x) = -\frac{1}{\pi}\int_0^t S_p^{1/2}(\xi)f(\xi)(\sum_{i=-\infty}^{\infty}\frac{1}{\xi + iL - x})\mathrm{d}\xi, \tag{4.51}$$

using the fact that $f(x)$ is periodic, being dependent only on the periodic boundary conditions, and where the new periodic version of $S(x)$, $S_p(x)$, is given by

$$S_p(x) = \prod_{j=-\infty}^{\infty}\frac{x - jL}{x - jL - t}. \tag{4.52}$$

The streamwise co-ordinate x is now given by $x = nL + x_s$ and is dependent on which blade we are considering and the shorter streamwise scale x_s. We can carry out the same procedure on the other relevant integral equations from chapter 3, with (3.59) becoming

$$M(x,\xi) = -\frac{1}{\pi}\int_0^t S_p^{1/2}(\xi_1)(\sum_{i=-\infty}^{\infty}\frac{m(\xi_1 + iL - \xi)}{\xi_1 + iL - x})\mathrm{d}\xi_1, \tag{4.53}$$

and (3.52) becoming

$$f(x) = \frac{1}{\pi}\int_0^L [v](\xi)(\sum_{i=-\infty}^{\infty} l(\xi + iL - x))\mathrm{d}\xi - < v > (x). \tag{4.54}$$

The Fredholm equation of the second kind (3.61) for ψ becomes

$$\psi(x) = h(x) + \frac{1}{\pi}\int_0^t S_p^{-1/2}(\xi)\psi(\xi)(\sum_{k=-\infty}^{\infty} M(x,\xi+kl))\mathrm{d}\xi. \tag{4.55}$$

To simplify the notation we introduce a new quantity $\hat{M}(x,\xi)$, where

$$\begin{aligned}\hat{M}(x,\xi) &= \sum_{k=-\infty}^{\infty} M(x,\xi+kl), \\ &= -\frac{1}{\pi}\int_0^t S_p^{1/2}(\xi_1)(\sum_{k=-\infty}^{\infty}\sum_{i=-\infty}^{\infty}\frac{m(\xi_1-\xi+(i-k)L)}{\xi_1-x+(i-k)L})\mathrm{d}\xi_1,\end{aligned} \tag{4.56}$$

again changing the order of the sum and the integral. This leaves (4.55) as

$$\psi(x) = h(x) + \frac{1}{\pi}\int_0^t S_p^{-1/2}(\xi)\hat{M}(x,\xi)\psi(\xi)\mathrm{d}\xi, \tag{4.57}$$

where

$$\psi(x) = S_p^{1/2}(x)[p](x). \tag{4.58}$$

The unknown y-shift can be determined by integrating the relevant boundary conditions from (4.44).

4.3 Solution method and comparisons

To make further progress we have to consider regions I and III numerically. For the viscous layer region I, the problem is very similar to that before in Chapter 3 only with there now being a periodicity requirement (4.28). The technique is also much as previously, with the same discretisation, changing the $|\tilde{Y}| \to \infty$ condition appropriately to satisfy (4.27). Satisfying the periodicity condition is achieved by

repeatedly iterating over the L-period until the velocity profiles at $x = L$ are identical, to within a reasonable accuracy, to their values on the previous sweep. So, given a starting profile, we sweep the boundary-layer solution over the blade and wake period to $x = L$. We then apply the necessary y-shift calculated from region III discussed below and this then yields the starting profile for the next sweep if convergence has not been attained. Once converged the necessary displacements $b_{\pm}$ can be determined.

The problems involved in evaluating the integrals in region III are again as before with $S_p(x)$ introducing a square root singularity and there remains the need to treat the integrals as principal values. As before we substitute for ξ and x in order to remove the square root singularities which transforms the Fredholm equation (4.57) to

$$\psi(t\sin^2\phi) = h(t\sin^2\phi) + \frac{2t}{\pi}\int_0^{\frac{\pi}{2}} \cos^2\theta \hat{S}_p^{-1/2}(t\sin^2\theta)\hat{M}(t\sin^2\phi, t\sin^2\theta)\psi(t\sin^2\theta)\mathrm{d}\theta \tag{4.59}$$

where

$$\hat{S}_p(x) = |\frac{x}{x-t}|S_p(x), \tag{4.60}$$

$$= \prod_{k=1}^{\infty}\frac{x^2 - k^2L^2}{(x-t)^2 - k^2L^2}. \tag{4.61}$$

Equation (4.51) for $h(x)$ becomes

$$h(t\sin^2\phi) = -\frac{2t}{\pi}\int_0^{\frac{\pi}{2}} \sin^2\theta \hat{S}_p^{1/2}(t\sin^2\theta)f(t\sin^2\theta)(\sum_{i=-\infty}^{\infty}\frac{1}{t\sin^2\theta - t\sin^2\phi + nL})\mathrm{d}\theta \tag{4.62}$$

and (4.56) for $\hat{M}(x,\xi)$ becomes

$$\hat{M}(t\sin^2\phi, t\sin^2\theta) = -\frac{2t}{\pi}\int_0^{\frac{\pi}{2}} \sin^2\theta_1 \hat{S}_p(t\sin^2\theta_1)G(\theta,\theta_1,phi,t)\mathrm{d}\theta. \tag{4.63}$$

where

$$G(\theta,\theta_1,\phi,t)=\sum_{j=-\infty}^{\infty}\sum_{i=-\infty}^{\infty}\frac{m(t\sin^2\theta_1-t\sin^2\theta+(i-j)L)}{t\sin^2\theta_1-t\sin^2\phi+iL} \tag{4.64}$$

These integrals can now be evaluated by truncating the sums and taking care of the Cauchy- type kernels where necessary using the NAG library routine as described earlier. The truncation of the sums was tested to ensure the final solution was not excessively dependent on it.

The solution is then determined iteratively. Firstly, starting from an initial y-shift guess, we solve the boundary layer region I until periodicity is achieved which determines the unknown $b_{\pm}(x)$ displacements. These then feed into the outer problem in region III which is solved by iterating the Fredholm equation (4.59) as in Chapter 3, to determine the velocity and pressure distributions and hence yielding a new y-shift guess and wake shape $s(x)$. This then passes back into the region I solution and the process starts again until successive y-shift estimates have converged to a specified accuracy, typically $O(10^{-5})$.

We present, in figures 4.6 and 4.7, two comparisons between the current solution method and the method of the previous chapter. The figures present the wake shapes for $h = 0.25$ and $h = 0.0625$, calculated both by the periodic approach and shown with the fourth wake shape from the five blade calculations presented in the previous chapter, with $L = 2$ and $t = 1$ in this case. The comparisons add weight to the structure proposed in this chapter with good agreement in both cases, particularly for the smaller h case where the solution appears to settle down into a periodic state far quicker than the large h case. Better agreement could probably be achieved by including the $c_{\pm}(x)$ effects, but these results appear encouraging with regard to the

validity of the three region structure and the periodicity assumption. In figures 4.8 and 4.9 we also present comparisons between the pressures beneath the blades at the same heights, comparing this periodic case with the pressure found under blade 4 of the five blade calculations presented earlier.

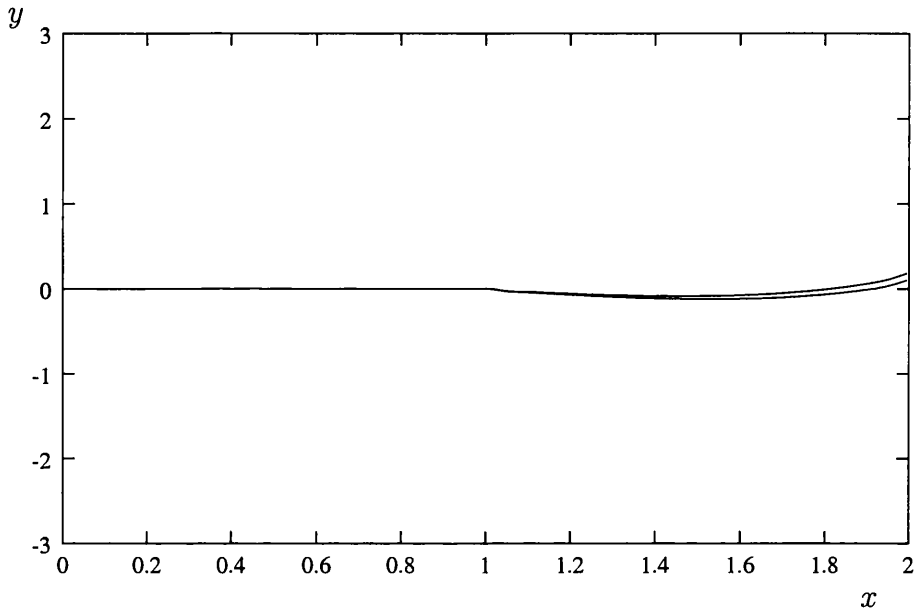

Figure 4.6: Comparison between the wake shapes $s(x)$ for the current periodic method and blade 4 of the five blade case from chapter 3 for $h = 0.25$. The shape from this chapter is the lower of the two.

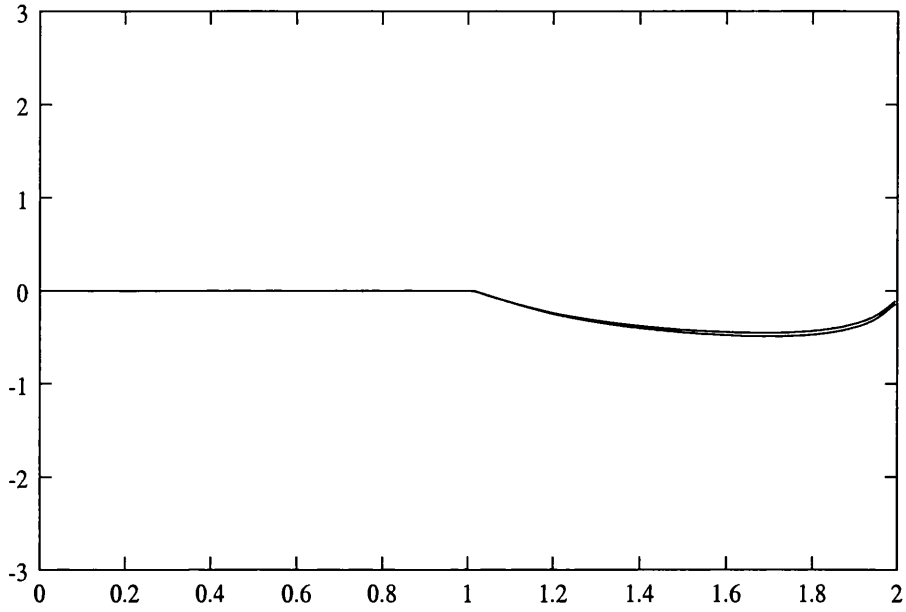

Figure 4.7: Comparison between the wake shapes $s(x)$ for the current periodic method and blade 4 of the five blade case from chapter 3 for $h = 0.0625$. The shape from this chapter is the lower of the two.

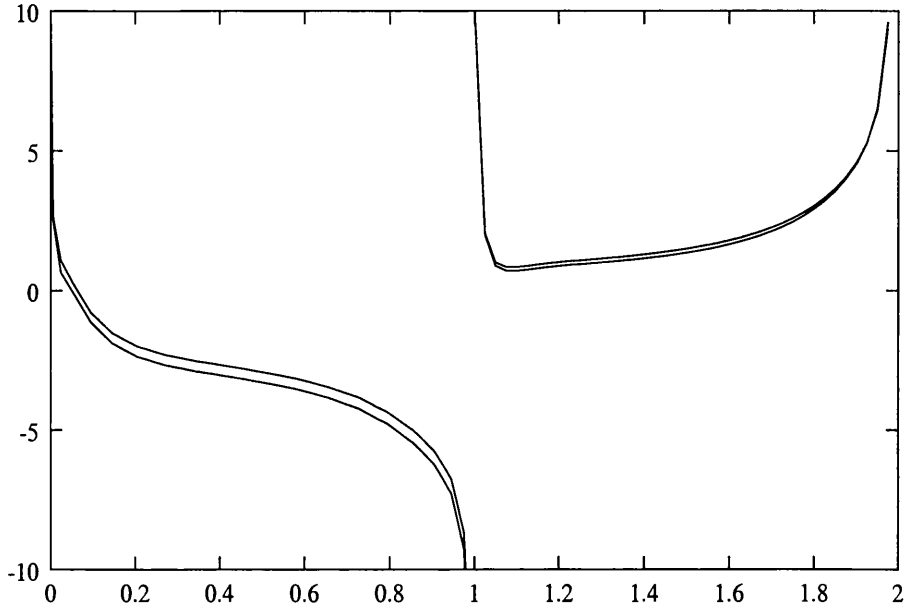

Figure 4.8: Comparison between the underneath pressures p^- for the current periodic method and for blade 4 of the five blade case from chapter 3 for $h = 0.25$. The shape from this chapter is the lower of the two.

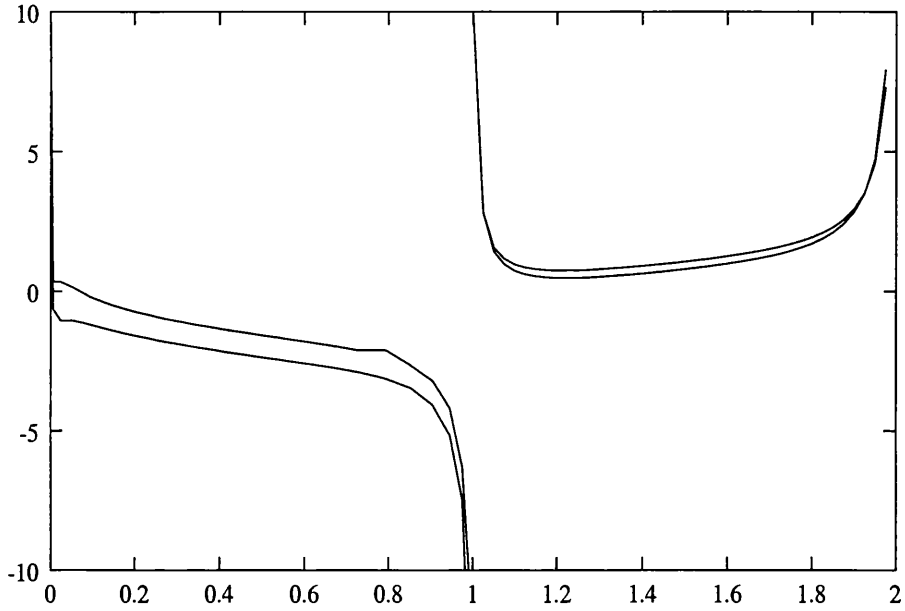

Figure 4.9: Comparison between the underneath pressures p^- for the current periodic method and for blade 4 of the five blade case from chapter 3 for $h = 0.0625$. The shape from this chapter is the lower of the two.

Chapter 5

Three-Dimensional Interactive Multi-Blade Flow

5.1 Introduction

We now abandon ground effect for the time being and instead consider some three-dimensional flows. In this chapter we examine interactive flow past many three-dimensional blades. As discussed in the previous chapter once many blades are passed a new structure emerges with the boundary layer effectively splitting into two, with one slowly growing tier containing mean Blasius flow and an inner tier containing periodic flow. However a new interaction appears once an $O(Re^{3/5})$ number of blades have been passed as discussed in Smith and Timoshin (1996b), Bowles and Smith (2000a), Bowles and Smith (2000b), and chapter 4 with a pressure-displacement interaction developing in the boundary layer. Here we consider a similar case but now with three dimensional blades. We consider the flow structure

and formulate the problem for the general case of three dimensional blades and then move on to examine a particular limit, that of short blades. The short blade limit, whereby the streamwise length of the blade becomes small compared to the length of the period whilst the spanwise length remains $O(1)$, is of interest as the dimensions of a typical rotor blade are similar.

The set-up of the problem is that of a large array of identical three dimensional blades, assumed flat here, and we focus on a single periodic region from one leading edge to the following leading edge. There are various mechanisms by which an $O(1)$ z-scale becomes important. One situation is that, as well as periodicity in x, we have a periodic structure in the z direction also, with the z-period L_1 say being $O(1)$. This corresponds to the blade having a three dimensional form repeated many times along it. Another possibility is that the geometry of the blade is such that there is three-dimensionality confined to an $O(1)$ length scale beyond which the blade is two-dimensional. In this case, rather than periodicity, we would require the three-dimensional solution to tend to the two-dimensional case at large spanwise distances.

The governing equations here are the non-dimensionalised, three-dimensional Navier-Stokes equations

$$\frac{\partial u}{\partial \hat{X}} + \frac{\partial v}{\partial y} + \frac{\partial w}{\partial z} = 0, \tag{5.1}$$

$$u\frac{\partial u}{\partial \hat{X}} + v\frac{\partial u}{\partial y} + w\frac{\partial u}{\partial z} = -\frac{\partial p}{\partial \hat{X}} + \frac{1}{Re}\left(\frac{\partial^2 u}{\partial \hat{X}^2} + \frac{\partial^2 u}{\partial y^2} + \frac{\partial^2 u}{\partial z^2}\right), \tag{5.2}$$

$$u\frac{\partial v}{\partial \hat{X}} + v\frac{\partial v}{\partial y} + w\frac{\partial v}{\partial z} = -\frac{\partial p}{\partial y} + \frac{1}{Re}\left(\frac{\partial^2 v}{\partial \hat{X}^2} + \frac{\partial^2 v}{\partial y^2} + \frac{\partial^2 v}{\partial z^2}\right), \tag{5.3}$$

$$u\frac{\partial w}{\partial \hat{X}} + v\frac{\partial w}{\partial y} + w\frac{\partial w}{\partial z} = -\frac{\partial p}{\partial z} + \frac{1}{Re}\left(\frac{\partial^2 w}{\partial \hat{X}^2} + \frac{\partial^2 w}{\partial y^2} + \frac{\partial^2 w}{\partial z^2}\right), \tag{5.4}$$

where the Reynolds number Re, based on the free stream velocity $U = 1$, the length of the x-period L and the kinematic viscosity of the fluid, is once again assumed to be large.

In section 5.2 below we set out the full three-dimensional problem, with what is effectively a triple-deck structure covering the entire period. The three decks are a periodic inner tier, a middle tier again containing mean Blasius flow and transferring displacement effects from the innermost viscous tier to the inviscid region outside, and the outer, inviscid tier serving to provide a relation between the pressure and displacement in the innermost tier as usual. The so-called condensed case is discussed before moving on, in section 5.3, to consider the short blade limit, introducing a new short x-scale while keeping the z-scale as before. The proposed flow structure in the innermost layer is based upon five regions, the sizes and forms of which are determined. We also consider some possible solutions for the pressure, which is found to drops abruptly across the short blade before slowly changing in the relatively long wake in order to satisfy the required periodicity in x.

5.2 The full three dimensional problem

The many blade limit considered in the previous chapter with no pressure-displacement interaction has boundary layer and wake thicknesses of $O(Re^{-1/2})$. The current structure emerges after a large number of blades have been passed, at a streamwise distance of $O(Re^{3/5})$, where the boundary layer thickness is then $O(Re^{-1/5})$ as discussed in Smith and Timoshin (1996a). At this stage the previously small outer pressure is now comparable with advective terms in the inner part of the bound-

ary layer and the flow becomes interactive with the pressure feeding back into the boundary layer equations. As in the previous chapter there are three y-scales of importance here now given by $y \sim O(Re^{-2/5})$ which is the viscous sublayer containing periodic flow, $y \sim O(Re^{-1/5})$ the boundary layer thickness, and $y \sim O(1)$ for the outer inviscid flow. The three-dimensionality is assumed to enter the problem by way of three-dimensional blade shapes with, for example, a varying shape of the leading and/or trailing edge. This z-dependence holds for all n blades which are taken to be identical.

It is possible in the current regime to carry out very similar analysis to the periodic many blade case in the previous chapter and we present an outline here to formulate the full three-dimensional interactive pressure-displacement problem before turning to a particular limit of interest. Once again there are two relevant x-scales, now described by $\hat{X} = x + Re^{3/5}x_l$. We obtain what is effectively a three-dimensional triple deck problem, albeit with a global rather than the usual local interaction. If we first consider the middle deck with normal co-ordinate given by $y = Re^{-1/5}y_1$ we expand the velocities and pressure, guided by the many blade limit considered in the previous chapter, as

$$u = u_0(x_l, y_1) + Re^{-1/5}u_1(x, y_1, z) + Re^{-2/5}u_2(x, y_1, z) + Re^{-3/5}u_3(x, y_1, z) + \ldots, \tag{5.5}$$

$$v = Re^{-2/5}v_1(x, y_1, z) + Re^{-3/5}v_2(x, y_1, z) + Re^{-4/5}v_3(x, y_1, z) + \ldots, \tag{5.6}$$

$$w = Re^{-2/5}w_1(x, y_1, z) + Re^{-3/5}w_2(x, y_1, z) + \ldots, \tag{5.7}$$

$$p = Re^{-2/5}P(x, z) + Re^{-3/5}p_2(x, y_1, z) + \ldots. \tag{5.8}$$

Substituting into the governing equations (5.1) - (5.4) leads to the usual middle deck

result (see for example Smith *et al* (1977)),

$$u_1 = A(x,z)\frac{\partial u_0}{\partial y_1}, \tag{5.9}$$

$$v_1 = -\frac{\partial A}{\partial x}u_0, \tag{5.10}$$

$$w_1 = \frac{D(x,z)}{u_0}, \tag{5.11}$$

where

$$\frac{\partial D}{\partial x} = -\frac{\partial p_1}{\partial z}, \tag{5.12}$$

and $A(x,z)$, $D(x,z)$ are unknown displacement effects. Determining the higher order terms in (5.5) - (5.8) is examined in Appendix B. It is shown there that this middle deck has, as in the two dimensional and the non-interactive cases, predominantly two-dimensional mean Blasius flow. This is initially perhaps somewhat surprising but given that in the two-dimensional case Blasius flow was generated regardless of the position of the trailing edge, even if the blade was very small compared to the size of the gap, it does appear to make sense here also as the precise blade geometry appears to be secondary.

In the upper deck where y is $O(1)$, the disturbances to the free stream $u = 1$, $v = w = p = 0$, are all $O(Re^{-2/5})$ and the pressure is governed by Laplace's equation. Matching the velocities between here and in the main deck leads to, as in Smith *et al* (1977), the pressure-displacement law

$$P(x,z) = -\frac{1}{2\pi}\int_{-\infty}^{\infty}\int_{-\infty}^{\infty}\frac{\frac{\partial^2 A}{\partial \xi^2}}{[(x-\xi)^2+(z-\eta)^2]^{1/2}}\mathrm{d}\xi\mathrm{d}\eta. \tag{5.13}$$

Moving into the lower deck where $y = Re^{-2/5}Y$, the periodic velocities and pressure expand as

$$(u,v,w,p) = (Re^{-1/5}U, Re^{-3/5}V, Re^{-1/5}W, Re^{-2/5}P) + \ldots, \tag{5.14}$$

and the equations of motion become the three-dimensional boundary layer ones:

$$\frac{\partial U}{\partial x}+\frac{\partial V}{\partial Y}+\frac{\partial W}{\partial z} = 0, \tag{5.15}$$

$$U\frac{\partial U}{\partial x}+V\frac{\partial U}{\partial Y}+W\frac{\partial U}{\partial z} = -\frac{\partial P}{\partial x}+\frac{\partial^2 U}{\partial Y^2}, \tag{5.16}$$

$$U\frac{\partial W}{\partial x}+V\frac{\partial W}{\partial Y}+W\frac{\partial W}{\partial z} = -\frac{\partial P}{\partial Z}+\frac{\partial^2 W}{\partial Y^2}. \tag{5.17}$$

The boundary conditions are given by

$$U = V = W = 0 \quad \text{on the blade at} \quad Y = 0, \tag{5.18}$$

$$\frac{\partial U}{\partial Y} = V = \frac{\partial W}{\partial Y} \quad \text{in the wake at} \quad Y = 0, \tag{5.19}$$

$$U \sim \lambda(Y + A(x,z)) \quad \text{as} \quad Y \to \infty, \tag{5.20}$$

$$W \sim \frac{D(x,z)}{\lambda Y} \quad \text{as} \quad Y \to \infty, \tag{5.21}$$

$$U, V, W, P \quad \text{L-periodic in } x, \tag{5.22}$$

along with the pressure-displacement law (5.13). These conditions correspond to no-slip on the blade, wake symmetry, the match of U and W with the main deck and the required periodicity, respectively. We also have some conditions in the z direction depending on the problem in question. For example if we have periodicity in z we require that

$$U, V, W, P \quad L_1\text{-periodic in } z. \tag{5.23}$$

Alternatively this condition could be replaced by a requirement of recovering the two-dimensional case as $|z| \to \infty$.

If we allow the size of the x-period L to become small whilst maintaining the governing equations (5.15) - (5.17) we reach the so called condensed case discussed in Bowles and Smith (2000a), Smith and Walton (1998) and references therein. This

short period implies using a new x scale given by $x = L\bar{x}$. In order to maintain the governing equations with this shorter streamwise scale the other co-ordinates, the velocities, the pressure and the displacement scale as

$$(Y, z, U, V, W, P, A) \sim (L^{1/3}\bar{y}, L\bar{z}, L^{1/3}\bar{u}, L^{-1/3}\bar{v}, L^{1/3}\bar{w}, L^{2/3}\bar{p}, L^{1/3}\bar{A}), \tag{5.24}$$

where the z scale is so as to maintain the aspect ratio of the problem, the U scale follows from the shear flow condition (5.20), the W and V scales are from continuity, the P scale follows as $P \sim U^2$ and the scale of the leading order displacement also follows from (5.20). Substitution into the governing equations and boundary conditions leaves them unchanged. However the pressure-displacement interaction is less straightforward. The lefthand side of (5.13) scales as P, i.e. $L^{2/3}$. The righthand side, on the other hand, scales as $\frac{AL^{-2}}{L}L^2 = L^{-2/3}$. Therefore in order to satisfy (5.13) we require the right-hand side to be identically zero, in other words we must have

$$\frac{\partial^2 \bar{A}}{\partial \bar{x}^2} = 0 \tag{5.25}$$

implying that

$$\bar{A} = b(\bar{z})\bar{x} + c(\bar{z}), \tag{5.26}$$

where b, c are unknown functions of z. Streamwise periodicity requires that $\bar{A}(x = L) = \bar{A}(x = 0)$, fixing $b(z)$ as zero and leaving us with the requirement

$$\bar{A} = c(\bar{z}). \tag{5.27}$$

It is this condensed case, equivalent to $\frac{\partial \bar{A}}{\partial \bar{x}} \equiv 0$, that we consider in the remainder of this chapter. Note it is important to include this function $c(\bar{z})$ here and not simply to take $A = 0$ as it was shown in Bowles and Smith (2000a) a periodic solution

could not be found without a non-zero displacement. Physically this condensed case corresponds to the situation with $n \gg Re^{\frac{3}{5}}$.

5.3 The short blade limit

Short blades, where the streamwise chord of the blade is small compared to the streamwise period L and the z scale which both remain $O(1)$, are physically important as, typically, a rotor blade has far more 'gap' than blade, with the distance from a trailing edge to the subsequent leading edge being much larger than the width of a blade. Guided by the two-dimensional case of Bowles and Smith (2000a) we propose a five region structure as in figure 5.1. This is based upon the assumption that any vorticity generated locally on the blade will not have diffused very far in the normal direction before the trailing edge is encountered. This suggests the local effects of the blade are confined to a thin layer surrounding it. This was shown to be the case in Bowles and Smith (2000a) and the assumptions seem sound here also. The relevant y-scales are unknown at present and are to be determined.

The short blade is assumed to be of length $O(\epsilon)$, where ϵ is small, and as such we introduce a new streamwise variable X where $\bar{x} = \epsilon X$. We also take it to have a straight leading edge (z-independent) and a trailing edge given by $X = T(Z)$ that varies in Z. We assume the outer layer to have thickness $O(\epsilon^{-n})$ where n is unknown but expected to be positive; this constant n is to be determined as part of the entire solution. There are two other y scales to be determined, that of the short, innermost layer covering the blade and near wake I and that of the middle layers II, III. The former is determined from the expected Blasius-type response on the blade. This

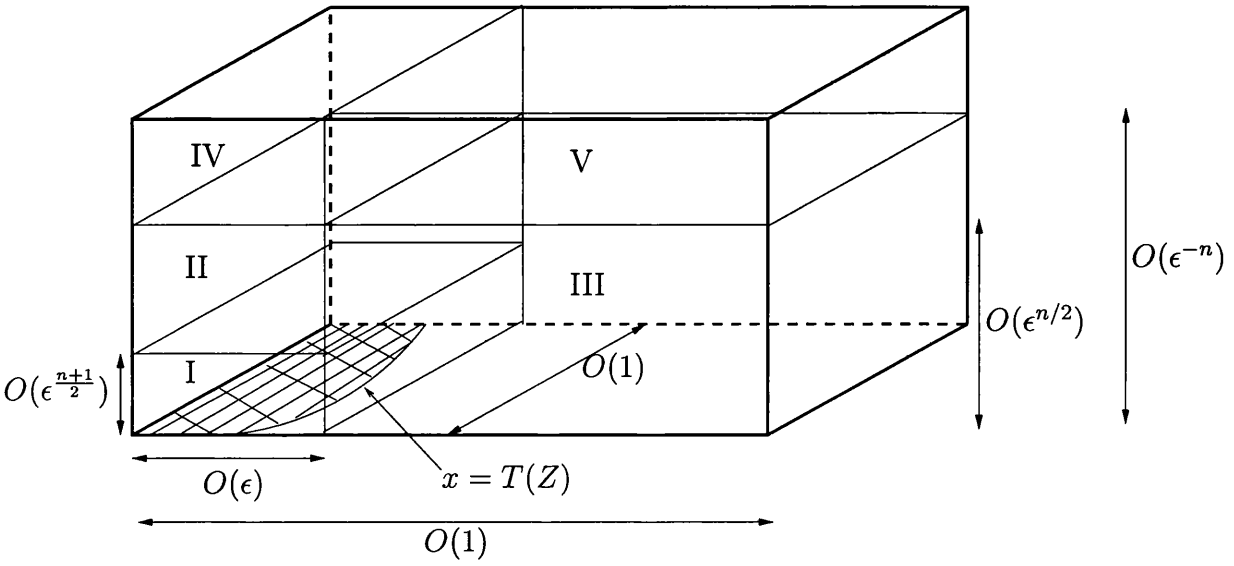

Figure 5.1: The proposed five region structure with the as yet undetermined y scales.

suggests the introduction of a normal coordinate η such that $y = (\frac{\epsilon X}{\sigma(z)\epsilon^{-n}})^{\frac{1}{2}}\eta$, where $\sigma(z)$ is the leading order scaled streamwise slip velocity at the blade/wake centre line in the outer regions IV and V. This implies a y scale of $O(\epsilon^{\frac{1+n}{2}})$ for the innermost region. To determine the final y-scale we note the Goldstein far wake spreads like $x^{1/2}$, so once the wake has reached the next leading edge $x = L$, then $X \sim O(\epsilon^{-1})$, implying $y \sim O(\epsilon^{\frac{1+n}{2}})O(\epsilon^{-\frac{1}{2}}) = \epsilon^{\frac{n}{2}}$ (the initial y-scale multiplied by the expected growth through the region).

We now consider each region in more detail.

5.3.1 Region I

In region I, the y-scalings discussed above suggest introducing the new normal coordinate Y, where $y = \epsilon^{\frac{n+1}{2}}Y$. We have the short x-scale given by X and z is $O(1)$

as it is throughout this section. The expected Blasius and Goldstein type responses in this region lead us to expect a viscous-inviscid balance between the $U\frac{\partial U}{\partial x}$ and $\frac{\partial^2 U}{\partial Y^2}$ terms in the streamwise momentum equation. This implies that the leading order U scale is given by ϵ^{-n} and the continuity equation then implies the leading order V scale and the velocities are expanded as

$$U = \epsilon^{-n} U_0(X, Y, z) + \ldots, \tag{5.28}$$

$$V = \epsilon^{-\frac{n+1}{2}} V_0(X, Y, z) + \ldots, \tag{5.29}$$

where neither W nor P, which are of $O(\epsilon^{(n+1)/2})$ and $O(\epsilon^{(1-n)/2})$ respectively, appear to leading order. These yield the leading order governing equations as

$$\frac{\partial U_0}{\partial X} + \frac{\partial V_0}{\partial Y} = 0, \tag{5.30}$$

$$U_0 \frac{\partial U_0}{\partial X} + V_0 \frac{\partial U_0}{\partial Y} = \frac{\partial^2 U_0}{\partial Y^2}, \tag{5.31}$$

subject to

$$U_0 \to \sigma(z) \quad \text{as} \quad Y \to \infty, \tag{5.32}$$

$$U_0 = V_0 = 0 \quad \text{on the blade}, \tag{5.33}$$

$$\frac{\partial U_0}{\partial Y} = V_0 = 0 \quad \text{in the wake}, \tag{5.34}$$

which are the match with region II and the usual no-slip and wake continuity conditions, respectively. The governing equations are quasi-two-dimensional with any z dependence being secondary. The solution on the blade is effectively the Blasius one given by

$$U_0 = \sigma(z) f_B'(\eta), \tag{5.35}$$

$$V_0 = \frac{1}{2}\sigma^{1/2} X^{-\frac{1}{2}} (\eta f_B'(\eta) - f_B(\eta)), \tag{5.36}$$

where the Blasius function $f_B(\eta)$ satisfies $f_B''' + \frac{1}{2} f_B f_B'' = 0$ and η is as defined above. (Details can be found in Appendix A.)

The solution in the wake, starting from the Goldstein near wake form at the trailing edge $x = T(z)$ and extending to the far-wake form at large X is given by

$$U_0 = \sigma(z)(1 - X^{-1/2} d e^{-\frac{\eta^2}{4}}), \tag{5.37}$$

$$V_0 = -\sigma^{\frac{1}{2}}(z) \frac{d}{2} X^{-1} \eta e^{-\frac{\eta^2}{4}}, \tag{5.38}$$

where $d = 2f_B''(0)$, and η is now given by

$$\eta = Y \sqrt{\frac{\sigma(z)}{X + q(z)}}, \tag{5.39}$$

due to the uncertainty in the trailing edge position. The varying position of the trailing edge causes this region to be quasi-two-dimensional, described by the quantity $q(z)$ in (5.39), as the switch from Blasius to Goldstein occurs at different X values as z is varied. This region also generates a viscous displacement thickness

$$\delta(X, z) = \sigma^{-\frac{1}{2}} X^{\frac{1}{2}} \int_0^\infty (1 - U_0(\eta)) \mathrm{d}\eta, \tag{5.40}$$

that is now z-dependent. It is $\delta(X, z)$ that transfers the three-dimensionality to the upper layers IV and V, with region IV also being quasi-two dimensional but region V being fully three-dimensional.

5.3.2 Region II

This region is effectively a passive buffer layer, passing displacements from the inner tier region I through to region IV. It is quasi-two-dimensional as it accommodates

the unknown disturbed wake profile which is z-dependent. The relevant x-scale is the short $O(\epsilon)$ one and the normal variable is given by $y = \epsilon^{n/2}\tilde{Y}$.

The velocities and pressure expand in a form guided by the expressions in the adjacent regions, namely

$$u = \epsilon^{-n}\sigma(z) + \epsilon^{n/2}\hat{u} + \ldots, \tag{5.41}$$

$$v = \epsilon^{-(n+1)/2}\sigma\frac{\partial\delta(X,z)}{\partial X} + \ldots, \tag{5.42}$$

$$w = O(\epsilon^{(n+1)/2}) \tag{5.43}$$

$$p = O(\epsilon^{(1-n)/2}), \tag{5.44}$$

where the leading order velocities are determined by substituting into the governing equations and applying the matching conditions

$$u \to \sigma(z) \quad \text{as} \quad \tilde{y} \to \infty, \tag{5.45}$$

$$v \to \sigma\frac{\partial\delta}{\partial X} \quad \text{as} \quad \tilde{y} \to 0, \tag{5.46}$$

from region IV and I respectively. The next order velocity $\hat{u}$ is determined in the next region below.

5.3.3 Region III

This longer region with the same y scale as region II arises from the spreading of the Goldstein far wake from region I to the next leading edge. The y coordinate is still $\tilde{Y}$ as in region II while we now have the $O(1)$ x-scale. On this scale the implied velocity and pressure expansions are given by

$$u = \epsilon^{-n}\sigma(z) + \epsilon^{n/2}\tilde{u}_1 + \ldots, \tag{5.47}$$

$$v = \epsilon^n \tilde{v}_1 + \ldots, \tag{5.48}$$

$$w = O(\epsilon^{(n+1)/2}), \tag{5.49}$$

$$p = \epsilon^{(1-n)/2} \tilde{p}_0. \tag{5.50}$$

The main governing equation is from the streamwise momentum balance leading to the diffusion equation

$$\sigma \frac{\partial \tilde{u}_1}{\partial x} = \frac{\partial^2 \tilde{u}_1}{\partial \tilde{Y}^2}. \tag{5.51}$$

This must be solved subject to the boundary conditions

$$\frac{\partial \tilde{u}_1}{\partial \tilde{Y}} = 0 \quad \text{at} \quad \tilde{Y} = 0, \tag{5.52}$$

$$\tilde{u}_1 \to \lambda_1(z)\tilde{Y} + \beta(z) \quad \text{as} \quad \tilde{Y} \to \infty, \tag{5.53}$$

$$\text{known starting profile at} \quad x = 0+, \tag{5.54}$$

$$L - \text{periodicity in} \quad x, \tag{5.55}$$

where (5.52) is required for wake symmetry, (5.54) is comprised of the far-wake form from region I and the unknown profile $\hat{u}(\tilde{Y}, z)$ from region II. Equation (5.55) requires that

$$\tilde{u}_1(x = L, \tilde{Y}, z) = \hat{u}(\tilde{Y}, z), \tag{5.56}$$

determining the unknown $\hat{u}$ from region II once $\tilde{u}_1$ is known.

If we integrate (5.51) with respect to $\tilde{Y}$ from 0 to ∞ we obtain

$$\sigma(z) \int_0^\infty \frac{\partial \tilde{u}}{\partial x} \mathrm{d}\tilde{Y} = \lambda_1(z), \tag{5.57}$$

where $\lambda_1(z) = \frac{\partial \tilde{u}}{\partial \tilde{Y}}(\tilde{Y} = \infty)$. Applying the continuity equation, this implies

$$\tilde{V}_1 \to -\frac{\lambda_1}{\sigma} \quad \text{as} \quad \tilde{Y} \to \infty. \tag{5.58}$$

In order to find the solution of $\tilde{u}_1$ we make the substitution

$$\tilde{u}_1 = x^{-1/2}G(\eta, z) + \lambda_1(z)\tilde{Y} + \beta(z) + \tilde{U} \tag{5.59}$$

which leaves $\tilde{U}$ satisfying the same governing equation (5.51) but now subject to the boundary conditions

$$\frac{\partial \tilde{U}}{\partial \tilde{Y}} = -\lambda_1(z) \quad \text{at} \quad \tilde{Y} = 0, \tag{5.60}$$

$$\tilde{U} \to 0 \quad \text{as} \quad \tilde{Y} \to \infty, \tag{5.61}$$

$$\tilde{U} \to g(\tilde{Y}, z) \quad \text{as} \quad x \to 0+, \tag{5.62}$$

$$L^{-1/2}G(\frac{\sigma^{1/2}\tilde{Y}}{L^{1/2}}, z) + \tilde{U}(L, \tilde{Y}, z) = g(\tilde{Y}, z) \quad \text{at} \quad x = L-, \tag{5.63}$$

where $G(\eta, z)$ is the z-dependent far wake form from equation (5.37) and $g(\tilde{Y}, z)(= \hat{\hat{u}} - \lambda_1(z)\tilde{Y} - \beta(z))$ is unknown. The solution of (5.51), (5.60) - (5.63) can be determined using the Fourier cosine transform in $\tilde{Y}$ defined here as

$$f^*(k) = \sqrt{\frac{2}{\pi}} \int_0^\infty f(\tilde{Y}) \cos(k\tilde{Y}) \mathrm{d}\tilde{Y}, \tag{5.64}$$

where * denotes the transformed quantity. Applying this transform to (5.51) we obtain

$$\sigma(z)\frac{\partial \tilde{U}^*}{\partial x} + k^2\tilde{U}^* = \lambda_1(z). \tag{5.65}$$

Solving this simple first order equation and applying the transform of the boundary condition (5.62) leads to the expression

$$\tilde{U}^* = \frac{\lambda_1(z)}{k^2} - (g^*(k, z) - \frac{\lambda_1(z)}{k^2})e^{-\frac{k^2 x}{\sigma}}, \tag{5.66}$$

for $\tilde{U}^*$. The constraint (5.63) then requires that

$$g* = \frac{L^{1/2}G^*}{1 - e^{-\frac{k^2 L}{\sigma}}} + \frac{\lambda_1}{k^2}. \tag{5.67}$$

Now from (5.37), $G = -\mu(z)e^{-\frac{\sigma^{1/2}}{L^{1/2}}\frac{\bar{Y}^2}{4}}$ which has a Fourier cosine transform given by Gradstein and Ryzhik (1965) as

$$G^* = -\bar{\mu}(z)e^{-\frac{k^2 L}{\sigma}}, \tag{5.68}$$

where $\bar{\mu} = \mu(\frac{2L}{\sigma})^{1/2}$. So performing the inverse transform gives

$$g(\tilde{Y}, z) = (\frac{2}{\pi})^{1/2} \int_0^\infty (\frac{-L^{1/2}\bar{\mu}(z)e^{-\frac{k^2 L}{\sigma}}}{1 - e^{-\frac{k^2 L}{\sigma}}} + \frac{\lambda_1}{k^2}) \cos(k\tilde{Y})\mathrm{d}k. \tag{5.69}$$

However, in order for the inverse transform to converge at $k = 0$, we also require that $\lambda_1(z) = -G^*(0, z)$. Thus, finally we obtain the well-behaved form for $g(\tilde{Y}, z)$:

$$g(\tilde{Y}, z) = -\frac{2L^{1/2}\mu}{\pi\sigma^{1/2}} \int_0^\infty (\frac{1}{e^{-k^2 L} - 1} - \frac{1}{k^2})e^{-\frac{k^2 L}{\sigma}} \cos(k\tilde{Y})\mathrm{d}k, \tag{5.70}$$

giving $\hat{\tilde{u}}$ as discussed above. The solution for $\tilde{U}$ then follows by applying the inverse transform to (5.66) with g now known.

5.3.4 Region IV

We are looking here at the short X-scale and the largest normal scale $y = \epsilon^{-n}\bar{Y}$. The velocities and pressure are expanded as follows, guided by the properties of regions I and II and guessing the size of the pressure to be such that the pressure gradient is comparable here with the leading order advective terms. Therefore we write

$$u = \epsilon^{-n}\bar{U}_0(\bar{Y}, z) + \epsilon^{(n+1)/2}\bar{U}_1(X, \bar{Y}, z) + \ldots, \tag{5.71}$$

$$v = \epsilon^{-(n+1)/2}\bar{V}_0(X, \bar{Y}, z) + \ldots, \tag{5.72}$$

$$w = \epsilon^{(n+1)/2}\bar{W}_1(\bar{Y}, z) + \ldots, \tag{5.73}$$

$$p = \epsilon^{(1-n)/2}\bar{P}_0(X, z) + \ldots. \tag{5.74}$$

Both $\bar{U}_0$ and $\bar{W}_1$ turn out to be arbitrary but with $\bar{U}_0(0,z) = \sigma(z)$. Substituting into the governing equations we find the leading order equations as

$$\frac{\partial \bar{U}_1}{\partial X} + \frac{\partial \bar{V}_0}{\partial \bar{Y}} = 0, \tag{5.75}$$

$$\bar{U}_0 \frac{\partial \bar{U}_1}{\partial X} + \bar{V}_0 \frac{\partial \bar{U}_0}{\partial \bar{Y}} = -\frac{\partial \bar{P}_0}{\partial X}. \tag{5.76}$$

Matching with region II yields the boundary condition

$$\bar{V}_0(X,0,z) = \sigma \frac{\partial \delta(X,z)}{\partial X}. \tag{5.77}$$

The three-dimensionality in $\delta(X,z)$ causes this region, similarly to region I, to be quasi-two-dimensional. Combining equations (5.75) and (5.76) and using the boundary condition (5.77) leads to the following equation for the pressure gradient:

$$\frac{\partial \bar{P}_0}{\partial X} = \frac{-\frac{\partial \delta}{\partial X}}{\int_0^\infty \frac{1}{\bar{U}_0^2} \mathrm{d}\bar{Y}}. \tag{5.78}$$

A straightforward integration then determines the total pressure change through the region as

$$\bar{P}_0(\infty,z) - \bar{P}_0(0,z) = \frac{-\delta(\infty,z)}{I(z)}, \tag{5.79}$$

where

$$I(z) = \int_0^\infty \frac{1}{\bar{U}_0^2} \mathrm{d}\bar{Y}, \tag{5.80}$$

as $\delta(\infty,z)$ is $O(1)$ and $\delta(0,z) = 0$.

5.3.5 Region V

In this region we return once again to the original streamwise variable x while the normal variable is that of region IV, namely $\bar{Y}$. In order to balance the viscous term

and the pressure gradient with the leading order advective terms, we expand the velocities and pressure in this region as

$$u = \epsilon^{-n}\hat{U}_0(\bar{Y},z) + \epsilon^{2n}\hat{U}_1(x,\bar{Y},z) + \ldots, \tag{5.81}$$

$$v = \epsilon^{n}\hat{V}_0(\bar{Y},z) + \ldots, \tag{5.82}$$

$$w = \epsilon^{2n}\hat{W}_1(x,\bar{Y},z) + \ldots, \tag{5.83}$$

$$p = \epsilon^{n}\hat{P}_0(x,z) + \ldots \tag{5.84}$$

The leading order streamwise velocity $\hat{U}_0(\equiv \bar{U}_0)$ is still arbitrary but must satisfy $\bar{U}_0 \sim \bar{Y} + c_0(z)$, where $c(z) = \epsilon^{-n}c_0(z) + \ldots$, as $\bar{Y} \to \infty$, in view of (5.27) and match with region III at $\bar{Y} = 0$. Likewise $\hat{W}_1$ is arbitrary but must match with the adjoining regions and satisfy (5.21). These expansions lead, once substituted into equations (5.15) - (5.17), to the linear viscous equations

$$\frac{\partial \hat{U}_1}{\partial x} + \frac{\partial \hat{V}_0}{\partial \bar{Y}} + \frac{\partial \hat{W}_1}{\partial z} = 0, \tag{5.85}$$

$$\hat{U}_0\frac{\partial \hat{U}_1}{\partial x} + \hat{V}_0\frac{\partial \hat{U}_0}{\partial \bar{Y}} + \hat{W}_1\frac{\partial \hat{U}_0}{\partial z} = -\frac{\partial \hat{P}_0}{\partial x} + \frac{\partial^2 \hat{U}_0}{\partial \bar{Y}^2}, \tag{5.86}$$

$$\hat{U}_0\frac{\partial \hat{W}_1}{\partial x} = -\frac{\partial \hat{P}}{\partial z}, \tag{5.87}$$

for the leading order velocity and pressure terms.

Substituting (5.85) into (5.86) and rearranging gives

$$-\hat{U}_0^2\frac{\partial}{\partial \bar{Y}}(\frac{\hat{V}_0}{\hat{U}_0}) = -\frac{\partial \hat{P}_0}{\partial x} + \frac{\partial^2 \hat{U}_0}{\partial \bar{Y}^2} + \hat{U}_0^2\frac{\partial}{\partial \bar{z}}(\frac{\hat{W}_1}{\hat{U}_0}). \tag{5.88}$$

This yields, on integration with respect to $\bar{Y}$,

$$\hat{V}_0 = \hat{U}_0[\frac{\partial \hat{P}_0}{\partial x}\int_0^{\bar{Y}} \frac{1}{\hat{U}_0^2}\mathrm{d}\bar{Y} - \int_0^{\bar{Y}} \frac{\frac{\partial^2 \bar{U}_0}{\partial \bar{Y}^2}}{\hat{U}_0^2}\mathrm{d}\bar{Y} - \int_0^{\bar{Y}} \frac{\partial}{\partial \bar{z}}(\frac{\hat{W}_1}{\hat{U}_0})\mathrm{d}\bar{Y} + B_0(z)] \tag{5.89}$$

for the normal velocity and

$$\frac{\partial \hat{P}_0}{\partial x} = \frac{1}{I}\int_0^\infty \frac{\frac{\partial^2 \bar{U}_0}{\partial \bar{Y}^2}}{\hat{U}_0^2} \mathrm{d}\bar{Y} + \frac{1}{I}\int_0^\infty \frac{\partial}{\partial \bar{z}}\left(\frac{\hat{W}_1}{\hat{U}_0}\right)\mathrm{d}\bar{Y} - \frac{B_0(z)}{I} \tag{5.90}$$

for the pressure, where $I(z)$ is as defined above. The function $B_0(z) = -\frac{\lambda_1(z)}{\sigma^2(z)}$ is required in order to match with region III as discussed in 5.3.3.

However we can now make use of the pressure periodicity to fix the unknown index n. We know, in order for the pressure to be periodic, that the sum of the pressure change in this region and the pressure change in region IV must be zero, hence we can write

$$\epsilon^n(\hat{P}_0(L,z) - \hat{P}_0(0,z)) = \epsilon^{(1-n)/2}\frac{\delta(\infty,z)}{I}, \tag{5.91}$$

and the unknown scale n is determined by the requirement

$$n = \frac{1-n}{2}, \tag{5.92}$$

implying $n = 1/3$, and also

$$\hat{P}_0(L,z) - \hat{P}_0(0,z) = \frac{\delta(\infty,z)}{I}. \tag{5.93}$$

If we now differentiate (5.90) with respect to x we obtain

$$\frac{\partial^2 \hat{P}_0}{\partial x^2} = \frac{1}{I}\int_0^\infty \frac{\partial}{\partial z}\left(\frac{\frac{\partial \hat{W}_1}{\partial x}}{\hat{U}_0}\right)\mathrm{d}\bar{Y}. \tag{5.94}$$

Substituting for $\hat{W}_1$ from equation (5.87) and carrying out the z differentiation inside the integral gives us

$$\frac{\partial^2 \hat{P}_0}{\partial x^2} = \frac{1}{I}\int_0^\infty \left(\frac{\frac{\partial^2 \hat{P}_0}{\partial z^2}}{\hat{U}_0} - 2\frac{\partial \hat{P}_0}{\partial z}\frac{\frac{\partial \hat{U}_0}{\partial z}}{\hat{U}_0^3}\right)\mathrm{d}\bar{Y}, \tag{5.95}$$

leading to the governing equation for $\hat{P}_0$

$$\frac{\partial^2 \hat{P}_0}{\partial x^2} + \frac{\partial^2 \hat{P}_0}{\partial z^2} - J(z)\frac{\partial \hat{P}_0}{\partial z} = 0, \tag{5.96}$$

where

$$J(z) = \frac{2}{I}\int_0^\infty \frac{\frac{\partial \hat{U}_0}{\partial z}\mathrm{d}\bar{Y}}{\hat{U}_0^3}. \tag{5.97}$$

So the pressure in this region must satisfy the governing equation (5.96), subject to the constraint (5.90) and the known pressure change through this region given by (5.93). To simplify the problem somewhat we introduce a new quantity Q, where

$$\frac{\partial Q}{\partial x} = \hat{P}_0. \tag{5.98}$$

Following through the same analysis as above we arrive at the following problem for Q:

$$\frac{\partial^2 Q}{\partial x^2} + \frac{\partial^2 Q}{\partial z^2} - J(z)\frac{\partial Q}{\partial z} = K(z), \tag{5.99}$$

where $J(z)$ is as before and

$$K(z) = \frac{1}{I}\int_0^\infty \frac{\frac{\partial^2 \hat{U}_0}{\partial \bar{Y}^2}}{\hat{U}_0^2}\mathrm{d}\bar{Y} - \frac{B_0}{I}. \tag{5.100}$$

This must be solved subject to the single condition

$$\frac{\partial Q}{\partial x}(L,z) - \frac{\partial Q}{\partial x}(0,z) = \frac{\delta(\infty,z)}{I}. \tag{5.101}$$

Unfortunately, due to the arbitrariness of $\hat{U}_0$ in this region completely determining Q, and consequently the pressure, is difficult. However, as an attempt to shed some light on the pressure solution we consider a few possible cases here. We will concentrate on the case of periodicity in z but the essentials should carry over to other relevant cases. Thus we also require

$$\frac{\partial Q}{\partial x} \quad \text{to be } L_1\text{-periodic in } Z, \tag{5.102}$$

in the analysis that follows.

Firstly, if we assume that the z-scale is considerable longer than the x-scale, taking $L_1 \gg L$, we write $z = L_1 Z$ and expand the quantities in (5.99) - (5.101) as

$$Q(x,Z) = Q_0(x) + \frac{1}{L_1}Q_1(x,Z) + \ldots, \tag{5.103}$$

$$K(Z) = K_0(Z) + \frac{1}{L_1}K_1(Z) + \ldots, \tag{5.104}$$

$$J(Z) = \frac{1}{L_1}J_1(Z) + \ldots, \tag{5.105}$$

$$\frac{\delta(\infty,Z)}{I} = \delta_0(Z) + \frac{1}{L_1}\delta_1(Z) + \ldots. \tag{5.106}$$

Substituting into (5.99) gives the leading order governing equation as

$$\frac{\partial^2 Q_0}{\partial x^2} = K_0(Z), \tag{5.107}$$

subject to

$$\frac{\partial Q_0}{\partial x}(L,Z) - \frac{\partial Q_0}{\partial x}(0,Z) = \delta_0(Z). \tag{5.108}$$

A simple integration of (5.107) and application of (5.108) gives Q_0 as

$$Q_0 = \frac{\delta_0(Z)x^2}{2L} + G(Z)x + H(Z), \tag{5.109}$$

where G and H are arbitrary functions of the integration. Finally this determines the leading order pressure as

$$\hat{P}_0 = \frac{\delta_0(Z)x}{L} + G(Z), \tag{5.110}$$

to within an arbitrary function of Z. The pressure is quasi-two dimensional and is identically the solution, as one might expect given the far longer z-scale, for the two dimensional case discussed in Bowles and Smith (2000a) with the pressure growing linearly through the present region. So from our analysis we can recover the two-dimensional case considered previously.

If we consider the opposite extreme with the z-scale being shorter than the x-scale, $L_1 \ll L$, we write $x = L\tilde{X}$ and, to leading order, the $\frac{\partial^2 Q}{\partial x^2}$ term does not appear in the governing equation leaving the leading order problem as

$$\frac{\partial^2 Q}{\partial z^2} - J(z)\frac{\partial Q}{\partial z} = K(z). \tag{5.111}$$

Rearranging and using an integrating factor leads to

$$\frac{\partial}{\partial z}\left(\frac{\partial Q}{\partial z} e^{-\int^z J(z)\mathrm{d}z}\right) = K(z) e^{-\int^z J(z)\mathrm{d}z}. \tag{5.112}$$

Integrating this twice with respect to z leads to

$$Q = \int^z e^{\int^z J(z_2)\mathrm{d}z_2}\left[\int^z K(z_1) e^{-\int^{z_1} J(z_2)\mathrm{d}z_2}\mathrm{d}z_1 + A\right]\mathrm{d}z \tag{5.113}$$

where A is a constant of integration. This expression for Q cannot satisfy the required pressure change through the region as it is not dependent on x. The explanation is believed to be that the pressure growth required in region V therefore does not happen on this length scale, rather it happens over a shorter x-scale given by $x = L_1\tilde{X}$ with $z = L_1\tilde{Z}$, reinstating the entire governing equation.

We now consider the x and z scales being comparable but assuming that the forcing term $J(z)$ is small. This reduces the governing equation to

$$\frac{\partial^2 Q}{\partial x^2} + \frac{\partial^2 Q}{\partial z^2} = K(z), \tag{5.114}$$

to leading order. This has the general solution

$$Q = (Ae^{\lambda x} + Be^{-\lambda x})\cos(\lambda z + \beta) + \hat{K} \tag{5.115}$$

where $\hat{K}(z)$ is a particular integral of $K(z)$ such that (5.114) is satisfied, i.e. $\frac{\partial^2 \hat{K}}{\partial z^2} = K(z)$. Periodicity in z, equation (5.102), requires

$$\lambda = \frac{2m\pi}{L_1} \quad \text{for} \quad m = 0, 1, 2, \ldots, \tag{5.116}$$

and the known change in $\frac{\partial Q}{\partial x}$, (5.101) requires that

$$\sum_{n=0}^{\infty} \lambda(A_m e^{\lambda L} - B_m e^{-\lambda L} - A_m + B_m)\cos(\lambda z + \beta) = \frac{\delta(z)}{I}. \tag{5.117}$$

This in turn gives a relation for A_m and B_m,

$$\lambda[A_m(e^{\lambda L} - 1) - B_m(e^{-\lambda L} - 1)] = \frac{2}{L_1 \lambda}\int_0^{L_1} \frac{\delta(z)}{I}\cos(\lambda z + \beta)\mathrm{d}z. \tag{5.118}$$

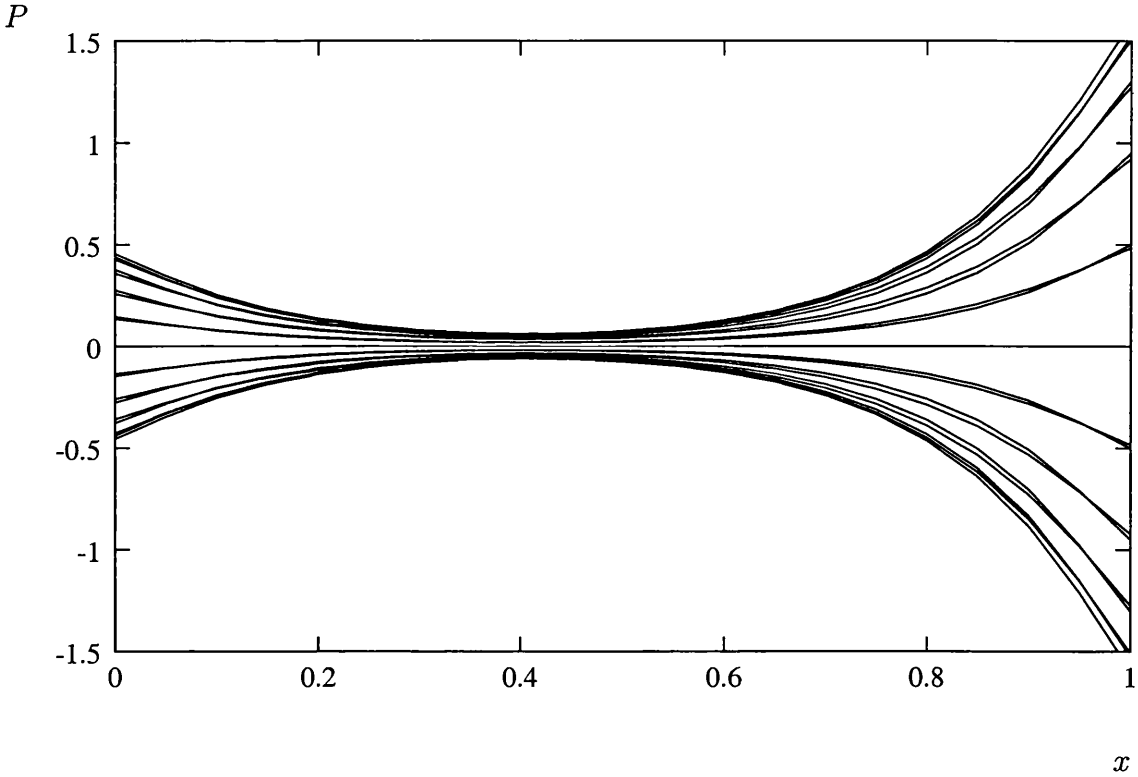

Figure 5.2: A sample pressure solution, varying in x for various z values, with $L_1 = 1$, $L = 1$ with $J = \sin(\frac{2\pi z}{L_1})$, $K = \cos(\frac{2\pi z}{L_1})$, $\delta = \sin(\frac{2\pi z}{L_1})$

We can also, assuming possible forms for $J(z)$, $K(z)$ and $\delta(\infty, z)$, attempt to solve (5.99) numerically. This was done by introducing an artificial $\frac{\partial Q}{\partial t}$ term into the governing equation and then, using a simple finite difference approximation, iterating

until a steady state was reached, i.e. $\frac{\partial Q}{\partial t} \equiv 0$, giving the desired Q profile. Presented in figures 5.2 and 5.3 are some P solutions for given J, K and δ profiles, varying the $L : L_1$ ratio as a check on some of the analysis above.

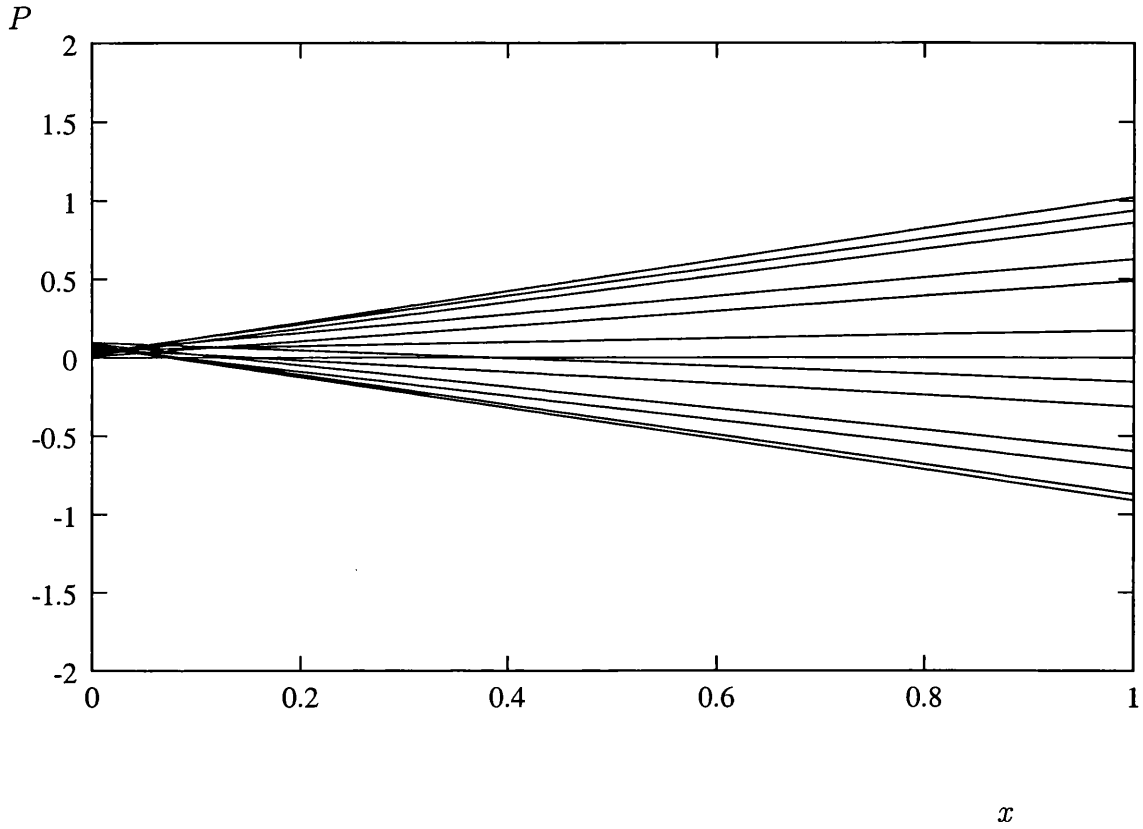

Figure 5.3: A sample pressure solution, varying in x for various z values, with $L_1 = 20$, $L = 1$ with J, K, δ as in figure 5.2. Note the pressure solution is nearly linear as suggested in the analysis in the text.

Chapter 6

Three-Dimensional Boundary-Layer Flow over a Hump; and Past a Trailing Corner

6.1 Introduction

This chapter considers two significant aspects of the flow structure of a rotor blade system. Firstly we consider the flow past a surface roughness and then, using the solution for the hump as guidance, propose a possible structure for the flow past a trailing corner (or blade tip).

For the hump flow, we consider a small hump embedded deep within the boundary layer. The major difference between this and previous investigations of three-dimensional hump flows, Smith *et al* (1977) for example, is that, rather than the flow approaching the hump being two-dimensional, here the on-coming profile is

three-dimensional also. The reason in the context of the present thesis is that the boundary layer induced by a rotor blade is comprised of a Blasius-type flow, from the flow past many blades in the azimuthal direction, and a radial jet, generated by the rotation as in the Von Karman solution. Outside the boundary layer, taking the coordinates to be rotating with the blade and there to be no external stream, the flow is only in the azimuthal direction to leading order with the other quantities being small perturbations of this free stream. Therefore in order to investigate the flow past a surface roughness in the current rotor blade regime we must take the approaching boundary layer to be of this three-dimensional form.

The trailing corner problem is also important but is difficult to formulate directly. The flow structure on the two trailing edges, away from the corner, is known (see figure 6.1). On the trailing edge perpendicular to the outer motion the Blasius-type flow dominates and we effectively find the traditional two-dimensional triple-deck problem. However on the other trailing edge, perpendicular to the jet, we find the radial flow becoming dominant and we obtain the double-deck structure of Smith and Duck (1977). See also figure 6.1. These two structures must match or combine at the trailing corner but the two effects happen on different streamwise scales with the triple-deck occuring at $O(Re^{-3/8})$ while the double deck structure has a scale of $O(Re^{-3/7})$. So direct matching is not possible and how the two fit together is not explicitly clear. However, using the analysis from the hump problem below, we are able tentatively to propose a possible structure.

The starting point is, as in chapter 5, the three-dimensional, non-dimensionalised, Navier- Stokes equations (5.1) - (5.4). In section 6.2 below, we consider the hump flow problem, describing the three-dimensional boundary layer, and set out the

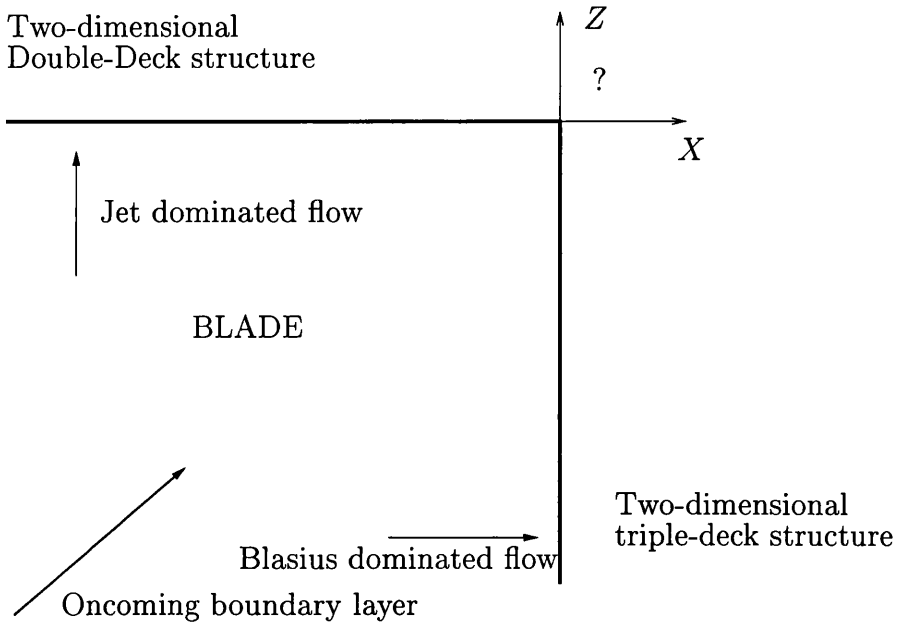

Figure 6.1: Sketch in planform of the trailing corner problem, illustrating the double- and triple- deck regions away from the corner and the unknown matching as the trailing corner is approached.

flow structure in this regime. In section 6.3 we examine the linearised problem, using the Fourier transform to determine the transformed solution for the pressure, displacement and velocities. In section 6.4 we seek to invert these transformed solutions using both a numerical Fast-Fourier Transform and certain asymptotic analysis; this reveals two corridor effects in the displacement: one aligned with the flow in the boundary layer and the other aligned with the outer free stream, a phenomenon confirmed by both approaches. In section 6.5, we investigate the influence of the double deck type structure in the context of the hump flow problem which, although the jet effect is secondary in this hump case, becomes important in the trailing corner context as the match between the two interactions is not obvious. Finally, in section 6.6, we explore a proposed formulation for the trailing corner problem, addressing the match between the triple-deck and double deck structures, based upon the findings of the jet effect analysis.

6.2 Problem formulation

The set-up of this hump flow problem is that of a three-dimensional hump embedded deep inside the boundary layer. The motion far upstream of the hump consists of a three-dimensional boundary layer, with classical thickness $O(Re^{-1/2})$ in non-dimensional terms. The boundary layer is, as discussed above, assumed to be a combination of a Blasius-like boundary layer (taken to be in the x direction), induced by the flow passing over many blades, and a Von Karman type jet (in the z direction) triggered by the rotation of the entire rotor blade. See figure 6.2 for a sketch of the assumed velocity profiles. Outside of the boundary layer the flow is essentially

uniform with $u = 1$, $v = w = p = 0$ to leading order.

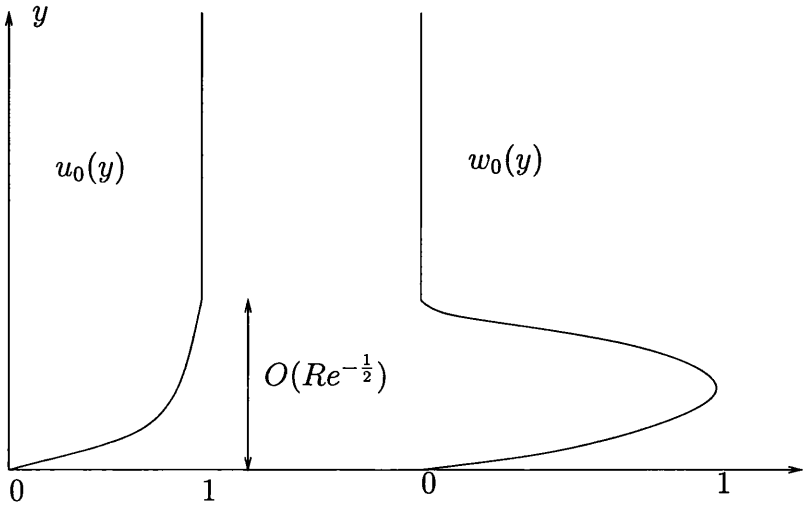

Figure 6.2: Sketches of the assumed oncoming velocity profiles u_0 and w_0, which are of Blasius and Von Karman types, respectively.

The structure of the flow over the hump is of a three-dimensional triple-deck form. We explore each of the three decks in turn here. It is this, rather than the double deck structure, that dominates as the triple-deck quantities (velocities, pressure and y-scales) are larger and so the double-deck, or jet, effect is not significant to leading order. As discussed below in 6.5 the jet effect can be observed but only at large distances in x, with z remaining small; otherwise its impact is negligible. The hump, as shown in figure 6.3, is assumed to have dimensions of $O(\epsilon^3)$ in the x and z directions and to be of height $O(\epsilon^5)$, where $\epsilon = Re^{-1/8}$ has been introduced for convenience. As such we introduce the new scales X and Z defined to be $x = \epsilon^3 X$ and $z = \epsilon^3 Z$, respectively. The y-scales of the three decks are, as usual, given by $y \sim O(\epsilon^4)$ in the main deck, $y \sim O(\epsilon^3)$ in the upper, inviscid deck and $y \sim O(\epsilon^5)$ in the lower deck.

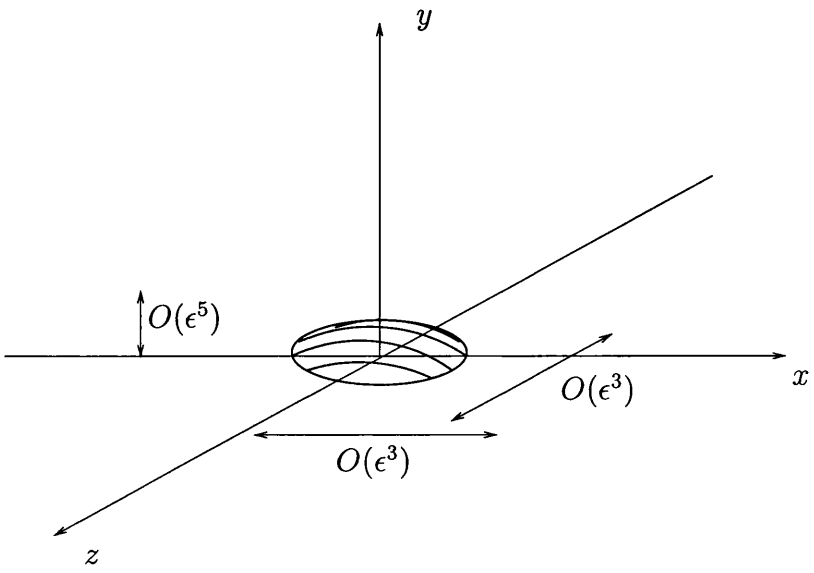

Figure 6.3: Sketch of the hump showing the length scales discussed in the text.

6.2.1 Main deck

In this deck, containing the bulk of the boundary layer flow, we introduce a new normal scale $\bar{y}$ given by $y = \epsilon^4 \bar{y}$, with ϵ as defined above. The velocities and pressure are given by

$$u = u_0(\bar{y}) + \epsilon A(X,Z)u_0' + \ldots, \tag{6.1}$$

$$v = \epsilon^2(-u_0\frac{\partial A}{\partial X} - w_0\frac{\partial A}{\partial Z}) + \ldots, \tag{6.2}$$

$$w = w_0(\bar{y}) + \epsilon A(X,Z)w_0' + \ldots, \tag{6.3}$$

$$p = \epsilon^2 P(X,Z) + \ldots, \tag{6.4}$$

to leading order, where $A(X,Z)$ is an unknown displacement function. These can be easily verified as providing a valid flow solution by substituting into the governing Navier-Stokes equations. The leading order velocities u_0 and w_0 describe oncoming three-dimensional boundary-layer flow as discussed above and shown in figure 6.2.

In order to match with the outer uniform flow these must satisfy

$$u_0(\bar{y}) \to 1, w_0(\bar{y}) \to 0, \quad \text{as} \quad \bar{y} \to \infty, \tag{6.5}$$

and it follows from (6.2) that

$$v \to -\frac{\partial A}{\partial X} \quad \text{as} \quad \bar{y} \to \infty. \tag{6.6}$$

This deck is, as usual in a triple deck problem, passively transferring displacement effects from the viscous sublayer, the lower deck, through to the inviscid upper deck and in turn determining the pressure-displacement law as discussed below.

6.2.2 Upper deck

In this upper region the y-scale is given by $y = \epsilon^3 \tilde{y}$. The velocities and pressure are expanded here as

$$(u, v, w, p) = (1 + \epsilon^2 \tilde{u}, \epsilon^2 \tilde{v}, \epsilon^2 \tilde{w}, \epsilon^2 \tilde{p}) + \ldots, \tag{6.7}$$

which corresponds to a small $O(Re^{-2/8})$ perturbation of the free stream driven by matching with the main deck via equation (6.6). The governing equations become, on substitution of (6.7) into the Navier-Stokes equations, the three-dimensional linearised Euler ones, namely

$$\frac{\partial \tilde{u}}{\partial X} + \frac{\partial \tilde{v}}{\partial \tilde{y}} + \frac{\partial \tilde{w}}{\partial Z} = 0, \tag{6.8}$$

$$\frac{\partial \tilde{u}}{\partial X} = -\frac{\partial \tilde{p}}{\partial X}, \tag{6.9}$$

$$\frac{\partial \tilde{v}}{\partial X} = -\frac{\partial \tilde{p}}{\partial \tilde{y}}, \tag{6.10}$$

$$\frac{\partial \tilde{w}}{\partial X} = -\frac{\partial \tilde{p}}{\partial Z}, \tag{6.11}$$

subject to

$$\tilde{v} \to -\frac{\partial A}{\partial X} \quad \text{as} \quad \tilde{y} \to 0, \tag{6.12}$$

from matching with the main deck, equation (6.6). We also require that the perturbation quantities are suitably bounded in the far-field. Also, in order to match with the main deck,

$$\tilde{p} \to P(X, Z) \quad \text{as} \quad \tilde{y} \to 0. \tag{6.13}$$

These governing equations, (6.8) - (6.11), yield Laplace's equation for $\tilde{p}$. This problem, as in Smith *et al* (1977) and chapter 5, leads to the relation

$$P(X, Z) = -\frac{1}{2\pi} \int_{-\infty}^{\infty} \int_{-\infty}^{\infty} \frac{\frac{\partial^2 A}{\partial \xi^2} \mathrm{d}\xi \mathrm{d}\eta}{[(X-\xi)^2 + (Z-\eta)^2]^{\frac{1}{2}}}, \tag{6.14}$$

the pressure-displacement interaction law.

Later, in 6.5, we consider the relation between the triple deck interaction law derived above and the double deck interaction law where $P = -\frac{\partial^2 A}{\partial Z^2}$ is the pressure-displacement relation, the derivation of which is discussed in Smith and Duck (1977) and Smith (1978). The pressure in the double deck problem is $O(Re^{-2/7})$ however (compared to $P \sim O(Re^{-2/8})$ in the present structure) and so is secondary to leading order.

6.2.3 Lower deck

In this innermost layer we introduce the normal scale $y = \epsilon^5 Y$. We expand the leading order quantities as

$$(u, v, w, p) = (\epsilon U, \epsilon^3 V, \epsilon W, \epsilon^2 P) + \ldots, \tag{6.15}$$

and substitute into the Navier-Stokes equation to give the leading order problem in this region as the boundary-layer equations

$$\frac{\partial U}{\partial X}+\frac{\partial V}{\partial Y}+\frac{\partial W}{\partial Z} = 0, \tag{6.16}$$

$$U\frac{\partial U}{\partial X}+V\frac{\partial U}{\partial Y}+W\frac{\partial U}{\partial Z} = -\frac{\partial P}{\partial X}+\frac{\partial^2 U}{\partial Y^2}, \tag{6.17}$$

$$U\frac{\partial W}{\partial X}+V\frac{\partial W}{\partial Y}+W\frac{\partial W}{\partial Z} = -\frac{\partial P}{\partial Z}+\frac{\partial^2 W}{\partial Y^2}. \tag{6.18}$$

These are to be solved subject to the requirements

$$U = V = W = 0 \quad \text{on} \quad Y = hf(X,Z), \tag{6.19}$$

$$U \to \lambda_1(Y + A(X,Z)) \quad \text{as} \quad Y \sim \infty, \tag{6.20}$$

$$W \to \lambda_2(Y + A(X,Z)) \quad \text{as} \quad Y \sim \infty, \tag{6.21}$$

$$A(X,Z) \to 0 \quad \text{as} \quad X \to -\infty, Z \to -\infty, \tag{6.22}$$

which are the no-slip conditions on the solid surface and hump which is described by $y = hf(X,Z)$ where h is a constant, two conditions from matching U and W between here and the main deck, and finally zero-disturbance far upstream of the hump, respectively. The constants λ_1, λ_2 are the magnitudes of the shear flows in the streamwise and spanwise directions, respectively.

6.3 The linearised problem and its solution

One useful aspect of addressing this hump problem, equations (6.16) - (6.22) and (6.14), is that it admits a linear solution. If we consider the problem with the height of the hump h being small, the velocities and pressures expand as

$$(U,V,W,P,A) = (\lambda_1 Y, 0, \lambda_2 Y, 0, 0) + h(\bar{u},\bar{v},\bar{w},\bar{p},\bar{A}) + \ldots, \tag{6.23}$$

and the governing equations become

$$\frac{\partial \bar{u}}{\partial X} + \frac{\partial \bar{v}}{\partial Y} + \frac{\partial \bar{w}}{\partial Z} = 0, \tag{6.24}$$

$$\lambda_1 Y \frac{\partial \bar{u}}{\partial X} + \lambda_2 Y \frac{\partial \bar{u}}{\partial Z} + \lambda_1 \bar{v} = -\frac{\partial \bar{p}}{\partial X} + \frac{\partial^2 \bar{u}}{\partial Y^2}, \tag{6.25}$$

$$\lambda_1 Y \frac{\partial \bar{w}}{\partial X} + \lambda_2 Y \frac{\partial \bar{w}}{\partial Z} + \lambda_2 \bar{v} = -\frac{\partial \bar{p}}{\partial Z} + \frac{\partial^2 \bar{w}}{\partial Y^2}, \tag{6.26}$$

now subject to

$$\bar{u} = -\lambda_1 f \quad \text{at} \quad Y = 0, \tag{6.27}$$

$$\bar{w} = -\lambda_2 f \quad \text{at} \quad Y = 0, \tag{6.28}$$

$$\bar{v} = 0 \quad \text{at} \quad Y = 0, \tag{6.29}$$

$$\bar{u} \to \lambda_1 \bar{A} \quad \text{as} \quad Y \to \infty, \tag{6.30}$$

$$\bar{v} \to \lambda_2 \bar{A} \quad \text{as} \quad Y \to \infty, \tag{6.31}$$

where (6.27) and (6.28) are from a Taylor expansion of (6.20) and (6.21), respectively, and the others follow straightforwardly from (6.23).

In order to solve this problem we make use of the double Fourier Transform defined here as

$$F^{**}(k, Y, l) = \int_{-\infty}^{\infty} \int_{-\infty}^{\infty} e^{-ikX - ilZ} F(X, Y, Z) \mathrm{d}X \mathrm{d}Z, \tag{6.32}$$

for any F, where ** denotes the transformed quantities. Applying this transform to the governing equations (6.24) - (6.26) gives

$$ik\bar{u}^{**} + \frac{\partial \bar{v}}{\partial Y}^{**} + il\bar{w}^{**} = 0, \tag{6.33}$$

$$iY(\lambda_1 k + \lambda_2 l)\bar{u}^{**} + \lambda_1 \bar{v}^{**} = -ik\bar{p}^{**} + \frac{\partial^2 \bar{u}}{\partial Y^2}^{**}, \tag{6.34}$$

$$iY(\lambda_1 k + \lambda_2 l)\bar{w}^{**} + \lambda_2 \bar{v}^{**} = -il\bar{p}^{**} + \frac{\partial^2 \bar{w}}{\partial Y^2}^{**}. \tag{6.35}$$

The transform of the pressure-displacement law (6.14) is given by

$$(k^2+l^2)^{1/2}\bar{p}^{**} = k^2\bar{A}^{**}. \tag{6.36}$$

The boundary conditions become, on applying the transform,

$$\bar{u}^{**} = -\lambda_1 f^{**} \quad \text{at} \quad Y=0, \tag{6.37}$$

$$\bar{w}^{**} = -\lambda_2 f^{**} \quad \text{at} \quad Y=0, \tag{6.38}$$

$$\bar{v}^{**} = 0 \quad \text{at} \quad Y=0, \tag{6.39}$$

$$\bar{u}^{**} \to \lambda_1\bar{A}^{**} \quad \text{as} \quad Y\to\infty, \tag{6.40}$$

$$\bar{w}^{**} \to \lambda_2\bar{A}^{**} \quad \text{as} \quad Y\to\infty. \tag{6.41}$$

In order to solve this problem we introduce four new quantities, γ, τ, μ and η where

$$\gamma = \lambda_2\bar{u}^{**} - \lambda_1\bar{w}^{**}, \tag{6.42}$$

$$\tau = \lambda_1\bar{u}^{**} + \lambda_2\bar{w}^{**}, \tag{6.43}$$

$$\mu = \lambda_1 k + \lambda_2 l, \tag{6.44}$$

$$\eta = \lambda_2 k - \lambda_1 l, \tag{6.45}$$

where μ and η are co-ordinates skewed along and normal to the direction of the flow in the main deck, respectively, and γ and τ are the velocities in those directions.

Considering two linear combinations of equations (6.34) and (6.35) in order to eliminate first τ and the γ, we obtain the governing equations in terms of our new quantities, namely

$$\frac{i}{(\lambda_1^2+\lambda_2^2)}[\mu\tau+\eta\gamma] + \frac{\partial\bar{v}^{*}*}{\partial Y} = 0, \tag{6.46}$$

$$i\mu Y\gamma = -i\eta\bar{p}^{**} + \frac{\partial^2\gamma}{\partial Y^2}, \tag{6.47}$$

$$i\mu Y\tau + (\lambda_1^2+\lambda_2^2)\bar{v}^{**} = -i\mu\bar{p}^{**} + \frac{\partial^2\tau}{\partial Y^2}. \tag{6.48}$$

Similar treatment of the boundary conditions lead to the new constraints

$$\tau = -(\lambda_1^2 + \lambda_2^2) f^{**} \quad \text{at} \quad Y = 0, \tag{6.49}$$

$$\gamma = 0 \quad \text{at} \quad Y = 0, \tag{6.50}$$

$$\tau \to (\lambda_1^2 + \lambda_2^2) \bar{A}^{**} \quad \text{as} \quad Y \to \infty, \tag{6.51}$$

$$\gamma \to 0 \quad \text{as} \quad Y \to \infty. \tag{6.52}$$

Equation (6.47) yields its solution first. After a slight rearrangement (6.47) becomes

$$\frac{\partial^2 \gamma}{\partial Y^2} - i\mu Y \gamma = i\eta \bar{p}^{**}. \tag{6.53}$$

This is virtually a driven Airy's equation for γ and has solution

$$\gamma = \frac{i\eta \bar{p}^{**}}{(i\mu)^{\frac{2}{3}}} L(t), \tag{6.54}$$

where

$$L(t) = -\frac{2}{3^{1/2}} \int_0^\infty \sin(\frac{1}{3}\xi^3 + \xi t - \frac{\pi}{6}) \mathrm{d}\xi, \tag{6.55}$$

and

$$t = (i\mu)^{\frac{1}{3}} Y. \tag{6.56}$$

This solution comes from knowing that the solution of

$$\frac{\partial^2 \hat{\gamma}}{\partial \hat{t}^2} - \hat{t}\hat{\gamma} = -\frac{1}{\pi}, \tag{6.57}$$

is given by

$$\hat{\gamma} = -\frac{L(\hat{t})}{\pi}, \tag{6.58}$$

with $L(0) = L(\infty) = 0$. Substituting the form of $\hat{t}$ for Y from (6.56) and rearranging causes (6.53) to have the same form as (6.57).

Now we must determine τ. To do this we consider (6.48), differentiate with respect to Y and substitute for $\frac{\partial \bar{v}^{**}}{\partial Y}$ from the transformed continuity equation (6.33), and obtain the following differential equation for τ:

$$\frac{\partial^3 \tau}{\partial Y^3} - iY\mu \frac{\partial \tau}{\partial Y} = -i\eta\gamma. \tag{6.59}$$

Once again we have a forced Airy's equation, but for $\frac{\partial \tau}{\partial Y}$ now. Equation (6.59) has solution

$$\frac{\partial \tau}{\partial t} = B(k,l)Ai(t) + \frac{\eta^2 \bar{p}^{**}}{(i\mu)^{\frac{5}{3}}} L'(t), \tag{6.60}$$

where

$$B(k,l)Ai'(0) + \frac{\eta^2 \bar{p}^{**}}{(i\mu)^{\frac{5}{3}}} = \frac{i\mu \bar{p}^{**}}{(i\mu)^{\frac{2}{3}}}, \tag{6.61}$$

from considering (6.48) at $Y = 0$. Integrating (6.60) with respect to Y from 0 to ∞ along with the boundary conditions (6.49) - (6.52) gives

$$(\lambda_1^2 + \lambda_2^2)A^{**} + (\lambda_1^2 + \lambda_2^2)f^{**} = \frac{B(k,l)}{3}. \tag{6.62}$$

If we then combine (6.62) with (6.61) and apply (6.36) we obtain, substituting for μ, η, an expression for the pressure transform:

$$\bar{p}^{**} = \frac{f^{**}}{-\frac{k^2+l^2}{\sigma(i(\lambda_1 k+\lambda_2 l))^{5/3}} - \frac{(k^2+l^2)^{1/2}}{k^2}} \tag{6.63}$$

where

$$\sigma = 3Ai'(0), \tag{6.64}$$

$$= -0.7764, \tag{6.65}$$

to four decimal places.

The other quantities follow and are given by

$$A^{**} = \frac{(k^2+l^2)^{1/2}}{k^2}\bar{p}^{**}, \tag{6.66}$$

$$u^{**} = \frac{\lambda_2\gamma + \lambda_1\tau}{(\lambda_1^2+\lambda_2^2)}, \tag{6.67}$$

$$v^{**} = \frac{\lambda_2\tau - \lambda_1\gamma}{(\lambda_1^2+\lambda_2^2)}. \tag{6.68}$$

6.4 Results

We now need to invert the transformed solutions for the pressure and displacement in order to determine their solutions. To perform the inversions we adopted a fast-Fourier-transform (FFT) numerical approach adapted from that in Press *et al* (1990). The accuracy of the method was tested by reproducing the results of Smith *et al* (1977), with which good agreement was found, and by varying the grid size and integration range to ensure sufficient accuracy. When needed in the calculations we take $\lambda_1/\lambda_2 = 1$.

We take the hump shape to be given by

$$f(X,Z) = \cos^2(\frac{1}{2}\pi(X^2+Z^2)^{1/2}) \quad \text{for} \quad X^2+Z^2<1, \tag{6.69}$$

$$= 0 \quad \text{otherwise.} \tag{6.70}$$

The results for the pressure $P(X,Z)$ and the displacement $A(X,Z)$ are displayed in figures 6.4 and 6.5.

The numerical results indicate two corridors of interest in the solution of the displacement $A(X,Z)$; one centred on the x-axis, aligned with the outer flow, and the other in the $\hat{X}(= N^{-1}(\lambda_1 X + \lambda_2 Z))$ direction, aligned with the boundary layer flow

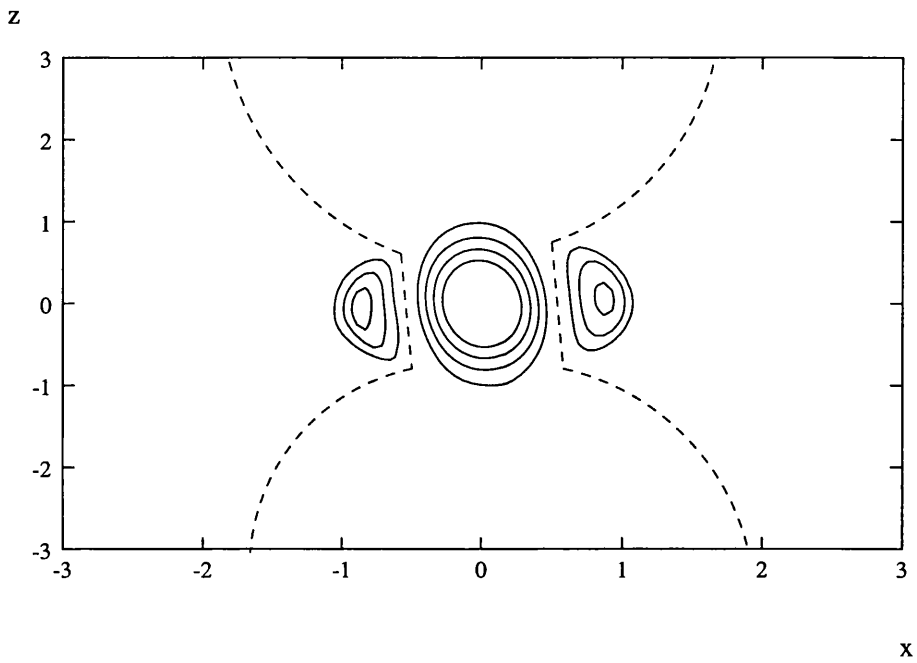

Figure 6.4: Contour Plot of the Pressure solution. The dashed line corresponds to$P = 0$. Between the lines $P < 0$ and P is positive elsewhere. The contour intervals are 0.02

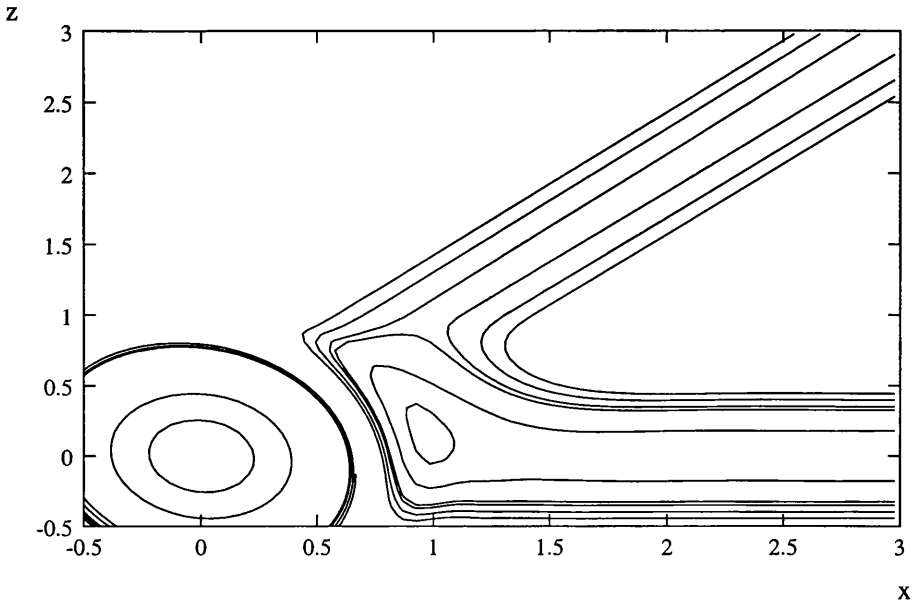

Figure 6.5: Contour Plot of the displacement A. The contour interval is 0.04.

in the main deck, where $N^2 = \lambda_1^2 + \lambda_2^2$. As these regions appear to be of some significance we consider now the limits of large x and $\hat{X}$, or equivalently in Fourier space small k and $\hat{k}(= N^{-1}(\lambda_1 k + \lambda_2 l))$.

At large radial distances, $X^2 + Z^2 \gg 1$, the pressure takes on a relatively simple form. If we consider equation (6.63) for $k^2 + l^2 \ll 1$, it reduces at leading order to

$$P^{**} = -\frac{k^2 f^{**}(0,0)}{(k^2+l^2)^{1/2}}. \tag{6.71}$$

If we invert (6.71) we obtain the asymptotic form of the pressure given by

$$P(X,Z) = \frac{(2X^2 - Z^2)}{(X^2+Z^2)^{5/2}} \frac{f^{**}(0,0)}{2\pi}. \tag{6.72}$$

This is a relatively simple solution and leaves no suggestion of a corridor effect (a fact borne out by the numerical results).

We now consider the displacement A where we expect to find the aforementioned corridor effect, with this quantity decaying more slowly in two narrow regions as discussed just above compared to the global decay. If we examine initially along the x-axis we have the transformed displacement A^{**} given by

$$A^{**} = \frac{-f^{**}}{\frac{k^2(k^2+l^2)^{1/2}}{\sigma(i(\lambda_1 k+\lambda_2 l))^{5/3}} + 1}. \tag{6.73}$$

Considering large x, this corresponds to small k, so for $k \ll 1$, $l \sim O(1)$, (6.73) becomes

$$A^{**} = \frac{-f^{**}}{1 + \frac{|l|k^2}{\sigma(i\lambda_2 l)^{5/3}}}. \tag{6.74}$$

As k is small we can expand this as

$$A^{**} = -f^{**} + \frac{|l|k^2}{\sigma(i\lambda_2 l)^{5/3}} f^{**} + \ldots. \tag{6.75}$$

Performing the inverse transform on this expression, using the relation

$$\Gamma(n)(ik)^{-n} \Leftrightarrow H(X)X^{n-1}, \tag{6.76}$$

where $\Leftrightarrow$ denotes a Fourier transform pair and $H(x)$ is the Heaviside function, gives

$$A \sim -f + \frac{H(X)X^{-3}}{\sigma\Gamma(-2)} G(Z), \tag{6.77}$$

with

$$G^*(l) = \frac{|l|f^{**}(0,l)}{(i\lambda_2 l)^{5/3}}. \tag{6.78}$$

We can invert (6.78) using the knowledge that

$$|l|f^{**}(0,l) \Leftrightarrow \int_{-\infty}^{\infty} \frac{f_1'(\eta)}{Z-\eta} \mathrm{d}\eta, \tag{6.79}$$

where

$$f_1(Z) = -\int_{-\infty}^{\infty} f(X,Z)\mathrm{d}X, \tag{6.80}$$

from Smith *et al* (1977). Then $G(Z)$ is obtained by performing a convolution of the right hand side of (6.79) with $\frac{H(Z)Z^{2/3}}{\lambda_2^{5/3}\Gamma(2/3)}$ (the inverse transform of $(i\lambda_2 l)^{-5/3}$). This yields

$$G(Z) = \frac{1}{\lambda_2^{5/3}\Gamma(2/3)} \int_z^\infty (s-Z)^{2/3} [\int_{-\infty}^\infty \frac{f_1'(\eta)}{s-\eta} \mathrm{d}\eta] \mathrm{d}s. \tag{6.81}$$

The aspect of this solution that is of most interest is the decay of the displacement with X given by $A + f \sim X^{-3}$, which is compared below with the decay outside of this narrow corridor.

If we now consider the $\hat{X}$ direction, we introduce $N\hat{k} = \lambda_1 k + \lambda_2 l$ and $N\hat{l} = \lambda_2 k - \lambda_1 l$, transforming (6.73) into

$$A^{**}(\hat{k},\hat{l}) = \frac{-f^{**}}{1 + \frac{\frac{1}{N^2}(\hat{k}^2+\hat{l}^2)^{1/2}(\lambda_1\hat{k}+\lambda_2\hat{l})^2}{\sigma(iN\hat{k})^{5/3}}} \tag{6.82}$$

We now consider large $\hat{X}$, requiring us to consider $\hat{k} \ll 1$, $\hat{l} \sim O(1)$. This assumption reduces (6.82) to

$$A^{**} = \frac{-f^{**}}{1 + \frac{|\hat{l}|(\lambda_2\hat{l})^2}{\sigma_1(i\hat{k})^{5/3}}}, \tag{6.83}$$

where $\sigma_1 = N^{11/3}\sigma$. As $\hat{k} \ll \hat{l}$ we can rewrite (6.83) as

$$A^{**} = \frac{\sigma_1(i\hat{k})^{5/3}}{|\hat{l}|(\lambda_2\hat{l})^2} f^{**}, \tag{6.84}$$

to leading order. Performing the inverse transform once again we obtain

$$A \sim \frac{H(\hat{X})\hat{X}^{-8/3}}{\Gamma(5/3)} G_1(\hat{Z}), \tag{6.85}$$

where

$$G_1^{**}(\hat{l}) = \frac{-\sigma_1 f^{**}}{|\hat{l}|(\lambda_2\hat{l})^2}. \tag{6.86}$$

Equation (6.86) can be inverted in much the same way as (6.79), multiplying top and bottom of the right-hand side by $|\hat{l}|$ and performing a convolution; we obtain

$$G_1(\hat{Z}) = \frac{\sigma_1}{\lambda_2^2\Gamma(3)}\int_{\hat{Z}}^{\infty}(s-\hat{Z})^3[\int_{-\infty}^{\infty}\frac{f_1'(\eta)}{s-\eta}\mathrm{d}\eta]\mathrm{d}s, \tag{6.87}$$

determining the form of the solution and the decay with increasing $\hat{X}$.

In order to confirm that the corridors are distinct from the rest of the flow we now consider large distances but not specifically inside either corridor, i.e. consider both X and Z becoming large. We once again examine (6.73) but this time with $k \sim l \ll 1$. This assumption leads to the equation

$$A^{**} + f^{**} = \frac{k^2(k^2+l^2)^{1/2}}{[i(\lambda_1 k + \lambda_2 l)]^{5/3}}\frac{f^{**}(0,0)}{\sigma}. \tag{6.88}$$

To invert this equation we firstly consider the $(k^2+l^2)^{1/2}$ part. The inverse transform of this is given by

$$(k^2+l^2)^{1/2} \Leftrightarrow \frac{-1}{2\pi}\frac{\Gamma(3/2)}{\Gamma(-1/2)}\frac{1}{(X^2+Z^2)^{3/2}}. \tag{6.89}$$

It follows that

$$k^2(k^2+l^2)^{1/2} \Leftrightarrow \frac{-1}{2\pi}\frac{\Gamma(3/2)}{\Gamma(-1/2)}\frac{\partial^2}{\partial X^2}(\frac{1}{(X^2+Z^2)^{3/2}}), \tag{6.90}$$

$$\Leftrightarrow \frac{-1}{2\pi}\frac{\Gamma(3/2)}{\Gamma(-1/2)}\frac{(12X^2-3Z^2)}{(X^2+Z^2)^{7/2}}. \tag{6.91}$$

If we now consider the other part of the transform $[i(\lambda_1 k + \lambda_2 l)]^{-5/3}$ we write this as $(i\hat{k})^{-5/3}$ which has an inverse given by

$$(i\hat{k})^{-5/3} \Leftrightarrow \frac{1}{\Gamma(5/3)}H(\hat{X})\hat{X}^{2/3}\delta(\hat{Z}), \tag{6.92}$$

$$= \hat{G}, \quad \text{say.} \tag{6.93}$$

From now on we will take $\lambda_1 = \lambda_2 = 1$ for simplicity. In order to determine the inverse transform of (6.88) we need to convolute (6.91) and (6.92). We do this by first writing (6.91) in terms of the $\hat{x}$ and $\hat{z}$ co-ordinates with

$$\frac{12X^2 - 3Z^2}{(X^2+Z^2)^{7/2}} = \frac{9\hat{X}^2 + 9\hat{Z}^2 + 30\hat{X}\hat{Z}}{(\hat{X}^2+\hat{Z}^2)^{7/2}}, \tag{6.94}$$

$$= \hat{F}, \quad \text{say.} \tag{6.95}$$

We can now perform the convolution

$$\hat{F} * \hat{G} = \int_{-\infty}^{\infty}\int_{-\infty}^{\infty} \frac{9\hat{s}^2 + 9\hat{t}^2 + 30\hat{s}\hat{t}}{(\hat{s}^2+\hat{t}^2)^{7/2}} H(\hat{s}-\hat{X})\delta(\hat{t}-\hat{Z})(\hat{s}-\hat{X})^{2/3}\mathrm{d}\hat{s}\mathrm{d}\hat{t}. \tag{6.96}$$

Doing the $\hat{t}$ integration first, making use of the properties of the delta-function, gives

$$\hat{F} * \hat{G} = \int_{-\infty}^{\infty} \frac{9\hat{s}^2 + 30\hat{s}\hat{Z} + 9\hat{Z}^2}{(\hat{s}^2+\hat{Z}^2)^{7/2}} H(\hat{s}-\hat{X})(\hat{s}-\hat{X})^{2/3}\mathrm{d}\hat{s}, \tag{6.97}$$

$$= \int_{\hat{X}}^{\infty} \frac{9\hat{s}^2 + 30\hat{s}\hat{Z} + 9\hat{Z}^2}{(\hat{s}^2+\hat{Z}^2)^{7/2}} (\hat{s}-\hat{X})^{2/3}\mathrm{d}\hat{s}, \tag{6.98}$$

on removing the Heaviside function. Now Gradstein and Ryzhik (1965) give

$$\int_u^{\infty} x^{-\lambda}(x^2+\beta^2)^{\nu}(x-u)^{\mu-1}\mathrm{d}x =$$
$$u^{\mu+\nu-\lambda}\frac{\Gamma(\mu)\Gamma(\lambda-\mu-2\nu)}{\Gamma(\lambda-2\nu)}{}_3F_2(-\nu, \frac{\lambda-\mu}{2}-\nu, \frac{1+\lambda-\mu}{2}-\nu; \frac{1+\lambda}{2}-\nu, \frac{1+\lambda}{2}-\nu, -\frac{\beta^2}{u^2}), \tag{6.99}$$

provided $0 < \mu < \lambda - 2\nu$, where ${}_3F_2(a,b,c;d,e,\beta)$ is a generalized hypogeometric series, see Gradstein and Ryzhik (1965) or Abramovich and Stegun (1972). The necessary constraint is satisfied in this case and so we can write, inverting (6.88),

$$A + f = \hat{x}^{-10/3}\bar{G}(\frac{\hat{x}}{\hat{z}}) \tag{6.100}$$

where

$$\frac{\bar{G}(\hat{t})}{9} = \Gamma_1(2)F_1(-2,-\hat{t}) + \frac{10}{3}\Gamma_1(1)\hat{t}F_1(-1,-\hat{t}) + \hat{t}^2\Gamma_1(0)F_1(0,\hat{t}), \tag{6.101}$$

and Γ_1 and F_1 are given by

$$\Gamma_1(\lambda) = \frac{\Gamma(\frac{1}{3})\Gamma(\lambda+\frac{20}{3})}{\Gamma(\lambda+7)}\frac{f^{**}(0,0)}{\sigma}, \tag{6.102}$$

$$F_1(\lambda,-\hat{t}) = {}_3F_2(\frac{7}{2},\frac{\lambda}{2}-\frac{10}{3};\frac{\lambda}{2}+\frac{7}{2},\frac{\lambda}{2}+\frac{7}{2},\hat{t}). \tag{6.103}$$

This solution is plotted in figure 6.6, based on using a NAG library routine. The solution shows the function $\bar{G}$ becoming singular along the two corridors where this solution breaks down and must be replaced by the more slowly decaying results from the corridor analysis presented earlier. The major point to note however is the comparison between the rates of decay along the $Z = 0$ and $\hat{Z} = 0$ line and the decay more globally. It is clear that the corridors, decaying at R^{-3} and $\hat{R}^{-8/3}$, persist further than the more global flow which decays as $R^{-10/3}$, where R denotes the radial distance.

6.5 Jet effect

In order to investigate the trailing corner problem we need to examine how the triple-deck structure discussed above interacts with the double deck structure of Smith and Duck (1977). To that end we examine here the impact of introducing the double-deck effect into the pressure-displacement relation. Originally this was thought to require elongating the hump in the $\pm x$-directions, triggering the double deck structure at large $|x|$ values, the only region in which the double- and triple-deck structures are of comparable size, in the existing triple-deck regime. However it is now thought, from considering the analysis below, that this effect is present even with the current non-elongated hump shape. What follows is effectively a composite

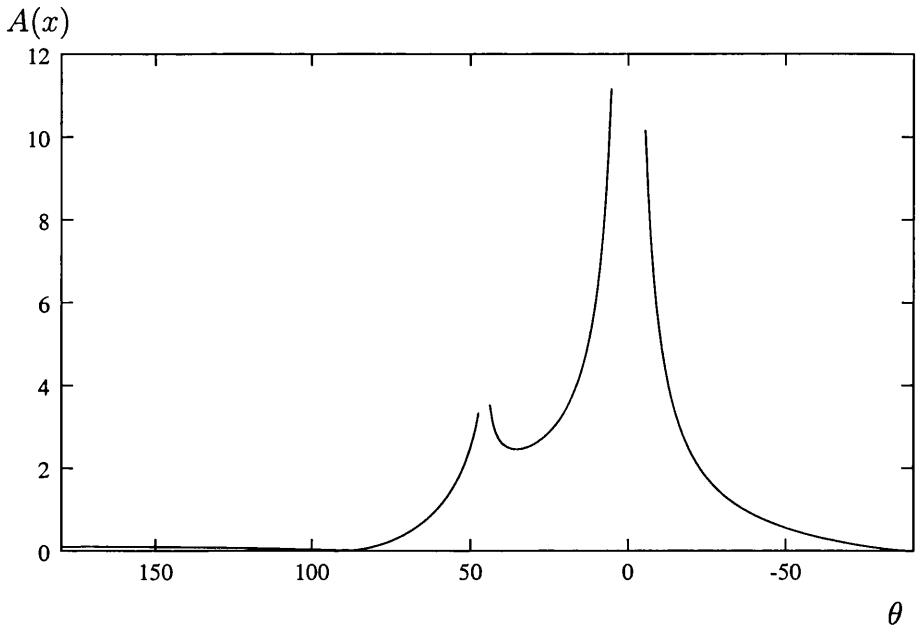

Figure 6.6: Plot of the farfield A(x) solution for varying θ, where $\tan\theta = x/z$. Note the corridor effects at $\theta = 0^o, 45^o$ where the solution is singular.

approach, see also Rhyzov and Terent'ev (1997), Davis (1991) and references therein. The only change to the main governing equations generated by introducing this new interaction is in the pressure-displacement law. The lower deck governing equations remain the same but the pressure-displacement law becomes

$$P(X,Z) = -\frac{1}{2\pi}\int_{-\infty}^{\infty}\int_{-\infty}^{\infty}\frac{\frac{\partial^2 A}{\partial\xi^2}\mathrm{d}\xi\mathrm{d}\eta}{[(X-\xi)^2+(Z-\eta)^2]^{\frac{1}{2}}} - \epsilon_1\frac{\partial^2 A}{\partial Z^2}, \tag{6.104}$$

where ϵ_1 is a small parameter corresponding to the relative strength of the double deck effect. This new term is small compared to the triple deck relation as the pressure in the double deck problem is $O(Re^{-2/7})$ while in the triple deck context the pressure is $O(Re^{-2/8})$. As examined below the ϵ_1 effect is only substantial at large $|X|$ values with $Z \sim O(1)$. Elsewhere the jet effect term is small compared to the triple-deck effect.

Considering the problem with this new pressure-displacement law leads, by carrying through the same analysis as before, to the adapted transformed pressure solution

$$P^{**} = \frac{-f^{**}(k,l)}{\frac{(k^2+l^2)^{1/2}}{k^2-\epsilon_1 l^2(k^2+l^2)^{1/2}} + \frac{(k^2+l^2)}{\sigma[i(\lambda_1 k+\lambda_2 l)]^{5/3}}}, \tag{6.105}$$

which is much the same as in section 6.3. As ϵ_1 is small the jet effect is generally secondary but it is significant if we consider $k \ll 1$, $l \sim O(1)$ (i.e. as $|X| \to \infty$, $z \sim O(1)$),

$$P^{**} \sim \frac{-f^{**}(0,l)}{\frac{|l|}{k^2-\epsilon l^2|l|} + \frac{l^2}{\sigma(i\lambda_2 l)^{5/3}}}. \tag{6.106}$$

To leading order this is given by

$$P^{**} = -\frac{k^2-\epsilon_1 l^2|l|}{|l|}f^{**}(0,l) + \ldots, \tag{6.107}$$

i.e we have

$$P^{**} = -\frac{k^2}{|l|}f^{**}(0,l) + \epsilon_1 l^2 f^{**}(0,l), \tag{6.108}$$

$$= P^{**}_{\mathrm{TD}} + \epsilon_1 P^{**}_{\mathrm{jet}}, \tag{6.109}$$

where P^{**}_{TD} is as before and

$$P^{**}_{\mathrm{jet}} = l^2 f^{**}(0,l). \tag{6.110}$$

Equation (6.109) can be inverted to give the leading order pressure at large upstream distances $-(X) \gg 1$ as

$$P_{\mathrm{TD}}(X,Z) = \frac{f^{**}(0,0)}{\pi X^3} \tag{6.111}$$

from (6.72), and

$$P_{\mathrm{jet}} = -\epsilon_1 \frac{\partial^2}{\partial Z^2}\int_{-\infty}^{\infty} f(X,Z)\mathrm{d}X. \tag{6.112}$$

Similar analysis can be carried out for the displacement $A(X,Z)$ which once again splits into two parts, the first being the same as the triple-deck solution and the second being specific to this double-deck case and only significant for $|X| \gg 1$, $Z \ll 1$. So it appears that the two structures join by means of the triple-deck solution decaying as $X \to -\infty$, $Z \ll 1$ and becoming comparable in scale and size with the double-deck solution of Smith and Duck (1977), whilst outside of this region the triple-deck structure describes the solution to leading order.

6.6 The trailing corner problem

In the present section, guided by the previous analysis in this chapter, we present a possible structure for the flow past the trailing corner, as drawn in figure 6.1. The

governing equations are the interactive boundary layer ones given by

$$\frac{\partial U}{\partial X}+\frac{\partial V}{\partial Y}+\frac{\partial W}{\partial Z} = 0, \tag{6.113}$$

$$U\frac{\partial U}{\partial X}+V\frac{\partial U}{\partial Y}+W\frac{\partial U}{\partial Z} = -\frac{\partial P}{\partial X}+\frac{\partial^2 U}{\partial Y^2}, \tag{6.114}$$

$$U\frac{\partial W}{\partial X}+V\frac{\partial W}{\partial Y}+W\frac{\partial W}{\partial Z} = -\frac{\partial P}{\partial Z}+\frac{\partial^2 W}{\partial Y^2}. \tag{6.115}$$

We require the no-slip conditions on the blade (locally a quarter plane),

$$U = V = W = 0 \quad \text{for} \quad X < 0 \quad \text{and} \quad Z < 0, \tag{6.116}$$

and symmetry conditions beyond the trailing edge

$$\frac{\partial U}{\partial Y} = V = \frac{\partial W}{\partial Y} = 0 \quad \text{for} \quad X > 0 \quad \text{or} \quad Z > 0. \tag{6.117}$$

Once again the main deck implies the matching conditions

$$U \sim \lambda_1(Y + A(X, Z)) \quad \text{as} \quad Y \to \infty, \tag{6.118}$$

$$W \sim \lambda_2(Y + A(X, Z)) \quad \text{as} \quad Y \to \infty. \tag{6.119}$$

The major change between this and a normal three-dimensional triple-deck problem comes in the pressure-displacement law which now includes a $\frac{\partial^2 A}{\partial Z^2}$ term. Guided directly by the results in the previous section we propose it takes the form

$$P(X,Z) = -\frac{1}{2\pi}\int_{-\infty}^{\infty}\int_{-\infty}^{\infty}\frac{\frac{\partial^2 A}{\partial \xi^2}\mathrm{d}\xi\mathrm{d}\eta}{[(X-\xi)^2+(Z-\eta)^2]^{\frac{1}{2}}} - \epsilon_2\frac{\partial^2 A}{\partial Z^2}, \tag{6.120}$$

where the small parameter ϵ_2 is unknown.

To determine the order of magnitude of ϵ_2 we compare the size of the two pressure terms in the triple and double deck structures as $X \to -\infty$. First however we need to determine the pressure decay in the triple deck structure as. At the trailing edge

$Z = 0$ as $X \to -\infty$ we expect a non-zero shear flow (W) coming off the blade. This imples, in view of the local behavour in Hakkinen and Rott (1962) that

$$P - P(0) \sim Z^{2/3} \quad \text{for} \quad Z \ll 1, \tag{6.121}$$

locally. Meanwhile in the farfield, $A \sim R^{1/3}$ for $-\frac{\pi}{2} < \theta < \pi$ (while $A \ll 1$ on the blade, $-\pi < \theta < -\frac{\pi}{2}$) from consideration of the general triple-deck problem (here $\tan\theta = x/z$). The pressure displacement law for the triple deck then implies that

$$P \sim R^{-2/3} f(\theta), \tag{6.122}$$

say. Balancing (6.121) and (6.122) far upstream implies $Z^{2/3} \sim |X|^{-2/3}$ as $X \to -\infty$ ($\theta \sim \pi$), i.e. $|Z| \sim |X|^{-1}$ is the scale of the local thickness, implying

$$P \sim |X|^{-2/3}, \tag{6.123}$$

there and giving the unknown pressure decay as $X \to -\infty$ near the blade edge. Therefore as $X \to -\infty$ the combined pressure is given by

$$P \sim Re^{-2/8}|X|^{-2/3} f(\theta) - Re^{-2/7}\frac{\partial^2 A}{\partial Z^2}, \tag{6.124}$$

where the powers of Re are known from the respective triple- and double-deck scalings. The two terms in (6.124) are comparable far upstream when

$$|X| \sim O(Re^{3/56}), \tag{6.125}$$

or in terms of the $O(1)$ quantity x,

$$|x| \sim O(Re^{-9/28}). \tag{6.126}$$

This suggests the flow at the corner is primarily governed by the triple-deck structure, with the double deck structure being secondary until X is of the order given in equation (6.125).

Chapter 7

Three-Dimensional Car Undertray Flows, and Blades Near the Ground

7.1 Introduction

In this chapter we return to considering ground effect, primarily examining the flow past a solitary three-dimensional blade operating very close to the ground so that, unlike the regime of Chapter 3, the ground is now inside the boundary layer with the ground clearance being of $O(Re^{-1/2})$.

The motivation for the work in this chapter is twofold. Firstly, this regime of a blade very close to the ground has implications in the design of car undertrays and front wings which seek to exploit ground effect to enhance and maximise downforce. Jones (2000) considered the two-dimensional case and Jones and Smith (2000) took this

further and also introduced the three-dimensional case considered here. Secondly, if we wish to extend the two-dimensional multi-blade problem of Chapter 3 to include even smaller ground clearances than were considered there, or to introduce three-dimensional blades, there are various aspects of this single blade case that need to be resolved before an attempt to increase the number of blades can be made.

This chapter sets out both the two-dimensional, single and many blade cases, and the single three-dimensional blade problem, looking in particular at large ground clearances within the $O(Re^{-1/2})$ range which, as discussed in Jones and Smith (2000), tends to be the most realistic range in applications. This limit simplifies the problem somewhat, causing it to become essentially inviscid, in particular in the gap between the ground and the underside of the blade. We briefly explore this limit in two dimensions with several blades present before turning to the three-dimensional case. A major problem in the three-dimensional regime, which is by no means fully resolved here, is determining the cross-over points, where inflow edges become outflow edges, which are generally unknown in advance. Whereas in two dimensions the difference between the leading and trailing edge is well defined it is not so obvious in three dimensions where the distinct boundary conditions should be applied (these conditions being a pressure jump at a leading or inflow edge and zero pressure at a trailing or outflow one).

Section 7.2 below reviews the single, two-dimensional blade regime considered in Jones (2000), Jones and Smith (2000), describing the necessity of a pressure jump condition at the leading edge and goes on to examine the case of many blades in the large-height limit where the flow takes on a relatively simple structure. This is shown to be consistent with the small height analysis of Chapter 3. In order to try

to exploit this relative simplicity, section 7.3 examines the three-dimensional case of a single three-dimensional blade. Section 7.4 then proceeds to present a numerical approach to solving a specific problem using an $O(h^4)$ accurate compact-difference approach and section 7.5 presents various results for a rectangular planform aligned at various angles to the oncoming flow. Finally, section 7.6 investigates several regions of interest highlighted by the results of 7.5, including the flow solution as an inflow (or leading) edge almost becomes an outflow (trailing) edge.

7.2 The two-dimensional problem

In this section we summarise the two-dimensional case of a blade with the ground within the boundary layer, as discussed above. We present the formulation of the problem here and then go on to consider the case with many blades present and an examination of a large height, inviscid limit.

The set-up of the problem is that of a single blade operating very close to the ground with $\bar{h} \sim O(Re^{-1/2})$, where $\bar{h}$ is a measure of the height of the blade from the ground. As such we write $\bar{h} = Re^{-\frac{1}{2}}h$ where h is $O(1)$. The blade shape is described by the functions $f(x)$ and $g(x)$ where $y = f(x)$, $y = g(x)$ describe the underside and upperside of the blade surface respectively and y is the scaled boundary-layer co-ordinate. Both $f(x)$ and $g(x)$ are assumed to be $O(1)$ and $f(0) = g(0) = h$. This is distinct from the structure examined in Chapter 3 where the ground clearance h was assumed to be $O(1)$ whilst the blades were slender and $O(Re^{-1/2})$. The ground now enters the boundary layer calculation directly via a moving ground condition requiring the ground to be moving with the free stream.

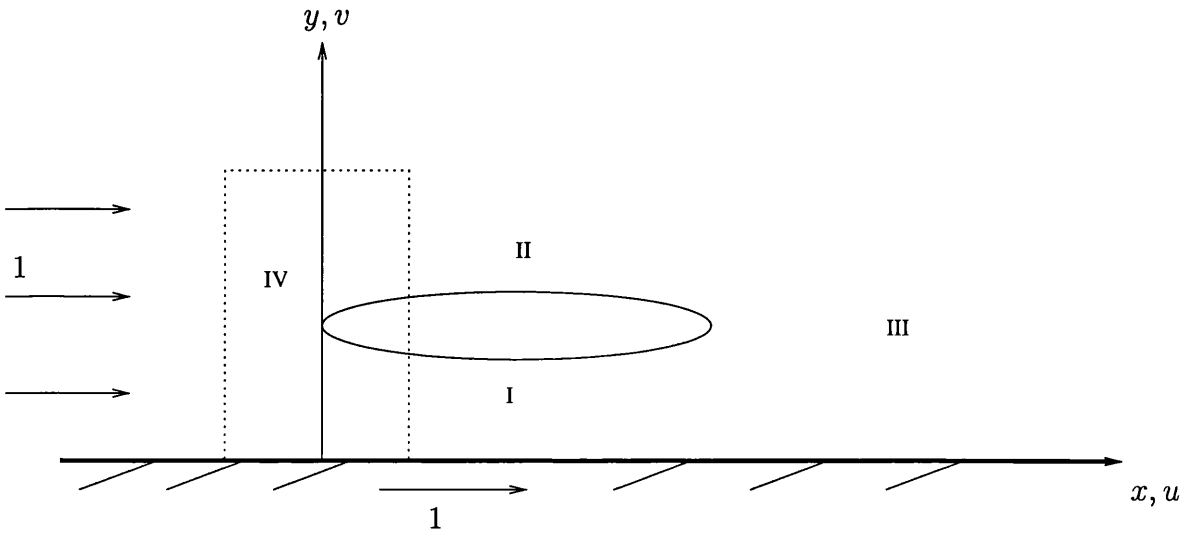

Figure 7.1: The flow structure and setup of the two-dimensional problem.

The flow structure is based upon four regions: region I is the gap between the underside of the blade and the ground, region II is above the blade, region III is beyond the trailing edge of the blade (the entire wake) and finally region IV is a distinct small region in the vicinity of the leading edge. See also figure 7.1. In regions I-III the leading order velocities and pressure are given by

$$(U, V, P) = (u, Re^{-1/2}v, p) \quad \text{with} \quad (X, Y) = (x, Re^{-1/2}y). \tag{7.1}$$

The governing equations are then the two-dimensional interactive boundary-layer equations

$$\frac{\partial u}{\partial x} + \frac{\partial v}{\partial y} = 0, \tag{7.2}$$

$$u\frac{\partial u}{\partial x} + v\frac{\partial u}{\partial y} = -\frac{\partial p}{\partial x} + \frac{\partial^2 u}{\partial y^2}, \tag{7.3}$$

$$0 = \frac{\partial p}{\partial y}. \tag{7.4}$$

These equations must be solved in each of the regions I, II and III subject to the

conditions

$$u = 1, v = 0 \quad \text{at} \quad y = 0, \tag{7.5}$$

$$u = v = 0 \quad \text{at} \quad y = f(x), \tag{7.6}$$

$$u = u_0, \quad p = p_0 \quad \text{at} \quad x = 0+, \tag{7.7}$$

$$p(1) = 0, \tag{7.8}$$

in the gap region I, which are the moving ground condition, the no-slip requirements at the underside of the blade described by $y = f(x)$, an inflow condition which is described in more detail below and a pressure continuity condition at the trailing edge, respectively. The pressure there is required to be zero as above the blade $p(x) \equiv 0$ because the latter pressure must match with the free-stream $U = 1$, $P = 0$ as $y \to \infty$. So above the blade, region II, we have the boundary conditions

$$u = v = 0 \quad \text{at} \quad y = g(x), \tag{7.9}$$

$$u \to 1 \quad \text{as} \quad y \to \infty, \tag{7.10}$$

$$p(x) \equiv 0, \tag{7.11}$$

which are for no slip on the upper side of the blade $y = g(x)$, matching with the free-stream velocity and matching the y-independent pressure with the zero pressure in the free-stream. The requirements in region III are given by

$$u = 1, v = 0 \quad \text{at} \quad y = 0, \tag{7.12}$$

$$u \to 1 \quad \text{as} \quad y \to \infty, \tag{7.13}$$

$$p(x) \equiv 0, \tag{7.14}$$

as described for the other regions. The starting condition for region III at $x = 1$ is a profile comprising of the flow at the trailing edge from regions I and II evaluated at

$x = 1$. Finally region IV determines the starting conditions in regions I and II. The Kutta condition requiring zero pressure at the trailing edge poses a slight problem with a non-zero pressure expected beneath the blade needing to become zero at the trailing edge. This implies a pressure jump at the leading edge (as the pressure is also zero upstream). This can be resolved by introducing a small region IV across which there is a streamwise jump of the pressure in the gap. The full solution in this region is given in Jones (2000) but we give the main features of this small Euler region IV here. Firstly, the Bernoulli quantity $p + \frac{1}{2}u^2$ is conserved through the region so that in the gap:

$$p(0+) = p_0 (= \frac{1}{2} - \frac{1}{2}u_0^2), \tag{7.15}$$

where u_0 and p_0 are constants, unknown in advance and are effectively fixed by the trailing edge condition. The starting velocity profile in the gap region is simply $u(x, y) = u_0$. Secondly, considering the solution above the blade implies that both the pressure and velocity remain unchanged across this leading edge region giving a starting profile with $u = 1$, $p = 0$ for all y.

Details of the solution and important features of the above problem are given in Jones and Smith (2000). One limit of particular importance is that of large heights as these tend to be the most realistic configurations in practice. The flow becomes essentially inviscid for large f values and conservation of vorticity implies that u is independent of y in the gap region I. The solution is relatively simple with

$$u = \frac{u_0 h}{f(x)}, \tag{7.16}$$

$$p = \frac{1}{2} - \frac{u_0^2 h^2}{2f^2(x)}, \tag{7.17}$$

where

$$u_0 = \frac{f(1)}{h}. \tag{7.18}$$

It is this relatively simple but physically important limit that inspires the work in the next section, which seeks to examine this limit but for a three-dimensional blade. There are several extra problems to address when working in the three-dimensional context as discussed below but it is hoped that the current limiting case may simplify the problem sufficiently to allow some progress to be made.

Before moving to the three-dimensional case we want to make a brief mention of the possibility of extending the present work to a multiple blade context (as, for example, in chapter 3). There appears to be one major challenge in general. The problem is due to the local leading edge region IV. Whereas in the situation discussed above the oncoming flow was known (simply $u = 1$) allowing an analytic solution, in a multi-blade case any subsequent blades are subject to an unknown, non-simple starting profile. This means the current leading edge solution will not be valid except for the first blade (or if the blades were very widely spread) and so a new approach to dealing with the leading edge region would be required, possibly along the lines of the leading edge pressure jump region in a different context described by Bowles and Smith (2000b). This is equivalent to the unknown y-shifts discussed in Chapter 3.

However some progress can be made in the large height limit where this leading edge problem effectively reduces to the single blade case at every leading edge. As set out above the flow between the ground and the underbody takes on a simple form given by (7.16) -(7.18), while above the blade we have the free-stream. At the

trailing edge $x = 1$ the velocity profile in the gap is given by

$$u = \frac{u_0 h}{f(1)}, \tag{7.19}$$

$$= 1, \tag{7.20}$$

from the known value of u_0 from (7.18). Therefore the starting profile for the wake region III is simply $u = 1$, $p = 0$ for all y, and so throughout region III until the next blade is encountered. Introducing an extra blade is straightforward then with each being effectively independent and

$$u = \frac{f_i(t_i)}{f_i(x)}, \tag{7.21}$$

$$p = \frac{1}{2} - \frac{f_i^2(t_i)}{f_i^2(x)}, \tag{7.22}$$

where f_i describes the underside of blade i which has a trailing edge at $x = t_i$. Outside of the gap the flow is the free-stream $u = 1$, $p = 0$.

The small h analysis examined in 3.6.2 considered the flow past several thin blades as the $O(1)$ height h was reduced. This should yield a range of h similar to that considered in the current limit of an $O(Re^{-1/2})$ height h as $h \to \infty$, if we reduce the $O(1)$ blades to being slender here also. To this end we write $f_i = h + f_{si}$ where the f_{si} describing the underside of the blades are small. The underbody shapes f_{si} are assumed to include the thickness of the boundary layer here. Equations (7.21) and (7.22) then become

$$u = 1 + \frac{1}{h}(f_{si}(t_i) - f_{si}(x)) + \ldots, \tag{7.23}$$

$$p = \frac{f_{si}(x) - f_{si}(t_i)}{h}. \tag{7.24}$$

In chapter 3, the pressure p_3 in this limit is given by

$$p_3 = \frac{1}{h}(p_{3i}(0) + f_{3i}(x) + \delta_-(x)), \tag{7.25}$$

from equation (3.112), where f_{3i} describes the underside of the slender blade i. However $(f_{3i} + \delta_-(x))$ is simply the thickness of the blade and boundary layer combined $(= f_{si})$ and so setting the constant $p_{3i}(0)$ to satisfy the zero pressure condition at the trailing edge we obtain

$$p_3 = \frac{1}{h}(f_{si}(x) - f_{si}(t_i)), \tag{7.26}$$

the same relation as (7.24). Hence the inviscid limit here is, as would be expected, equivalent to the small h limit from Chapter 3.

7.3 The three-dimensional problem

Encouraged by the simplification offered by considering large h in the two-dimensional case, we now begin an investigation of a three-dimensional blade very near to the ground. Assuming the same structure holds for the three-dimensional case the governing boundary layer equations are given by

$$\frac{\partial u}{\partial x} + \frac{\partial v}{\partial y} + \frac{\partial w}{\partial z} = 0, \tag{7.27}$$

$$u\frac{\partial u}{\partial x} + v\frac{\partial u}{\partial y} + w\frac{\partial u}{\partial z} = -\frac{\partial p}{\partial x} + \frac{\partial^2 u}{\partial y^2}, \tag{7.28}$$

$$0 = \frac{\partial p}{\partial y}, \tag{7.29}$$

$$u\frac{\partial w}{\partial x} + v\frac{\partial w}{\partial y} + w\frac{\partial w}{\partial z} = -\frac{\partial p}{\partial z} + \frac{\partial^2 w}{\partial y^2}. \tag{7.30}$$

These are to be solved subject to the boundary conditions in the gap between the body and the ground

$$u = 1, \quad v = w = 0 \quad \text{at} \quad y = 0, \tag{7.31}$$

$$u = v = w = 0 \quad \text{at} \quad y = f(x,z), \tag{7.32}$$

$$u\cos\beta + w\sin\beta = \cos\beta \quad \text{at inflow edges}, \tag{7.33}$$

$$p = 0 \quad \text{at trailing edges}, \tag{7.34}$$

where $\tan\beta = \frac{\partial K}{\partial x}$ and $K_{\pm}(x)$ is such that $z = K_{\pm}(x)$ describes the edges of the blade planform. These boundary conditions correspond to the moving ground condition, no-slip on the underside of the blade, an inflow condition derived by considering the equivalent of the thin region IV from the two-dimensional case (and ensures no jump in the tangential velocity) and finally the by now familiar Kutta condition of pressure continuity at the trailing edge.

While equations (7.27) - (7.34) describe the entire problem we are still missing one factor, namely where the inflow and outflow conditions are appropriate. In the two-dimensional case the edge $x = 0$ is obviously inflow while the $x = 1$ edge is an outflow (or trailing) edge. Unfortunately in three-dimensions we cannot generally make similar assumptions of the positions of inflow and outflow edges in advance nor, therefore, where each type of boundary condition is appropriate. The positions of the two distinct types of edges will be determined by the planform shape and the thickness $f(x,z)$.

Heartened by the success of the limiting case in the two-dimensional regime we turn now to the limit of large h which, to repeat, tends to be the most realistic range. Considering the governing equations (7.27) - (7.30) indicates that u and w may be independent of the normal coordinate y throughout the gap. It follows that $v = -y(\frac{\partial u}{\partial x} + \frac{\partial w}{\partial z})$ from (7.27) and tangential motion on the underside of the body implies $\frac{\partial(uf)}{\partial x} + \frac{\partial(wf)}{\partial z} = 0$. Introducing the velocity potential ϕ, where $u = \frac{\partial \phi}{\partial x}$, $w = \frac{\partial \phi}{\partial z}$

leads to the single governing equation

$$\frac{\partial}{\partial x}(f\frac{\partial \phi}{\partial x}) + \frac{\partial}{\partial z}(f\frac{\partial \phi}{\partial z}) = 0, \tag{7.35}$$

or

$$f(\frac{\partial^2 \phi}{\partial x^2} + \frac{\partial^2 \phi}{\partial z^2}) + \frac{\partial f}{\partial x}\frac{\partial \phi}{\partial x} + \frac{\partial f}{\partial z}\frac{\partial \phi}{\partial z} = 0, \tag{7.36}$$

for ϕ. From an application of Bernoulli's equation the pressure is given by

$$p = \frac{1}{2}(1 - (\frac{\partial \phi}{\partial x})^2 - (\frac{\partial \phi}{\partial z})^2) \tag{7.37}$$

and so the boundary condition at outflow edges requires that $p = 0$ or, from (7.37)

$$(\frac{\partial \phi}{\partial x})^2 + (\frac{\partial \phi}{\partial z})^2 = 1 \quad \text{at outflow edges.} \tag{7.38}$$

At inflow edges however p,u and w are unknown (as there is a jump in p and the normal velocity via the now quasi-two-dimensional region IV. These jumps are unknown in advance and are effectively fixed by the need to satisfy the trailing edge condition). However we do have the constraint

$$\phi = x \quad \text{at inflow edges,} \tag{7.39}$$

from an integration of (7.33) with respect to x.

As discussed above, further progress on determining a solution is generally dependent on finding some method of distinguishing leading and trailing edges (or the cross-over points where the two interchange). However here we adopt a simple geometry where the inflow and outflow edges are explicitly known or can be assumed so, within certain bounds as we shall see. The specific planform we investigate is a rectangle of side 1 in the x direction and 1/2 in the z direction with the oncoming stream

aligned at an angle of incidence α (see figure 7.2). This is equivalent to having the planform at an angle in the uniform stream in the x direction as described above. Assuming the angle α is not too small or too close to $\pi/2$ the sides $x = 0$ and $z = 0$ are both known (or taken) to be inflow edges, while the other two sides $x = 1$ and $z = 1/2$ are outflow edges. We take the underbody shape to be given by

$$f(x, z) = (1 - \Gamma x(1 - x)^2 z^2 (\frac{1}{2} - z)^2), \tag{7.40}$$

where Γ is a constant and is taken as $\Gamma = 30$ in the numerical calculations that follow.

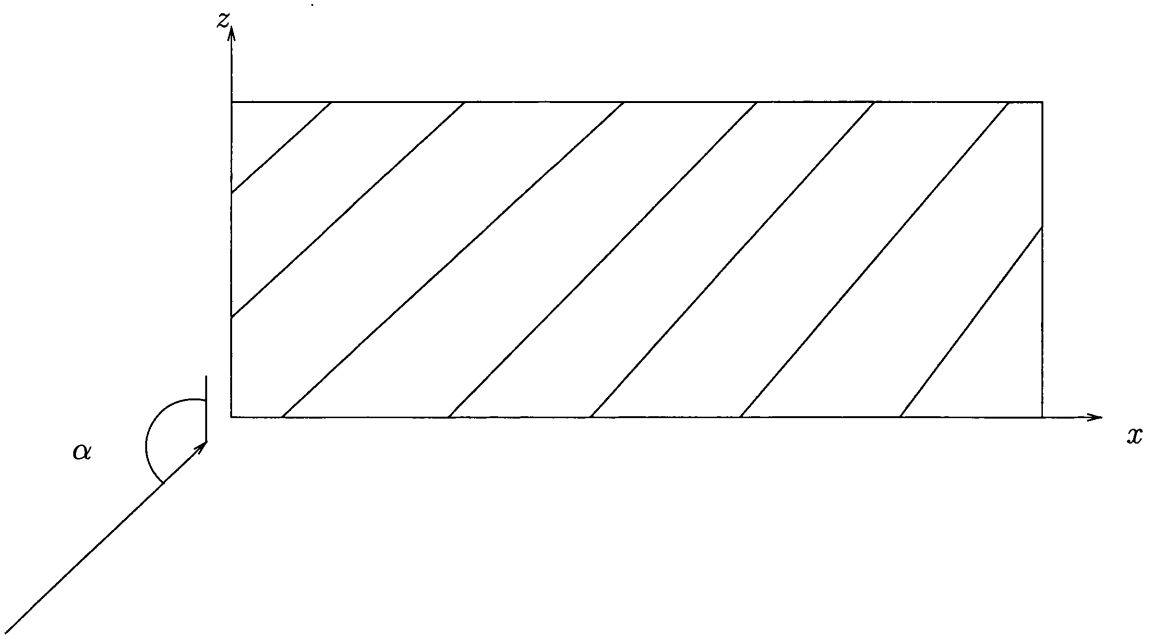

Figure 7.2: Rectangular planform and direction of the oncoming flow.

For clarity then we repeat the problem to be solved, with co-ordinates aligned with the planform. The single governing equation is

$$\frac{\partial^2 \phi}{\partial x^2} + \frac{\partial^2 \phi}{\partial z^2} + \frac{1}{f}(\frac{\partial f}{\partial x}\frac{\partial \phi}{\partial x} + \frac{\partial f}{\partial z}\frac{\partial \phi}{\partial z}) = 0, \tag{7.41}$$

and must be solved subject to

$$\phi = x\cos\alpha + z\sin\alpha \quad \text{at inflow edges} \quad x = 0 \quad \text{or} \quad z = 0, \tag{7.42}$$

$$(\frac{\partial\phi}{\partial x})^2 + (\frac{\partial\phi}{\partial z})^2 = 1 \quad \text{at outflow edges} \quad x = 1 \quad \text{or} \quad z = \frac{1}{2}. \tag{7.43}$$

We now seek to develop an accurate numerical scheme to solve this problem.

7.4 Compact difference solution

In this section we describe the compact difference discretisation used to solve the problem defined by equations (7.41) - (7.43). We are attempting to obtain a fourth-order accurate solution. The method used is adapted from that described in Spotz (1995), Carey and Spotz (1997), Spotz (1998) and references therein. We rewrite the governing equation (7.41) as

$$-(\frac{\partial^2\phi}{\partial x^2} + \frac{\partial^2\phi}{\partial z^2}) + c\frac{\partial\phi}{\partial x} + d\frac{\partial\phi}{\partial z} = 0, \tag{7.44}$$

where

$$c(x,z) = -\frac{1}{f}\frac{\partial f}{\partial x} \tag{7.45}$$

and

$$d(x,z) = -\frac{1}{f}\frac{\partial f}{\partial z}. \tag{7.46}$$

In what follows we assume a grid evenly spaced in both x and z, and define ϕ_{ij} to be

$$\phi_{ij} = \phi(i\Delta, j\Delta), \tag{7.47}$$

and likewise for other quantities, where Δ is the step size. Throughout this section we make use of various centred difference approximations and their errors all of which are defined and given in appendix C.

In order to derive a fourth order accurate discretisation of the problem we firstly replace the derivatives in (7.44) with the standard centred difference operators to give

$$-\delta_x^2\phi_{ij} - \delta_y^2\phi_{ij} + c_{ij}\delta_x\phi_{ij} + d_{ij}\delta_y\phi_{ij} - \tau_{i,j} = 0, \tag{7.48}$$

where δ_x and δ_y are the centred difference operators and are all defined in appendix C. For example

$$\delta_x\phi_{ij} = \frac{\phi_{i+1j} - \phi_{i-1j}}{2\Delta}, \tag{7.49}$$

and so on. The quantity τ_{ij} is the total truncation error from introducing the centred difference approximations in (7.48) and is given by

$$\tau_{ij} = \frac{\Delta^2}{12}[2(c\frac{\partial^3\phi}{\partial x^3} + d\frac{\partial^3\phi}{\partial z^3}) - (\frac{\partial^4\phi}{\partial x^4} + \frac{\partial^4\phi}{\partial z^4})] + O(\Delta^4). \tag{7.50}$$

Ignoring this truncation error τ_{ij} gives an $O(\Delta^2)$ accurate discretisation of the problem. (It should be noted that a second-order accurate method has been attempted for the current problem of interest but convergence could only be achieved for a very narrow range of alignment angles α.) However, in order to secure $O(\Delta^4)$ accuracy we now seek approximations to the derivatives in (7.50) in order to include them in the finite difference formulation (7.48). We obtain expressions for these derivatives by differentiating the governing equation (7.44) to yield

$$\frac{\partial^3\phi}{\partial x^3} = -\frac{\partial^3\phi}{\partial x\partial z^2} + c\frac{\partial^2\phi}{\partial x^2} + \frac{\partial c}{\partial x}\frac{\partial\phi}{\partial x} + d\frac{\partial^2\phi}{\partial x\partial z} + \frac{\partial d}{\partial x}\frac{\partial\phi}{\partial z}, \tag{7.51}$$

$$\begin{aligned}\frac{\partial^4\phi}{\partial x^4} = &-\frac{\partial^4\phi}{\partial x^2\partial z^2} + c\frac{\partial^3\phi}{\partial x^3} + 2\frac{\partial c}{\partial x}\frac{\partial^2\phi}{\partial x^2} + \frac{\partial^2 c}{\partial x^2}\frac{\partial\phi}{\partial x} \\ &+d\frac{\partial^3\phi}{\partial x^2\partial z} + 2\frac{\partial d}{\partial x}\frac{\partial^2\phi}{\partial x\partial z} + \frac{\partial^2 d}{\partial x^2}\frac{\partial\phi}{\partial z},\end{aligned} \tag{7.52}$$

$$\frac{\partial^3\phi}{\partial z^3} = -\frac{\partial^3\phi}{\partial x^2\partial z} + c\frac{\partial^2\phi}{\partial x\partial z} + \frac{\partial c}{\partial z}\frac{\partial\phi}{\partial x} + d\frac{\partial^2\phi}{\partial z^2} + \frac{\partial d}{\partial z}\frac{\partial\phi}{\partial z}, \tag{7.53}$$

$$\frac{\partial^4\phi}{\partial z^4} = -\frac{\partial^4\phi}{\partial x^2\partial z^2} + c\frac{\partial^3\phi}{\partial x\partial z^2} + 2\frac{\partial c}{\partial z}\frac{\partial^2\phi}{\partial x\partial z} + \frac{\partial^2 c}{\partial z^2}\frac{\partial\phi}{\partial x}$$

$$+d\frac{\partial^3\phi}{\partial z^3}+2\frac{\partial d}{\partial z}\frac{\partial^2\phi}{\partial z^2}+\frac{\partial^2 d}{\partial z^2}\frac{\partial\phi}{\partial z}. \tag{7.54}$$

Now each of the ϕ derivative terms on the right-hand sides of equations (7.51) - (7.54) has compact $O(\Delta^2)$ approximations at each node ij (see appendix C for a complete list of the approximations and operators). For example if we take the first of the derivatives in equation (7.51), it can be expressed as

$$\frac{\partial^3\phi}{\partial x\partial z^2}=\delta_x\delta_z^2\phi_{ij}-\frac{\Delta^2}{12}[2\frac{\partial^5\phi}{\partial x^3\partial z^2}+\frac{\partial^5\phi}{\partial x\partial z^4}]+O(\Delta^4), \tag{7.55}$$

and so on for all the other terms. All of the terms on the left-hand side of equations (7.51) - (7.54) therefore have $O(\Delta^2)$ accurate approximations.

If we return to considering the truncation error τ_{ij}, each of the derivative terms on the right hand side of (7.50) can now be replaced by the expressions given in equations (7.51) - (7.54). In turn the derivatives on the right-hand side of (7.51) - (7.54) can be replaced by the compact approximations as discussed just above along with $O(h^2)$ errors, as demonstrated in equation (7.55). The $O(\Delta^2)$ errors from these difference approximations now lead to $O(\Delta^4)$ errors in the truncation error equation and as such are now incorporated into the $O(\Delta^4)$ terms.

Replacing the truncation error as described above the discretisation of (7.44) becomes

$$\begin{aligned}&-A_{ij}\delta_x^2\phi_{ij}-B_{ij}\delta_z^2\phi_{ij}+C_{ij}\delta_x\phi_{ij}+D_{ij}\delta_z\phi ij+\\&\frac{\Delta^2}{6}[\delta_x^2\delta_z^2\phi_{ij}-c_{ij}\delta_x\delta_z^2\phi_{ij}-d_{ij}\delta_x^2\delta_z\phi_{ij}-G_{ij}\delta_x\delta_z\phi_{ij}]+O(\Delta^4)=0,\end{aligned} \tag{7.56}$$

where

$$A_{ij} \;=\; 1+\frac{\Delta^2}{12}(c_{ij}^2-2\delta_x c_{ij}), \tag{7.57}$$

$$B_{ij} = 1 + \frac{\Delta^2}{12}(d_{ij}^2 - 2\delta_z d_{ij}), \tag{7.58}$$

$$C_{ij} = c_{ij} + \frac{\Delta^2}{12}(\delta_x^2 c_{ij} + \delta_z^2 c_{ij} - c_{ij}\delta_x c_{ij} - d_{ij}\delta_z c_{ij}), \tag{7.59}$$

$$D_{ij} = d_{ij} + \frac{\Delta^2}{12}(\delta_x^2 d_{ij} + \delta_z^2 d_{ij} - c_{ij}\delta_x d_{ij} - d_{ij}\delta_z d_{ij}), \tag{7.60}$$

$$G_{ij} = \delta_z c_{ij} + \delta_x d_{ij} - c_{ij} d_{ij}. \tag{7.61}$$

The $O(\Delta^2)$ terms in (7.56) - (7.60) are from the expansion of the truncation error. Finally, expanding the forms for the finite difference operators in equation (7.56) (as given in appendix C), we obtain the complete compact discretisation, accurate to $O(\Delta^4)$. It is given by

$$\begin{aligned} &NW\phi_{i-1j+1} + N\phi_{ij+1} + NE\phi_{i+1j+1} + W\phi_{i-1j} \\ &+M\phi_{ij} + E\phi_{i+1j} + SW\phi_{i-1j-1} + S\phi_{ij-1} + SE\phi_{i+1j-1} = 0, \end{aligned} \tag{7.62}$$

where the coefficients are:

$$NW = -\frac{1}{6\Delta^2} - \frac{c_{ij}}{12\Delta} + \frac{d_{ij}}{12\Delta} - \frac{G_{ij}}{24}, \tag{7.63}$$

$$N = -\frac{B_{ij}}{\Delta^2} + \frac{D_{ij}}{2h} + \frac{1}{3\Delta^2} - \frac{d_{ij}}{6\Delta}, \tag{7.64}$$

$$NE = -\frac{1}{6\Delta^2} + \frac{c_{ij}}{12\Delta} + \frac{d_{ij}}{12\Delta} + \frac{G_{ij}}{24}, \tag{7.65}$$

$$W = -\frac{A_{ij}}{\Delta^2} - \frac{C_{ij}}{2\Delta} + \frac{1}{3\Delta^2} + \frac{c_{ij}}{6\Delta}, \tag{7.66}$$

$$M = 2\frac{A_{ij}}{\Delta^2} + 2\frac{B_{ij}}{\Delta^2} - \frac{2}{3\Delta^2}, \tag{7.67}$$

$$E = -\frac{A_{ij}}{\Delta^2} + \frac{C_{ij}}{2\Delta} + \frac{1}{3\Delta^2} - \frac{c_{ij}}{6\Delta}, \tag{7.68}$$

$$SW = -\frac{1}{6\Delta^2} - \frac{c_{ij}}{12\Delta} - \frac{d_{ij}}{12\Delta} + \frac{G_{ij}}{24},, \tag{7.69}$$

$$S = -\frac{B_{ij}}{\Delta^2} - \frac{D_{ij}}{2\Delta} + \frac{1}{3\Delta^2} + \frac{d_{ij}}{6\Delta}, \tag{7.70}$$

$$SE = -\frac{1}{6\Delta^2} + \frac{c_{ij}}{12\Delta} - \frac{d_{ij}}{12\Delta} - \frac{G_{ij}}{24}. \tag{7.71}$$

So this determines the discretisation of the governing equation and we are now left to determine an $O(\Delta^4)$ accurate way of fixing the boundary condition on the outflow edge, equation (7.43). In other words we need to find an $O(\Delta^4)$ accurate discretization of the boundary condition

$$(\frac{\partial\phi}{\partial x})^2 + (\frac{\partial\phi}{\partial z})^2 = 1. \tag{7.72}$$

If we consider the $\frac{\partial\phi}{\partial x}$ term first, the centred difference approximation is given by

$$(\frac{\partial\phi}{\partial x})^2 = (\delta_x\phi_{ij} - \frac{\Delta^2}{6}\frac{\partial^3\phi}{\partial x^3} + O(\Delta^4))^2. \tag{7.73}$$

Expanding this equation and ignoring terms of $O(\Delta^4)$ leads to

$$(\frac{\partial\phi}{\partial x})^2 = (\delta_x\phi_{ij})^2 - \frac{\Delta^2}{3}\delta_x\phi_{ij}\frac{\partial^3\phi}{\partial x^3}. \tag{7.74}$$

However, as determined earlier, we can replace $\frac{\partial^3\phi}{\partial x^3}$ by a centred difference approximation with an $O(\Delta^2)$ error (as in equation (7.51)). Performing this operation, and carrying out the identical procedure for $\frac{\partial^3\phi}{\partial z^3}$ gives

$$\begin{aligned}&(\delta_x\phi_{ij})^2 - \frac{\Delta^2}{3}\delta_x\phi_{ij}(-\delta_x\delta_z^2\phi_{ij} + c_{ij}\delta_x^2\phi_{ij} + d\delta_x\delta_z\phi_{ij})\\ -\ &\frac{\Delta^2}{3}\delta_z\phi_{ij}(-\delta_z\delta_x^2\phi_{ij} + c_{ij}\delta_x\delta_z\phi_{ij} + d_{ij}\delta_z^2\phi_{ij}) = 1,\end{aligned} \tag{7.75}$$

to fourth order accuracy. On each boundary then we also have to deal with grid points laying beyond the planform boundary(at $x = 1+\Delta$ for example). As usual we deal with these points by applying the discretisation of the governing equation on the boundary (at $x = 1$ for example) and combine it with the boundary condition (7.75) to eliminate the extra points from the discretisation. The other major problem is the nonlinearity of the boundary conditions. This can prove problematic but with the iteration regime employed here, iterating point-by-point around the planform,

the condition is simplified to solving a quadratic equation for ϕ_{ij} at each boundary point. An alternative, which also proved successful, is to lag the non-linear terms in ϕ_{ij}, using the previous guess for the solution at the current station, enabling the solution to be iterated line-by-line.

Unfortunately there still remains an unresolved issue at the outflow-outflow corner $x = 1$, $z = 1/2$. This is somewhat problematic as, due to the restricted geometry, we were unable to derive a compact difference formulation using the above method. Several methods of applying the boundary condition at this corner point were tried, of which two proved successful. Firstly, we attempted to used only an $O(\Delta^2)$ accurate version at the corner point (while keeping $O(\Delta^4)$ accuracy elsewhere). The method seemed to work but is obviously not satisfactory in an overall $O(\Delta^4)$ accurate scheme. Secondly, we decided to maintain the $O(\Delta^4)$ accuracy and instead abandon the compact grid at the corner point. As such we used an $O(\Delta^4)$ accurate, five point one-sided difference expansion at the corner. So for example $\frac{\partial \phi}{\partial x}$ at the corner is given by

$$\frac{\partial \phi}{\partial x} = \frac{1}{12\Delta}[25\phi_{N_x N_z} - 48\phi_{N_x-1 N_z} + 36\phi_{N_x-2 N_z} - 16\phi_{N_x-3 N_z} + 3\phi_{N_x-4 N_z}], \quad (7.76)$$

where $N_x = 1/\Delta$, $N_z = 1/(2\Delta)$ are the number of grid points in the x and z directions, respectively. The $\frac{\partial \phi}{\partial z}$ term is treated similarly.

So we now have a full, $O(\Delta^4)$ accurate, discretisation of our problem and are in a position to solve it. In light of the nonlinear boundary conditions on the outflow edges it was found to be easier to iterate point-by-point rather than line-by-line as the boundary conditions were more straightforward to apply, effectively becoming linear in the iteration. It was also necessary to use under-relaxation in order to

achieve convergence at some angles α.

7.5 Results

In this section we present numerical results, obtained using the method detailed in 7.4, showing the velocities and pressure produced for various alignment angles α ranging from $\alpha = 45^o$ to $\alpha = 7.5^o$. Figures 7.3 to 7.6 show these quantities as x varies for various values of z.

Obtaining convergence at modest angles ($15 < \alpha < 45$) is relatively straightforward, however if we reduce the angle further convergence becomes increasingly more difficult to obtain. In fact the smallest angle for which we achieved convergence was $\alpha = 7.5^o$, the results for which are presented in figure 7.7. One matter to note from this small angle case is the normal velocity, w, along $z = 1/2$. Whereas in the previous examples the velocity was $O(1)$, it now appears to be tending towards zero with a minimum only just above zero near $x = 0.65$. It is thought that reducing α further could mean that this ceases to be an outflow point altogether and we would have a cross-over point, with the outflow switching to inflow. This could explain the failure of the numerical scheme as the assumption that the cross-over points are only at the corners would no longer be valid, and at present the method does not incorporate a change-over of boundary conditions.

Further evidence that a cross-over point may be approaching is given in figures 7.8 and 7.9 which show the streamlines for the $\alpha = 25^o$ case and the small angle $\alpha = 7.5^o$ case. It can be seen that, while in the 25^o case the streamlines clearly enter through the $x = 0$ and $z = 0$ edges, leaving through the trailing edges, in the $\alpha = 7.5^o$ case

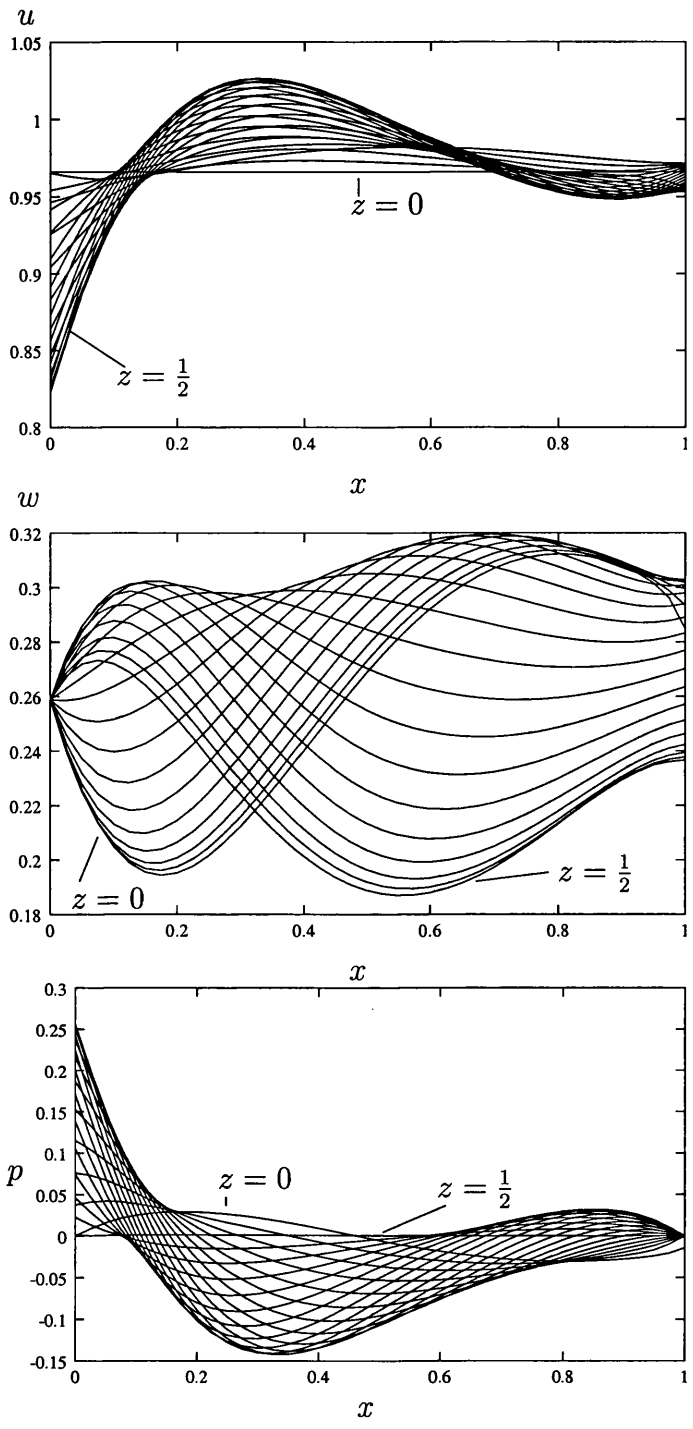

Figure 7.3: Velocity profiles and pressure for $\alpha = 15^o$, showing the values as x varies for different z values.

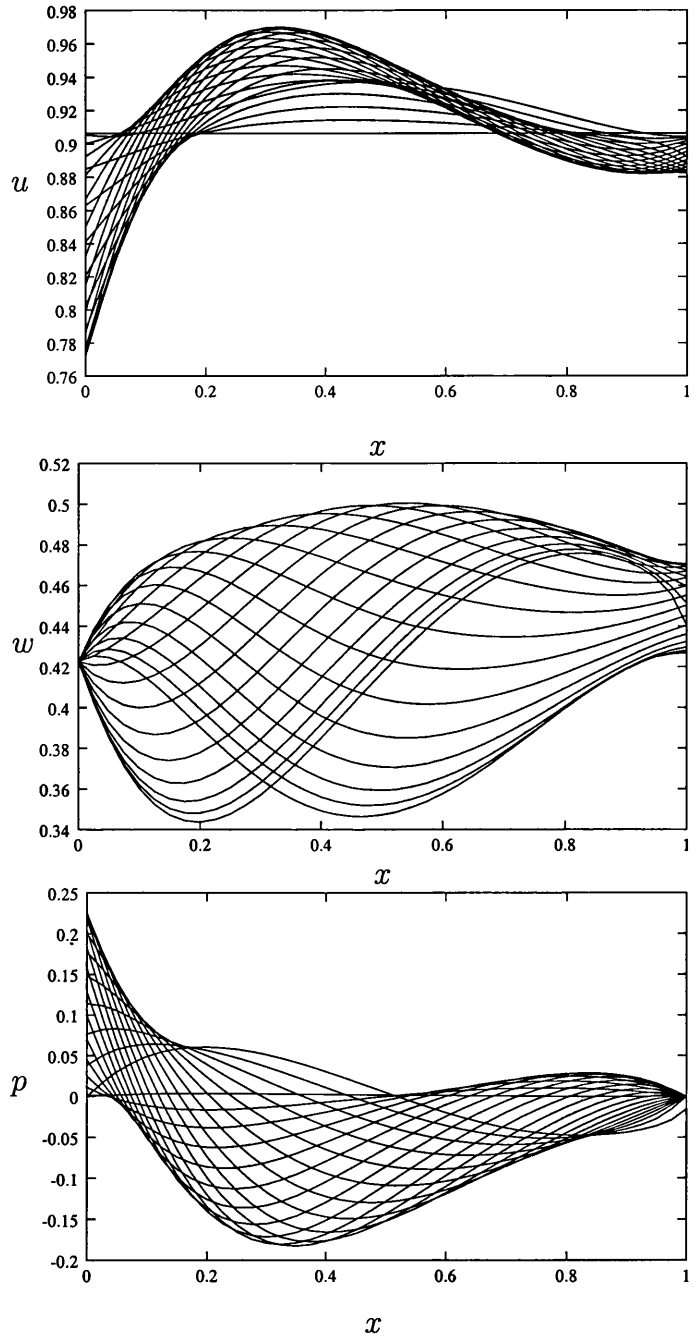

Figure 7.4: As figure 7.3 but for $\alpha = 25^o$.

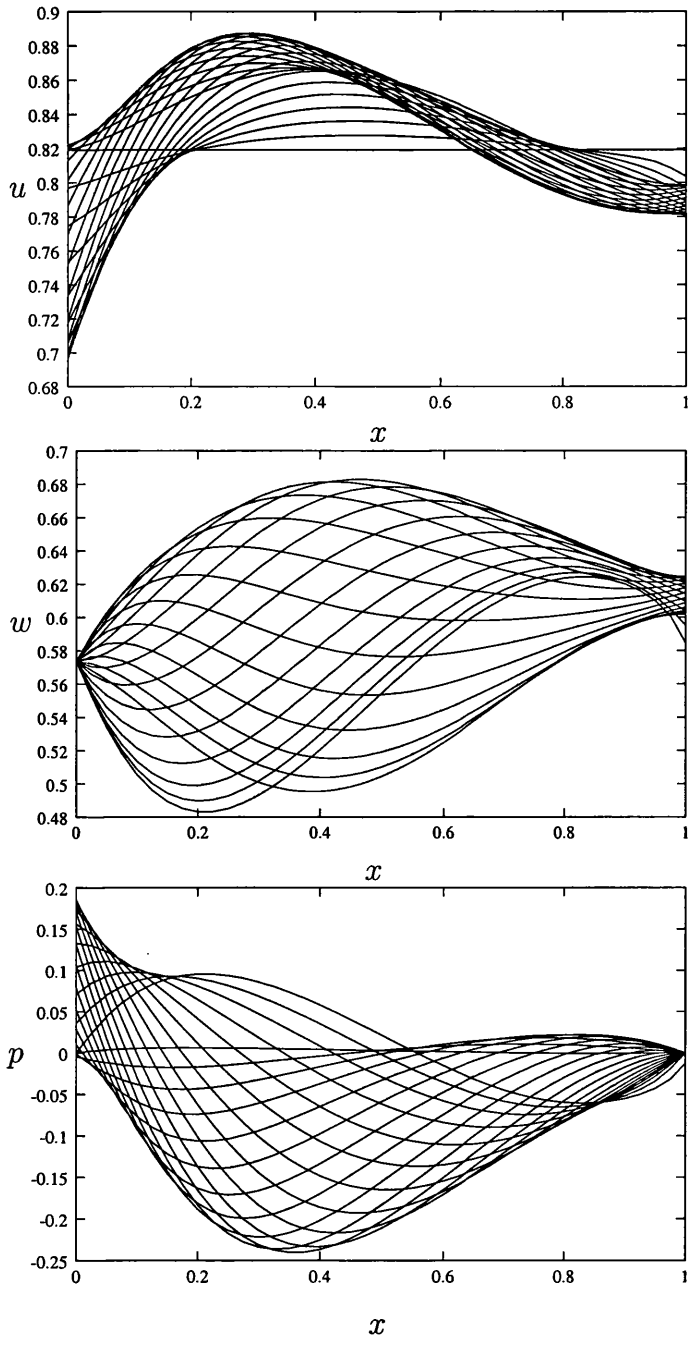

Figure 7.5: As figure 7.3 but for $\alpha = 35^o$.

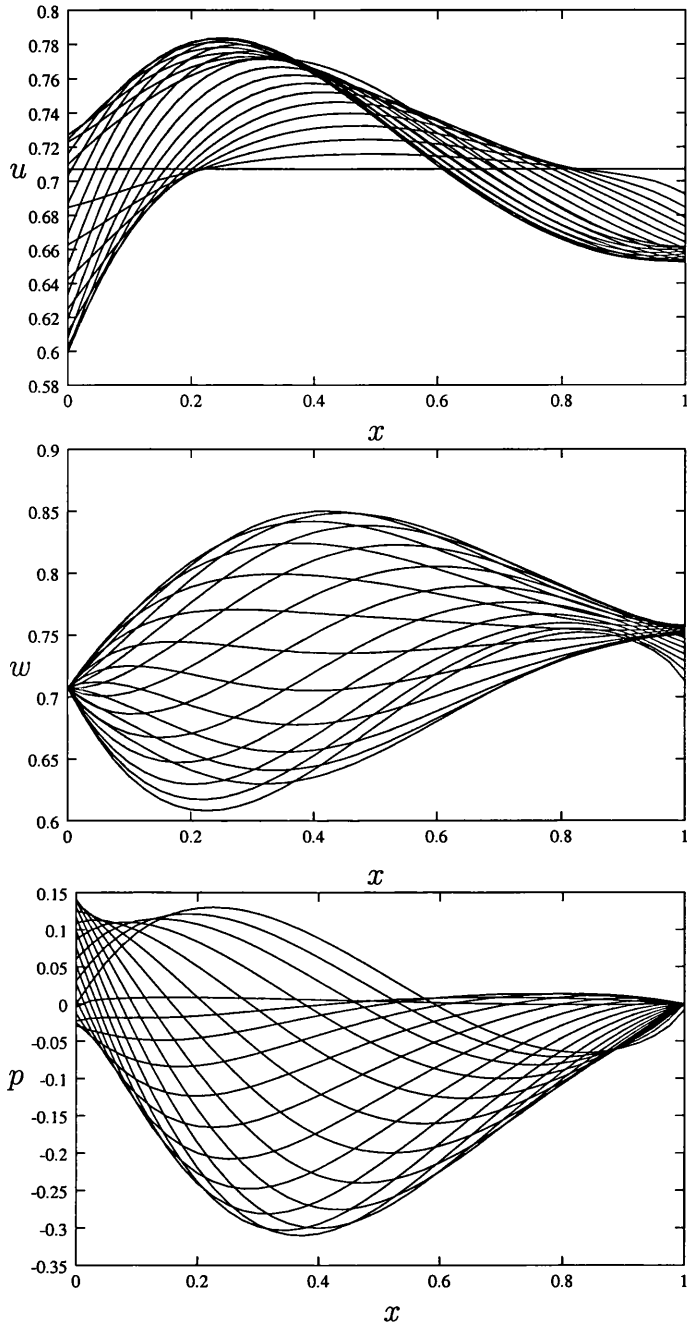

Figure 7.6: As figure 7.3 but for $\alpha = 45^o$.

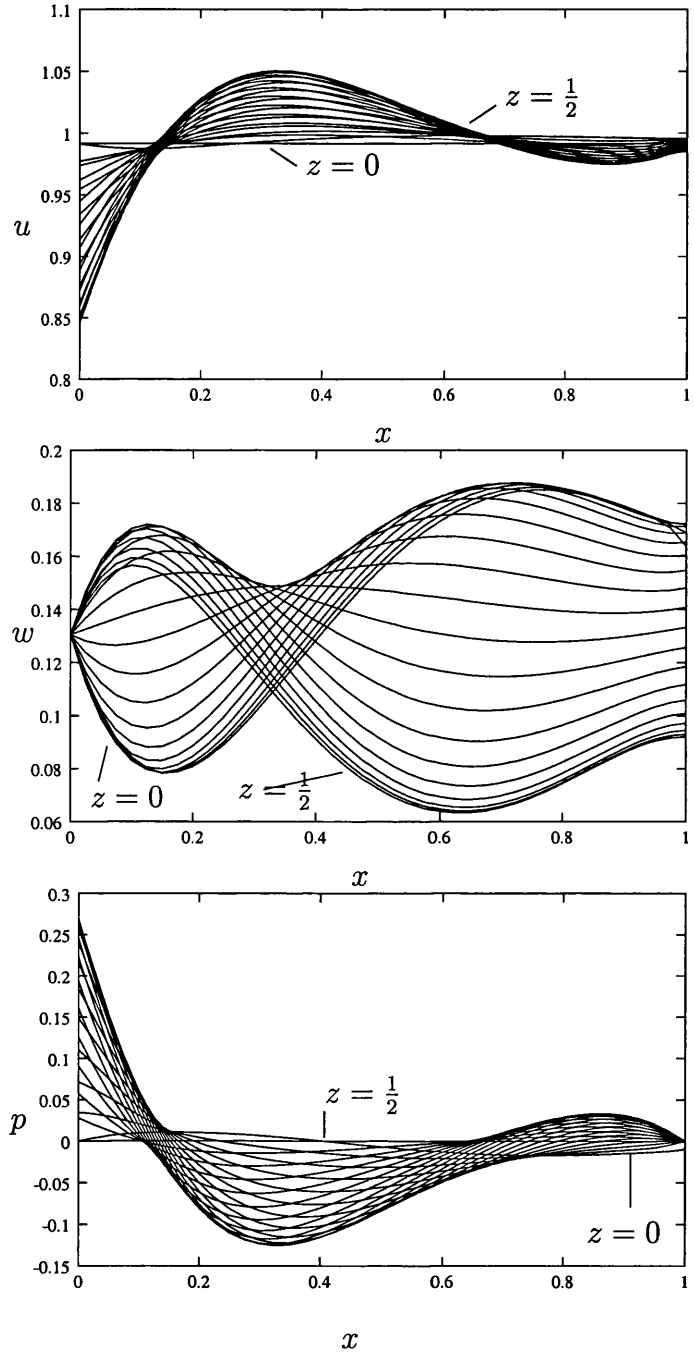

Figure 7.7: As figure 7.3 but for $\alpha = 7.5^o$.

it is not so clear as the streamlines run almost parallel to the $z = 1/2$ edge, once again suggesting the outflow is being significantly reduced.

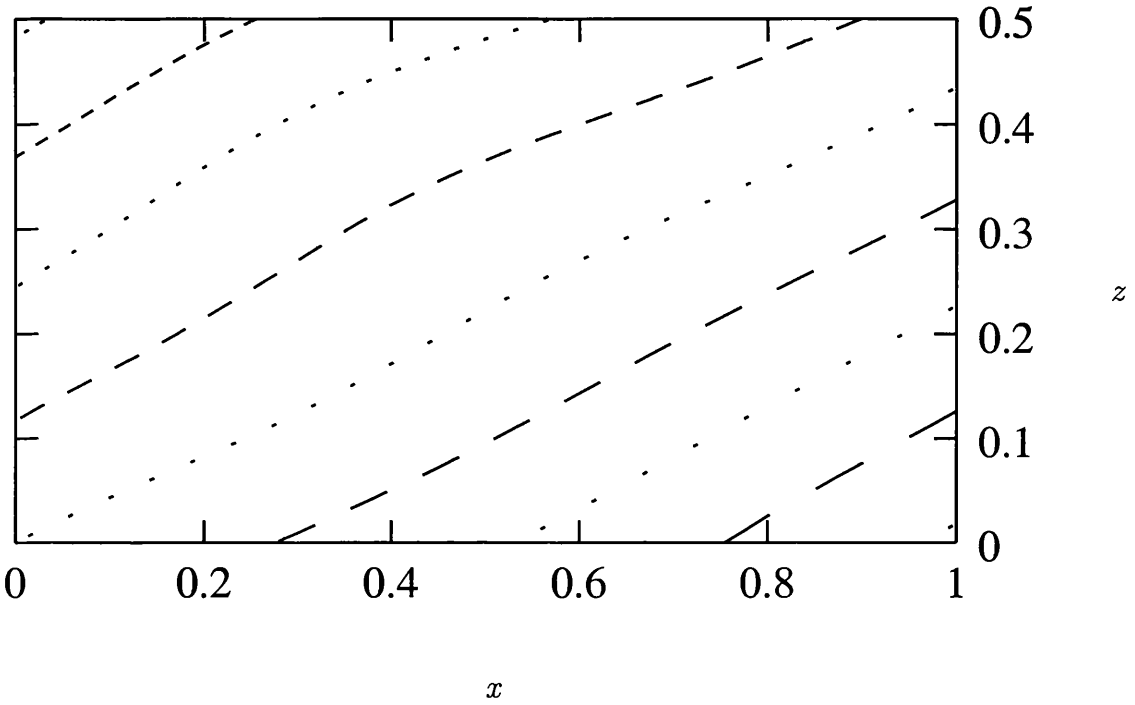

Figure 7.8: Streamlines for $\alpha = 25^o$.

Observe in the results the reduced pressure and increased velocities in the middle in line with the presence of the narrowest gap there. The well of reduced pressure points to a downforce on the blade. These results are found to agree with those presented in Jones and Smith (2000).

7.6 Local analysis

There are four localised regions that, guided by the numerical results, seem worthy of further investigation: the local flow near the corners (inflow-inflow, outflow-outflow

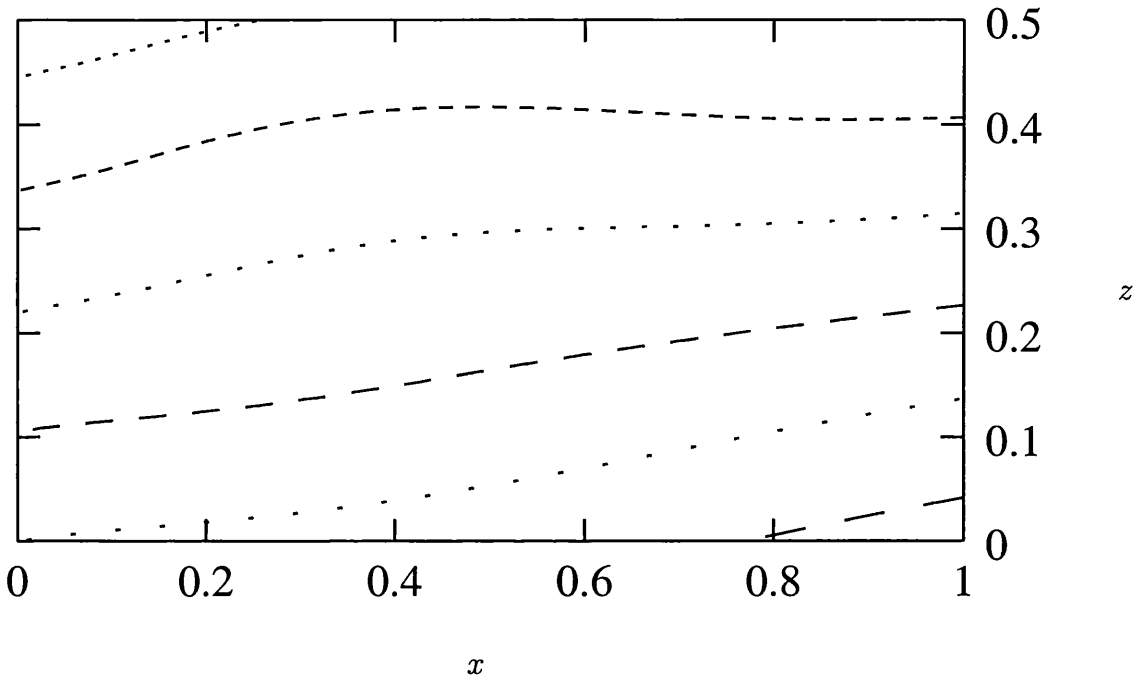

Figure 7.9: Streamlines for $\alpha = 7.5^o$.

and inflow-outflow) and the case where an inflow edge is on the verge of becoming an outflow one when the normal velocity becomes small. We consider each in turn here.

7.6.1 Inflow-inflow corner

Firstly we consider the inflow-inflow corner around $x = 0$, $z = 0$ as in figure 7.10.

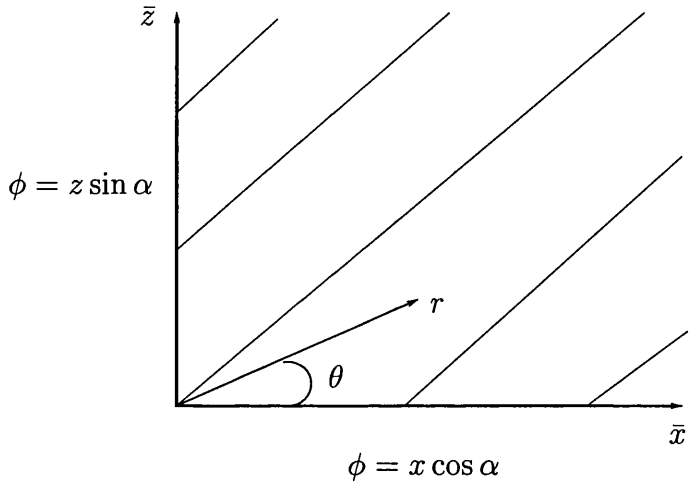

Figure 7.10: Flow geometry and co-ordinates for the inflow-inflow corner.

We introduce the local co-ordinates $\bar{x}$ and $\bar{z}$ given by $x = \epsilon\bar{x}$ and $z = \epsilon\bar{z}$, respectively. This change of co-ordinates gives the local undertray shape as

$$f(\bar{x}, \bar{z}) = 1 - \epsilon^3 \frac{\Gamma}{4} \bar{x}\bar{z}^2. \tag{7.77}$$

Substitution of the new co-ordinates and the expansion of the underbody shape implies the form

$$\phi(\bar{x}, \bar{z}) = x \cos\alpha + z \sin\alpha + \epsilon^2 \phi_2, \tag{7.78}$$

for the velocity potential which satisfies the boundary conditions at the edges $\bar{x} = 0$ and $\bar{z} = 0$ and leads to the problem

$$\nabla^2 \phi_2 = 0, \tag{7.79}$$

to be solved subject to, in polar co-ordinates (see figure 7.10)

$$\phi_2 = 0 \quad \text{on} \quad \theta = 0, \frac{\pi}{2}. \tag{7.80}$$

The solution of this problem is given by

$$\phi_2 = a_2 r^2 \sin 2\theta, \tag{7.81}$$

where a_2 is an undetermined constant, dependent on the global solution. If we consider this solution at $\theta = 0$ for example we obtain the velocities given by

$$u = \cos\alpha + \ldots, \tag{7.82}$$

$$w = \sin\alpha + \epsilon^2 a_2 x + \ldots. \tag{7.83}$$

The implied linear trend in w and u being effectively a constant varying with α both fit comfortably with the numerical results presented in section 7.5 near the inflow-inflow corner.

7.6.2 Outflow-outflow corner

We move from the inflow-inflow corner to examine the flow at the opposite end near the outflow-outflow corner in the vicinity of $x = 1$, $z = 1/2$ as in figure 7.11. As such we consider the local co-ordinates defined as

$$x = 1 + \epsilon\bar{x}, \tag{7.84}$$

$$z = \frac{1}{2} + \epsilon\bar{z}. \tag{7.85}$$

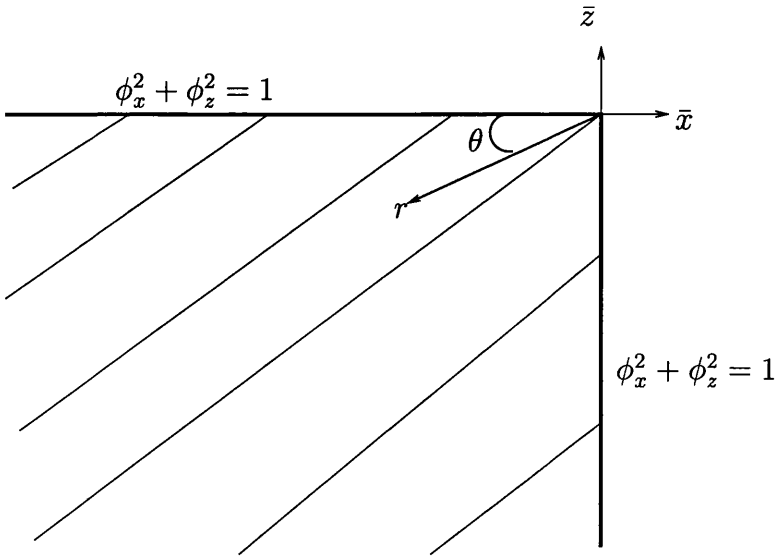

Figure 7.11: Flow geometry and co-ordinates for the outflow-outflow corner.

Substituting into the form for f these co-ordinates imply

$$f(\bar{x}, \bar{z}) = 1 - \epsilon^4 \frac{\Gamma}{4} \bar{x}^2 \bar{z}^2 + \dots . \tag{7.86}$$

Considering the governing equation along with these expansions suggest the form

$$\phi = (x \cos\alpha + z \sin\alpha) + \epsilon^3 \phi_3(\bar{x}, \bar{z}) + \dots , \tag{7.87}$$

for the velocity potential ϕ. Substituting the form of ϕ, along with the local co-ordinates and expanded form for f, shows the governing equation and boundary conditions identically satisfied at leading order (by the $(x \cos\alpha + z \sin\alpha)$ part) and the problem for ϕ_3 to be Laplace's equation

$$\nabla^2 \phi_3 = 0, \tag{7.88}$$

subject to the boundary conditions which at this order become

$$\cos\alpha \frac{\partial \phi_3}{\partial \bar{x}} + \sin\alpha \frac{\partial \phi_3}{\partial \bar{z}} = 0 \quad \text{on} \quad \bar{z} = 0 \quad \text{and on} \quad \bar{x} = 0. \tag{7.89}$$

We solve this using polar coordinates defined as $\bar{x} = -r\cos\theta$, $\bar{z} = -r\sin\theta$ (see also figure 7.11) and arrive at the solution

$$\phi_3 = b_3 r^3 \sin(3\theta + \alpha) + b_1 r \sin(\theta + \alpha), \tag{7.90}$$

where b_3 and b_1 are unknown constants. So for example, on $\theta = 0$ (or alternatively $\bar{z} = 0$) the velocities expand as

$$u = \cos\alpha - \epsilon^3 \sin\alpha(3b_3x^2 + b_1), \tag{7.91}$$

$$v = \sin\alpha + \epsilon^3 \cos\alpha(3b_3x^2 + b_1), \tag{7.92}$$

which once again appear consistent with section 7.5.

7.6.3 Inflow-outflow corner

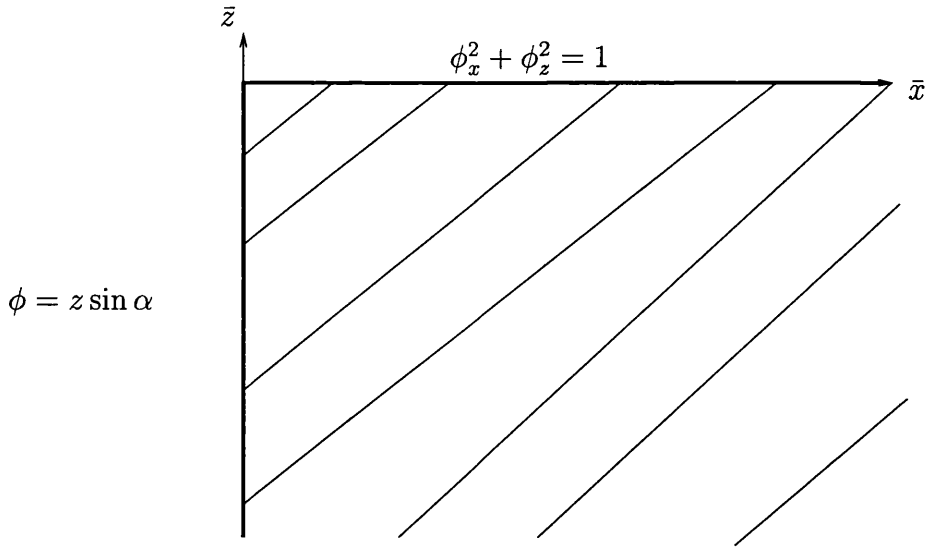

Figure 7.12: Flow geometry and co-ordinates for the inflow-outflow corner.

We move now to examine the flow at the inflow-outflow corner in the vicinity of $x = 0$, $z = 1/2$ as in figure 7.12. In contrast to the previous two corners this

time we must deal with mixed boundary conditions. As before we introduce local co-ordinates, now defined as

$$x = \epsilon\bar{x}, \tag{7.93}$$

$$z = \frac{1}{2} + \epsilon\bar{z}. \tag{7.94}$$

Substituting into the form for f these co-ordinates imply

$$f(\bar{x},\bar{z}) = 1 - \epsilon^4\frac{\Gamma}{4}\bar{x}^2\bar{z}^2 + \ldots. \tag{7.95}$$

Considering the governing equation along with these expansions suggest the form

$$\phi = (x\cos\alpha + z\sin\alpha) + \epsilon^n\bar{\phi}(\bar{x},\bar{z}) + \ldots, \tag{7.96}$$

for the velocity potential ϕ. Substituting the form of ϕ, along with the local co-ordinates and expanded form for f, shows the governing equation and boundary conditions identically satisfied at leading order (by the $(x\cos\alpha + z\sin\alpha)$ part) and the problem for $\bar{\phi}$ to be Laplace's equation

$$\nabla^2\bar{\phi} = 0, \tag{7.97}$$

subject to

$$\bar{\phi} = 0 \quad \text{on} \quad \theta = -\frac{\pi}{2}, \tag{7.98}$$

$$\cos\alpha\frac{\partial\bar{\phi}}{\partial r} + \frac{\sin\alpha}{r}\frac{\partial\phi}{\partial z} = 0 \quad \text{on} \quad \theta = 0, \tag{7.99}$$

with polar co-ordinates as defined earlier. Laplace's equation yields solutions in the form

$$\bar{\phi} = \sum_0^\infty r^n(a_n\cos(n\theta) + b_n\sin(n\theta)). \tag{7.100}$$

Equation (7.98) requires

$$a_n \cos\frac{n\pi}{2} = b_n \sin\frac{n\pi}{2}, \tag{7.101}$$

while boundary condition (7.99) requires

$$a_n \cos\alpha = -b_n \sin\alpha, \tag{7.102}$$

in order to be satisfied. Combining these gives

$$a_n(\cos\alpha \sin\frac{n\pi}{2} + \cos\frac{n\pi}{2}\sin\alpha) = 0, \tag{7.103}$$

implying

$$\sin(\frac{n\pi}{2} + \alpha) = 0, \tag{7.104}$$

and that

$$n = 2k - \frac{2\alpha}{\pi}, \quad \text{with} \quad k = 1, 2, 3, \ldots \tag{7.105}$$

such that $n > 1$ for the solution to remain finite. So, for example, with $\alpha = \pi/4$ we obtain

$$\bar{\phi} \sim r^{3/2}(a_{3/2}\cos(\frac{3\theta}{2}) + b_{3/2}\sin(\frac{3\theta}{2})) + O(r^{7/2}). \tag{7.106}$$

Once again this can be reasonably compared with the numerical results of the previous section 7.5. For example see figure 7.6 near $z = 1/2$, $x = 0$ where (7.106) implies

$$w \sim \cos\alpha + \epsilon^{3/2}\frac{3}{2}a_{3/2}\bar{z}^{1/2}, \tag{7.107}$$

comparing well with the numerical results. Likewise for other α values.

7.6.4 Nearing an inflow-to-outflow (cross-over) point

As discussed earlier the numerical method works well if the angle of alignment of the blade α is not too close to either zero or $\pi/2$. Once α leaves this range convergence

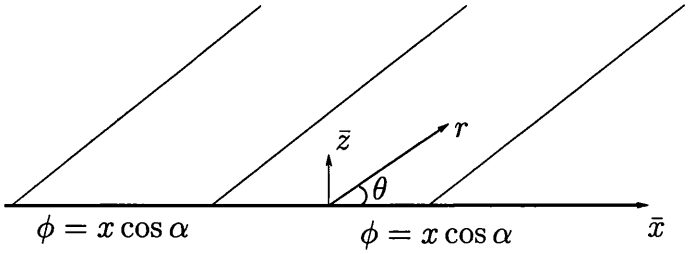

Figure 7.13: Flow geometry and co-ordinates for the inflow edge near x_0 where the normal velocity approaches zero as a potential cross-over point is reached

is impossible to obtain and this is believed to be caused by the assumption that the cross-over points are situated at the corners breaks down. Instead, at least on one side if not both, there is numerical evidence that the flow is approaching a cross-over point with the velocity perpendicular to the edge going towards zero. In order to examine this local region we look at the side $z = 0$ and, assuming the velocity is approaching zero near $x = x_0$, we introduce the local coordinates

$$x = x_0 + \epsilon\bar{x}, \tag{7.108}$$

$$z = \epsilon\bar{z}, \tag{7.109}$$

with ϵ once again small. Once again the shape of the undertray is unimportant to leading order and we expand the velocity potential as

$$\phi = x_0\cos\alpha + \epsilon\bar{x}\cos\alpha + \epsilon^3\bar{\phi} + \ldots, \tag{7.110}$$

where the lower order terms satisfy the governing equation and single boundary condition $\phi = x\cos\alpha$ on $z = 0$ identically. The normal velocity $w = \frac{\partial\phi}{\partial z} \sim O(\epsilon^3)$ is also small (as assumed) and we are left with

$$\nabla^2\bar{\phi} = 0, \tag{7.111}$$

subject to

$$\bar{\phi} = 0 \quad \text{on} \quad \bar{z} = 0. \tag{7.112}$$

Once again we adopt polar coordinates (now defined as $\bar{x} = r\cos\theta$, $\bar{z} = r\sin\theta$) and, using the standard known solutions of Laplace's equation we obtain

$$\bar{\phi} = \sum_{1}^{3} a_n r^n \sin(n\theta). \tag{7.113}$$

As we have assumed x_0 to be the cross over point, in order to have the minimum perpendicular velocity there we require $a_2 = 0$ giving

$$\bar{\phi} = a_3 r^3 \sin(3\theta) + a_1 r \sin\theta \tag{7.114}$$

and the tangential and normal velocities as

$$u = \cos\alpha + \epsilon^3 6 a_3 \bar{x}\bar{z} + \ldots, \tag{7.115}$$

$$w = \epsilon^3[3a_3(x^2 + z^2) + a_1] + \ldots, \tag{7.116}$$

respectively. This implies that locally the normal velocity w should have a parabolic form. Such a form is in qualitative agreement with the numerical results for $\alpha = 7.5^o$. As discussed above, for smaller angles the numerical method breaks down.

Chapter 8

Conclusions and Further Work

8.1 Summary

In Chapter 2 we studied the flow induced by an axisymmetric disc rotating close to the ground; specifically concentrating on the distortion of the layer shape beyond the disc rim induced by the presence of the ground. The relevance of the problem to a general rotor blade was discussed and the far-field response for any slender, bounded rotor blade was determined. The full problem was then considered, initially via an approximate pressure continuity condition, examining the impact of varying the height of the disc above the ground and the impact of a body shape positioned beneath the disc. As might have been expected the layer shape becomes increasingly distorted from the horizontal as the height of the disc is decreased. The solution method was then shown to be readily extendable to a more physically accurate pressure condition dependent on the layer shape.

We considered in Chapter 3 the flow past a sequence of thin aerofoils traveling

parallel with and close to the ground. This required treatment of both the viscous boundary layer problem and the inviscid potential flow which become coupled in this many blade context. The outer, inviscid problem required pressure continuity upstream, in each of the wakes and at each trailing edge. The inviscid solution was determined in the form of two coupled singular integral equations; one of which had to be solved first to give the lift distribution across each of the blades before the remainder of the solution could be determined. This then fed back into the boundary layer problem via unknown y-shifts in the wake centre-line shapes. Two asymptotic limits were considered, those of small and large ground clearances. The pressure difference (or lift) on each blade was seen to increase as the inverse of the ground clearance as the height of the blades was reduced.

In Chapter 4 the periodic limit of the problem discussed in Chapter 3 was examined. This arises after sufficiently many blades have been passed at which stage the flow was shown to take on a relatively simple form. The boundary layer part of the solution effectively splits into two parts, one slowly growing as increasingly more blades are passed and an inner layer that is periodic, varying only over the shorter leading edge to leading edge period. The problem still required coupling with the inviscid problem which was solved as above except that now the periodicity allowed some simplification.

Abandoning ground effect temporarily, the subject of Chapter 5 was interactive flow past multiple three-dimensional blades. It was shown that once an $O(Re^{3/5})$ number of blades have been passed a new interaction appears which is distinct from those discussed before, with the pressure now entering the boundary-layer equations. Once again a two tier structure was detected in the boundary layer and the solution in the

periodic innermost tier was considered before examining a physically important case of short blades. The flow structure and some possible solutions were determined, driven by the requirement that the pressure be periodic across each blade-wake period. The pressure was found to drop abruptly across the short blade requiring the pressure to grow slowly through the relatively long wake to match at the subsequent leading edge.

In Chapter 6 the flow past the trailing corner of a rotating blade was considered via a prior investigation of the flow past a three-dimensional hump embedded within a three dimensional boundary layer. The linearised version of the flow past a hump was examined using the Fourier transform and two distinct corridor effects were observed and confirmed by analytical considerations. The solution shed much light on the trailing corner problem, specifically presenting a possible mechanism for the triple deck structure and the jet-induced double deck structure combining at the corner.

Finally, Chapter 7 returned to investigating ground effect, studying a solitary, three-dimensional blade in extreme ground effect, operating very close to the ground. The two-dimensional problem and the relevance to the many blade case were discussed before a compact-difference numerical scheme was derived to investigate a particular three-dimensional case. The specific problems associated with a three dimensional blade were discussed, where the inflow and outflow edges (and their distinct boundary conditions) are unknown in advance.

The highlights of the present study are felt to be within Chapters 3, 5 and 7, speifically the handling of the unusual viscous-inviscid interactions including ground effect, the examination of three-dimensional blade-wake interactions and the likewise

new features found for a three-dimensional blade very near the ground.

8.2 Further work

The investigations in this thesis have thrown up various avenues for further work. In the opinion of the author some of the most interesting include the following:

1. Further investigation is necessary into the flow with three-dimensional blades discussed in chapter 7. In particular a greater understanding of the inflow-outflow cross-over points is required before further progress can be made on a general blade shape. One possible technique for determining their position could be to assume their location initially, solve the problem and then check if the inflow and outflow edges are all consistent with the initial assumption, leading to an updated guess at the cross-over positions.

2. Greater study of the three-dimensional interactive cases of chapter 5 could prove fruitful. It may be possible to extend the short blade analysis to cover the case of finite blades, examining the blade tip, or to non-symmetric blades (for small non-symmetries in the current regime). Short blade analysis could also be extended to cover general non-symmetric three-dimensional blades, or lifting cases, possibly requiring pressure adjustment at the leading edge as in Bowles and Smith (2000b). Study of the full problem for general blades, both symmetric and non-symmetric, would also be appropriate.

3. Further investigation into the trailing corner problem of chapter 6 could likewise prove useful. Not only is confirmation required on the assumed structure

but a detailed examination of the blade tip problem could lend some insight into the generation of tip vortices.

4. Obviously the solution for a general three-dimensional non-symmetric system of rotor blades (near to or away from the ground) is still very difficult but some progress may be made there also. It would require a coupling of a three-dimensional boundary-layer solution with the solution of the outer inviscid problem. While the boundary layer part can be solved (Smith and Timoshin (1996a)) the major sticking point remains the outer problem requiring a solution of Laplace's equation for the pressure on each side of the rotor subject to matching with the boundary layer and pressure continuity in the wakes. Whether the axisymmetric approach used for the disc in chapter 2 could be extended (perhaps via a panel method for the entire problem) remains to be seen.

Appendix A

Some Standard Results

This Appendix outlines various standard results utilised in the main text. No attempt is made to derive the solutions here. All the quantities in this appendix are assumed to be suitably non-dimensionalised.

A.1 The Blasius solution for the flow past a flat plate

Firstly we consider the boundary layer on the surface of a flat plate as considered by Blasius (1908). It is a solution of the two dimensional boundary layer equations

$$\frac{\partial u}{\partial x} + \frac{\partial v}{\partial y} = 0, \tag{A.1}$$

$$u\frac{\partial u}{\partial x} + v\frac{\partial u}{\partial y} = \frac{\partial^2 u}{\partial y^2}. \tag{A.2}$$

These need to be solved subject to the boundary conditions

$$u = v = 0 \quad \text{on} \quad y = 0, \tag{A.3}$$

$$u \rightarrow 1 \quad \text{as} \quad y \rightarrow \infty, \tag{A.4}$$

$$u = 1 \quad \text{upstream}, \tag{A.5}$$

which are the no-slip conditions on the plate and matching with the free-stream $u = 1$, both for large y and upstream.

The Blasius solution takes the form

$$u = f'(\eta), \tag{A.6}$$

$$v = (\frac{1}{2x})^{1/2}(\eta f'(\eta) - f(\eta)), \tag{A.7}$$

where

$$\eta = (\frac{1}{2x})^{1/2} y, \tag{A.8}$$

and the function $f(\eta)$ satisfies the ordinary differential equation

$$f''' + f f'' = 0. \tag{A.9}$$

The boundary conditions become, in terms of f,

$$f(0) = f'(0) = 0, \quad f'(\infty) = 1. \tag{A.10}$$

A.2 The Von Karman solution for the flow induced by an infinite rotating disc

The Von Karman solution, Von Karman (1921), is the solution for an infinite rotating disc lying in the plane z=0. In this case the velocities (u, v, w) are given, in terms of cylindrical polar co-ordinates (r, z, θ), by

$$u = r f'(z), \tag{A.11}$$

$$v = -2f(z), \tag{A.12}$$

$$w = rg(z). \tag{A.13}$$

The unknown functions f and g are found to satisfy the equations

$$(f')^2 - 2ff'' - g^2 - f''' = 0, \tag{A.14}$$

$$2(f'g - fg') = g'', \tag{A.15}$$

which must be solved subject to

$$f(0) = f'(0) = 0, \quad g(0) = 1, \tag{A.16}$$

$$f' \to 0, \quad g \to 0 \quad \text{as} \quad z \to \infty. \tag{A.17}$$

A.3 The triple-deck structure

The triple-deck structure introduced by Stewartson (1969) and Messiter (1970) was found to be necessary to resolve the flow at the trailing edge of a flat plate. It has subsequently been applied to many other problems such as the flow past a surface roughness and the separation of a boundary layer. It is based upon a three-tier representation of the flow structure: an inner viscous sublayer, the lower deck, the viscous main deck and an inviscid outer tier, the upper deck. The structure has an x-scale defined by $x = Re^{-3/8}X$.

In the main deck, where $y = Re^{-1/2}Y$, the solution takes on the relatively simple linearised form

$$u(X,Y) = u_b(Y) + Re^{-1/8}A(X)u_b'(Y) + \ldots, \tag{A.18}$$

$$v(X,Y) = -Re^{-1/4}A'(X)u_b(Y) + \ldots, \tag{A.19}$$

$$p(X,Y) = Re^{-1/4}P(X) + \ldots, \tag{A.20}$$

where $A(X)$ is an unknown function and u_b is the oncoming Blasius flow.

In the upper deck, where $y = Re^{-3/8}\hat{y}$, we find

$$u(X,\hat{y}) = 1 + Re^{-1/4}\hat{u}(X,\hat{y}) + \ldots, \tag{A.21}$$

$$v(X,\hat{y} = Re^{-1/4}\hat{v}(X,\hat{y}) + \ldots, \tag{A.22}$$

$$p(X,\hat{y}) = Re^{-1/4}\hat{p}(X,\hat{y}) + \ldots. \tag{A.23}$$

The solution in this region leads to the pressure-displacement interaction law which takes the form

$$P(x) = -\frac{1}{\pi}\int_{-\infty}^{\infty}\frac{A'(\xi)}{\xi - x}\mathrm{d}\xi. \tag{A.24}$$

The lower deck, where $y = Re^{-5/8}\tilde{y}$, has a solution of the form

$$u(X,\tilde{y}) = Re^{-1/8}\tilde{u}(X,\tilde{y}) + \ldots, \tag{A.25}$$

$$v(X,\tilde{y}) = Re^{-3/8}\tilde{v}(X,\tilde{y}) + \ldots, \tag{A.26}$$

$$p(X,\tilde{y}) = Re^{-1/4}P(X). \tag{A.27}$$

The problem to be solved in this lower deck is then

$$\frac{\partial\tilde{u}}{\partial X} + \frac{\partial\tilde{v}}{\partial\tilde{y}} = 0, \tag{A.28}$$

$$\tilde{u}\frac{\partial\tilde{u}}{\partial X} + \tilde{v}\frac{\partial\tilde{u}}{\partial\tilde{y}} = -P'(X) + \frac{\partial^2\tilde{u}}{\partial\tilde{y}^2}, \tag{A.29}$$

subject to no-slip or symmetry conditions at $\tilde{y} = 0$, a matching condition with the main deck and a matching condition upstream. $A(X)$ is determined by matching with the main deck via the condition

$$\tilde{u} \sim \lambda(\tilde{y} + A(X)) \quad \text{as} \quad \tilde{y} \to \infty, \tag{A.30}$$

where λ denotes $\mathrm{d}u_b/\mathrm{d}Y$ at $Y = 0$. This lower deck problem must be solved in conjunction with the pressure displacement law (A.24).

A.4 The double-deck structure

While the triple-deck structure is appropriate as Blasius flow or any boundary layer beneath a non-zero stream passes over a trailing edge (or a surface roughness, etc.), a different representation is required when a wall jet approaches a trailing edge, such as at the rim of a rotating disc. This problem was investigated by Smith (1978) and Smith and Duck (1977). The important x length scale in this case is given by $x = Re^{-3/7}X$ rather than the $O(Re^{-3/8})$ scale for the triple deck case. In the current circumstances the solution essentially divides into two parts (the double deck).

Firstly in region I, when $y \sim O(Re^{-1/2})$, the velocities take the form

$$u = u_0(y) + Re^{-1/7}u_1(X,y) + \ldots, \tag{A.31}$$

$$v = Re^{-3/14}v_1(X,y) + \ldots, \tag{A.32}$$

$$p = Re^{-2/7}p_1(X,y) + \ldots, \tag{A.33}$$

where $u_0(y) \geq 0$ is the velocity profile of the approaching jet, satisfying $u_0(\infty) = 0$, $u_0(0) = 0$, $u_0'(0) = \lambda$. These lead to the solutions

$$u_1 = A(X)u_0'(y), \tag{A.34}$$

$$v_1 = -A'(X)u_0(y), \tag{A.35}$$

$$\frac{\partial p_1}{\partial y} = -u_0(y)\frac{\partial v_1}{\partial X} = A''(X)u_0^2, \tag{A.36}$$

where $A(X)$ is an unknown function. This then yields the relation

$$p_1(X,y) = P(X) + A''(X)\int_o^y u_0^2 \mathrm{d}y. \tag{A.37}$$

In order to ensure $p_1 \to 0$ as $y \to \infty$ we require

$$P(X) = -\gamma A''(X) \quad \text{where} \quad \gamma = \int_0^\infty u_0^2 \mathrm{d}y. \tag{A.38}$$

Taking $\gamma = 1$ gives the pressure-displacement interaction law

$$P(X) = -A''(X). \tag{A.39}$$

The second region occurs near the wall, with $y = Re^{-1/7}\hat{y}$. The velocities and pressure are expanded as

$$u = Re^{-1/7}\hat{u} + \ldots, \tag{A.40}$$

$$v = Re^{-5/14}\hat{v} + \ldots, \tag{A.41}$$

$$p = Re^{-2/7}P(X), \tag{A.42}$$

leading to the viscous governing equations

$$\frac{\partial \hat{u}}{\partial X} + \frac{\partial \hat{v}}{\partial \hat{y}} = 0, \tag{A.43}$$

$$\hat{u}\frac{\partial \hat{u}}{\partial X} + \hat{v}\frac{\partial \hat{u}}{\partial \hat{y}} = -P'(x) + \frac{\partial^2 \hat{u}}{\partial \hat{y}^2}. \tag{A.44}$$

These must be solved subject to

$$\hat{u} = \hat{v} = 0 \quad \text{at} \quad \hat{y} = 0, \tag{A.45}$$

$$\hat{u} \sim \frac{1}{2}\lambda(\hat{y} + A(X)) \quad \text{as} \quad \hat{y} \to \infty, \tag{A.46}$$

which are the no-slip conditions and matching with zone I.

Appendix B

Mean Blasius Flow in the Interactive Regime

This appendix determines the higher order terms in the main deck of chapter 5. The next order governing equations are given by

$$\frac{\partial u_2}{\partial x} + \frac{\partial v_2}{\partial y} + \frac{\partial w_1}{\partial z} = 0, \tag{B.1}$$

$$u_0\frac{\partial u_2}{\partial x} + u_1\frac{\partial u_1}{\partial x} + v_2\frac{\partial u_0}{\partial y} + v_1\frac{\partial u_1}{\partial y} = -\frac{\partial p_1}{\partial x}, \tag{B.2}$$

$$u_0\frac{\partial w_2}{\partial x} + u_1\frac{\partial w_1}{\partial x} + v_1\frac{\partial w_1}{\partial y} = -\frac{\partial p_2}{\partial z}. \tag{B.3}$$

Substituting from equation (B.1) for u_2 into (B.2) and inserting the known expressions for u_1, v_1, w_1 from chapter 5, we obtain, after a little rearrangement,

$$\frac{\partial}{\partial y}(\frac{v_2}{u_0}) = -A\frac{\partial A}{\partial x}\frac{\partial}{\partial y}(\frac{\frac{\partial u_0}{\partial y}}{u_0}) + \frac{\frac{\partial p_1}{\partial x}}{u_0^2} - \frac{\frac{\partial D}{\partial z}}{u_0^2}. \tag{B.4}$$

Integrating with respect to y gives an expression of v_2:

$$v_2 = -A\frac{\partial A}{\partial x}\frac{\partial u_0}{\partial y} + u_0(\frac{\partial p_1}{\partial x} - \frac{\partial D}{\partial z})\int \frac{1}{u_0^2}\mathrm{d}y + \frac{\partial B}{\partial x}u_0, \tag{B.5}$$

where $B(x,z)$ is an arbitrary function corresponding to a displacement effect. Continuity, equation (B.1), then yields u_2 as

$$u_2 = \frac{A^2}{2}\frac{\partial^2 u_0}{\partial y^2} + B\frac{\partial u_0}{\partial y} - \frac{p_1}{u_0} - \frac{\partial u_0}{\partial y}\int \frac{1}{u_0^2}\mathrm{d}y \int (\frac{\partial p_1}{\partial x} - \frac{\partial D}{\partial z})\mathrm{d}x. \tag{B.6}$$

At the next order still the continuity and streamwise momentum equations are given by

$$\frac{\partial u_0}{\partial x_L} + \frac{\partial u_3}{\partial x} + \frac{\partial v_3}{\partial y} + \frac{\partial w_2}{\partial z} = 0, \tag{B.7}$$

$$\begin{aligned} u_0\frac{\partial u_0}{\partial x_L} + u_1\frac{\partial u_2}{\partial x} + u_0\frac{\partial u_3}{\partial x} + u_2\frac{\partial u_1}{\partial x} \\ +v_1\frac{\partial u_2}{\partial y} + v_2\frac{\partial u_1}{\partial y} + v_3\frac{\partial u_0}{\partial y} + w_1\frac{\partial u_1}{\partial z} &= -\frac{\partial p_2}{\partial x} + \frac{\partial^2 u_0}{\partial y^2}. \end{aligned} \tag{B.8}$$

Considering (B.7) first, if we integrate over the L-period with respect to x, followed by integrating over the L_1-period with respect to z we obtain

$$\frac{\partial u_0}{\partial x_L} + \frac{\partial \hat{v_3}}{\partial y} = 0, \tag{B.9}$$

where $\hat{v_3} = \frac{1}{LL_1}\int_0^{L_1}\int_0^{L} v_3 \mathrm{d}x\mathrm{d}z$ is the mean value of v_3 in x and z.

If we now consider (B.8) we re-write it as

$$u_0\frac{\partial u_0}{\partial x_L} + u_0\frac{\partial u_3}{\partial x} + v_3\frac{\partial u_0}{\partial y} + \frac{\partial}{\partial x}(u_1u_2) + v_1\frac{\partial u_2}{\partial y} + v_2\frac{\partial u_1}{\partial y} + w_1\frac{\partial u_1}{\partial z} = -\frac{\partial p_2}{\partial x} + \frac{\partial^2 u_0}{\partial y^2}. \tag{B.10}$$

Most of the terms here can be dealt with directly by integrating over the relevant period as in the previous paragraph. However three of the terms require closer inspection, namely

$$v_1\frac{\partial u_2}{\partial y} + v_2\frac{\partial u_1}{\partial y} + w_1\frac{\partial u_1}{\partial z}, \tag{B.11}$$

where all the velocity terms are known. Substituting the known forms from chapter 5 and from above these terms (B.11) become, after some rearrangement,

$$u_0 \quad \frac{\partial^2 u_0}{\partial y^2}[-\frac{\partial}{\partial x}(AB) - \frac{1}{3}\frac{\partial(A^3)}{\partial x}] + u_0\frac{\partial u_0}{\partial y}\int \frac{1}{u_0^2}\mathrm{d}y\frac{\partial}{\partial x}[A\int(\frac{\partial p_1}{\partial x} - \frac{\partial D}{\partial z})\mathrm{d}x]$$

$$+ \quad \frac{\frac{\partial u_0}{\partial y}}{u_0}[D\frac{\partial A}{\partial z} - p_1\frac{\partial A}{\partial x} + \frac{\partial A}{\partial x}\int(\frac{\partial p_1}{\partial x} - \frac{\partial D}{\partial z})\mathrm{d}x.] - \frac{1}{6}\frac{\partial(A^3)}{\partial x}\frac{\partial^3 u_0}{\partial y^3}. \tag{B.12}$$

It can be shown that integration of this expression (B.12) over the x and z periods, applying periodicity in the velocities, pressure and displacements, leaves zero; some terms giving zero directly with others requiring an integration by parts first. Thus if we integrate (B.8) over the x and z periods and apply the periodicity conditions we obtain

$$u_0\frac{\partial u_0}{\partial x_L} + \hat{v_3}\frac{\partial u_0}{\partial y} = \frac{\partial^2 u_0}{\partial y^2}. \tag{B.13}$$

Equations (B.9) and (B.13) are those for the Blasius boundary layer and, as in chapter 4, satisfy the same boundary conditions. Therefore in this three-dimensional case we still find that, as in the two-dimensional and non-interactive cases for many blades, the middle deck contains mean Blasius flow.

Appendix C

Truncation Errors and Difference Operators

We list here the difference operators and the associated truncation errors for various derivative terms used in chapter 7 of the thesis.

C.1 Difference operators

The expansions of various differentials used in the main text:

$$\frac{\partial \phi}{\partial x} = \delta_x \phi_{ij} - \frac{\Delta^2}{6}\frac{\partial^3 \phi}{\partial x^3} + O(\Delta^4), \tag{C.1}$$

$$\frac{\partial^2 \phi}{\partial x^2} = \delta^2 \phi_{ij} - \frac{\Delta^2}{12}\frac{\partial^4 \phi}{\partial x^4} + O(\Delta^4), \tag{C.2}$$

$$\frac{\partial^2 \phi}{\partial x \partial z} = \delta_x \delta_z \phi_{ij} - \frac{\Delta^2}{6}[\frac{\partial^4 \phi}{\partial x^3 \partial z} + \frac{\partial^4 \phi}{\partial x \partial z^3}] + O(\Delta^4), \tag{C.3}$$

$$\frac{\partial^3 \phi}{\partial x \partial z^2} = \delta_x \delta_z^2 \phi_{ij} - \frac{\Delta^2}{12}[\frac{\partial^5 \phi}{\partial x^4 \partial z} + 2\frac{\partial^5 \phi}{\partial x^2 \partial z^3}] + O(\Delta^4), \tag{C.4}$$

$$\frac{\partial^3 \phi}{\partial x^2 \partial z} = \delta_x^2 \delta_z \phi_{ij} - \frac{\Delta^2}{12}[\frac{\partial^5 \phi}{\partial x^4 \partial z} + 2\frac{\partial^5 \phi}{\partial x^2 \partial z^3}] + O(\Delta^4), \tag{C.5}$$

$$\frac{\partial^4\phi}{\partial x^2\partial z^2} = \delta_x^2\delta_z^2\phi_{ij} - \frac{\Delta^2}{12}[\frac{\partial^6\phi}{\partial x^4\partial z^2} + \frac{\partial^6\phi}{\partial x^2\partial z^4}] + O(\Delta^4). \tag{C.6}$$

C.2 The δ-operators

The definitions of the various δ difference operators used in the text and above:

$$\delta_x\phi_{ij} = \frac{\phi_{i+1j} - \phi_{i-1j}}{2\Delta}, \tag{C.7}$$

$$\delta_x^2\phi_{ij} = \frac{\phi_{i+1j} - 2\phi_{ij} + \phi_{i-1j}}{\Delta^2}, \tag{C.8}$$

$$\delta_x\delta_z\phi_{ij} = \frac{\phi_{i+1j+1} - \phi_{i-1j+1} - \phi_{i+1j-1} + \phi_{i-1j-1}}{4\Delta^2}, \tag{C.9}$$

$$\delta_x^2\delta_z\phi_{ij} = \frac{2(\phi_{ij-1} - \phi_{ij+1}) + \phi_{i+1j+1} - \phi_{i+1j-1} + \phi_{i-1j+1} - \phi_{i-1j-1}}{2\Delta^3}, \tag{C.10}$$

$$\delta_x\delta_z^2\phi_{ij} = \frac{2(\phi_{i-1j} - \phi_{i+1j}) + \phi_{i+1j+1} - \phi_{i-1j+1} + \phi_{i+1j-1} - \phi_{i-1j-1}}{2\Delta^3}, \tag{C.11}$$

$$\delta_x^2\delta_z^2\phi_{ij} = \frac{4\phi_{ij} - 2(\phi_{i+1j} + \phi_{i-1j} - \phi_{ij+1} + \phi_{ij-1})}{\Delta^4} + \frac{\phi_{i+1j+1} + \phi_{i+1j-1} + \phi_{i-1j+1} + \phi_{i-1j-1}}{\Delta^4}. \tag{C.12}$$

Bibliography

M. Abramowitz and I. A. Stegun , 1972, *Handbook of Mathematical Functions*, Dover.

G. K. Batchelor, 1967, *Introduction to Fluid Dynamics.* Cambridge University Press.

B. De Bernardinis and D. W. Moore, 1986 , A ring vortex representation of an axi-symmetric vortex sheet, in *Studies of Vortex Dominated Flows* (ed. M. Y. Hussain and M. D. Salas), Springer ,33 – 43

H Blasius, 1908. *Z. Math Phys*, 56, 1-37 (Translated as "the boundary layers in fluids with little friction", *Tech. Memo. Math. advis. comm. aeronaut*, Wash., no 1256.).

D.B. Bliss and W.O. Miller, 1990, efficient free wake calculations using analytical numerical matching, *J. AM. Hel. Soc.*, **39th**.

R. G. A. Bowles and F. T. Smith, 2000a, Interactive flow past multiple blades and wakes, *Quart. J. Mech. and Appl. Math.*,**53**, 207 – 251.

R. G. A. Bowles and F. T. Smith, 2000b, Lifting multi-blade flows with interaction, *J. Fluid Mech.*, **415**, 203 – 226.

A R S Bramwell, 1976, *Helicopter Dynamics.* Edward Arnold.

F.X. Caradonna, 1992, The application of CFD to rotary wing aircraft. *NASA TM 102803.*

F.X. Caradonna and C. Tung, 1981, Experimental and analytical studies of a model helicopter rotor in hover, *NASA TM 81232.*

C. F. Carey and W. F. Spotz, 1997, Higher-order compact mixed methods, *Communications in numerical methods in engineering*, **13**, 553-564.

G. F. Carrier, M Krook and C. E. Pearson, 1966, *Functions of a Complex Variable*, McGraw-Hill Book Company.

A. T. Conlisk, 1997, Modern helicopter aerodynamics, *Ann. Rev. Fluid Mech.*, **21**, 515 – 567.

L. F. Crabtree, D. Kuchemann and L. Sowerby, 1963, in *Laminar Boundary Layers* (ed. L Rosenhead), chapter 8. Oxford University Press.

D. A. R. Davis, 1991, *On linear and nonlinear instability in boundary layers with cross flow.*, Ph.D. Thesis, University of London.

R. Debuchy, A. Dyment, H. Muhe, P. Michau, 1998, Radial inflow between a rotating and a stationary disc ,*Eur. J. Mech. B/Fluids*, **17**, 791 – 810.

P. W. Duck and O.R. Burggraf, 1986, Spectral solutions for three-dimensional triple-deck flow over surface topography, *J. Fluid Mech.*, **162**, 1 – 22.

T.A. Egolf and S.P Sparks, 1986, A full potential rotor analysis with wake influence using an inner-outer domain technique, *Prc. Annu. Forum Am. Hel. Soc.*, 42nd, 997 – 1011.

A. Gessow, 1986, Understanding and predicting helicopter behavior - then and now, *J. Am. Hel. Soc.*, **31(1)**,3 – 28.

A. Gessow and G. Myers, 1952, *Aerodynamics of helicopter.* New York: Fredrick Ungar

H. Glauert, 1937, *The Elements of Aerofoil and Airscrew Theory.* Cambridge University Press.

S.A. Gorton, D.R. Poling, L. Dadone, 1995, Laser velocimetry and blade pressure measurements of a blade-vortex interaction, *J. Am Hel. Soc.*, **40(2)**, 15 – 23.

I. S. Gradstein and I. M. Ryzhik, 1980 , *Tables of Integrals, Series and Products*, fifth edition. Academic Press

R. J. Hakkinen and N. Rott, 1962, Similar solutions for merging shear flows, *J. Aeorspace Sciences*, **29**, 1134.

R. J. Hakkinen and N. Rott, 1965, Similar solutions for merging shear flows ii, *AIAA*, **3**, 1553.

A.A. Hassan, C. Tung, L.N. Sankar, 1992, Euler solutions for self-generated rotor blade-vortex interactions, *Int. J. Num. Meth. Fluids*, **15**, 427 – 51.

J. L. Hess, 1990, Panel methods in computational fluid dynamics. *Annu. Rev. Fluid Mech.* **22**, 255 – 274.

J. L. Hess and A. M. O. Smith, 1967, Calculation of potential flow about arbitrary bodies, *Prog. in Aero. Sci.* **8**, 1 – 138.

D.R. Hoad, 1990, Rotor induced-inflow-ratio measurements and CAMRAD calculations, *NASA TP 2946*, **January 1990**.

D.R. Hoad, S.L. ALthoff and J.W. Wlliot, 1988, Rotor inflow variability with advance ratio, *Proc. of the 44th Annual Forum of the Am. Hel. Soc.*,Washington DC, June 16th-18th, 57 – 72.

W. Johnson, 1980, *Helicopter Theory.* Princeton University Press.

W. Johnson, 1986, Recent developments in rotor-wing aerodynamic theory. *AIAA J.*, **24(8)**, 1219 – 44.

M. A. Jones, 2000, *Mechanisms in Wing-In Ground Effect Aerodynamics*, Ph.D. Thesis, University of London.

M. A. Jones and F. T. Smith, 2000 (submitted), Fluid motion for car undertrays in ground effect, to appear in *Phil. Tran. Roy. Soc. A*, 2002.

Th. Von Karman, 1921, Uber laminare und turbulente reiburg. *Z. angew. math. mech.*, **1**, 233 – 251.

H. Lamb, 1932, *Hydrodynamics*, Cambridge University Press.

A. J. Landgrebe, 1972, The wake geometry of a hovering rotor and its influence on rotor performance, *J. Am. Hel. Soc.*, **17**, 3 – 15.

M. J. Lighthill, 1964, *Introduction to Fourier Analysis and Generalised Functions.* Cambridge University Press.

M. J. Lighthill, 1979, A simple fluid flow model of ground effect on hovering, *J. Fluid Mech.*, **93**, 781 – 797.

L.G. Loitsianskii, 1962, *Laminar Boundary Layer.* Moscow:Phismatgiz.

P.F. Lorber, 1991, Aerodynamic results of a pressure-instrumented model rotor test at the DNW, *J. Am. Hel. Soc.*, **36(4)**, 66 – 76.

K.W. McAlister, C.A. Schuler, L. Branum and J.C. Wu, 1995, 3-D measurements near a hovering rotor for determining profile and induced drag, *NASA TP 3577*, **August 1995**.

W.J. McCroskey, 1995, Vortex wakes of rotor craft, *AIAA paper 95-0530.*

A. F. Messiter, 1970, Boundary layer flow near the trailing edge of a flat plate. *SIAM J. Appl. Math.*, **18**, 241 – 257.

P. M. Morse and H. Feshbach, 1953, *Methods of Theoretical Physics (volumes I and II)*, McGraw-Hill Book Company.

N. I. Muskhelishvili, 1946, *Singular Integral Equations*, second edition. Noordhoff-Groningen-Holland.

J. N. Newman, 1982, Analysis of small-aspect-ration lifting surfaces in ground effect. *J. Fluid mech.*, **117**, 305 – 314.

S. Newman, 1994, *The foundations of helicopter flight*, Edward Arnold.

N. C. Ovenden, 2001, *The effect of increasing localized suction on a boundary layer and the generation of horseshoe vortices*, Ph.D. Thesis, University of London.

D.T. Papageorgiou and F. T. Smith, 1988, Non-Linear instability of the wake behind a flat plate placed parallel to a uniform stream, *Proc. R. Soc. Lond. A*,**419**,1 – 28.

S.P. Parthasarathy, Y.I. Cho and L.H. Black, 1985, Wide-field shadowgraph flow visualization of tip vortices generated by a helicopter rotor, *AIAA 85-1557*, **July 1985**.

J.J.Phillipe, P. Roesch, A.M. Dequin, A. Cler, 1985, A survey of recent developments in helicopter aerodynamics. *AGARD-LS-139, Helicopter Aeromechanics*, **April 1985**, 2 – 1 – 2 – 40.

W. H. Press, S. A. Teukolsky, W. T. Vetterling and B. P. Flannery, 1995, *Numerical Recipies in FORTRAN: the Art of Scientific Computing.*. Cambridge University Press.

K. Ramachandran, S. Schlechtriem, F.X. Caradonna, J Steinhoff, 1993, The application of vorticity embedding to the computation of advancing rotor flows, *Annu. Forum Am. Hel. Soc.*, 49th, May 19-21, 1993, 571 – 84.

G. Reichert, 1985, Helicopter aeromechanics - introduction and historical review. *AGARD-LS-139, Helicopter Aeromechanics*, **April 1985**, 1 – 1 – 1 – 23.

O.S. Rhyzov and Terent'ev, 1997, *Nonlinear waves in 3-D boundary layer*, IUTAM symposium on Nonlinear stability and transition in three-dimensional boundary layers.

J. Seddon, 1990, *Basic Helicopter Dynamics*, BSP Professional Books. Oxford.

F. T. Smith, 1973, Laminar flow over a small hump on a flat plate. *J. Fluid Mech.*, **57**, 803 – 24.

F. T. Smith, 1978, A Note On a Wall Jet Negotiating a Trailing Edge, *Quart. J. of Mech. and Applied Math.*,**Vol. XXXI Pt. 4**,473 – 479.

F. T. Smith, 1982, On the High Reynolds Number Theory of Laminar Flows, *IMA Journal of Applied Math.*,**28**, 207 – 281.

F. T. Smith, P. W. M. Brighton, P. S. Jackson and J. C. R. Hunt, 1981, On boundary-layer flow past two-dimensional obstacles, *J. Fluid. Mech.*, **113**, 123 – 152.

F. T. Smith and P. W. Duck, 1977, Separation of jets or thermal boundary layers from a wall, *Q. Jl. Mech. Appl. Math.*, **vol XXX**, part 2, 143 – 156.

F. T. Smith, R. I. Sykes and P. W. M. Brighton, 1977, A two-dimensional boundary layer encountering a three-dimensional hump, *J. Fluid Mech.*, **83**, 163 – 176..

F. T. Smith and S. N. Timoshin (1996a), Blade-wake interactions and rotary boundary layers, *Proc. Roy. Soc. A*, **452**, 1301 – 1329.

F. T. Smith and S. N. Timoshin, 1996b, Planar flows past thin multi-blade configurations, *J. Fluid Mech.* **324**, 355 – 377.

F. T. Smith and A. G. Walton, 1998, Flow past a two- or three-dimensional steep-edged roughness.,*Proc. R. Soc. A*, **454**.

W. F. Spotz, 1995, *High-Order Compact Finite Difference Schemes for Computational Mechanics*, Thesis, University of Texas at Austin.

W. F. Spotz, 1997, Accuracy and Performance of Numerical Wall Boundary Condi-

tions for Steady, two-dimensional, Incompressible Streamfunction Vorticity, *Int. J. Numer. Meth. Fluids*, **28**, 737 – 757.

W. F. Spotz and G. F. Carey, 1998, Iterative and Parallel Performance of High-Order Compact Systems, *SIAM J. Sci. COMPUT.*, **vol. 10**, No. 1, 1 – 14.

G.R. Srinivasan and L.N. Sankar, 1995, Status of Euler and Navier-Stokes CFD methods for helicopter applications, *Am. Hel. Soc. Specialists Meetin on Aeormechanics Technology and Product Design*, October 11-13, 1995.

W.Z. Steniewski and C. N. Keys, 1984, *Rotary-Wing Aerodynamics*, Vol. **I** and **II**. Dover.

K. Stewartson, 1969, On the flow near the trailing edge of a flat plate, *Mathematika*, **16**, 106 – 121.

K. Stewartson, 1970, On laminar boundary layers near corners, *Q. J. Mech. Appl. Math.*, **XXIII** part 2, 137 – 152.

R. I. Sykes, 1980, On three-dimensional boundary-layer flow over surface irregularities, *Prc. R. Soc*, **A373**, 311 – 329.

E. O. Tuck and T. M. Bentwich, 1983, Sliding sheets: lubrication with comparable viscous and inertia forces, *J. Fluid Mech.*, **41**, 769 – 792.

S. E. Widnall and T. M. Barrows, 1970, An analytical solution for two and three dimensional wings in ground effect, *J. Fluid Mech.*, **41**. 769 – 792.

J. Zbrozek, 1950, Ground effect on the lifting rotor, *Aero. Res. Counc. Rep. and Memor*, **no. 2347**.